Molecular control of actin cortex architecture during cell division

Neža Vadnjal

Supervisor:

Professor Ewa K. Paluch

Doctor of Philosophy

UCL

I, Neža Vadnjal, confirm that the work presented in this thesis is my own. Where information has been derived from other sources, I confirm that this has been indicated in the thesis.

Abstract

Animal cell shape is controlled by gradients in contractile tension of the actin cortex. The cortex is a thin actomyosin network supporting the plasma membrane. At the molecular level, contractile tension is generated by myosin motors pulling on actin filaments. Alongside myosin, actin connectivity has been shown to be key to cortical tension regulation. Understanding molecular organisation of the actin cortex is thus key to understanding cortical tension.

To understand how cortical composition changes when tension changes, and to identify potential molecular regulators of cortical tension, I firstly compared protein composition of interphase and mitotic cortices. Indeed, interphase and mitotic cells were previously shown to differ in cortical tension. I isolated cortical fractions from cells in these stages of cell cycle, by isolating cortex-enriched blebs. Using mass spectrometry, we detected over 922 proteins in blebs isolated from synchronised cells. Among 238 actin-related proteins, we showed a role for septins in the regulation of the mitotic cell shape. Overall, we created a comprehensive dataset of potential regulators of cortex mechanics.

In the second part of my PhD, I focused on the role of actin crosslinkers in cortex tension regulation. In particular, I focused on the role of actin crosslinker size for their localisation and in tension regulation. To this aim, we created artificial crosslinkers, for which I was able to modulate size independently of other features. We created artificial crosslinkers between 5 and 35 nm long, which successfully localised to actin structures. I investigated the role of artificial crosslinkers in the control of cortical thickness, tension and cell division.

Together, in this thesis, I investigate new levels of regulation of cortical organisation and tension at the molecular level.

Impact statement

Cell shape changes are key to a variety of fundamental physiological processes such as cell division, migration and animal morphogenesis. Animal cell shape is controlled by the cell cortex, a thin actomyosin network supporting the plasma membrane. In my thesis, I investigated how the cortex is organised at the molecular level.

In the first part of my PhD, I compared the protein composition of cortices isolated from cells with high and low tension. Mass spectrometry of isolated cortices was done in collaboration with Philippe Roux' lab (University of Montreal). The collaboration was important as the Roux lab's extensive expertise in mass spectrometry greatly complements the Paluch lab's expertise in studies of actin networks and cells. In this part of the project, we identified a dataset of potential regulators of cortical tension and cellular shape. This dataset resulted in a publication [Vadnjal et al., 2022] and will serve as a resource to cell and developmental biologists interested in the regulation of cell shape, and to biophysicists studying cell mechanics.

In a second part of my project, I investigated the role of protein size in actin cortex regulation. To this aim, we established a collaboration with Fabio Parmeggiani (University of Bristol). Through this collaboration we joined Dr. Parmeggiani's expertise in designing synthetic proteins and ours in cell biology and biomechanics. We created artificial crosslinkers for which we can modulate size independently of other features by changing the number of identical repeat domains and were able to express them in mammalian cells. These artificial crosslinkers will allow the investigation of crosslinker size in cortex tension generation and in the future can be expanded as a tool to study the organisation of other actin networks and eventually other cellular components. To expand the use of artificial crosslinkers and investigate how artificial crosslinkers organise reconstituted actin networks, we are also working with Guillaume Romet-Lemonne's and Anotine Jégou's lab (Institut Jacques Monod), whose lab has extensive expertise investigating actin *in vitro*.

Additionally, super-resolution microscopy techniques are essential for the study of the organisation of the actin cortex. I closely worked with the group of Ricardo Henriques, which allowed me to acquire the expertise in novel super-resolution microscopy approaches (such as DNA-PAINT and ExM) to study actin cortex organisation. These cross-disciplinary collaborations enabled us to use cutting-edge approaches from different disciplines and thus led to additional insight into understanding cell shape control.

Finally, during my PhD, Paluch lab relocated to University of Cambridge. I performed some of the experiments described in this thesis at the new lab, transitioning the expertise and linking the teams and my wider scientific communities at both universities.

UCL Research Paper Declaration Form: referencing the doctoral candidate's own published work(s)

Please use this form to declare if parts of your thesis are already available in another format, e.g. if data, text, or figures:

- have been uploaded to a preprint server;
- are in submission to a peer-reviewed publication;
- have been published in a peer-reviewed publication, e.g. journal, textbook.

This form should be completed as many times as necessary. For instance, if you have seven thesis chapters, two of which containing material that has already been published, you would complete this form twice.

1. For a research manuscript that has already been published (if not yet published, please skip to section 2)**:**		
a) Where was the work published? (e.g. journal name)	Journal of Cell Science	
b) Who published the work? (e.g. Elsevier/Oxford University Press):	Company of Biologists	
c) When was the work published?	26/08/2022	
d) Was the work subject to academic peer review?	Yes	
e) Have you retained the copyright for the work?	Yes	
[If no, please seek permission from the relevant publisher and check the box next to the below statement]: ☒ *I acknowledge permission of the publisher named under 1b to include in this thesis portions of the publication named as included in 1a.*		
2. For a research manuscript prepared for publication but that has not yet been published (if already published, please skip to section 3)**:**		
a) Has the manuscript been uploaded to a preprint server? (e.g. medRxiv):	Please select.	**If yes, which server?** Click or tap here to enter text.
b) Where is the work intended to be published? (e.g. names of journals that you are planning to submit to)	Click or tap here to enter text.	
c) List the manuscript's authors in the intended authorship order:	Click or tap here to enter text.	
d) Stage of publication	Please select.	

3. For multi-authored work, please give a statement of contribution covering all authors (if single-author, please skip to section 4**):**

Neza Vadnjal, Philippe Roux, and Ewa Paluch designed the research; Neza Vadnjal carried out most of the experiments. Geneviève Lavoie helped with mass spectrometry and qPCR; Neza Vadnjal, Sami Nourreddine, and Philippe Roux analysed the mass spectrometry data; Neza Vadnjal and Ewa Paluch wrote the paper; Murielle Serres provided technical support and conceptual advice.

4. In which chapter(s) of your thesis can this material be found?

Results: Interphase and mitotic cells differ in the protein composition of the actin cortex

5. e-Signatures confirming that the information above is accurate (this form should be co-signed by the supervisor/ senior author unless this is not appropriate, e.g. if the paper was a single-author work):

Candidate:	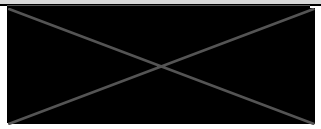	**Date:**	30/08/2022
Supervisor/ Senior Author (where appropriate)**:**	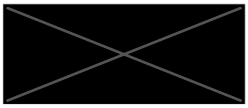	**Date:**	31/08/2022

Acknowledgements

Firstly, I want to thank the examiners, Nate Goehring and Margaret Gardel, for agreeing to read my thesis.

This thesis, the project, and my overall PhD would not have happened without Ewa. Ewa, thank you for introducing me to biophysics and the opportunity to work on such an interesting project in an interdisciplinary, fun environment. Although between the lab move and the pandemic, this journey was not always easy, I have never regretted joining your lab for my PhD.

This project would also not be what it is without multiple collaborators I got to work with in the last few years: Philippe Roux, Geneviève Lavoie, Sami Nourredine, Fabio Parmeggiani, Guillaume Romet-Lemonne, Antoine Jégou, and Alex Winkel. Thank you for contributing to this project and overall being great people to work with. I also want to thank Ricardo Henriques and his group for accepting me to their lab and helping me merge the expertise. I would also like to thank my thesis committee, Guillaume Charras, Alan Lowe, and Franck Pichaud for their advice in developing this project. Finally, I would like to thank Garance Dombret and Mark Carrington, who worked with me during their Master's and rotation projects, for helping to develop some of the ideas in this thesis and for being excellent students to work with.

I will always treasure the last few years for the amazing people I got to meet and spend my days with. I feel like I have overlapped with two generations of the lab, the one from London and the one from Cambridge. All of you made this time special for me. I am happy for the friendships I have built with so many of you also beyond the lab. As the name says, being part of the Paluch Lab Cool Kids Squad was truly cool and a great initiation to the lab: Sascha, we have been friends much longer than lab-mates but I still remember our first climb; Davide, your encouragement at the beginning of my PhD was

actually more significant than I realised at the time, thank you for that and for your everyday friendliness; Henry, I think the title BLFF says it all, it was very fun to share an office, lab and quite a lot of social life with you, I really think you should return to Europe. Murielle, thank you for helping me set up my project, I learned a lot from you and without you I wouldn't be the scientist I am today. Agathe, you are the person I have spent the longest in the lab with and I am very happy it was you, who was there for pretty much all of it. In London, I was drawn to the lab from the beginning for the amazing community socially and scientifically that it was. Matt, Dani, Irene, Mali, Meghan, thank you for being part of it and making it so special. I am happy we continue to have a nice community in Cambridge. Wolfi, while I don't miss the London-Cambridge commute, I really enjoyed our chats during it. Ruby, you have been a great person to share all the ups and downs of transitioning to Cambridge with and working on the cortex together. Fiona, thank you for trying to make the move to Cambridge as smooth as possible. Aki, I am sorry you didn't stay in Cambridge for longer. Iskra, it was very nice to be surrounded by your positivity during my final year. Marta and Geraldine, I am happy that the lab is growing again and being restored to a formed glory of lab with multiple excellent postdocs. Margherita, Will, Tasmin, Jeanne I think Cool Kids Squad needs a Cambridge edition, including the merchandise.

I really enjoyed my last few years even more because of the amazing environment at both departments, I was a part of. Everyone from Mao, Chubb and Franze labs has been a great and fun lab-space neighbour. Ale, Natalie, Gabriel it was very fun to be in a students' office with all of you. I am also incredibly thankful for the friendships I have built outside the lab. I really enjoyed all the fun we shared at Friday drinks, Secret Boardgame Society, yoga and other events. Megan and Joe, in the first year we called ourselves a fun year and I think we stayed that despite perhaps with fewer people. Also, whoever wins that battle of becoming a GSK CEO, I am expecting amazing gifts and loads of drinks from you. Rici, I think drinks with someone who can balance multiple straws on their face are simply more fun. Aakriti, I think you earned an honorary LMCB student status. Giulia and Sophie, I am really happy you realised that Cambridge is the cool place to be and I still get to see you so often. These last years would not have been the same without all of you.

I am very glad to have had amazing flatmates during my PhD. Silvia (and Francesco for a bit), I really enjoyed living with someone I got along with so well, I am happy we stayed

friends and live close to each other again. Paula, through multiple lockdowns in the last couple of years, it was invaluable to live with such a nice person.

I am beyond thankful to my friends outside the lab, I am very happy to have all of you in my life. Santhiya and Cinderella, our annual trips will be one of the best memories from this period. Brina, Kevin, Nina, Nina, Lora, Klara, Nuša, thank you for the random messages on the group chats, making my visits home so enjoyable, and generally being a reminder that I am more than just a scientist.

Finally, the biggest thank you to my family for believing in me, supporting me, and providing me with opportunities that made it all possible. My grandparents: babi Majda, babi Cvetka, dedi Rado, and dedi Miro (whom unfortunately will not get to see the end of this journey), thank you for being so proud of me. My siblings, Brina and Urban, thank you for being you, for making me feel you are always there for me. Most of all thank you to my parents, mami and oči, thank you for always supporting me, believing in me, and being there for me.

Hvala!

Contents

List of Figures

List of Tables

Chapter 1

Introduction

1.1 The actin cortex controls cell shape

Different animal cell types display a wide variety of shapes (Figure 1.1A). A cell's physical environment affects its shape [Thompson, 2014]. Cell shape changes are key in many fundamental processes such as epithelial morphogenisis, cell migration, or cell division [Clark and Paluch, 2011, Lecuit and Lenne, 2007, Paluch and Heisenberg, 2009]. For example, during cell division, cells round up at the onset of mitosis, start to elongate during anaphase, and are divided into two daughter cells during cytokinesis (Figure 1.1B). These clear changes in cell shape are essential for successful cell division and thus building of a tissue from a single cell [Lancaster and Baum, 2014]. Understanding mechanical properties of the cell is thus key to understanding cell shape, its maintenance, and its changes. In this thesis, I explore molecular mechanisms driving cell shape changes particularly in the context of cell division.

At the molecular level, cell mechanics is primarily controlled by the cytoskeleton, which is composed of actin filaments, microtubules, and intermediate filaments [Alberts et al., 2014]. These filaments assemble into networks that determine the spatial organisation and the mechanical properties of the cell. Particularly, the actin cytoskeleton and more specifically the actin cortex is essential for maintaining cell shape [Levayer and Lecuit, 2012, Salbreux et al., 2012].

The cell cortex is an actomyosin network supporting the plasma membrane of animal cells. In round (eg. mitotic), amoeboid, polarised epithelial or in suspended cells, the actin cortex is the most prominent actin structure [Levayer and Lecuit, 2012, Salbreux

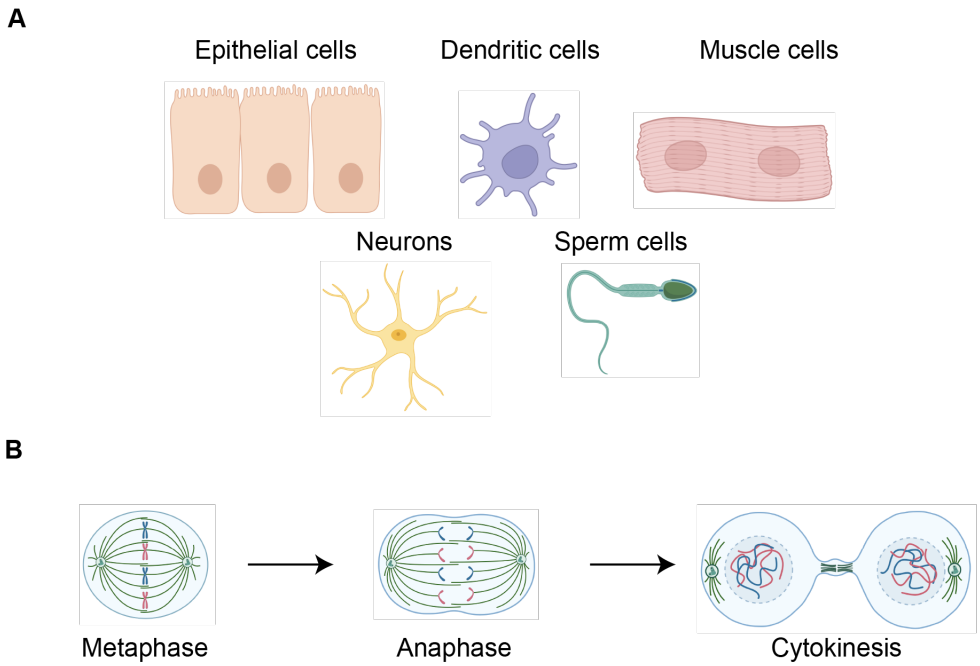

Figure 1.1: **Different shapes of animal cells.** (A) Schematic representation of cell shape of different animal cells: epithelial, dendritic, muscle, neurons, and sperm cells. These are the examples of only some of the cell types that drastically differ. (B) Cell shape changes during cell division. During mitosis cell rounds up, gets elongated during anaphase, and separates in two cells by cleavage furrow ingression during cytokinesis.

et al., 2012]. It maintains the mechanical integrity of animal cells, resisting external and internal forces acting on the cell surface. Myosin motors create contractile tension in the actin cortex. Local changes in cortical tension lead to local contractions and induce cell shape changes essential in processes such as cell division, cell migration, and epithelial morphogenesis (Figure 1.2) [Bray and White, 1988, Levayer and Lecuit, 2012]. In this thesis, I focus on the protein composition and nanoscale organisation of the actomyosin cortex and how its organisation affects the generation of tension gradients.

1.2 Actin cortex composition

The actomyosin cortex is composed of actin, myosin, actin nucleators, severing proteins, crosslinkers, bundlers, cortex-to-membrane linkers and other proteins, which make up $\sim$ 150 nm thick with $\sim$ 20 nm meshsize network (in mitotic cells) (Figure 1.3, 1.4). [Biro et al., 2013, Bovellan et al., 2014, Serres et al., 2020, Svitkina, 2020]. Mass spectrometry of cortical fractions from human melanoma cells (M2) showed the presence of more than 170 actin-binding proteins, actin regulatory proteins, and proteins associated with actin-binding proteins [Biro et al., 2013]. These included different isoforms of myosin mo-

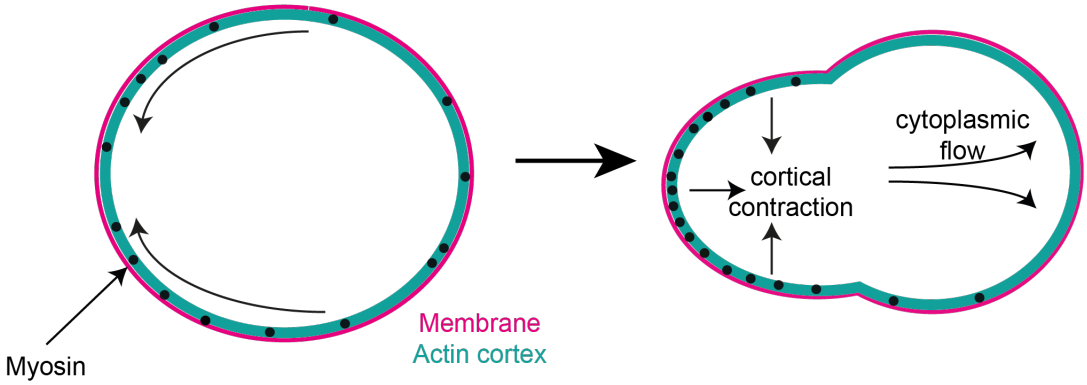

Figure 1.2: **Tension gradients lead to local contractions and cell shape changes.** Myosin motors generate cortical tension by pulling on actin filaments. Gradients in cortical tension lead to local contractions, which create cell shape changes.

tors and actin, actin nucleators, capping proteins, crosslinkers, turnover-control proteins, membrane linkers, regulators of contractility, network regulators, adaptor proteins, Rho-GTPases, RhoGEFs, and RhoGAPs. In this section, I describe some of these main protein groups, which make up the cortical actomyosin network: actin, myosin, actin nucleators, actin assembly and disassembly regulators, actin crosslinkers, actin-to-membrane linkers, and septins.

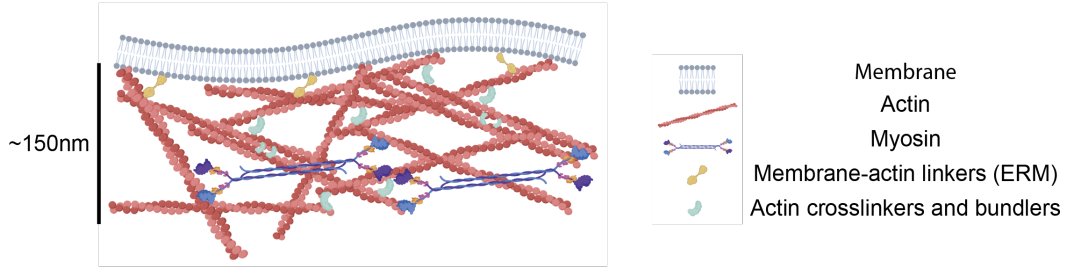

Figure 1.3: **Actin cortex composition and organisation.** The actin cortex is a ∼ 150 nm thick actomyosin network underneath the plasma membrane composed of actin, myosin and multiple other (actin-binding) proteins.

1.2.1 Actin

F-actin is a polymer composed of G-actin monomers, a 375 amino-acid polypeptide, highly conserved among eukaryotes [Alberts et al., 2014]. In vertebrates there are three isoforms (alpha, beta, gamma) of actin with highly conserved sequences. The actin filament is ∼ 8 nm wide polymer arranged in a right-handed double helix [Egelman, 1985, Holmes et al., 1990]. The crossover distance of the helix is 36 nm, which equals to 13 actin

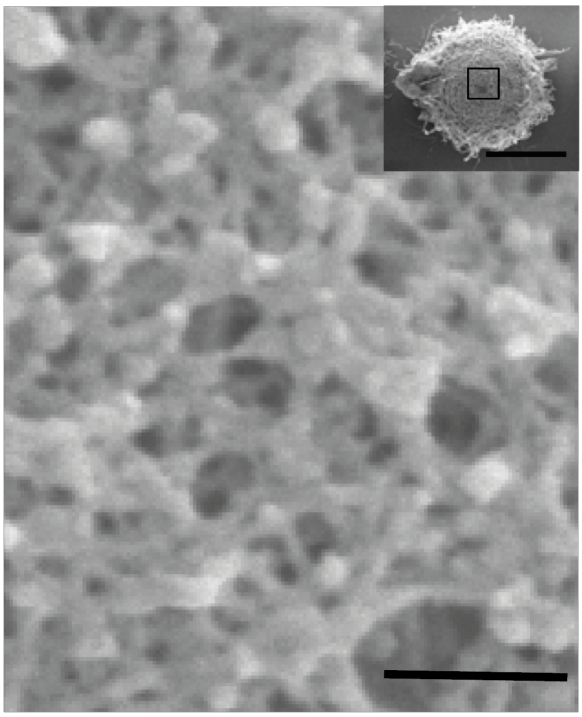

Figure 1.4: **Scanning electron microscopy image (SEM) of the actin cortex.** SEM image of the actin cortex of the mitotic cell (inset) showing a dense actomyosin network. Scale bars = 100 nm, 10 µm (inset). Courtesy of Dr. Priyamvada Chugh.

monomers (Figure 1.5). The persistence length of actin filament is 17.7 µm [Gittes et al., 1993]. F- actin has a polarised structured with a pointed and a barbed end (Figure 1.5), named after visual appearance of the filament when it is decorated with myosins. Due to the structural differences, actin polymerisation is much faster at the barbed end of the filament [Narita et al., 2011, Pollard and Mooseker, 1981]. F-actin is polymerised in three steps: activation, nucleation, and elongation [Pollard, 1986]. During activation G-actin monomers bind to ATP and Ca^{2+}. During nucleation actin monomers join into unstable dimers and trimers. Nucleation is accelerated by specialised actin nucleating proteins. After monomer concentration exceeds a critical concentration, nucleation is followed by rapid elongation. The elongation occurs through addition of G- actin monomers at the barbed end of the filament. ATP-bound monomers polymerise $\sim$ 50 times faster than ADP-bound monomers.

1.2.2 Myosin motors

Myosins are actin-binding motor proteins that generate a force through ATP hydrolysis coupled to changes in affinity for actin [Alberts et al., 2014]. This process leads to contractility of actomyosin networks. There are 139 members of the myosin superfamily

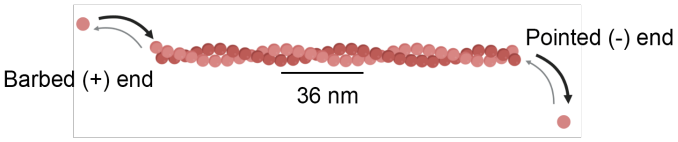

Figure 1.5: **Actin filament schematic.** Actin filament is a double helix with a crossover distance of 36 nm including 13 actin monomers. Actin filament has a polar structure with pointed (-) and barbed end (+).

[Hodge and Cope, 2000]. The most abundant myosins detected in the cortex are members of non-muscle myosin II (NMII) group. There are 3 NMII isoforms (A, B, and C) in the cortex [Vicente-Manzanares et al., 2009]. NMII consists of heavy chain (HC), regulatory light chains (RLC), and essential light chains (ELC). In mammalian cells, the globular domain of the heavy chain contains actin-binding and ATP-binding sites. Light and heavy chains are essential for NMII native dimer conformation. In mammalian cells, NMII isoforms coassemble in 300 nm long heterotypic fibres, called minifilaments [Beach et al., 2014, Shutova et al., 2014]. In the mammalian cortex, contractility is mostly generated by NMII A and B. Biochemically, NMII can be regulated through reversible phosphorylation of RLC and HC [Vicente-Manzanares et al., 2009].

1.2.3 Actin nucleators

Actin polymerisation is initiated by actin nucleators which bring several actin subunits together [Campellone and Welch, 2010]. The 2 main groups of actin nucleators are Arp 2/3 complex and formins. In proteomic analysis of the cell cortex, the formin mDia1 and the Arp2/3 complex were found as the most common actin nucleators [Bovellan et al., 2014, Chan et al., 2019]. Formin-nucleated cortical actin filaments are $\sim$ 10 times longer than Arp 2/3 filaments but represent only 10 % of all cortical actin filaments [Fritzsche et al., 2016].

Arp 2/3 is a 7 subunit protein which through activation by nucleation-promoting factor (such as, but not limited to, WASP, WAVE or WASH) initiates polymerisation of a new actin filament at a 70°angle from an already existing filament leading to the formation of a branched actin network [Goley and Welch, 2006]. In contrast, formins nucleate actin into unbranched filaments. There are at least 15 different mammalian formins characterised in 7 subclasses [Campellone and Welch, 2010]. The extend of nucleation of branched filaments compared to straight filaments does not only depend on the amount of different nucleating factors. For instance, a nucleation promoting factor SPIN90 interacts with both Arp2/3

and mDia1 [Cao et al., 2020]. In cells, where both nucleators are present, SPIN90 forms ternary structures with Arp 2/3 and mDia1. By binding both nucleators, SPIN90 favours increased proportion of elongated filaments at the cell cortex. Taken together, the balance between branched and unbranched filaments is regulated through multiple interconnected mechanisms.

1.2.4 Actin assembly and disassembly regulators

The length of F-actin filaments is not only controlled by actin nucleators but also through other types of F-actin- or G-actin-binding proteins. By binding actin, these proteins control actin assembly and disassembly [Pollard et al., 2000]. Actin monomer binding proteins bind to monomeric G-actin. This group includes thymosin-beta 4 and profilin. By binding to ATP-actin monomers, thymosin-beta 4 inhibits actin filament polymerisation, while the function of profilin is more complex. Because of its binding of monomeric actin, profilin was initially considered an actin sequestering protein. However, profilin promotes ADP to ATP conversion on monomers and thus barbed end polymerisation [Goldschmidt-Clermont et al., 1992, Mockrin and Korn, 1980]. Other types of actin filament length regulators such as members of the ADF/cofilin family sever F-actin and thus affect actin network organisation [Bamburg and Bernstein, 2008]. By severing actin filaments, ADF/cofilin provides additional filament ends. This can either lead to increased filament depolymerisation, or in the presence of high amount of actin monomers, creates new ends for monomer binding. Another group of proteins regulating actin assembly dynamics are capping proteins, such as CapZ, which by binding to barbed end of the actin filament prevent actin elongation [Edwards et al., 2014].

1.2.5 Actin crosslinkers

Actin crosslinkers crosslink or bundle two or more actin filaments together and are thus essential in creating different higher order actin structures. Crosslinking of the actin filaments is essential for maintaining mechanical properties of the cells [Gardel et al., 2006, Sato et al., 1987, Xu et al., 1998]. Actin crosslinkers either have two actin binding domains (ABDs) on the same polypeptide or form dimers from two monomers with single ABD. The two classes of actin crosslinkers either bundle or crosslink actin filaments arranging them into parallel arrays, or binding filaments together at a larger angle creating looser meshworks [Nakamura et al., 2002, Xu et al., 1998]. Many different actin crosslinkers have been identified in the cell cortex [Biro et al., 2013], which differ in multiple properties

including their size and role [Bartles, 2000, Pollard, 2016].

Alpha-actinin is a $\sim$ 35 nm dimer that bundles actin filaments with opposite polarities into loose bundles [Meyer and Aebi, 1990]. There are 4 different isoforms of alpha actinin (1, 2, 3 and 4), all of which have been detected in the actin cortex [Biro et al., 2013].

Plastin (fimbrin), has a distance of $\sim$ 8 nm between its ABDs [Klein et al., 2004, Winkelman et al., 2016]. It creates very dense bundles of actin filaments [Bretscher, 1981].

Fascin is a globular protein with $\sim$ 5 nm long structure [Jansen et al., 2011]. It bundles actin filaments into strong bundles.

Filamin is a 160 nm long dimer with $\sim$ 100 nm distance between its ABDs [Tyler et al., 1980]. It crosslinks actin filaments at a high angle angle and creates highly viscous actin gels [Nakamura et al., 2002]. Besides maintaining mechanical properties of the cells, filamin also has a role in cell adhesion, migration and cell spreading [Nakamura et al., 2011].

1.2.6 Actin-to-membrane linkers

Membrane linkers bind actin filaments to the membrane and thus regulate the mechanical properties of the cell by linking the cell cortex movements with the movements of the plasma membrane [Nambiar et al., 2009, Sato et al., 1992]. Myosin 1 and ERM (ezrin, radixin, moesin) proteins are the most abundant members of this group.

1.2.7 Septins

Septins are a group of GTP-binding proteins often considered a fourth component of the cytoskeleton [Mostowy and Cossart, 2012, Spiliotis, 2018, Spiliotis and Nakos, 2021]. They bind actomyosin cytoskeleton, microtubules and membrane. There are 13 septins in mammalian cells, divided into 4 homology groups (SEPT2, SEPT3, SEPT7 and SEPT6) (Figure 1.6). Septins are divided into homology groups based on the differences in their GTPase activity [Spiliotis and Nakos, 2021]. In mammalian cells, septins can assemble into oligomers, mostly hexamers and octamers, through binding of their GTPase domains. The oligomer assembly is driven by the differences in GTPase activity and expression levels of individual septins. Each homology group consists of multiple paraloges except for septin 7, which is the only member of SEPT7 homology group and it is essential for oligomer formation. SEPT7 forms the core of the septin oligomer. Members of SEPT3 group (septin 3, 9, 12) are only present in octamer structures (Figure 1.6).

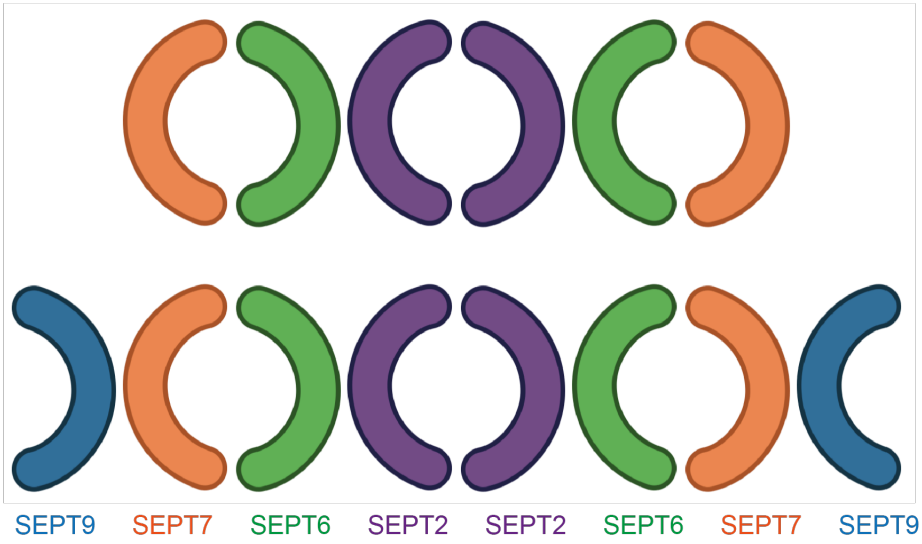

Figure 1.6: **Schematic representation of septin oligomers and septin groups.** Septins are divided into four homology groups (SEPT2, SEPT3, SEPT7 and SEPT6) which can form heterohexamers and heterooctamers.

Septins localise to the cell cortex and play a key role during division in budding yeast [Bridges and Gladfelter, 2015, Gladfelter et al., 2001]. Septin assembly during the cell cycle is regulated by Cdc42. During the cell cycle septin organisation changes between bud emergence and cytokinesis driving the separation of daughter cell. At the onset of division septin arranged as a radial array of double filaments forms an hourglass structure between mother cell and bud of a yeast cell [Ong et al., 2014]. Later during the cell division septin filaments disassemble and reassemble into double ring characterised by a 90°change in septin orientation. This reorganisation is regulated by post-translation modifications and by septin-associated proteins [Marquardt et al., 2021]. At the onset of division septins serve as scaffold for the assembly of the cytokinetic machinery and as a diffusion barrier for mother and bud membranes.

The role of septins during cell division of other organisms is less clear. In mammalian cells, septins interact and colocalise with anillin, an actin actin-crosslinker, which translocaltes from the nucleus during cytokinesis and drives cleveage furrow ingression [Kinoshita et al., 2002, Oegema et al., 2000]. In *Drosophila melanogaster* together with anillin, septin affects contractile ring closure and midbody assembly during which septin and anillin

potentially work on membrane extrusion, which is important for ring closure [Amine et al., 2013]. Additionally, mutations in septins of *Drosophila melanogaster* affected myosin and actin levels and distribution during cytokinesis, which suggests a role for septins in cortex organisation during cell division [Mavrakis et al., 2014].

In mammalian cells, septin 2, 6 and 9 were found to localise to the mitotic cell cortex and later along with septin 7 and 11 to the cleavage furrow [Estey et al., 2010, Gilden et al., 2012]. Septins also colocalise with actin filaments during interphase and depletion of septins was shown to affect actin organisation [Kinoshita et al., 2002, Spiliotis and Nakos, 2021]. Septins can crosslink actin filaments into circular or linear bundles. Additionally, septins 2 and 9 were shown to bind myosin [Joo et al., 2007, Smith et al., 2015]. Septin 2 was shown to be important for scaffolding non-muscle myosin 2 of mammalian cells to its kinases while in reconstituted systems septin 9 affects actin-dependent ATPase activity of myosins.

Septins were also shown to affect mechanical properties of dividing cells. Depletion of septins 2, 7, and 11 in HeLa cells was shown to delay cleavage furrow ingression while septin 9 and potentially 8 lead to a decrease in mitotic rounding force as measured by atomic force microscopy [Estey et al., 2010, Toyoda et al., 2017]. Depletion of septin 2 and 11 in interphase HeLa cells also affected cell elasticity [Mostowy et al., 2011]. Additionally, septins have a role during other processes driven by cortex tension such as amoeboid migration [Gilden and Krummel, 2010, Gilden et al., 2012, Tooley et al., 2009]. Depletion of septin 7 led to defects in T-cell morphology and cell migration exhibiting bigger protrusions and more blebbing. Cells depleted in septin 7 also needed longer than wild type cells for bleb retraction during blebbing due to changes in media osmolarity. While at least some of the septin paraloges seem to important for regulation of cortical tension their role at the onset of mammalian cell division, during cell rounding, remains to be established.

1.3 Mechanical properties of the cortex

Animal cell shape changes are driven by mechanical properties of the cell surface, which is comprised by the cell membrane and the cortex. In most cells with an actomyosin cortex, surface tension is mainly defined by the cortical tension with a negligible contribution by the membrane tension [Clark and Paluch, 2011, Levayer and Lecuit, 2012, Salbreux et al., 2012]. Cortical tension is defined as a force per unit length exerted on the cortex cross-section by the surrounding network. It results in hydrostatic pressure on the cell. The

hydrostatic pressure balances the osmotic pressure difference between inside and outside of the cell, connecting cortical tension to cell volume [Stewart et al., 2012, Tinevez et al., 2009]. Gradients in cortical tension lead to cell shape changes in processes such as division or migration [Bergert et al., 2015, Reichl et al., 2008, Sedzinski et al., 2011].

Cortical tension can be measured via compression, stretching or pulling of the cells or without direct contact using laser ablation [Chugh and Paluch, 2018, Clark et al., 2014]. Atomic force microscopy (AFM) allows for measuring cortical tension through compression. For tension measurements via AFM, the cell is compressed by a flat AFM cantilever, and tension is calculated from the force exerted by the cell on the cantilever upon compression. This approach is most efficient for measuring the cortical tension of round, isolated cells [Chugh et al., 2017, Fischer-Friedrich et al., 2014, Stewart et al., 2011, Toyoda et al., 2017]. Alternatively, cortical tension can be measured by micropipette aspiration which only requires a portion of a cell and can therefore be used on adherent cells [Chaigne et al., 2013, Maître et al., 2012, 2016, Tinevez et al., 2009]. For cortical tension measurements via micropipette aspiration, tension is calculated from the pressure required to aspirate part of a cell. While AFM gives higher resolution measurements, micropipette aspiration works better on cells that are not round. Finally, for tension measurements via laser ablation, direct contact with a cell is not required, which makes it suitable method for cortical tension measurements in tissues. With this method, the cortex is locally disrupted by a pulsed laser and relative tension can be calculated based on the recoil of the cortex around the disruption [Mayer et al., 2010].

At the molecular level cortical tension is generated by the cortical actomyosin network [Chugh and Paluch, 2018, Koenderink and Paluch, 2018, Salbreux et al., 2012]. Particularly, contractile forces are generated by myosin motors walking towards the barbed ends of actin filaments. Understanding the molecular and nanoscale organisation of the cortical actomyosin network is thus key to understanding how cortical tension is controlled.

1.4 Control of cortex mechanics

1.4.1 Cortical tension control by non-muscle myosin II

Cortical tension and thus tension-driven processes, such as cell division, are primarily controlled by myosin motors, particularly NMII [Bergert et al., 2012, Ramanathan et al., 2015, Sedzinski et al., 2011, Stewart et al., 2011, Tinevez et al., 2009]. For example, in

mitotic cells, cortical tension decreases by $\sim$ 80 % upon treatment with myosin inhibitor blebbistatin [Chugh et al., 2017, Ramanathan et al., 2015].

From the three NMII isoforms (A, B and C), A and B are more broadly expressed and their organisation and function are better characterised [Shutova and Svitkina, 2018]. Due to the highest ATPase activity, NMIIA is the fastest between the three isoforms while with its high duty ratio and thus affinity for actin, NMIIB is much slower. Different (A and B) isoforms thus have different functions for regulation of cortical tension. In fibroblast cells, NMIIA knockout led to much lower cortical stiffness compared to NMIIB knockout [Yamamoto et al., 2019]. Overall, NMIIA contributes more to generating cortical contractility while NMIIB stabilises the actomyosin cortex and maintains cortical contractility due to longer binding of actin by NMIIB [Dey et al., 2017, Taneja and Burnette, 2019, Taneja et al., 2020, Yamamoto et al., 2019].

Biochemically NMII is regulated through phosphorylation [Shutova and Svitkina, 2018, Vicente-Manzanares et al., 2009]. Upstream phosphorylation is regulated by multiple kinases including ROCK, MLCK, MRCK, PAK, and citron kinase. Phosphorylation of Ser19 and Thr18 of RLC activates NMII ATPase, which increases the motor activity of NMII but it does not affect its affinity for actin. Phosphorylation of RLC also opens up the folded NMII molecule and releases RLC interaction with the rod of HC, which allows the formation of bipolar NMII minifilaments. In contrast, phosphorylation of HC prevents polymerisation of NMII minifilaments. Phosphorylation of all NMII isoforms is regulated in the same way. Therefore, to understand how differences in actomyosin contractility arise from different isoforms, it is crucial to gain insight into the differences in their localisation.

Recent advances in resolution of electron and light microscopy enabled the investigation of molecular organisation of different NMII minifilaments. In U2OS (human sacronoma) and REF52 (rat fibroblasts) cells, NMII isoforms were shown to co-assemble into $\sim$ 300 nm heterotypic bipolar minifilaments with similar ratio of A and B isoforms at the beginning of minifilament polymerisation [Beach et al., 2014, Shutova et al., 2014]. However, the distribution between NMIIA and B became less uniform during polarisation of the cells. The uneven distribution between the isoforms is consistent with differences in the function of different isoforms in tension generation. A recent study using U2OS cells also showed a change in size and organisation of NMIIA within minifilaments during cytokinesis [Fenix et al., 2016]. In particular, at the cleavage furrow, NMIIA minifilaments firstly expanded through the increase in the number of motors within the minifilament, then multiple mini-

filaments concatenated forming NMIIA stacks, large multimolecular assemblies. Taken together, these new finding indicate that NMII minifilaments have a complex nanoscale organisation understanding of which will be important for understanding molecular control of contractile force generation within the actomyosin networks.

1.4.2 Actin network organisation and contractility

Bipolar NMII minifilaments generate force by walking towards barbed ends of F-actin filaments. This process can either produce contractile or extensile forces [Koenderink and Paluch, 2018, Murrell et al., 2015]. The type of the force will depend on the actin organisation. In a network with random filament polarities, such as the actin cortex (Figure 1.4), contractile and extensile forces should be equal unless the symmetry between contractile and extensile forces is broken.

Different mechanisms have been proposed for the symmetry breaking in disordered networks. For instance, contractility of reconstituted disordered actomyosin networks, can arise from filament buckling [Lenz et al., 2012, Murrell and Gardel, 2012]. Filament buckling shortens the filament, releases extensile forces and leads to the shortening of the actomyosin bundle. Alternatively, actomyosin network can self-organise into more contractile configuration either via filament treadmilling or myosin stalling [Kruse and Jülicher, 2000, Oelz et al., 2015].

All of these mechanisms require network connectivity through crosslinking. Connectivity is also key for contractility propagation across the network [Alvarado et al., 2013, Belmonte et al., 2017, Ennomani et al., 2016, Janson et al., 1991]. In fact, the highest contractility of the different reconstituted actin networks was observed at the intermediate connectivity which was regulated by the amount of crosslinkers [Ennomani et al., 2016].

In the actin cortex, actin organisation and in particular actin connectivity, defined by a number of crosslinks per filament, are increasingly being shown as important regulators of cortical tension [Chugh et al., 2017, Ding et al., 2017]. But, due to its dense thin structure, bellow the resolution limit of the light microscope, visualisation of the actin cortex and its organisation remain challenging. However, recently measurements of cortical thickness offered an insight into the relationship between cortical actin organisation and tension [Chugh et al., 2017, Clark et al., 2013]. For instance, changes in cortical actin thickness were observed concurrently with changes in tension (Figure 1.7) [Chugh et al., 2017, Serres et al., 2020]. It was shown that mitotic cells have higher cortical tension and

lower cortex thickness compared to interphase cells. These findings were also supported by computational simulations, linking actin connectivity and cortical tension (Figure 1.8) [Chugh et al., 2017]. Together, these findings suggest that cortex organisation, measured by cortical thickness, plays a role in tension control.

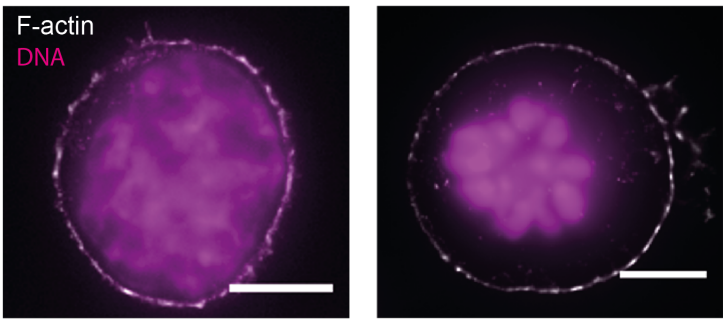

Interphase cells
High cortex thickness
Low cortex tension

Mitotic cells
Low cortex thickness
High cortex tension

Depleted protein	Thickness increase/ decrease	Tension increase/ decreas	Reported in
Arp2/3	increase	not measured	Chaigne et al., 2013
CAPZB	increase	decrease	Chugh et al., 2017
DIAP1	decrease	decrease	Chugh et al., 2017
CFL1	increase	decrease	Chugh et al., 2017
VIM	increase	decrease	Serres et al., 2020
PLEC	increase	decrease	Serres et al., 2020

Figure 1.7: **Changes in cortical thickness can be associated with cortical tension.** Interphase and mitotic cells differ in cortical tension and actin thickness. Similarly changes in cortical thickness and tension have been observed upon depletion of different actin binding proteins (ARP2/3, CAPZB, DIAP1, CFL1, VIM, PLEC) suggesting a relationship between actin organisation (thickness) and tension. Images of interphase and mitotic embryonic stem cells stained for F-actin (phalloidin) and DNA (DAPI) are courtesy of Binh-An Truong-Quang. Scale bars= 5 µm.

1.4.3 Regulators of actomyosin contractility and cortical tension

At the molecular level, the organisation and connectivity of the isotropic actin cortex can be controlled by multiple different proteins [Biro et al., 2013, Bovellan et al., 2014]. Experimentally, changing the levels of different actin binding proteins, in particular actin filament length regulators and crosslinkers, were shown to affect cortical tension [Chugh et al., 2017, Ding et al., 2017, Logue et al., 2015, Serres et al., 2020, Toyoda et al., 2017].

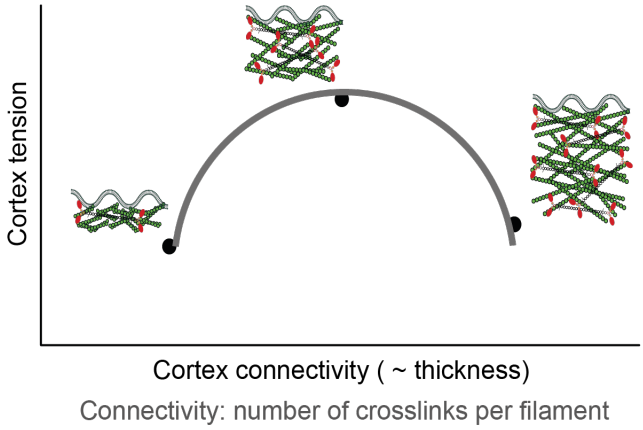

Figure 1.8: **Cortical connectivity regulates tension.** Experimental and computational data suggests that the connectivity of the actin cortex (defined as the number of crosslinks per filament) affects cortical tension. Cortical thickness is used as an experimental readout of cortical connectivity [Chugh et al., 2017].

In round mitotic cells, different actin filament length regulators were shown to affect cortical thickness and tension [Chugh et al., 2017]. Depletion of the actin severing protein cofilin (COF) and the capping protein Z B (CAPZB) led to a thicker actin cortex while depletion of diaphanous 1 (DIAP1) led to a thinner cortex compared to wild type HeLa cells. These differences in the effects of different proteins on cortical thickness is likely due to differences in their role on actin length regulation. Interestingly, depletion of all these proteins led to to lower cortical tension in cells synchronised in mitosis. These experimental observations were complemented by a theoretical model predicting highest contractility at an intermediate connectivity of the actin network [Chugh et al., 2017]. The role for actin length regulation and crosslinking in cortical tension and thickness control, was also confirmed by depletion of SPIN90, an upstream regulator of Arp2/3 and DIAP1 [Cao et al., 2020]. SPIN90 modulates the activity and interactions of these two most abundant actin nucleators in the cortex and thus precisely controls cortical actin length and branching. SPIN90 depletion in mitotic HeLa cells led to a decrease in cortical thickness and tension. Depletion of actin nucleators was also shown to affect tension driven processes [Litschko et al., 2019]. Depletion of DIAP1 formins in *Dictyostelium discoideum* affected actin dynamics and led to defects in cytokinesis, development and (amoeboid) migration. Together, these findings strongly suggest that actin length regulators affect cortical organisation and tension.

Specific candidate actin crosslinkers were also shown to affect actin contractility and cortical tension [Ding et al., 2017, Ennomani et al., 2016, Logue et al., 2015, Toyoda et al.,

2017]. Alpha-actinin was shown to affect contractility of reconstituted actin networks and cortical tension [Ennomani et al., 2016, Logue et al., 2015, Toyoda et al., 2017]. Measured by AFM, alpha-actinin 4 was shown to affect mitotic rounding force in HeLa cells [Toyoda et al., 2017]. Depletion of alpha-actinin 4 by different sets of esiRNA led to a decrease in mitotic rounding force. In human melanoma cells, alpha-actinin depletion and overexpression were also shown to decrease or increase cortical tension, respectively [Logue et al., 2015]. In the same study, a mutation in growth factor receptor kinase substrate 8 (EPS8) actin bundling domain was shown to decrease cortical tension and affect bleb-based migration leading to fewer migratory cells. This phenotype could be partially rescued by overexpression of alpha-actinin. Plastin, along with fimbrin and dynacortin was also identified as a regulator of cortical contractility and tension-driven processes [Ding et al., 2017, Reichl et al., 2008]. In *Caenorhabditis elegans*, mutation of plastin 1 led to failures in embryogenesis and was shown to cause defects in cleavage furrow ingression during cytokinesis [Ding et al., 2017]. These experimental findings were complemented by a computational simulation which predicted highest contractility at the intermediate amount of crosslinkers when keeping the amount of myosin motors constant. Depletion of plastin 1 (fimbrin), along with dynacortin was also shown to affect cortical tension in *Dictyostelium discoideum* [Reichl et al., 2008]. Depletion of fimbrin and dynacortin affected dynamics of cytokinesis and cortical tension. Interestingly, cells depleted of fimbrin and dynacrotin affected cortical mechanics differently depending on the presence of myosin. Fimbrin depletion only led to a decrease in cortical tension of cells depleted of wild type myosin and substituted with 10-fold slower myosin motor while dynacortin reduced cortical tension also in the presence of myosin. These findings suggest a role of actin crosslinkers in tension generation and that their role can be affected by myosin. Aadditionally, plastin and fascin were shown to affect tissue morphogenesis in *Drosophila melanogaster* [Krueger et al., 2019]. Knockdown of fimbrin and fascin affected actin organisation and led to defects in cellularisation. Taken together, crosslinkers can affect cortical tension. However, a comprehensive understanding of how different crosslinkers differ in cortical tension regulation remains to be established.

Finally, other cytoskeletal and actin-binding proteins besides crosslinkers and length regulators can also affect cortical tension [Duarte et al., 2019, Serres et al., 2020, Toyoda et al., 2017]. An esiRNA screen of 1013 mitotic proteins identified 134 genes of which depletion reproducibly changed mitotic rounding force [Toyoda et al., 2017]. 49 of these proteins for which the phenotype was confirmed with a second set of esiRNA sequences, were fur-

ther characterised. Interestingly, these 49 proteins primarily localise not only to the cell cortex but also to the cell surface, centrosome, kinetochore, spindle, and other structures suggesting that cortex tension control is also coupled to other cellular components. In line with this, a recent study showed that the intermediate filament vimentin also controls cortical thickness, tension and affects cell division [Duarte et al., 2019, Serres et al., 2020]. In mitotic cells, the vimentin network localises underneath the cortex. Laser ablation of vimentin led to local flattening of round mitotic cell surface, changing the curvature of the cell [Serres et al., 2020]. While the precise mechanism is unknown, the authors suggest that vimentin offers structural support to the cellular cortex counter-acting its contractility. Taken together, cortical tension seems to be maintained through a variety of mechanisms by multiple different cytoskeletal proteins.

Overall, different-actin binding proteins are involved in controlling cortical tension. In particular, actin connectivity, maintained through actin crosslinking, is key in controlling cortical tension and thus multiple fundamental physiological processes. However, thorough understanding of the role of all actin crosslinkers and actin-binding proteins detected in the cortex remains to be established [Koenderink and Paluch, 2018]. To address this question, we firstly need a comprehensive list of which are the key actin binding proteins present in the cortices and better understanding of their interactions with each other.

1.5 Nanoscale organisation of the cortex

The contractility of actomyosin networks, including the cortex, is controlled by the NMII localisation and activity, along with the organisation of the actin scaffold (reviewed in Koenderink and Paluch [2018]). Therefore, to fully understand how cortex tension is controlled at the molecular level, protein composition of the cortex and their cortical organisation need to be determined.

The cell cortex is only $\sim$ 150 nm thick with a meshsize of $\sim$ 20 nm in mitotic HeLa cells (Figure 1.4) [Chugh et al., 2017, Clark et al., 2013], which is below the resolution of conventional light microscopy. Therefore, investigating the nanoscale organisation of the actin cortex is challenging and only possible via advanced imaging methods such as super-resolution and electron microscopy. A recent study from Paluch lab, investigated the localisation of $\sim$ 300 nm big NMII minifilaments within the interphase and mitotic cortex via stochastic reconstruction microscopy (STORM) [Truong Quang et al., 2021]. In mitotic HeLa cells with high cortical tension, NMII minifilaments were observed to

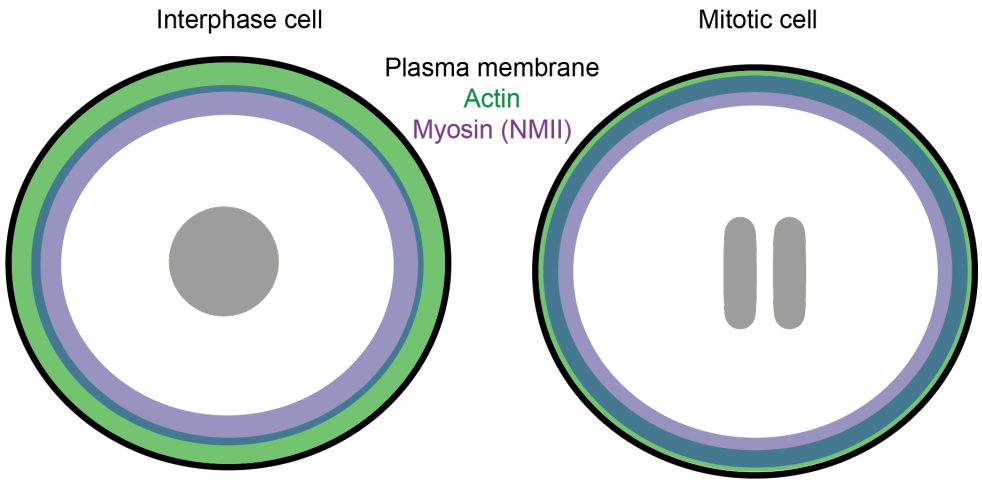

Figure 1.9: **Myosin (NMII) penetrates further into the high tension mitotic cortex compared to the low tension interphase cortex.** Schematic representation of non-muscle myosin II (NMII) localisation within the actin cortex of mitotic (high tension) and interphase (low tension) cells. NMII penetrates further into the cortical level of mitotic cells suggesting NMII localisation based regulation of cortical tension [Truong Quang et al., 2021].

penetrate much further into the cortex compared to interphase cells with low cortical tension, suggesting that nanoscale NMII localisation within the cortex plays a role in tension generation (Figure 1.9) [Truong Quang et al., 2021]. The authors hypothesised that NMII minifilament localisation depended on actin organisation, particularly the density of the cortical actin network. Indeed, perturbations of the actin organisation with the Arp2/3 inhibitor CK666 and the actin polymerisation inhibitor cytochalasin D both increased NMII penetration into the actin cortex and increased cortical tension. In contrast, activation of Arp2/3 by overexpression of N-WASP domain VVCA, decreased the amount of NMII penetration into cortical actin and decreased cortical tension. Together, these findings suggested that the actin density affects NMII localisation and thus cortical tension.

In the same study, some other actin binding proteins of different sizes were also localised within the actin cortex. Interestingly, NMII, alpha-actinin and moesin which differ in their sizes also differed in their nanoscale localisation within the cortex [Truong Quang et al., 2021]. $\sim$ 300 nm big NMII did not completely penetrate into the cortical actin, $\sim$ 35 big alpha-actinin completely overlapped with the actin cortex while $\sim$ 14 nm big moesin was closer to the plasma membrane then the cytoplasm (Figure 1.10). Together, these findings suggest that the localisation of the proteins within the dense actin cortex is influenced by their size. However, these proteins do not only differ in their size but also other properties such as actin binding dynamics or interactions with other proteins

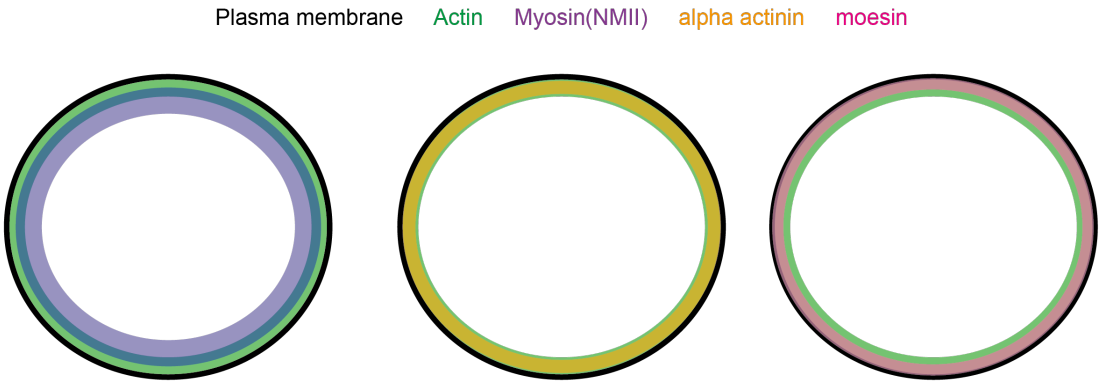

Figure 1.10: **NMII, alpha-actinin and moesin localise differently within the actin cortex.** Within the actin cortex NMII (purple), $\sim$ 300 nm, was shown to have biggest overhang into the cytoplasm, alpha actinin (orange), $\sim$ 35 nm, colocalised with the actin cortex, and moesin (magenta), $\sim$ 14 nm, localised closer to the plasma membrane. The schematic is a graphic summary of findings from Truong Quang et al. [2021], which suggest that the size of the proteins might have affected their localisation.

and structures. In particular, the localisation of moesin close to the membrane might be mostly due to its membrane-binding function. An approach where only protein size is modulated independently of other properties will be useful to examine the role of size in protein localisation within the cortex.

Recently, steric effects were suggested to determine localisation of actin-binding proteins within reconstituted actin network [Winkelman et al., 2016]. Actin-crosslinkers have a range of sizes from $\sim$ 5 nm (eg. plastin, fascin), $\sim$ 35 nm (eg. alpha-actinin), to $\sim$ 100 nm filamin (Figure 1.11). Within reconstituted actin network, alpha-actinin segregated from smaller crosslinkers such as fascin and espin leading to differently bundled domains within the actin network (Figure 1.12) [Winkelman et al., 2016]. This intrinsic segregation of crosslinkers was possibly due to steric effects. A computational model further explained the segregation of differently sized crosslinkers with differences in the protein size, persistence length of actin filaments and in non-equilibrium system with the rate of actin polymerisation [Freedman et al., 2019]. The authors suggest crosslinkers for which the length can be modulated as a key to deciphering the roles of different mechanisms in crosslinker segregation. A possible approach is suggested based on a related study where SpAin1 and alpha-actinin 4, yeast and human homolgues were compared for their crosslinking function [Li, 2014]. Bigger SpAin1 proteins were engineered by cloning spectrin alpha-actinin domains behind SpAin1 actin binding sides. However, these additional domains did not only change protein size but also dimerisation properties of the protein.

Therefore, to be able to address the role of protein size a different domain should be added to a consistent actin binding domain.

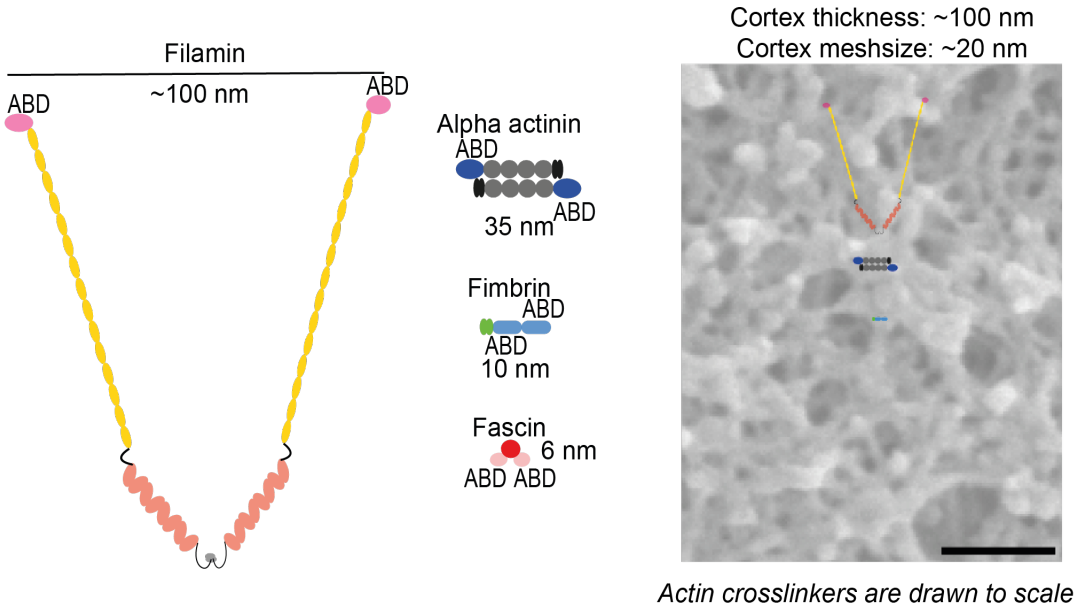

Figure 1.11: **Actin crosslinkers have a range of sizes.** The actin crosslinkers have a range of sizes from 5-100 nm. Schematic representation (left) showing the structure of representative crosslinkers and their sizes. The range in the sizes potentially leads to differences in the localisation within the actin cortex given cortical density and thickness (right). SEM image is courtesy of Dr. Priyamvada Chugh.

Figure 1.12: **Actin crosslinkers with different sizes sterically segregate.** *In vitro* actin crosslinkers of different sizes sterically segregate and form networks of different densities [Winkelman et al., 2016].

Despite the lack of more controlled evidence that the size affects the localisation of actin-binding proteins, independently of any other features, steric segregation might be important in organising actin networks. In particular, in the dense actin networks such as the actin cortex, the range of the sizes of actin binding proteins and specifically actin crosslinkers could drive protein localisation within the cortex, actin structure organisation, and consequently in tension generation (Figure 1.11).

1.6 Model systems to study mechanics and organisation of the cortex

1.6.1 Cell division

Changes in cortical tension drive multiple physiological processes involving changes in cell shape, including cell division. Cell division in most cell types entails two distinct processes

of shape change. Firstly, cell rounds up at the onset of cell division, before mitosis, which is followed by cleavage furrow ingression during cytokinesis. Both of these processes are driven by changes in cortical tension (Figure 1.13) [Cadart et al., 2014, Clark and Paluch, 2011].

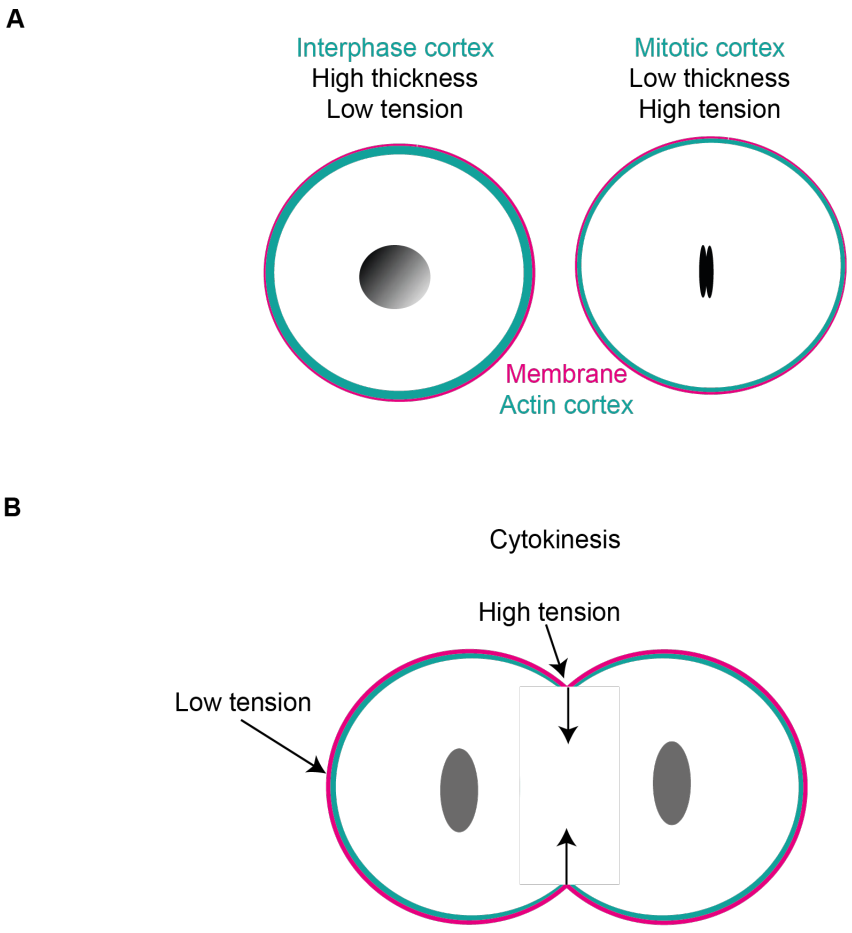

Figure 1.13: **Cell division as a model to study changes in cortical tension.** (A) Round interphase and mitotic cells differ in cortical organisation (thickness) and tension. Along with their homogeneous cortex and comparable shapes this makes them a suitable model to study cortex tension. (B) Cytokinesis is driven by gradients in cortical tension with higher tension at the cleavage furrow than the poles.

Rounded mitotic cell shape is fundamental for successful chromosome segregation and thus successful cell division [Lancaster et al., 2013]. Cell rounding at the onset of mitosis is driven by an increase in cortical tension [Fischer-Friedrich et al., 2014, Maddox and Burridge, 2003, Stewart et al., 2011]. When detached, interphase cells display a round shape with continuos actin cortex similar to mitotic cells. However, cortical tension differs between round interphase and mitotic cells [Chugh et al., 2017, Fischer-Friedrich et al., 2014, Ramanathan et al., 2015]. Round interphase and mitotic cells are a popular system to study differences in cortical tension due to their uniform cortex, shape which is easily

comparable, and the possibility of maintaining the cells in these stages of low and high tension over long periods of times [Chugh et al., 2017, Ramanathan et al., 2015, Serres et al., 2020, Truong Quang et al., 2021]. Recently, interphase and mitotic cortices were also shown to differ in actin thickness and nanoscale NMII localisation [Chugh et al., 2017, Truong Quang et al., 2021]. Therefore, interphase and mitotic cells can also be utilised as a model to study nanoscale differences in cortical organisation related to changes in cortical tension (Figure 1.13A).

While round interphase and mitotic cells are suitable models for comparing relatively static systems with low and high tension, cleavage furrow ingression is driven by gradients in cortical tension. Higher cortical tension at the cellular equator compared to cell poles causes furrow ingression (Figure 1.13B) [Maddox and Burridge, 2003, Matzke et al., 2001, Sedzinski et al., 2011, White and Borisy, 1983]. Furrow ingression is driven by actomyosin contractile ring, a structure of closely packed actin filaments parallel to the cleavage axis and NMII minifilaments [Fenix et al., 2016, Fujiwara and Pollard, 1976, Maupin and Pollard, 1986, Schroeder, 1973]. NMII is enriched in the contractile ring. The precise nanoscale organisation and NMII localisation during formation of cytokinetic tension gradients still remains to be established. However, the requirement for gradients in cortical tension for successful cleavage furrow ingression makes cytokinesis a good model for studying the molecular control of cortical tension.

In my research, I use both interphase and mitotic cells and cells undergoing cytokinesis as models to study tension generation at the nanoscale level.

1.6.2 Cortex enriched blebs

Blebs are spherical plasma membrane protrusions normally appearing on the cell surface during cell migration, cytokinesis, cell spreading, virus infection, and apoptosis [Charras and Paluch, 2008, Charras, 2008, Paluch and Raz, 2013]. Cellular blebbing proceeds in four stages: bleb initiation, expansion, cortex assembly within the bleb and bleb retraction (Figure 1.14). Blebbing of a cell is initiated by a break in membrane to cortex attachment, local rupture of the actin cortex, or inhibition of myosin contractility. Afterwards, bleb expansion is driven by hydrostatic pressure. Growing blebs are devoid of actomyosin cortex, and after the cortex re-polymerises within the blebs, the contractile cortical tension drives bleb retraction. Overall, these properties make blebs a convenient model to study cortex-tension generation.

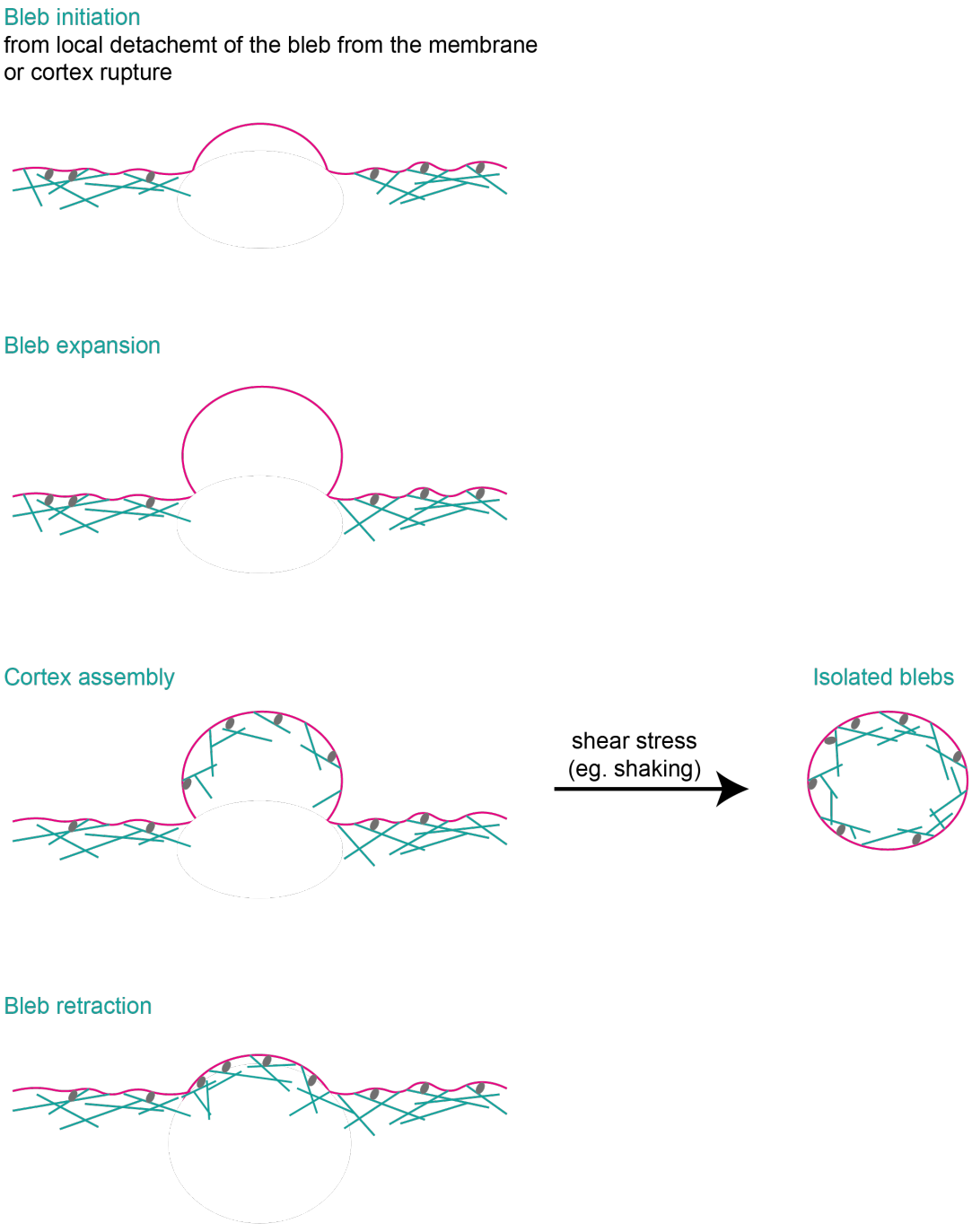

Figure 1.14: **Blebs can be used to study changes in cortex tension and organisation.** Blebbing is initiated by local membrane-to-cortex detachment or cortex rupture, which leads to bleb expansion due to hydorstatic pressure. After the actin cortex gets reassembled in the blebs, it creates contractile forces leading to bleb retraction. Shear stress on the blebbing cells can lead to detachment of the blebs from the cells. Isolated blebs re-establish the cortex making blebs a suitable model system to investigate the cortex.

Investigation of the dynamics of bleb formation and retraction was key to understanding cortical structure and mechanics [Charras et al., 2006, 2008, Tinevez et al., 2009]. Bleb retraction was shown to be driven by a sequential assembly of membrane-to-cortex attachment (ERM proteins), actin, actin bundling and crosslinking proteins (such as alpha-actinin, coronin and tropoymosin) and finally myosin and fimbrin. These findings on cortex assembly within blebs offered an insight into assembly of the contractile cortex [Charras et al., 2006]. Similarly, investigation of the mechanics of tension-driven bleb expansion and retraction demonstrated the key role myosin plays in regulation of contractile cortical tension [Tinevez et al., 2009].

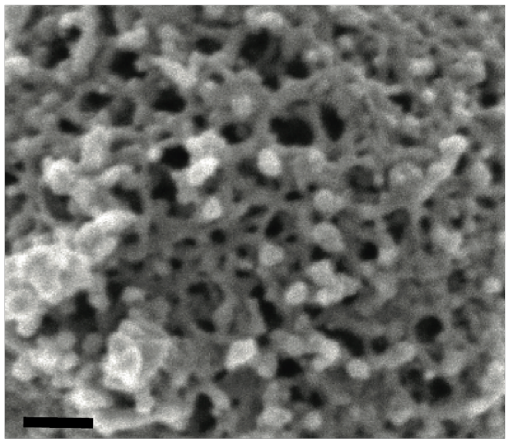

Figure 1.15: **The cortex from isolated bleb resembles the cellular cortex.** Scanning electron micrograph (SEM) of the cortex from an isolated bleb. Scale bar= 50 nm. The image is modified from Cassani [2019].

Finally, by applying shear stress to blebbing cells, blebs can be separated from the cells and form minimal membrane-bound system containing cortex (Figure 1.14) [Biro et al., 2013, Bovellan et al., 2014]. Isolated blebs can re-assemble the actin cortex similar to the cortex of a cell (Figure 1.15) [Biro et al., 2013]. After supplementation with ATP, the cortex of isolated blebs exhibits similar dynamics to the cellular cortex. As such blebs were utilised to enrich for the cortex for proteomic analysis, enabling the identification of the diversity in proteins present in the cortex and important regulators of the cortical structure [Biro et al., 2013, Bovellan et al., 2014]. More recently, blebs were used for structural studies of the nanoscale organisation of the actomyosin cortex, otherwise technically impossible in much bigger cells [Cassani, 2019, Chikina et al., 2019].

In summary, blebs are a good model to study the actomyosin cortex and its mechanics. The possibility of bleb isolation offers an excellent minimal system of membrane-bound dynamic cortex and as such can be used to study the molecular composition and nanoscale

organisation of the cortex.

1.7 Aims

The organisation and in particular the connectivity of the actin cortex are increasingly being identified as key determinants of cortical tension. Increasing evidence shows that cortical actin connectivity affects cortical tension. Actin connectivity is controlled by the amount of crosslinking and filament length. There are multiple possible actin crosslinkers, length regulators and other actin-related proteins present in the cortex that can potentially regulate cortical tension but their role has not been studied systematically.

In this thesis, I focus on the role of cortical proteins, and in particular actin crosslinkers and their size, in cortical tension regulation. To answer which are the most important actin crosslinkers (and other actin proteins) for tension generation and what is the role of crosslinker size in cortex tension regulation, I had two main aims:

1. Identify changes in cortical protein levels between low and high tension cortices. To this aim, we characterised changes in proteic composition of cortices from interphase and mitotic cells.

2. Investigate the role of the size of actin crosslinkers for their localisation and role in cortex tension generation. To this aim, we developed artificial crosslinkers to investigate the role of crosslinker size in tension generation and localisation within a dense actin network independently of other features.

Chapter 2

Results

In the first part of this section, I identify differences in protein composition of the actin cortex from interphase and mitotic cells, which are known to differ in cortical tension [Chugh et al., 2017, Fischer-Friedrich et al., 2014]. To do so, I isolated the actin cortex by isolating cortex enriched blebs from cells synchronised in interphase and mitosis and characterise the protein composition of these blebs by mass spectrometry. Mass spectrometry was performed by Dr. Geneviève Lavoie and Dr. Philippe Roux at the University of Montreal and I collaborated with Dr. Sami Nourreddine and Dr. Philippe Roux for the analysis of the mass spectrometry results. Through further investigation of one of the candidates identified, the septin family of proteins, I demonstrate that this dataset is an important resource for a systematic investigation of regulators of cortical mechanics and thus cell shape.

In the second part of this section, I focus on how protein size, specifically the size of actin crosslinkers affects their localisation and thus role in tension generation. For this, we created artificial crosslinkers in collaboration with Dr. Fabio Parmeggiani. We can change the size of these artificial crosslinkers by changing the number of identical repeat domains without changing any other part of the sequence. In this chapter, I mainly focus on differences in cortical localisation and on cell mechanics during division of cells expressing artificial crosslinkers of varying sizes.

2.1 Interphase and mitotic cells differ in the protein composition of the actin cortex

It was recently shown by Paluch lab and others that besides myosin localisation and activity, the connectivity of the actin network is also key for controling cortical tension [Chugh et al., 2017, Ding et al., 2017, Ennomani et al., 2016]. Connectivity can be affected by the number of crosslinks and length of the filaments. Indeed, depletion of candidate actin-binding proteins affecting actin polymerisation and nucleation (DIAPH1, PFN1, DBN1, CYFIP1), and actin bundling and crosslinking (ACTN4, PLST1) have been shown to affect cortex mechanics [Chugh et al., 2017, Logue et al., 2015, Toyoda et al., 2017]. However, these were only a few candidates that were tested while systematic investigations of cortex tension regulation have been significantly hindered by our limited understanding of how cortical composition changes when tension changes.

Thus, I set out to systematically investigate the role of actin crosslinkers for cortex tension regulation in cells. Given that there were multiple possible crosslinkers present in the cortex, I firstly wanted to determine which crosslinkers were most likely to significantly impact cortex tension by comparing their cortical levels in interphase and mitotic cells, which were previously shown to differ in cortical tension [Chugh et al., 2017]. I firstly attempted to compare levels of crosslinkers with immunofluorescence, which I describe in more detail at the beginning of this section. However, this approach proved challenging, I thus turned to mass spectrometry of cortical fractions. We performed mass spectrometry on cortex-enriched blebs isolated from synchronised cells, where we detected 2268 proteins allowing us to create a comprehensive resource of changes in protein composition between interphase and mitotic cortices. This resource allows for systematic investigations of the molecular control of mitotic cell shape and actin cortex mechanics beyond actin crosslinkers. In the second part of this section, I describe the development of the protocol for bleb isolation along with the analysis of mass spectrometry results. Finally, I show that our dataset led to identification of septins, in particular septin 9 as regulators of cell shape during cell division.

Most of the data from this chapter led to a publication (see Appendix B) [Vadnjal et al., 2022].

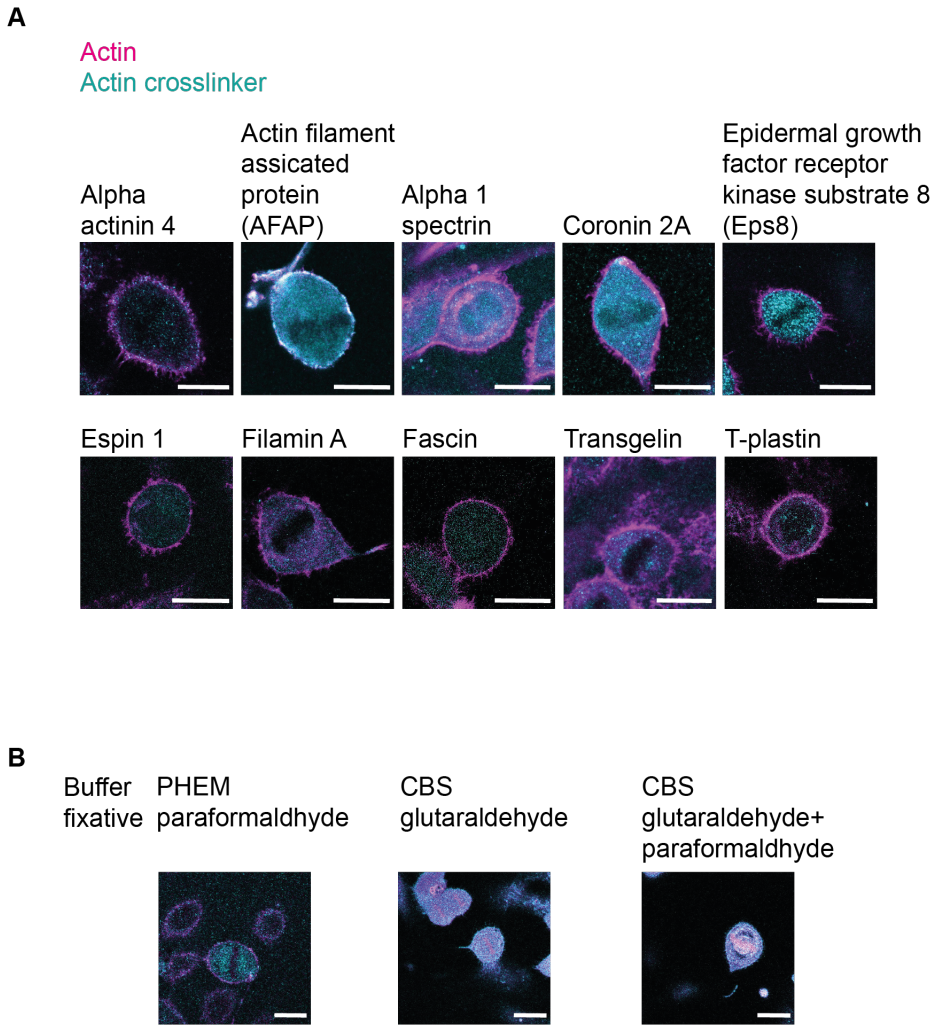

Figure 2.1: **Fluorescencent labelling of actin crosslinkers at the cortex of mitotic cells.** (A) Fluorescent labelling of actin crosslinkers (cyan) and F-actin (magenta) in mitotic cells. A representative example of the labelling is shown for proteins from protein groups: alpha actinin, actin filament associated protein, spectrin, coronin, epidermal growth factor receptor, espin, filamin, fascin, transgelin, plastin. Antibodies used for the images shown here are marked in bold in Table 2.1. Samples were fixed with 4% paraformaldehyde in cytoskeleton buffer with sucrose (CBS). (B) Representative examples of different types of fixation tested with PHEM instead of CBS buffer or glutaraldehyde fixation methods tested with the antibody against alpha-actinin 4 (cyan) and F-actin (phalloidin, magenta). Scale bars = 20 µm.

2.1.1 Comparison of actin-binding protein levels in the actin cortex with immunofluorescence

To systematically investigate the role of actin crosslinkers in controlling cortex tension, I firstly wanted to identify candidate crosslinkers (Table 2.1) which are likely important in tension generation. To this aim, I wanted to compare cortical levels of actin crosslinkers between interphase and mitotic cells, which are known to differ in tension. I wanted to compare cortical levels rather than whole cell levels of crosslinkers to account for any differences in localisation rather than total cellular protein levels. I firstly planned to do this comparison by immunostaining actin crosslinkers in mitotic cells and interphase.

I tested multiple antibodies commercially available against various crosslinkers (Table 2.1) in round mitotic HeLa cells. Most of these crosslinkers were previously shown to localise to the cortex, detected in cortical fractions, or in purified F-actin from mitotic cells [Biro et al., 2013, Charras, 2008, Serres et al., 2020]. To stain for these crosslinkers, I firstly used a combination of permeabilisation and fixation with 4 % paraformaldehyde in cytoskeleton buffer, supplemented with sucrose to maintain osmotic balance (CBS), following a protocol routinely used in the lab for preserving the underlying structure of the actin cortex (Figure 2.1). Most of the antibodies seemed to bind unspecifically or with only a mild enrichment at the cortex (summarised in Table 2.1, representative examples shown in Figure 2.1A) with only a few examples (eg. actin filament associated protein) having a clear cortical enrichment of the actin crosslinkers. Overall, the staining achieved using this protocol could not be used for comparison of cortical levels between interphase and mitosis for most of the antibodies against various crosslinkers tested.

To increase antibody specificity to cortical actin and decrease (unspecific) cytoplasmic binding, I tested a few different methods of fixation (Figure 2.1B). Firstly, I replaced CBS with a different buffer frequently used for fixation of cytoskeletal components, a PHEM buffer. Fixation with PHEM buffer and paraformaldehyde led to similar results to fixation in CBS buffer (Figure 2.1A). Additionally, I tested glutaraldehyde in place of paraformaldehyde and a combination of paraformaldehyde and glutaraldehyde as fixative against alpha actinin 4 (Thermo Fischer) (Figure 2.1). Despite varying the concentration of fixatives the immunofluorescence labelling and thus image quality did not improve.

Overall, these results suggested that an extensive optimisation would be required for immunostaining of actin crosslinkers. This optimisation could take a long time without guarantees of success as some antibodies might not work regardless of fixation and stain-

Antibody	Isoform	Company	Catalogue number	Comments on staining
AFAP (actin filament associated protein)		**Protein Tech**	**21093-1AP**	**cotical; most specific and cortical of the tested antibodies**
Alpha actinin	pan	Santa Cruz	sc7453	not working
Alpha actinin	2	Thermo Fischer	701914	cytoplasmic, unspecific except excluded from DNA
Alpha actinin	4	Abcam	ab108198	not working
Alpha actinin	**4**	**Zymed**	**42-1400**	**cytoplasmic, unspecific**
Alpha actinin	4	Santa Cruz	sc49332	not working
Coronin	1B	Santa Cruz	sc271375	cytoplasmic, unspecific except excluded from DNA
Coronin	**2A**	**Santa Cruz**	**sc376194**	**cytoplasmic, somewhat cortical**
Coronin	6	Thermo Fischer	PA524759	cytoplasmic, unspecific except excluded from DNA
Coronin	7	Invitrogen	PA572695	not working
Espin		**Santa Cruz**	**sc393469**	**cytoplasmic, unspecific**
Eps8 (Epidermal growth factor receptor kinase substrate 8)		**Abcam**	**ab124882**	**cytoplasmic, unspecific**
Fascin	**pan**	**Milipore**	**MAB3582**	**cytoplasmic, unspecific**
Fascin	1	Santa Cruz	sc-21743	cytoplasmic, unspecific except excluded from DNA
Filamin	1	Abnova	H00002316-M01	not working
Filamin	**1**	**Santa Cruz**	**sc-28284**	**cytoplasmic, unspecific except excluded from DNA**
Filamin	1	Cell Signalling	4762S	cytoplasmic, unspecific
Filamin	2	Abcam	ab97457	cytoplasmic, somewhat cortical; excluded from DNA
Filamin	3	Cell Signalling	86972S	not working
Filamin	3	Sigma	HPA006135	cytoplasmic, unspecific except excluded from DNA
Plastin	1	Abcam	ab94605	cytoplasmic, unspecific except excluded from DNA
Plastin	2 (L)	Invitrogen	MA511921	cytoplasmic, somewhat cortical; excluded from DNA
Plastin	**3 (T)**	**Abcam**	**ab137585**	**cytoplasmic, somewhat cortical**
Spectrin	**alpha1**	**abcam**	**ab11751**	**cytoplasmic, unspecific**
Spectrin	beta1	Abcam	ab2808	not working
Transgelin	**pan**	**Invitrogen**	**PA529767**	**cytoplasmic, unspecific except excluded from DNA**
Transgelin	2	Santa Cruz	sc166697	cytoplasmic, somewhat cortical; excluded from DNA

Table 2.1: **Effectivity of the antibodies tested for immunofluorescence staining of actin crosslinkers.** 27 different antibodies were tested to label actin crosslinkers in the cortex. Antibodies in bold are shown in Figure 2.1.

ing conditions. Since I wanted to systematically compare levels of most crosslinkers present in cells to identify key candidates for future experiments, this approach of labelling with immunofluorescence was inefficient.

2.1.2 Isolation of cellular blebs enriched for the actin cortex from synchronised cells

Instead of comparing the levels of actin crosslinkers in interphase and mitotic cortices with immunofluorescence, I performed a mass spectrometry of cortices isolated from synchronised cells (Figure 2.2). To obtain interphase cells, I synchronised HeLa cells in G1/S phase using thymidine (Figure 2.2A). Excess thymidine in cellual medium prevents progression of cells past G1/S division checkpoint. Synchronised interphase cells were then detached

using trypsin and maintained in suspension (Figure 2.2B, top panel). Trypsin was previously shown not to affect cortical organisation and tension [Chugh et al., 2017]. To obtain mitotic cells, HeLa cells were synchronised using Eg5 inhibitor S-Trityl-L-Cystine (STLC), which prevents bipolar spindle formation and blocks cells in prometaphase. I further enriched for mitotic cells by mechanically separating them from adherent cells through a mitotic shake-off, which led to a population of rounded mitotic cells (Figure 2.2B, bottom panel).

To identify proteins most likely to play a role in the cortical tension increase between interphase and mitosis, I wanted to identify any differences in localisation and expression by only comparing cortical protein levels rather than whole cell protein levels. To enrich for the actin cortex over the rest of the cell for proteomic analysis, a protocol was previously developed for isolation of cortex-enriched blebs from unsynchronised cells [Biro et al., 2013, Bovellan et al., 2014]. I decided to use the same approach with synchronised cells. Besides differences in synchronisation which required higher cell numbers than when cells were not synchronised, cells, used in previous publications, were attached to the surface which made bleb isolation from the cells easier. Taken together, I had to significantly adapt this previously published protocol to isolate blebs from synchronised unattached cells.

Overall, bleb isolation involved the following steps (Figure 2.3): blebbing was induced using the actin depolymerising drug Latrunculin B [Spector et al., 1983] and blebs were detached from cells by shear stress. Blebs were then separated from the cells through filtration. To facilitate cortex re-assembly, the bleb membrane was then permeabilised by addition of haemolysin A with an exogenous ATP regeneration system (a mixture of UTP, ATP, creatine phosphate, creatine kinase) added to the buffer (Figure 1D). Haemolysin A allowed the entry of the ATP regeneration system in the blebs, which was essential for the establishment of a dynamic cortex resembling the cortex of the cells and important for visualisation of the cortex in blebs in control experiments.

When I first tested the protocol, I observed that mitotic HeLa cells yielded much fewer blebs than the constitutively blebbing unsynchronised M2 cells used in previous studies [Biro et al., 2013, Bovellan et al., 2014]; to account for this limited output and the loss of cells during synchronisation, I considerably increased the amount of cells used. To yield sufficient protein amount for mass spectrometry, I used 15 T175 flasks of cells at 80 % confluency synchronised in interphase and 60 T175 flasks of cells synchronised in mitosis per replicate.

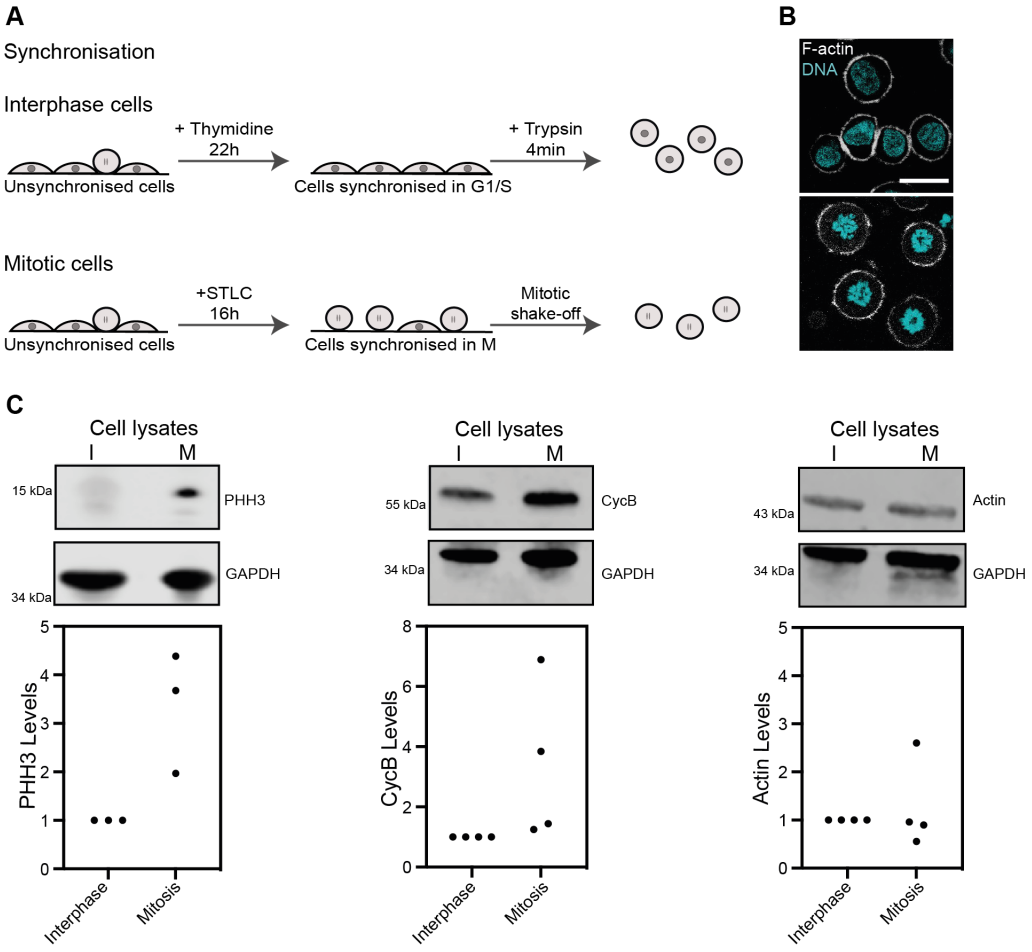

Figure 2.2: **Cell synchronisation in interphase and mitosis.** (A) Schematic describing cell synchronisation in interphase (top) and mitosis (bottom). Cells were synchronised in interphase (G1/S phase) with a 22 h thymidine treatment, detached from the dish and rounded up using trypsin. For synchronisation in mitosis, cells were treated with Eg5 inhibitor STLC for 16 h, followed by a mitotic shake-off. (B) Representative confocal images of synchronised interphase (upper panel) and mitotic (lower panel) cells. Cyan: DAPI (DNA), white: phalloidin (F-actin). DAPI staining shows the nuclear organisation of DNA in cells synchronised in interphase and condensed chromosomes in cells synchronised in mitosis. Scale bar= 20 µm. (C) Fluorescent western blot analysis with quantification of interphase and mitotic cell lysates for the mitotic markers phosphorylated histone H3 and cyclin B, and for actin, confirming synchronisation at the cell population level. GAPDH: loading control. The images are inverted contrast fluorescent western blots.

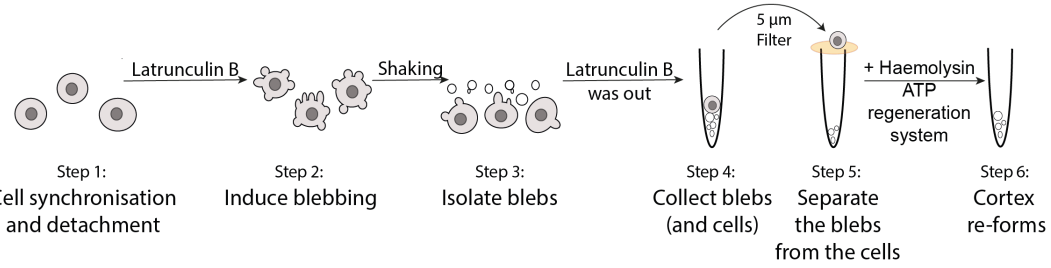

Figure 2.3: **Isolation of cortex-enriched blebs from the cells.** Schematic depicting the bleb isolation protocol. Blebs were isolated from round cells synchronised in interphase or mitosis (Step 1). Blebbing was induced by treatment with the actin depolymerising drug Latrunculin B (Step 2). Blebs were detached from the cells with sheer stress (Step 3) and separated blebs were isolated from the cells using a 5 µm filter (Steps 4, 5). Re-assembly of a dynamic actin cortex was induced in blebs through addition of ATP regenerating system. The alpha-toxin haemolysin was used to permeabilise the blebs and this allow ATP regeneration system uptake (Step 6).

Secondly, blebs separated from detached cells were much more difficult to completely filter from the cells, since unlike with attached cells, where almost only blebs were floating following bleb detachment, both blebs and cells were in suspension, which required more stringent filtration. To obtain a pure sample only containing blebs, I tested two different filters used in Step 5 (Figure 2.3). I compared a Pluristrainer 5 µm and a Sartorious Minisart 5 µm Syringe Filter. Bleb isolation using Pluristrain filters yielded $\sim$ 6.5 µg of protein per T175 flask of detached interphase cells while Minisart filters yielded only $\sim$ 1 µg of protein per T175 flask of detached interphase cells. I examined the composition of these samples prepared with different filters with a western blot (Figure 2.4A). I stained for alpha-actinin 1, beta-actin and histone H3. Consistent with the lower starting protein amount of the Minisart sample in comparison to the the Pluristrain blebs and whole cell samples, the levels of the proteins detected by western blot were also lower. However, while there was a faint signal for actin and alpha-actinin 1, there was no signal for histone H3 in the Minisart samples, suggesting that the isolation method with Minisart filters successfully enriches for actin and actin-binding proteins and depletes other such as nuclear (histone H3) proteins. In contrast, samples obtained with Pluristrain filters were enriched in actin and alpha-actinin 1 compared to cell samples but also showed high levels of histone H3. Since I required a high enrichment for the actin cortex and as low amounts of proteins from cellular cytoplasm as possible, I decided to proceed with Minisart filters.

Additionally, I confirmed that bleb isolation following the steps described in Figure 2.3 with bleb separation using Minisart filters enriches for actin and actin-binding proteins

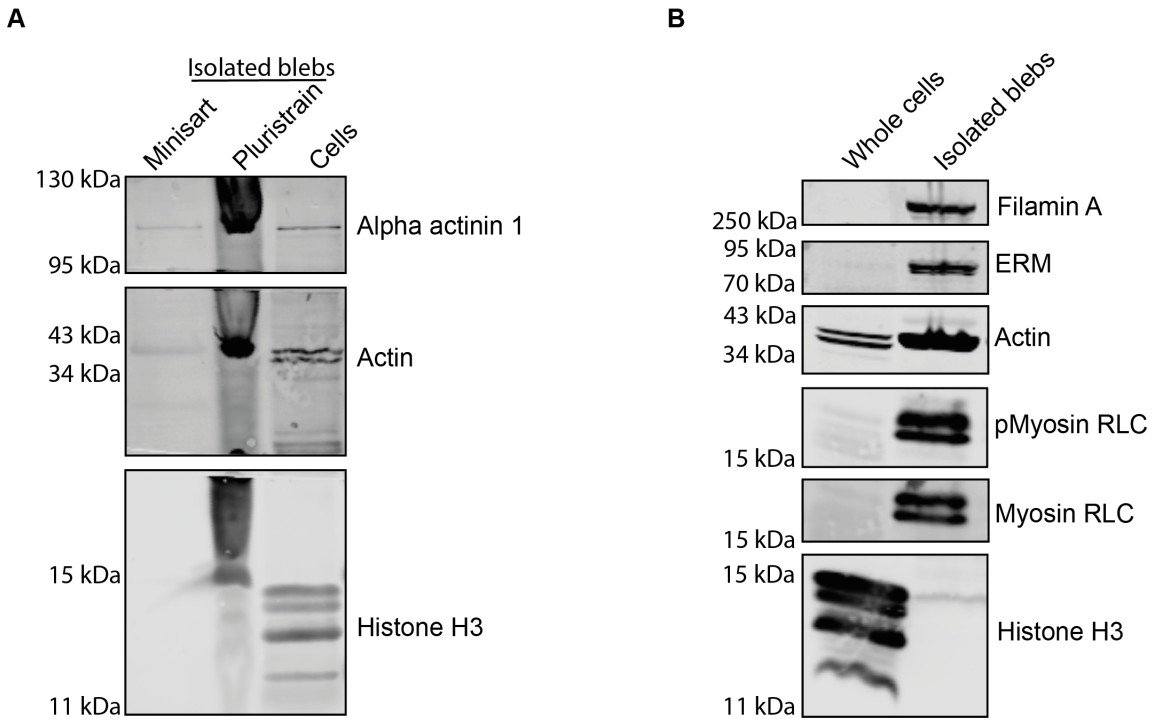

Figure 2.4: **Comparison of different filters for separation of the blebs from the cells.** (A) Levels of alpha-actinin 1, actin and histone H3 in bleb samples isolated with Minisart or Pluristrain filters and in whole cells. (B) Levels of actin, histone H3, and actin-binding proteins (myosin regulatory light chain (RLC), phosphorylated myosin RLC, ezrin-radixin-moesin (ERM), and filamin) in a similar amount of protein obtained from blebs isolated with Minisart filters or from whole cells. The figure shows inverted contrast fluorescent western blot images.

and depletes other cellular components. I compared levels of representative cytoplasmic and actin-binding proteins with western blot (Figure 2.4B). I found that, the sample from isolated blebs was clearly enriched in the actin-binding proteins filamin A, ezrin-radexin-moesin, myosin regulatory light chain, phosporylated myosin regulatory light chain and actin while depleted in histone H3 in comparison to whole cell samples when similar amounts of total protein were compared. Fluorescent imaging of a sample of isolated blebs stained for F-actin (phalloidin) also showed an enrichment of blebs and no cells in the samples (Figure 2.5A). Fluorescence super-resolution imaging also confirmed that isolated blebs from synchronised cells re-established a continuous cortex with similar thickness to a mitotic cortex (Figure 2.5B). Overall, bleb isolation with Minisart filters yielded blebs that can successfully re-establish an actin cortex and that are considerably enriched for actin and actin-binding proteins.

To further enrich for the actin cortex from isolated blebs and remove cytoplasm from the blebs, I tested a treatment with a bleb lysis buffer (BLB) buffer [Biro et al., 2013]

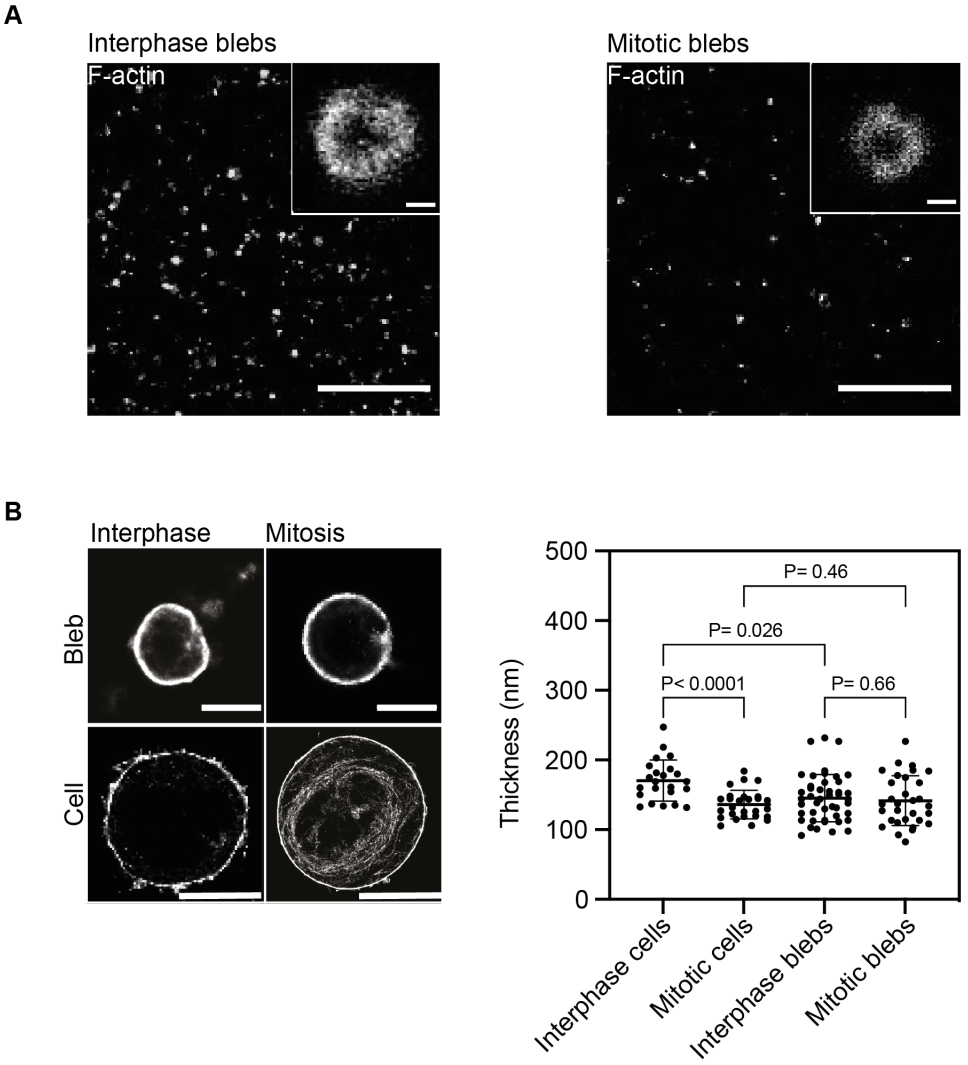

Figure 2.5: **Isolated blebs.** (A) Representative confocal images of the actin cortex in blebs isolated from interphase (top) and mitotic (bottom) cells. White: phalloidin (F-actin) Insets: individual blebs. Scale bars= 20 µm; 0.5 µm (inset). (B) Stochastic Optical Reconstruction Microscopy (STORM) of the actin cortex in blebs isolated from interphase and mitotic cells, re-established after the treatment with ATP regeneration system and quantification of cortical thickness. Statistics: Total 23 (interphase cells), 27 (mitotic cells), 45 (interphase blebs), 31 (mitotic blebs) individual cells from 3 independent experiments. Each dataset passed the normality test and Welch's t-test was used for comparison. White: phalloidin (F-actin) Scale bars= 2 µm (blebs), 10 µm (cells).

(Figure 2.6). The BLB buffer should separate soluble (cytoplasm) from insoluble (cortex) fraction of the bleb. After treatment with BLB buffer, I compared levels of various actin-binding proteins in the soluble and insoluble fractions. Contrary to my expectations, many actin-binding proteins (filamin A, ERM, myosin RLC) were not enriched for in the insoluble fraction. Equally, GAPDH, a cytoplasmic protein, was only moderately depleted in the insoluble fraction compared to the soluble fraction. Only alpha-actinin 1 showed the expected enrichment in the insoluble fraction. Based on these results, I concluded that BLB treatment did not further enrich for actin and actin-binding proteins in isolated bleb samples and decided to use complete blebs rather than BLB treated blebs for further analysis.

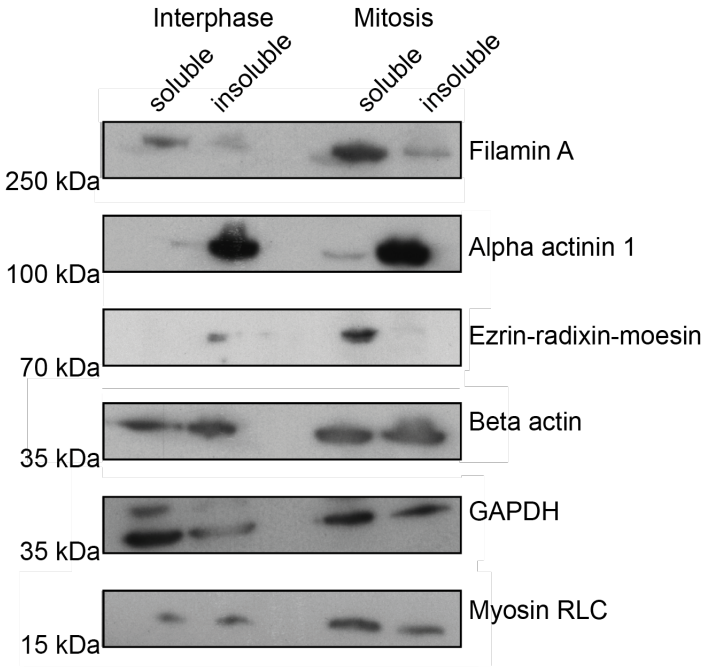

Figure 2.6: **Comparison of actin-binding protein levels in the soluble and insoluble fractions after treatment of isolated blebs with BLB buffer.** Levels of filamin A, alpha-actinin 1, ezrin-radixin-moesin, actin, myosin regulatory light chain, GAPDH in the soluble and insoluble fraction of isolated blebs after treatment with BLB buffer. Western blots were developed using ECL.

The final protocol for bleb isolation from synchronised cells involved cell synchronisation in interphase using thmidydine and in mitosis using STLC (Figure 2.2). Interphase cells were rounded and detached with trypsin and mitotic cells with a mitotic shake off which also further enriched for mitotic cells. This protocol led to two clearly different populations of cells (Figure 2.2B, C), both with a round continuous cortex (Figure 2.2B). Blebbing of

these synchronised cells was induced with Latrunculin B treatment and blebs were removed from the cells with shear stress (Figure 2.3). Filtration with Minisart filters successfully separated blebs from the cells (Figure 2.4B, 2.5). Following a treatment with haemolysin A and an ATP regeneration system, blebs successfully re-established an actin cortex and were enriched in the actin and actin-binding proteins compared to whole cells. Before mass spectrometry, a small fraction of the sample was fixed and stained with phalloidin (Figure 2.5A) as a control to confirm successful bleb isolation and ability of blebs to re-establish the cortex. Triplicate samples of interphase and mitotic blebs were isolated following this protocol and used for further analysis with mass spectrometry.

2.1.3 Proteomic composition of blebs isolated from interphase and mitotic cells

To identify proteins potentially involved in the regulation of cortical tension in cortex-enriched blebs isolated from interphase and mitotic cells, I collaborated with Dr. Geneviève Lavoie and Dr. Philippe Roux to perform liquid chromatography (LC)-tandem mass spectrometry (LC-MS/MS) of the isolated blebs. They separated proteins from each of three biological replicates of blebs, that I lysed in denaturing Laemmeli buffer, by SDS-PAGE (Figure 2.7A). Following in-gel trypsin digestion and analysis by LC-MS/MS of purified peptides, they identified 117088 unique peptides from 2268 unique proteins in interphase and mitosis (Figure 2.7B-D). For further analysis we only considered proteins that were detected from at least 2 unique peptides. The levels of each detected protein in each of the replicates in interphase and mitosis were normalised to the total peptides in the sample and to the total peptides in the first replicate of interphase blebs (Figure 2.8, bottom panel) to account for any differences in total protein levels detected between the replicates.

In collaboration with Dr. Sami Nourreddine and Dr. Philippe Roux, I then analysed changes in (normalised) levels of proteins detected by mass spectrometry. Overall, 1793 and 2164 different proteins were detected in biological triplicates of blebs isolated from interphase and mitotic cells, respectively (Figure 2.9A). Out of these, 922 proteins with a unique peptide number above 2 and normalised spectral count above 2 were present in both interphase and mitotic blebs (Figure 2.9B). These 922 proteins were used for further analysis.

Among these 922 proteins, there were proteins known to change in levels between in-

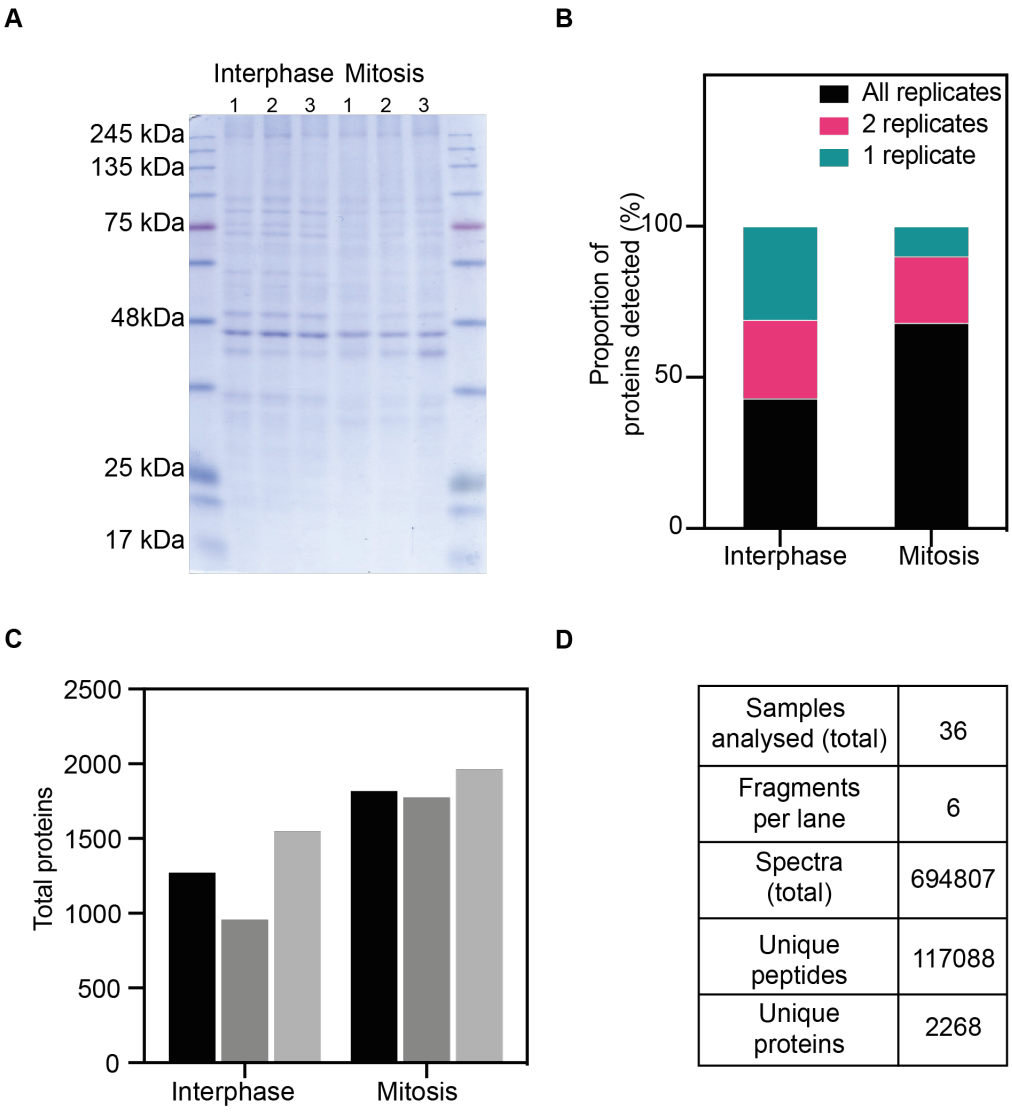

Samples analysed (total)	36
Fragments per lane	6
Spectra (total)	694807
Unique peptides	117088
Unique proteins	2268

Figure 2.7: **Proteomic composition of interphase and mitotic blebs.** (A) Coomassie staining of isolated blebs from interphase and mitosis in the three experimental replicates used for mass spectrometry. (B) Percentage of proteins detected in all, two or one of the replicates. (C) Number of proteins detected in each replicate. (D) Overall readouts of the mass spectrometry analysis of samples. Experiments and analysis presented in this Figure were performed by Dr. Geneviève Lavoie and Dr. Philippe Roux, University of Montreal.

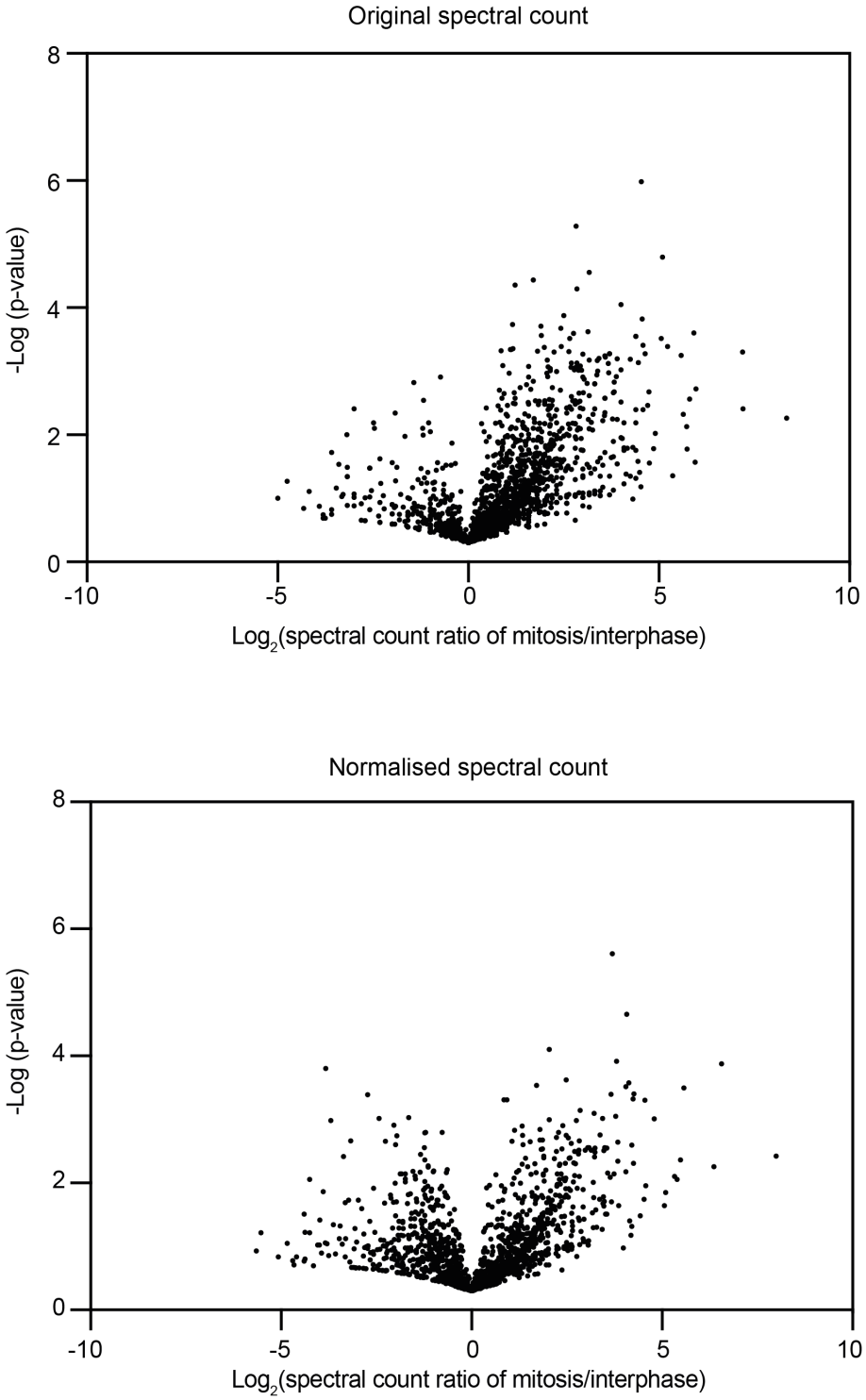

Figure 2.8: **Normalisation of protein levels detected by mass spectrometry.** Protein levels detected by mass specrometry of triplicates from interphase and mitotic blebs (top) were normalised to the total peptide count in each individual replicate and to the ratio of the total peptide count from the replicate to the total peptide count from the first replicate of interphase blebs (bottom). These data were analysed by Dr. Philippe Roux, University of Montreal.

terphase and mitotic cortices, which I considered as controls (Figure 2.9C). These included cyclin-dependent kinase 1 (CDK1), a known cell-cycle regulator that increases in levels in mitosis [Lee and Nurse, 1987] and anillin, cortical protein that translocates from the nucleus to the actin cortex in mitosis [Field and Alberts, 1995]. Levels of both CDK1 and anillin were higher in mitotic compared to interphase blebs. Additionally, consistent with recent findings demonstrating a role for intermediate filament protein vimentin in the mitotic cortex [Duarte et al., 2019, Serres et al., 2020] the levels of vimentin were much higher in mitotic blebs. Finally, caldesmon, which dissociates from actin filaments during mitosis [Yamashiro et al., 1990], was detected at lower levels in mitotic compared to interphase blebs. Together, these changes in CDK1, anillin, vimentin and caldesmon levels confirmed that the mass spectrometry of isolated blebs was successful in identifying proteins for which cortical levels change between interphase and mitosis.

Then, we explored the overall composition of the blebs. Firstly, we performed a Gene Ontology (GO) analysis of 922 proteins detected in interphase and mitosis (Figure 2.10). Cellular component GO terms describing actin filament (P-value= 4.68×10^{-11}), actomyosin (P-value= 3.78×10^{-14}), cell cortex (P-value= 1.60×10^{-25}) and actin cytoskeleton (P-value= 3.74×10^{-38}), GO terms related to molecular functions describing cadherin binding (P-value= 4.23×10^{-103}), cell adhesion molecule binding (P-value= 3.08×10^{-93}), cytoskeletal protein binding (P-value= 6.56×10^{-42}), actin binding (P-value= 1.54×10^{-35}), structural constituent of cytoskeleton (P-value= 3.851×10^{-17}) and GO terms describing biological processes for actin filament-based process (P-value= 7.85×10^{-32}), cytoskeleton organisation, (P-value= 1.013×10^{-30}), cell cycle (P-value= 1.22×10^{-17}), actin filament-based movement (P-value= 0.45×10^{-4}) were all significantly enriched for in our dataset of proteins detected in the blebs.

Taken together, GO analysis of terms describing cellular components, molecular function and biological processes related to the cell surface, and in particular actin structures, suggested that isolated blebs are indeed enriched in actin cortex components and are thus a good model system to analyse cortex composition.

2.1.4 Differences in protein levels between blebs isolated from interphase and mitotic cells

After analysing the overall protein composition of the blebs, I focused on the levels of specific proteins detected and compared their levels between interphase and mitotic blebs

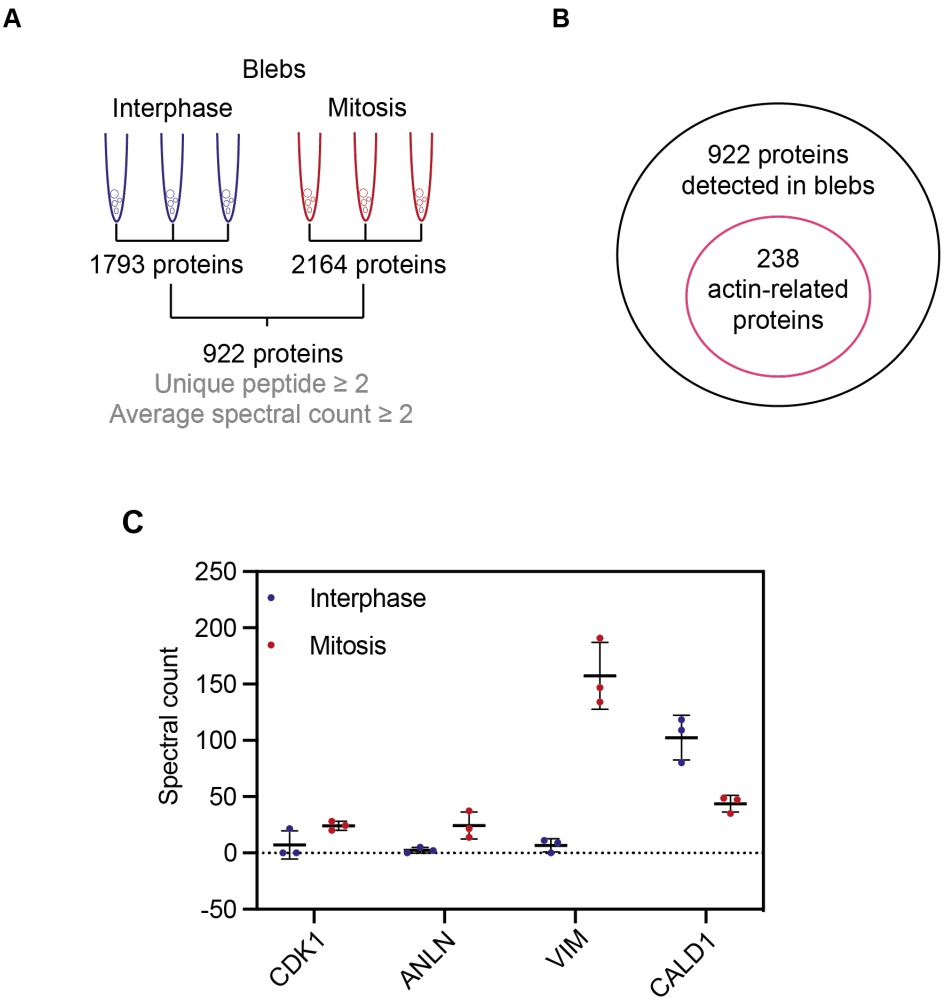

Figure 2.9: **Representation of proteins detected in interphase and mitotic blebs.** (A) Schematic of proteins detected in blebs by mass spectrometry. 1793 and 2164 different proteins were detected in blebs isolated from interphase and mitotic cells, respectively. Out of these, 922 proteins were selected for further analysis based on unique peptide number and normalised spectral count above 2 in both interphase and mitotic blebs. This analysis was performed by Dr. Sami Nourreddine. (B) Schematic of actin-related proteins among all proteins detected in blebs. (C) Spectral counts in the mass spectrometry analysis of mitotic and interphase blebs for cyclin-dependent kinase 1 (CDK1), anillin (ANLN), vimentin (VIM), caldesmon (CALD1), proteins known to change in levels at the cortex between interphase and mitosis. Each data point corresponds to an individual replicate, with mean ± 1 standard deviation shown.

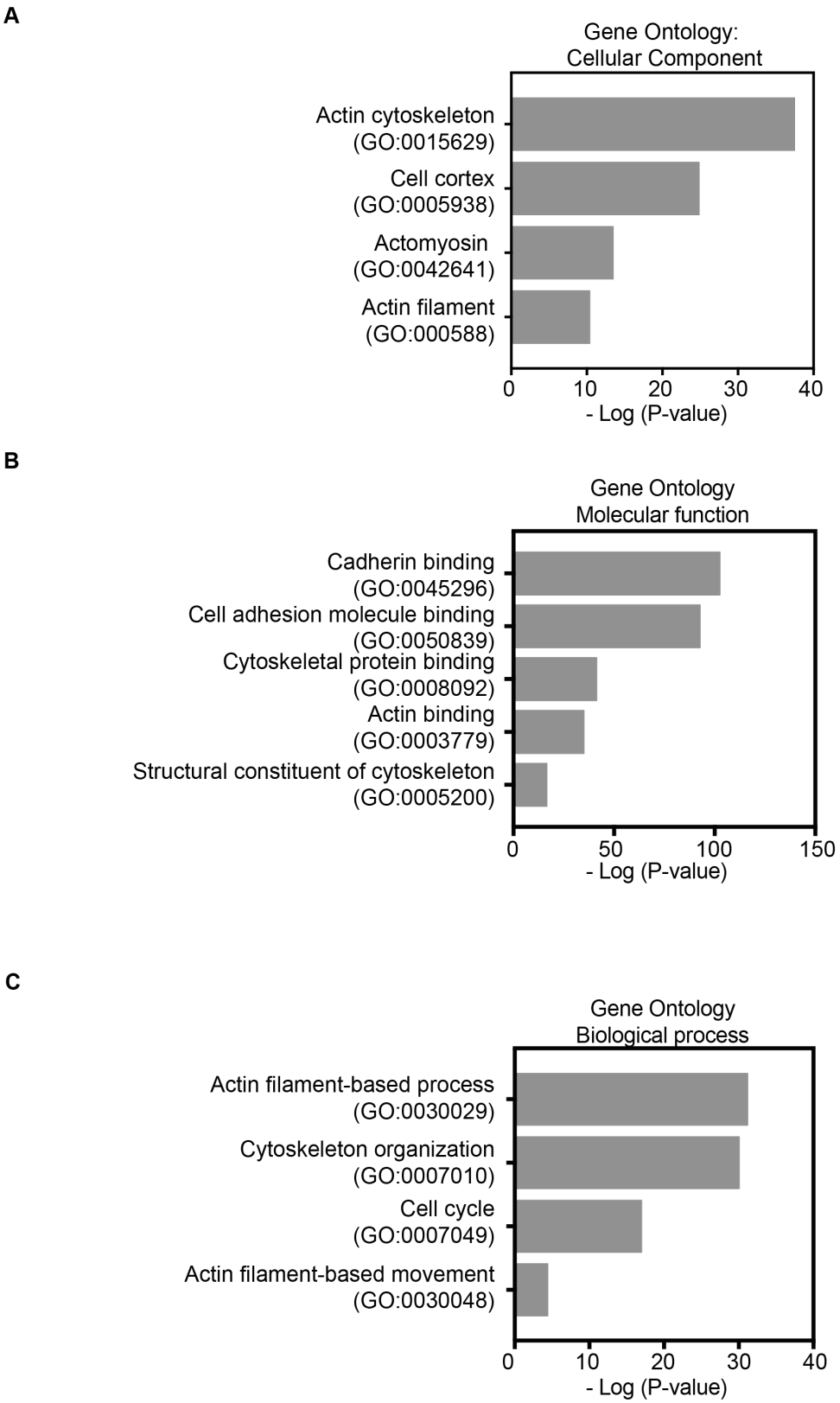

Figure 2.10: **Gene Ontology (GO) analysis of proteins detected in blebs.** Gene Ontology (GO) analysis of 922 proteins detected, focusing on GO terms for cellular component (A), molecular function (B), and biological process (C) related to cell surface.

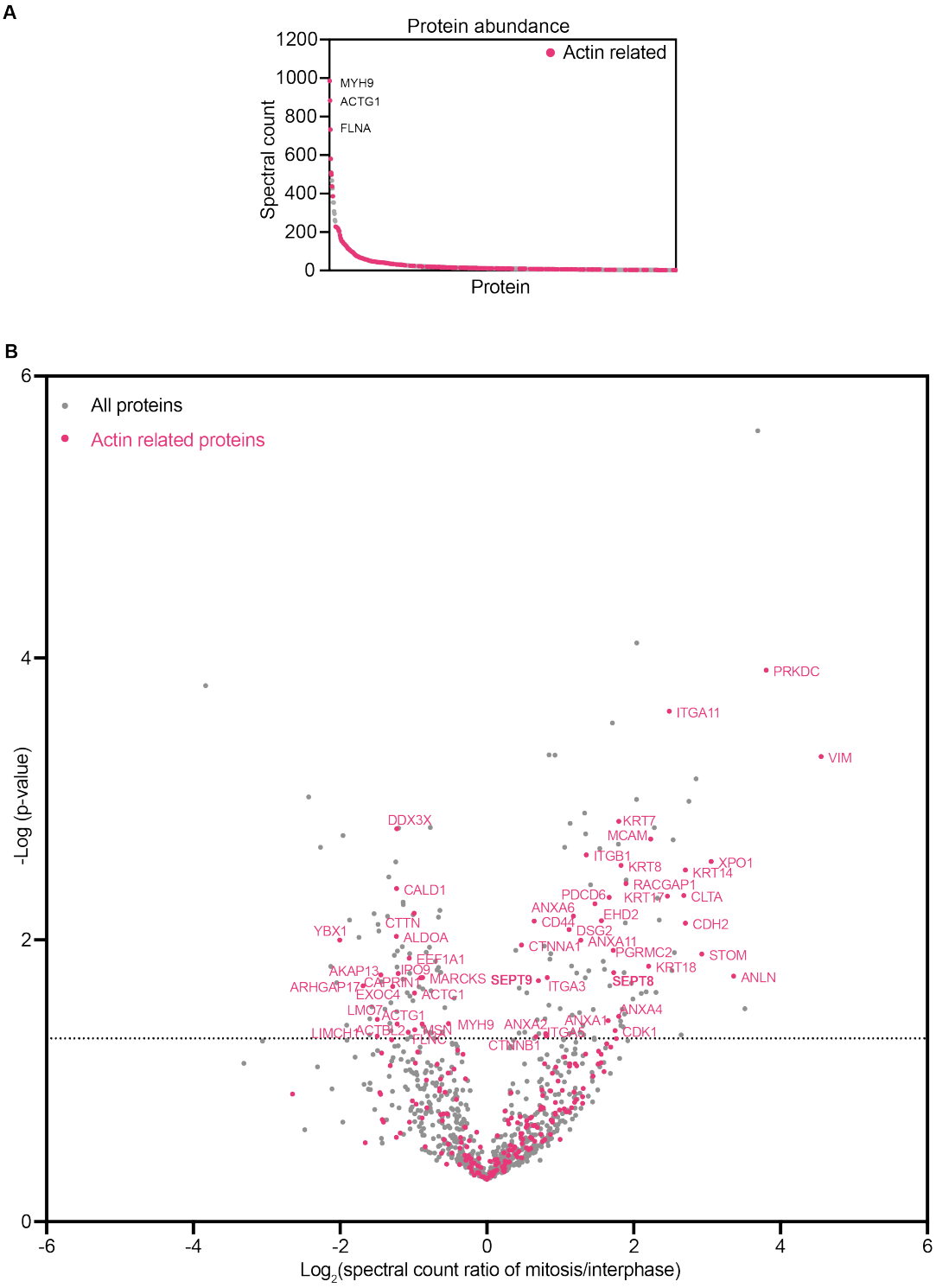

Figure 2.11: **Levels of individual proteins detected in blebs.** (A) Average spectral counts in all replicates from interphase and mitotic blebs of the 922 proteins. (B) Volcano plot of the 922 selected proteins detected in blebs, showing the enrichment (x-axis) and the significance of this enrichment (P-values, y-axis) between interphase and mitosis. Dotted line highlights -Log10 (P-value) = 1.3, corresponding to P-value= 0.05. Statistics: Student's t-test. Magenta dots: actin related proteins.

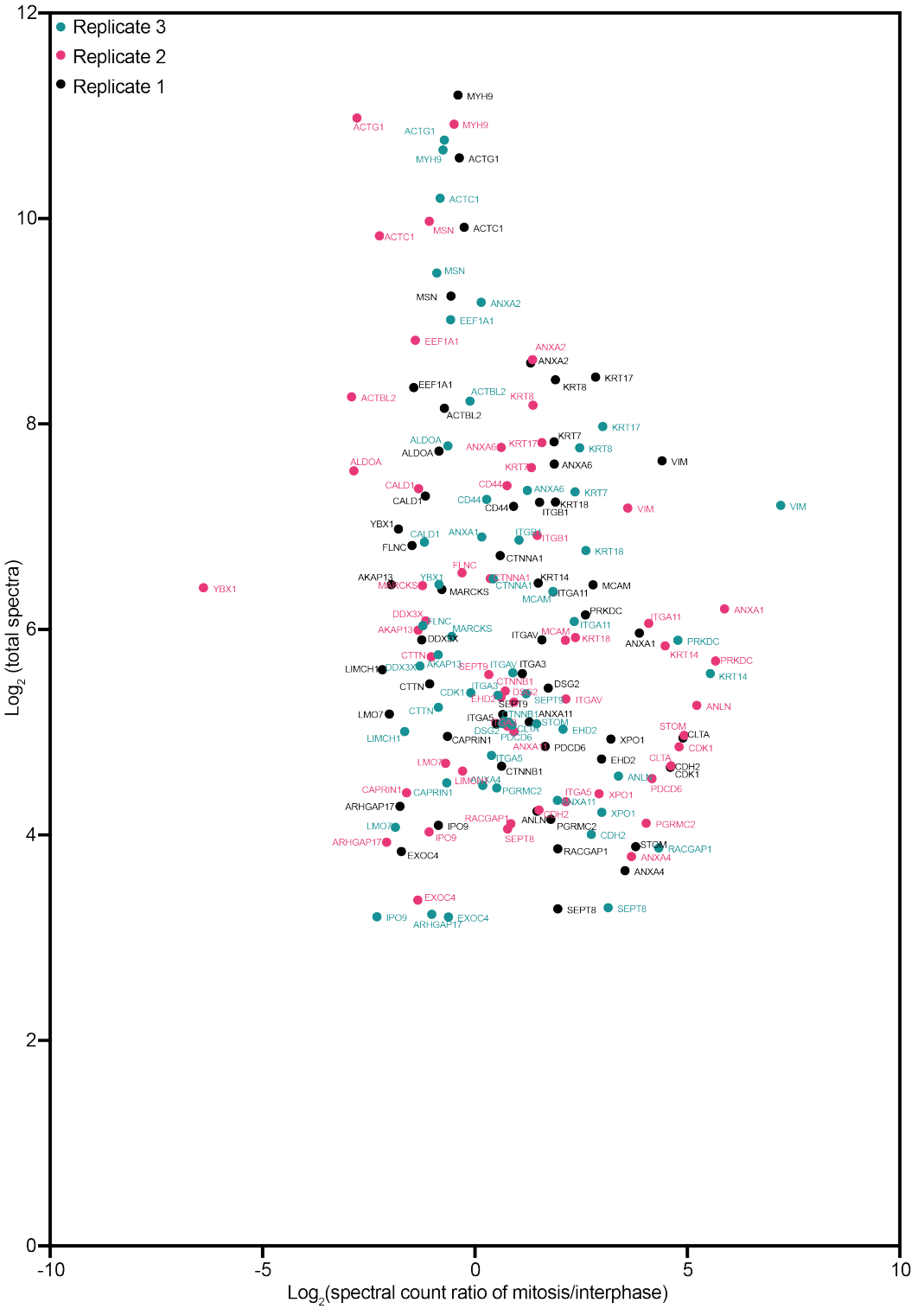

Figure 2.12: **Experimental replicates for actin binding proteins that significantly change between interphase and mitotic blebs.** Volcano plot of 54 actin-related proteins that significantly change in levels in blebs from interphase compared to mitotic cells, showing enrichment between interphase and mitosis (x-axis) and combined total of spectra (y-axis). Data points for all three experimental replicates are shown individually.

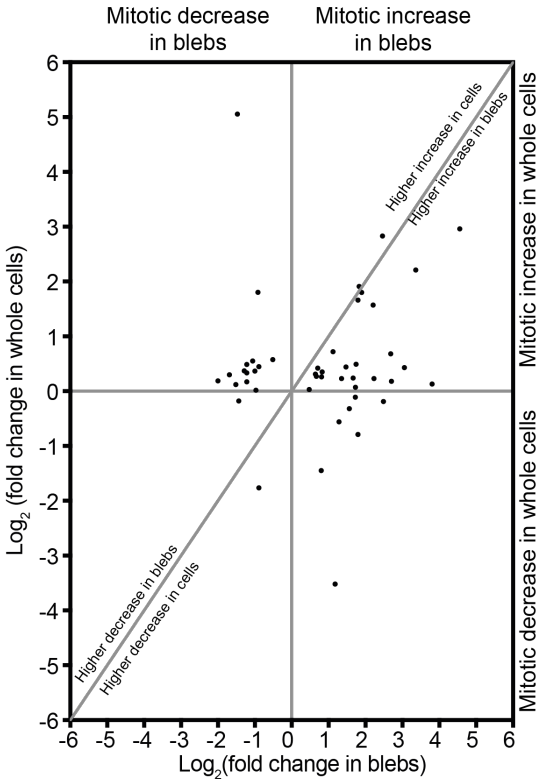

Mitotic decrease in blebs increase in cells

Protein	Log_2FC bleb	Log_2FC cell	Ratio FC (bleb/cell)
FLNC	-0.971	0.0164	0.504
MYH9	-0.515	0.575	0.470
MSN	-0.889	0.447	0.396
CTTN	-1.00	0.365	0.388
ALDOA	-1.22	0.170	0.382
CALD1	-1.22	0.334	0.341
ACTBL2	-1.06	0.550	0.328
LIMCH1	-1.51	0.120	0.320
EXOC4	-1.29	0.370	0.317
IPO9	-1.22	0.487	0.307
ARHGAP17	-1.69	0.298	0.252
YBX1	-2.00	0.188	0.219
CAPRIN1	-0.916	1.80	0.152
LMO7	-1.47	5.05	0.0108

Mitotic decrease in blebs and cells

Protein	Log_2FC bleb	Log_2FC cell	Ratio FC (bleb/cell)
MARCKS	-0.889	-1.76	1.83
AKAP13	-1.43	-0.179	0.419

Mitotic increase in blebs decrease in cells

Protein	Log_2FC bleb	Log_2FC cell	Ratio FC (bleb/cell)
ANXA6	1.18	-3.52	26.0
ITGA11	2.49	-0.186	6.37
ANXA4	1.80	-0.787	5.60
ANXA2	0.800	-1.45	4.74
EHD2	1.56	-0.321	3.68
ANXA11	1.28	-0.556	3.57
PGRMC2	1.72	-0.11	2.75

Mitotic increase in blebs and cells

Protein	Log_2FC bleb	Log_2FC cell	Ratio FC (bleb/cell)
PRKDC	3.80	0.132	12.7
XPO1	3.05	0.427	6.18
CDH2	2.70	0.177	5.76
CLTA	2.68	0.682	4.00
MCAM	2.23	0.230	4.00
SEPT8	1.73	0.068	3.16
VIM	4.55	2.96	3.01
PDCD6	1.66	0.236	2.69
CDK1	1.74	0.494	2.38
ANLN	3.36	2.21	2.23
ITGB1	1.35	0.231	2.17
ITGAV	1.47	0.438	2.05
KRT18	2.20	1.57	1.55
ITGA5	0.807	0.258	1.46
ITGA3	0.824	0.346	1.39
CTNNA1	0.475	0.0265	1.37
DSG2	1.12	0.719	1.32
CTNNB1	0.669	0.270	1.32
CD44	0.642	0.307	1.26
SEPT9	0.705	0.416	1.22
KRT7	1.80	1.66	1.10
RACGAP1	1.90	1.80	1.07
KRT8	1.83	1.91	0.945
KRT17	2.46	2.83	0.774

Figure 2.13: **Comparison of protein levels detected in blebs and whole cells.** Changes in actin-related protein levels between interphase and mitosis in blebs (x-axis) and cells (y-axis) (mass spectrometry of the whole cells from [Heusel et al., 2020]).

(Figure 2.11). Out of the 922 detected proteins only 180 significantly differed in protein levels between interphase and mitosis (corresponding to a P-value = 0.05, data points above the dashed line in Figure 2.11B). This suggests that cortex composition is largely similar between interphase and mitosis.

I further narrowed down the list of candidates by focusing on actin-related proteins. I selected these by overlapping our mass spectrometry dataset with a previously published list of F-actin binding proteins identified by a pull down of F-actin binding cellular fractions [Serres et al., 2020], which I complemented with a manual curation to select additional actin-related proteins. Based on these criteria, I identified 238 actin-related proteins out of 922 proteins found in cortex-enriched blebs (Figure 2.9A, magenta dots on Figure 2.11). These included many proteins known to directly bind and regulate actin filaments, as well as membrane and adhesion proteins, the intermediate filaments vimentin and keratin, and various Rho-GTPases and their regulators. Additionally, the other proteins found in blebs included tubulins and microtubule-binding proteins, as well as multiple factors involved in intracellular trafficking, which might also indirectly interact with the actin cortex. Out of the 238 identified actin-related proteins, 54 significantly changed in levels between interphase and mitotic blebs (P-value$\leq$ 0.05). This reduced list represents actin-related proteins that most consistently changed levels in cortex-enriched blebs between interphase and mitotic cells (Figure 2.12, Table 2.2). I particularly focused on these 54 actin-related proteins to identify potential novel regulators of cortex mechanics.

To investigate a potential cause for the changes in levels in these proteins in blebs, I compared the differences in levels between interphase and mitotic blebs to differences in interphase and mitosis measured by mass spectrometry of whole cells (measured by by [Heusel et al., 2020]) (Figure 2.13). Due to a complexity of data extraction for protein levels in whole blebs, we only focused on subset of proteins, specifically 54 actin-related proteins that significantly changed in levels between interphase and mitotic blebs. Interestingly, for most of the examined proteins, the degree of change in blebs and cells was not the same. The highest proportion of proteins examined, increased in mitotic cells and blebs, however for most of these proteins the increase was higher in blebs compared to cells. The second largest group were proteins that increased in mitotic cells but decreased in blebs. Of note, there are differences in the set up of proteomic analysis of whole cells and blebs including cell synchronisation and mass spectrometry. Still, the comparison of a subset of cortical protein levels in blebs vs whole cells suggests that many of the

identified proteins translocate to/from the actin cortex between interphase and mitosis independently of changes in the expression levels.

2.1.5 Regulators of cortex mechanics in isolated blebs

To identify some key candidate regulators of cortex mechanics among the 238 actin-related proteins identified in blebs, and specifically among the 54 proteins that significantly changed levels between interphase and mitotic blebs, I overlapped this dataset with a previously published screen of regulators of mitotic rounding force [Toyoda et al., 2017] and a literature-based list of proteins related to contraction [Zaidel-Bar et al., 2015].

I found that 103 of the 238 actin-related proteins detected in blebs had been tested in the mechanical screen of mitotic rounding force regulators. In the literature-based list, named contractome, only 54 out of the 238 actin-related proteins from blebs were listed. To identify candidate regulators of cortex mechanics, I focused on the proteins detected in the mechanical screen of mitotic rounding force regulators. Out of the proteins tested in the mechanical screen, detected in blebs, 10 were shown to reproducibly and significantly reduce mitotic rounding force upon depletion. These 10 regulators of cortex mechanics included a positive control in the mechanical screen [Toyoda et al., 2017], the heavy chain of non-muscle myosin IIA (MYH9), upstream regulators of actomyosin dynamics (RAC1, ROCK2), septin (SEPT9), and proteins involved in the control of actin organisation. Consistent with previous studies on how actin length regulators (e.g. DIAPH1, PFN1) and crosslinkers (e.g. ACTN4) affect force generation in actomyosin networks [Chugh et al., 2017, Ennomani et al., 2016, Logue et al., 2015], the last category of proteins overlapping in our mass spectrometry of the blebs and the mechanical screen included proteins affecting actin polymerisation and nucleation (DIAPH1, PFN1, DBN1, CYFIP1), and actin bundling and crosslinking (ACTN4, FSCN1). Interestingly, MYH9 and SEPT9 were the only two proteins out of the 10 cortex mechanics regulators that were shown to affect mitotic rounding force and also significantly changed in levels between interphase and mitotic blebs.

Taken together, further scrutiny of the mass spectrometry dataset with a particular focus on actin-related proteins identified multiple potential regulators of cortex mechanics between interphase and mitosis. The list included proteins that were previously explored for their role in mechanical regulation as well as novel candidates previously unexplored. Here, I demonstrate the use of this resource by focusing on septins.

Enriched in mitotic cortex fraction				
Protein Symbol	Ratio of spectral count (Mitosis/ Interphase)	P-value	Mitoitc rounding force changes (Toyoda et al., 2017)	Present in contractome (Zaidel-Bar et al., 2015)
VIM	23.49	0.00050	n.t	
PRKDC	13.96	0.00012	n.t	
ANLN	10.27	0.018	no change	yes
XPO1	8.31	0.0028	n.t	
STOM	7.61	0.013	n.t	
KRT14	6.52	0.0032	n.t	
CDH2	6.51	0.0076	n.t	
CLTA	6.42	0.0048	n.t	
ITGA11	5.60	0.00024	no change	
KRT17	5.50	0.0049	n.t	
MCAM	4.69	0.0019	n.t	
KRT18	4.61	0.015	n.t	
RACGAP1	3.72	0.0040	no change	yes
KRT8	3.55	0.0030	n.t	
ANXA4	3.47	0.035	n.t	
KRT7	3.47	0.0014	n.t	
CDK1	3.35	0.044	no change	
SEPT8	3.31	0.017	potentially lower force	yes
PGRMC2	3.30	0.012	n.t	
PDCD6	3.17	0.0050	n.t	
ANXA1	3.14	0.037	n.t	
EHD2	2.95	0.0073	n.t	
ITGAV	2.77	0.0055	no change	
ITGB1	2.55	0.0025	no change	
ANXA11	2.43	0.010	n.t	
ANXA6	2.26	0.0068	n.t	
DSG2	2.17	0.0084	n.t	
ITGA3	1.77	0.018	no change	
ITGA5	1.75	0.048	no change	
ANXA2	1.74	0.046	n.t	
SEPT9	1.63	0.019	lower force	
CTNNB1	1.59	0.049	no change	
CD44	1.56	0.0074	n.t	
CTNNA1	1.39	0.011	no change	

Enriched in interphase cortex fraction				
Protein Symbol	Ratio of spectral count (Mitosis/Interphase)	P-value	Mitoitc rounding force changes (Toyoda et al., 2017)	Present in contractome (Zaidel-Bar et al., 2015)
YBX1	0.25	0.01	n.t.	
ARHGAP17	0.31	0.021	n.t.	
LIMCH1	0.35	0.048	n.t.	
LMO7	0.36	0.037	n.t.	
AKAP13	0.37	0.018	n.t.	
EXOC4	0.41	0.021	n.t.	
ALDOA	0.43	0.0094	no change	
CALD1	0.43	0.0043	no change	yes
DDX3X	0.43	0.0016	n.t.	
ACTG1	0.43	0.039	no change	yes
IPO9	0.43	0.017	n.t.	
ACTBL2	0.48	0.045	n.t.	
EEF1A1	0.48	0.014	n.t.	
CTTN	0.50	0.0065	n.t.	yes
ACTC1	0.51	0.024	no change	
FLNC	0.51	0.043	n.t.	
CAPRIN1	0.53	0.019	n.t.	
MSN	0.54	0.039	no change	
MARCKS	0.54	0.019	no change	
MYH9	0.70	0.039	lower force	yes

Table 2.2: **Actin-related proteins detected in isolated blebs showing a significant difference in levels between interphase and mitosis.** Fold-change and exact P-values were calculated from normalised spectral counts detected in blebs in 3 experimental replicates. Fourth column: rounding force changes upon protein depletion, as reported in [Toyoda et al., 2017]; n.t. (not tested): protein not examined in the mechanical screen in [Toyoda et al., 2017]; no change: protein for which no change was detected with any of the esiRNA tested; potentially lower force: protein for which the change in rounding force was detected with some but not all of the esiRNA sequences tested; lower force: protein for which rounding force changed with all esiRNA sequences tested [Toyoda et al., 2017]. Fifth column: protein was detected as part of contractome [Zaidel-Bar et al., 2015].

2.1.6 Effects of septin 9 on cell division mechanics

I firstly focused on the role of one of the identified candidates (septin 9) in cell division. Septin 9 was the only protein which both significantly (P= 0.039, Figure 2.14B) differed in levels between interphase and mitotic blebs and was previously shown to affect mitotic rounding force [Toyoda et al., 2017] (Table 2.2). Septins are a group of actin, membrane and microtubule binding proteins often considered a fourth component of the cytoskeleton [Mostowy and Cossart, 2012]. Septins are classified in 4 different groups (SEPT2, SEPT3, SEPT6, SEPT7) with septin 9 being the only member of the SEPT3 group detected in blebs. Septin 9 has previously been shown to affect abscission at the end of cell division [Estey et al., 2010]. Septin 9 and 2 have also been shown to localise to the cell cortex during mitosis but their role in early stages of cell division remained to be explored. I thus focused on the role of septin 9 during mitotic rounding.

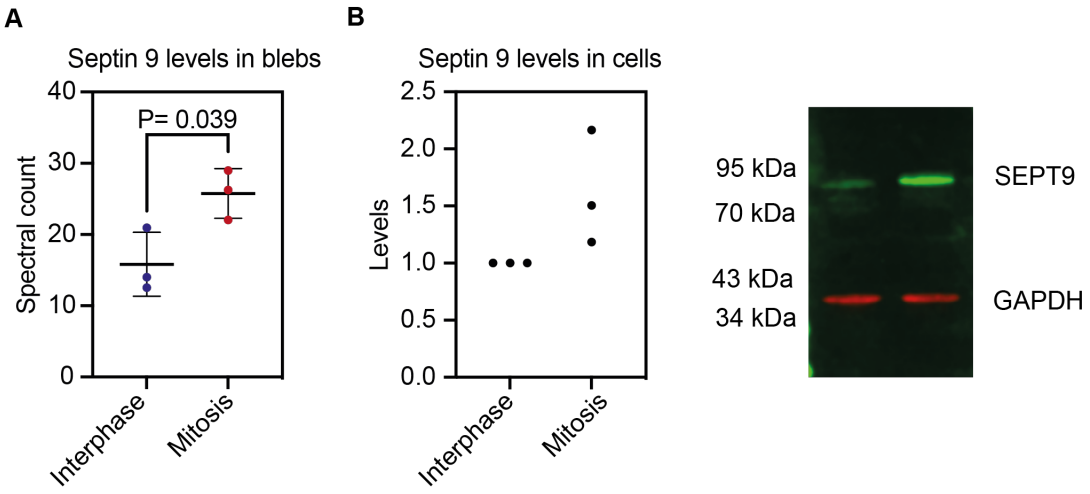

Figure 2.14: **Levels of septin 9 in blebs and cells.** (A) Septin 9 levels in interphase and mitotic blebs detected with mass spectrometry. (B) Fluorescent western blot (right) and quantification (left) of septin 9 levels in mitotic and interphase whole cell lysates, normalised to the loading control GAPDH, relative to interphase levels. Each data point corresponds to an individual replicate, with mean ± 1 standard deviation shown. Statistics: Student's t-test.

I firstly showed that the levels of septin 9 also changed between interphase and mitotic cells (Figure 2.14B). Then, I focused on the effects of septin 9 depletion during early stages of mitosis. I depleted septin 9 using siRNA treatment (Figure 2.15) and imaged cells overnight (Figure 2.16). I quantified the rounding time by defining the start of rounding as the first frame when I visually detect the onset of retraction in spread cells, and the end of rounding when the cell is completely round (Figure 2.16B, left). I found cells depleted for septin 9 took slightly longer to round up at the onset of mitosis. Cells depleted in septin 9 took on average 40 min to round up compared to control cells taking on average 37.8 min. I also quantified the timing of ingression after mitosis, which I defined as the time from the last frame where aligned chromosomes are observed to the point of maximum cell ingression. Interestingly, I observed no differences in the timing of ingression, with cells in both conditions taking on average 12 min (Figure 2.16B, right). Finally, I quantified mitotic cell shape in cell's midplane (Figure 2.16C). Cells depleted in septin 9 displayed bigger midplane area and were less circular and more elongated compared to control cells.

Taken together, these data suggests that depletion of septin 9 leads to defects in cortex driven cell rounding at the onset of mitosis. This identification of septin 9 as an regulator of cell shape during mitosis confirms the effectiveness of our mass spectrometry dataset for the identification of cell surface mechanics regulators.

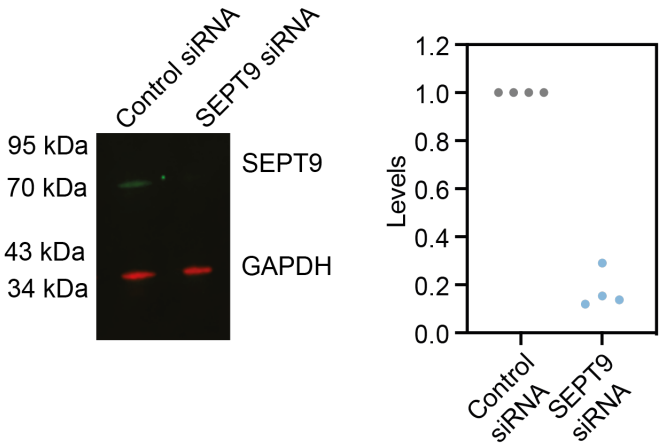

Figure 2.15: **Cellular levels of septin 9 upon siRNA depletion.** Fourescent western blot and quantification of septin 9 levels in cells upon 48h of siRNA treatment (left). Membrane is representative of n= 4 samples used for quantification (right). Quantified levels were normalised to the loading control (GAPDH) and control siRNA conditions.

2.1.7 Effects of septin 9 depletion on cortex thickness

I then investigated the nanoscale effects of septin 9 depletion on the actin cortex. Since actin cortex thickness is related to changes in cortical tension, which drive cell shape changes, I measured the effect of SEPT9 depletion on cortex thickness (Figure 2.17).

I measured cortical actin thickness by acquiring Stochastic Optical Reconstruction Microscopy (STORM) data of the actin cortex labelled with phalloidin conjugated to Alexa-647 dye (Figure 2.17A) and measuring cortex thickness as the full width at half maximum (FWHM) of the transversal intensity profiles across the cell boundary of cells, using a method developed in the lab [Truong Quang et al., 2021]. Comparison of cortical thickness of mitotic cells treated with control and SEPT9 pool siRNA showed a slight but significant increase ($\sim$ 10 nm) in cortical thickness for cells depleted of SEPT9 with a pool of 4 different siRNA sequences.

To confirm the difference in cortical thickness upon SEPT9 depletion, I also measured cortical thickness of mitotic cells treated with individual siRNA molecules (Figure 2.17B). But, I was not able to replicate the difference in thickness observed with a siRNA pool treatment. None of the conditions with individual siRNA treatments showed a significant increase in cortical thickness upon septin 9 depletion. This might be due to individual siRNAs affecting different septin 9 isoforms. However, $\sim$ 10 nm difference is very low and

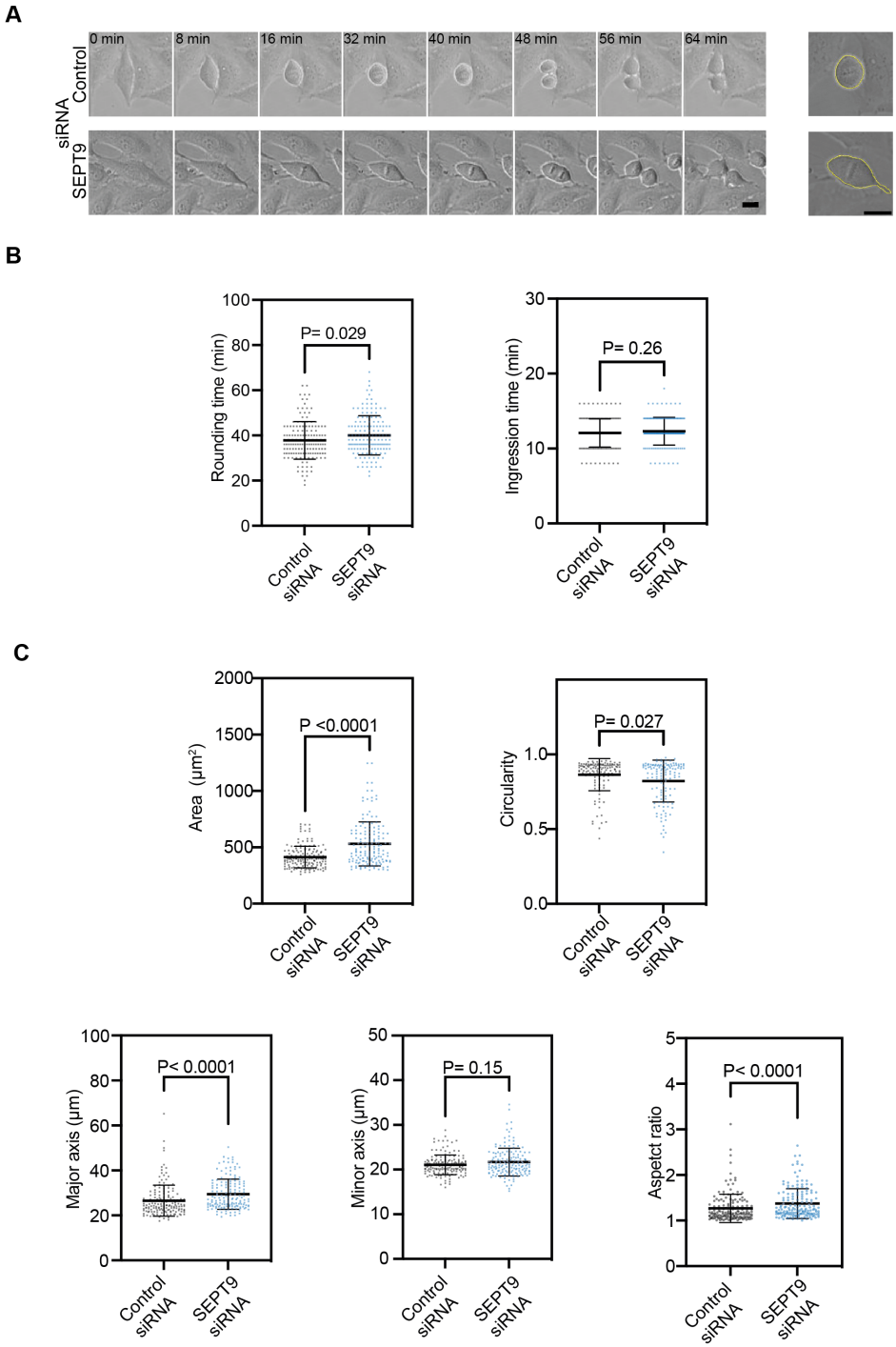

Figure 2.16: **Effects of septin 9 depletion on cell division.** (A) Brighfield timelapse (every 10 min) of cell division of cells treated with siRNA against septin 9 (bottom) and control siRNA (top) and an example of cell segmentation for cell shape analysis (right). Scale bar= 20 µm. (B) Timing of cell rounding at the onset of mitosis and cleavage furrow ingression timing during cytokinesis. (C) Quantification of cell area, circularity (defined as $4\pi \times area \div perimeter^2$), major axis, minor axis and aspect ratio in mitosis of control and SEPT9 siRNA treated cells. Graph, mean ±1 standard deviation. Statistics: Data points were pooled from 3 independent experiments (performed on different days). Datasets did not pass the test for normal distribution, therefore Mann-Whitney test was used to compare the conditions.

at the edge of the resolution limit. Therefore, differences in observed phenotype between the pool and individual siRNAs could be due to technical challenges related to detection.

Taken together, these data suggest that depletion of septin 9 does not strongly affect actin cortex thickness in mitotic cells. Although some differences were observed with a pool of 4 different siRNA molecules, that difference is not substantial and septin 9 most likely causes changes in cortical tension and cell shape via an alternative mechanism.

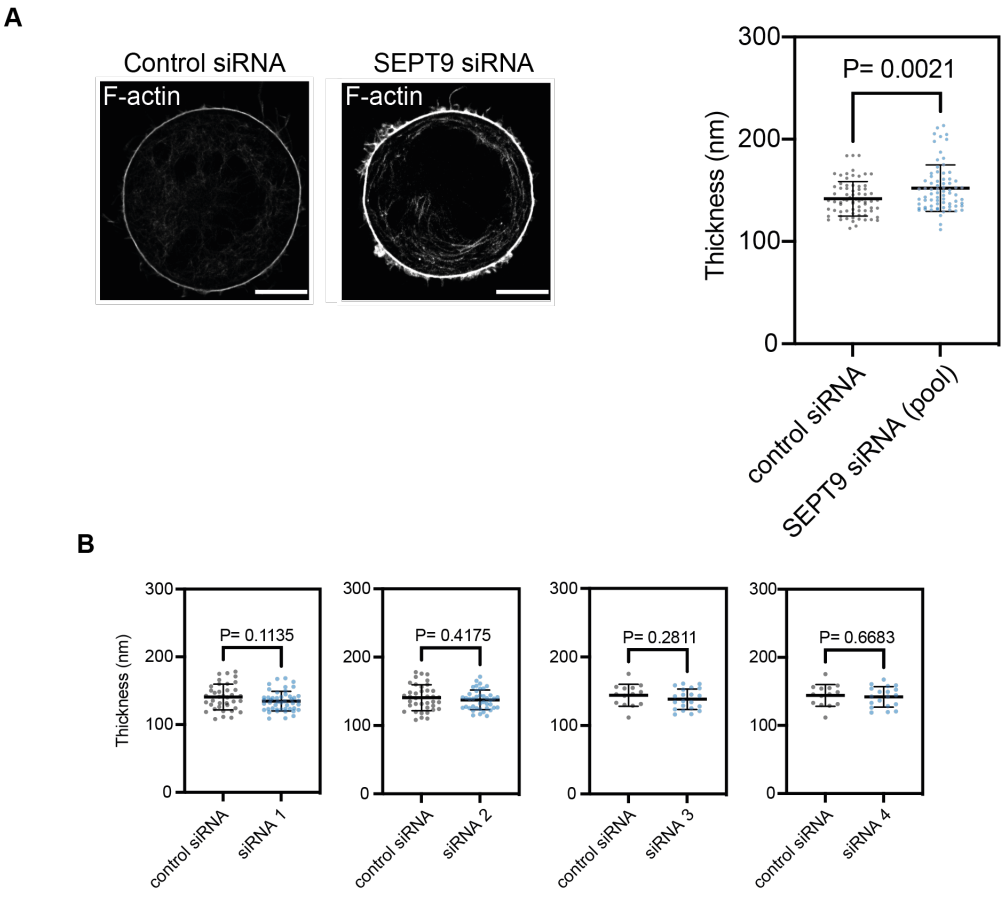

Figure 2.17: **Effects of septin 9 depletion on the actin cortex thickness.** (A) Stochastic Optical Reconstruction Microscopy (STORM) reconstructed image of the actin cortex at the cellualar midplane of control and SEPT9 siRNA treated cells (left). White= F-actin (phalloidin). Scale bar= 5 µm. Cortical thickness measured as full width at half maximum (FWHM) of the transversal intensity profiles across the cell boundary of control and SEPT9 siRNA treated cells (right), and 4 individual siRNAs (B). Statistics: Data points were pooled across 3 independent experiments. All datasets passed normality test and were compared using Welch's t-test.

2.1.8 The role of other septins on cell division mechanics

I then asked what is the role of other septins in cell shape control and whether they compensate each other's activity or could work in a complex. Multiple members of the septin family have been detected in blebs: septin 2, septin 6, septin 7, septin 8, septin

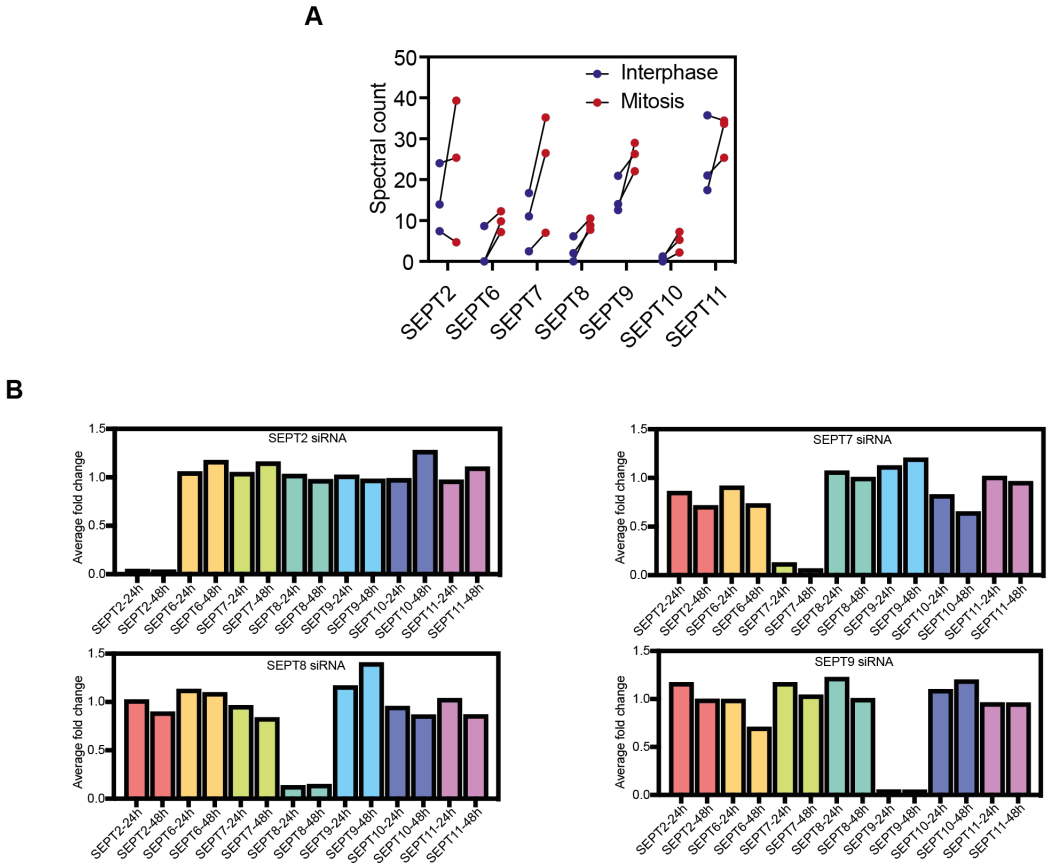

Figure 2.18: **Levels of septin 2, septin 6, septin 7, septin 8, septin 9, septin 10, and septin 11 upon qPCR treatment.** (A) Spectral counts of septins (septin 2, septin 6, septin 7, septin 8, septin 9, septin 10, and septin 11) identified in interphase and mitotic blebs by mass spectrometry. (B) Levels of septins identified in blebs 24h and 48h after depletion of septin 2, septin 7, septin 8, and septin 9 as measured by qPCR by Dr. Geneviève Lavoie. Graph: average of three independent experiments.

9, septin 10, and septin 11 with only septin 8 and septin 9 changing significantly in their levels between interphase and mitotic blebs (Figure 2.18A). Septin family members can form higher order structures and based on their position in those structures are divided in 4 groups (Figure 1.6).

To investigate whether other septins alongside septin 9 affect cellular mechanics in mitosis, I depleted a septin from each of 4 septin groups. If multiple septins from the same group were detected in blebs, I selected the septin with the lowest P-value for the change in levels between interphase and mitotic blebs. I thus depleted septin 2, septin 7, septin 8. I quantified the effect of the depletion of these septins on cell division dynamics and mitotic cell shape (Figure 2.18B, 2.19). Unlike depletion of septin 9, depletion of septin 2, septin

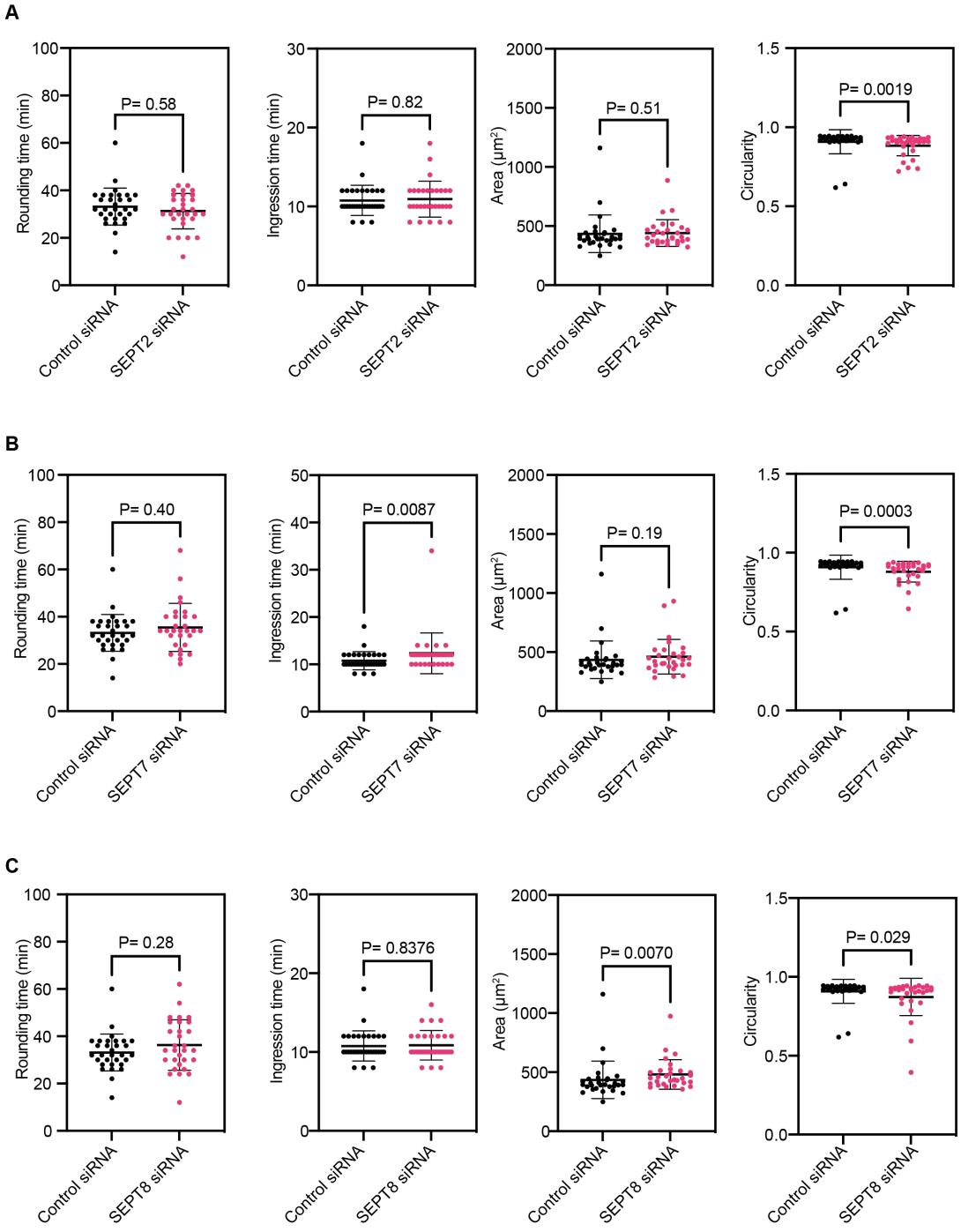

Figure 2.19: **Cell division dynamics and mitotic cell shape upon depletion of septin 2, septin 7, and septin 8.** Mitotic rounding time, cleveage furrow ingression time, and area and circularity of mitotic cells upon depletion of septin 2 (A), septin 7 (B), and septin 8 (C) with siRNA pool compared to siRNA control. Graph, ±1 mean standard deviation. Statistics: Data points were pooled from 3 independent experiments. Datasets did not pass the test for normal distribution and were compared with Mann-Whitney test.

7, or septin 8 did not affect mitotic rounding but septin 7 depletion slightly prolonged the time of furrow ingression from 10.8 min in controls cells to 12.3 min in cells depleted for septin 7. Interestingly, depletion of all these other septins resulted in significantly less circular mitotic cells but only septin 8 significantly affected cellular area during mitosis (Figure 2.19). Taken together, septins from all 4 groups affect mitotc cell shape, suggesting a role of a septin group during mitosis.

To assess whether the observed phenotypes could be due to compensation by other septins, Dr. Geneviève Lavoie measured expression levels of other septins upon depletion of septin 2, septin 7 septin 8, and septin 9 (Figure 2.18B). Depletion of these septins only slightly affected expression of other septins detected in blebs, however we did not observe any specific pattern that would suggest clear compensation among different septins.

Finally, septin 7 was previously shown to affect recruitment of other septins [Estey et al., 2010] and affect tension driven processes such as cell migration [Tooley et al., 2009]. I thus examined the role of depletion of septin 7 on cortical actin thickness in mitotic cells (Figure 2.20). STORM did not show any significant difference in cortical actin thickness during mitosis in SEPT7 depleted cells in comparison to control cells.

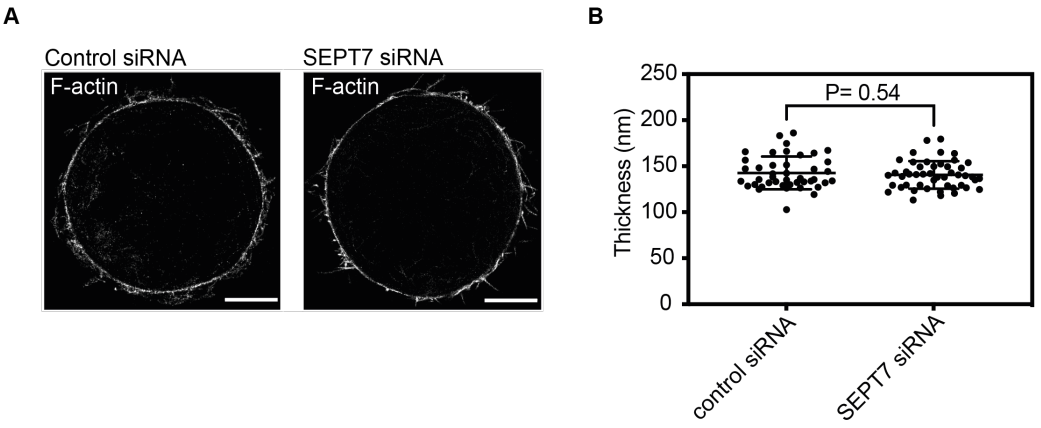

Figure 2.20: **Effects of septin 7 depletion on actin cortex thickness.** (A) Stochastic Optical Reconstruction Microscopy (STORM) image of the actin cortex at the cellualar midplane of control and SEPT7 siRNA treated cells. White= F-actin (phalloidin). Scale bars= 5 µm. (B) Cortical thickness measured as full width at half maximum (FWHM) of their transversal intensity profiles across the cell boundary of control and SEPT7 (pool) siRNA treated cells. Graph, mean ±1 standard deviation. Statistics: Data points were pooled across 3 independent experiments. All datasets passed normality test and were compared using Welch's t-test.

Taken together, these data show that septins, in particular septin 2, septin 7, septin 8, and septin 9 play a role in controlling cell mechanics as their depletion affects mitotic cell

shape. The effects of individual septins on shape of cells in culture is modest but statistically significant. In the future, the effects of depletion of multiple septins simultaneously, particularly from the same homology group needs to be examined for a more comprehensive understanding of the role of the entire protein family. Furthermore, it would be interesting to see how depletion of septin(s) affect cell shape under confinement. Finally, the molecular mechanism of how septins affect cell mechanics remains an open question for future studies. Still, the identifications of septins as a potential regulators of cell shape highlights the potential of the resource created by mass spectrometry of interphase and mitotic blebs for identification of novel regulators of cortex mechanics and a more comprehensive understanding of proteomic changes in the cortex composition between interphase and mitosis.

2.1.9 Levels of actin crosslinkers in interphase and mitotic blebs

Finally, I asked whether actin crosslinkers levels varied in interphase and mitotic blebs.

At least 17 different isoforms of actin crosslinkers from 8 different groups were detected in blebs by mass spectrometry (Figure 2.21). Interestingly, filamin C (FLNC) was the only crosslinker to significantly vary in levels between interphase and mitotic cortices (Table 2.2, Figure 2.12, Figure 2.11). However, FLNC levels in blebs were comparably low with respect to other detected crosslinkers (Figure 2.21). Although, most crosslinkers did not significantly change in levels between interphase and mitotic blebs (Figure 2.21), some of them, including alpha-actinin 4 (ACTN4), were previously shown to affect mitotic rounding force [Toyoda et al., 2017].

Taken together, differences in levels between interphase and mitotic cortices can highlight certain regulators of cortex mechanics as demonstrated by the identification of septins as regulators of mitotic cell shape. However, the role of actin crosslinkers in cortical tension generation at the early stages of cell division does not seem to be primarily regulated through changes in their levels.

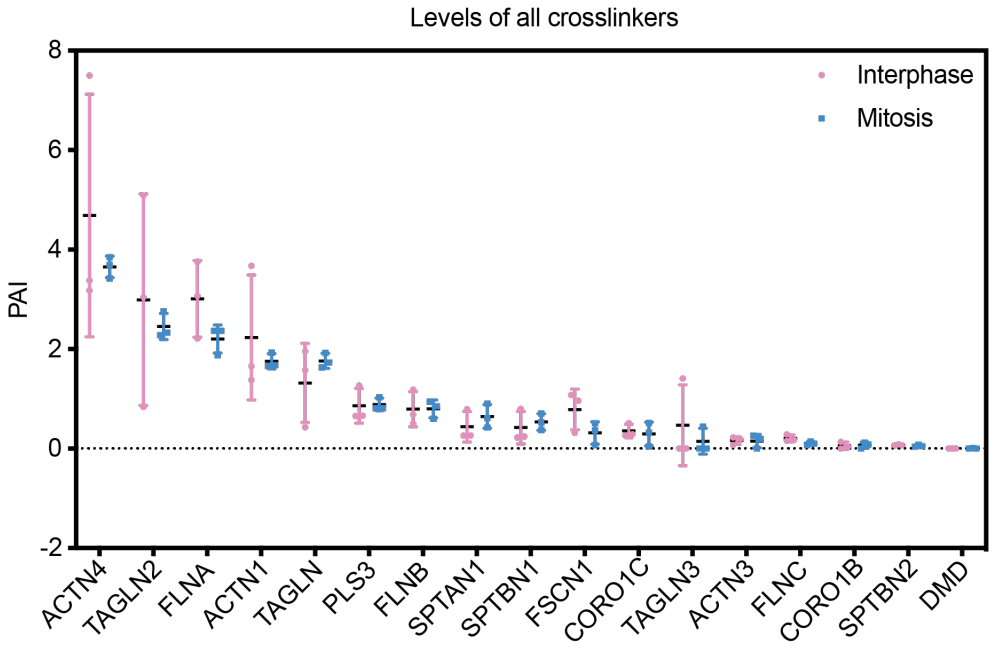

Figure 2.21: **Levels of actin crosslinkers in cortex enriched blebs.** Levels of actin crosslinkers in interphase and mitotic blebs as detected by mass spectrometry. PAI= spectral count/ molecular weight. Each point represents an independent replicate. Error bars: mean ±1 standard deviation.

2.2 The role of actin crosslinker size in cortex organisation and mechanics

In the second part of my project, I focused on how the size of the actin crosslinkers affects their localisation within the actin cortex and consequently cortical mechanics. To examine the role of size independently of other properties of actin crosslinkers, I collaborated with Dr. Fabio Parmeggiani (University of Bristol). Through this collaboration, we created artificial crosslinkers, synthetic proteins with actin binding domain for which we can change size by inserting varying numbers of identical repeat domains.

In this section, I describe the development of the artificial crosslinkers and the phenotypes observed in cells expressing them.

2.2.1 Design of artificial crosslinkers of different sizes

Endogenously present actin crosslinkers differ in multiple properties including size, actin binding dynamics, affinity, interactions with other proteins etc. Since I wanted to systematically examine the role of crosslinker size in controlling cortical mechanics, I collaborated with Dr. Fabio Parmeggiani to create artificial crosslinkers.

A

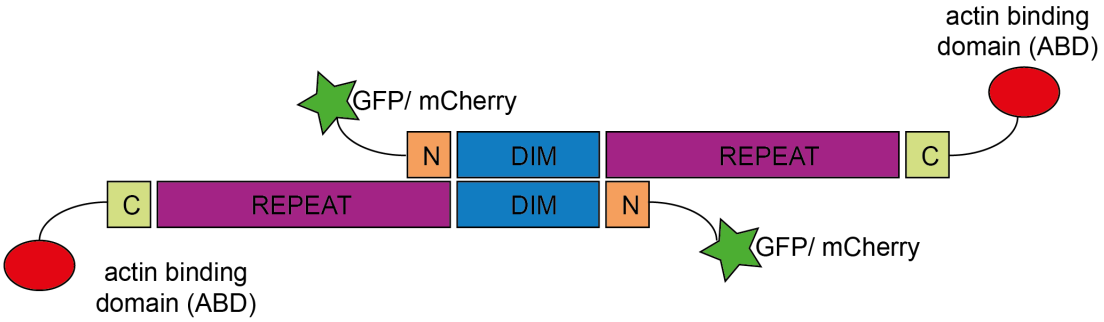

B

Number of repeats	Size (nm)- Ank1 repeat domain	Size (nm)- D18 repeat domain
0	5.4	5.2
1	7.5	6.7
2	9.2	7.6
3	10.9	8.1
4	12.4	9.4
5	13.7	10.9
6	14.9	12.7
7	15.7	15.1
8	16.9	17
9	17.8	19.1
17	14.9	32.7

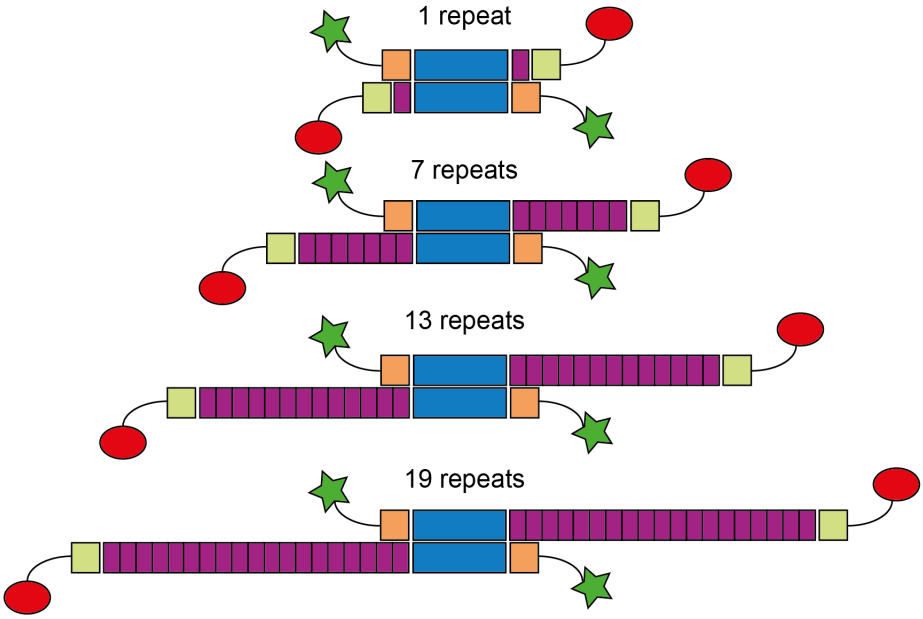

Figure 2.22: **Design of artificial crosslinkers.** (A) Schematic of the artificial crosslinker containing actin binding domain (ABD), fluorescent protein (GFP), dimerisation domain and repeat domain through which the size of the artificial crosslinker is modulated by changing the number of repeats with an identical sequence. (B) Predicted size of the artificial crosslinkers given the number of repeats (left) for two different repeat sequences tested Ank1 and D18 and schematic representation of D18 artificial crosslinkers of different sizes.

Using computational predictions of protein structure, Dr. Fabio Parmeggiani was able to combine modular units of repeat domains with a dimerisation domain, fluorescent protein sequence, and an actin binding domain [Baker et al., Brunette et al., 2015, Fallas et al., 2016, Parmeggiani and Huang, 2017, Yeh et al., 2018, 2020] designing an artificial protein sequence for which he was able to predict a size (Figure 2.22). We tested two different types of repeat domains (Ank1 and D18). Based on computational predictions of protein shape, increasing the number of these domains would firstly increase the size of the protein but after a certain threshold (9 repeats for Ank1 and 18 repeats for D18) the protein would start to curl leading to a decrease in the distance between actin binding domains. We predicted that we can create artificial crosslinkers containing the same building blocks between 5.2 to 32 nm long (Figure 2.22B).

After predicting the shape and size of the proteins designed with repeat domains, we used commercial services (Thermo Fischer) to synthesise basic artificial crosslinkers and insert plasmids with additional repeat units to make longer artificial crosslinkers (Figure 2.23). To allow expression in mammalian cells, we selected pcDNA 3.1 plasmids to carry the sequence encoding artificial crosslinkers. Initially, an artificial crosslinker with 1 repeat was commercially synthesised and cloned into a pcDNA plasmid (Figure 2.23, left). Additionally, multiple consecutive (6 in the case of D18 domain) repeats were also commercially synthesised in a separate insert plasmid (Figure 2.23, middle). These additional 6 D18 repeats were then cloned into a pcDNA 3.1 plasmid containing the sequence for the artificial crosslinker with one repeat domain, making a 7 D18 repeat artificial crosslinker (Figure 2.23, right). These three plasmids were all cloned commercially. The design of these plasmids, allowed me to further expand the number of the repeats in the artificial crosslinkers. Using restriction-ligation reaction, I cloned additional 6 repeats into the existing plasmids to create even bigger artificial crosslinkers. I cloned the additional domains using BamHI and BsaI restriction sites on the insert plasmid, and BamHI and NheI on pcDNA 3.1 plasmid already containing 7 repeats (and later 13 repeats) crosslinker (Figure 2.24). Following these steps, I expanded the original artificial crosslinker sizes to 13 and 19 repeats in total.

Taken together, after the basic sequences with 1 and 6 D18 repeat domains were synthesised commercially, I was further able to clone additional repeats into the artificial crosslinkers creating 1, 7, 13 or 19 repeats artificial crosslinkers with a range of sizes between $\sim$ 5 and $\sim$ 30 nm (Figure 2.22B, Table 2.3).

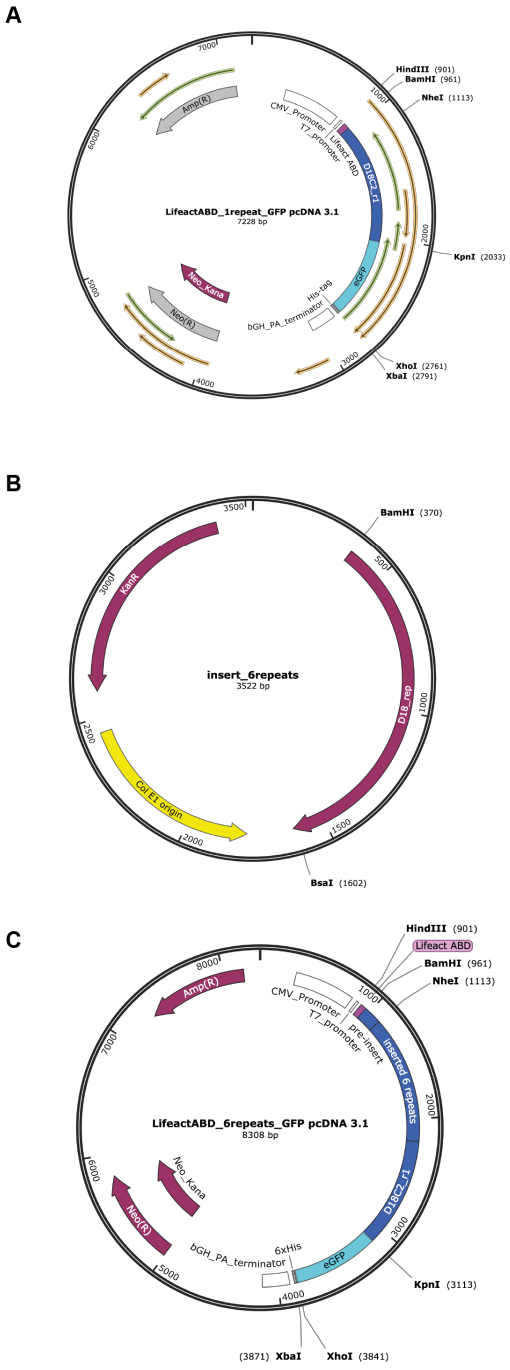

Figure 2.23: **Plasmids for expression of crosslinkers with different sizes.** Plasmid maps of (A) pcDNA 3.1 plasmid with an artificial crosslinker containing 1 D18 repeat used for expression of 1 D18 repeat artificial crosslinker, (B) plasmid containing a sequence for 6 D18 repeats, which was used to clone additional 6 repeats into 1 repeat plasmid (A) and create a 7 repeats pcDNA 3.1 plasmid (C). These plasmids were commercially synthesised based on the protein sequence we provided. Further plasmids (12 and 18 added repeats) were cloned by me using plasmids from (B) and (C).

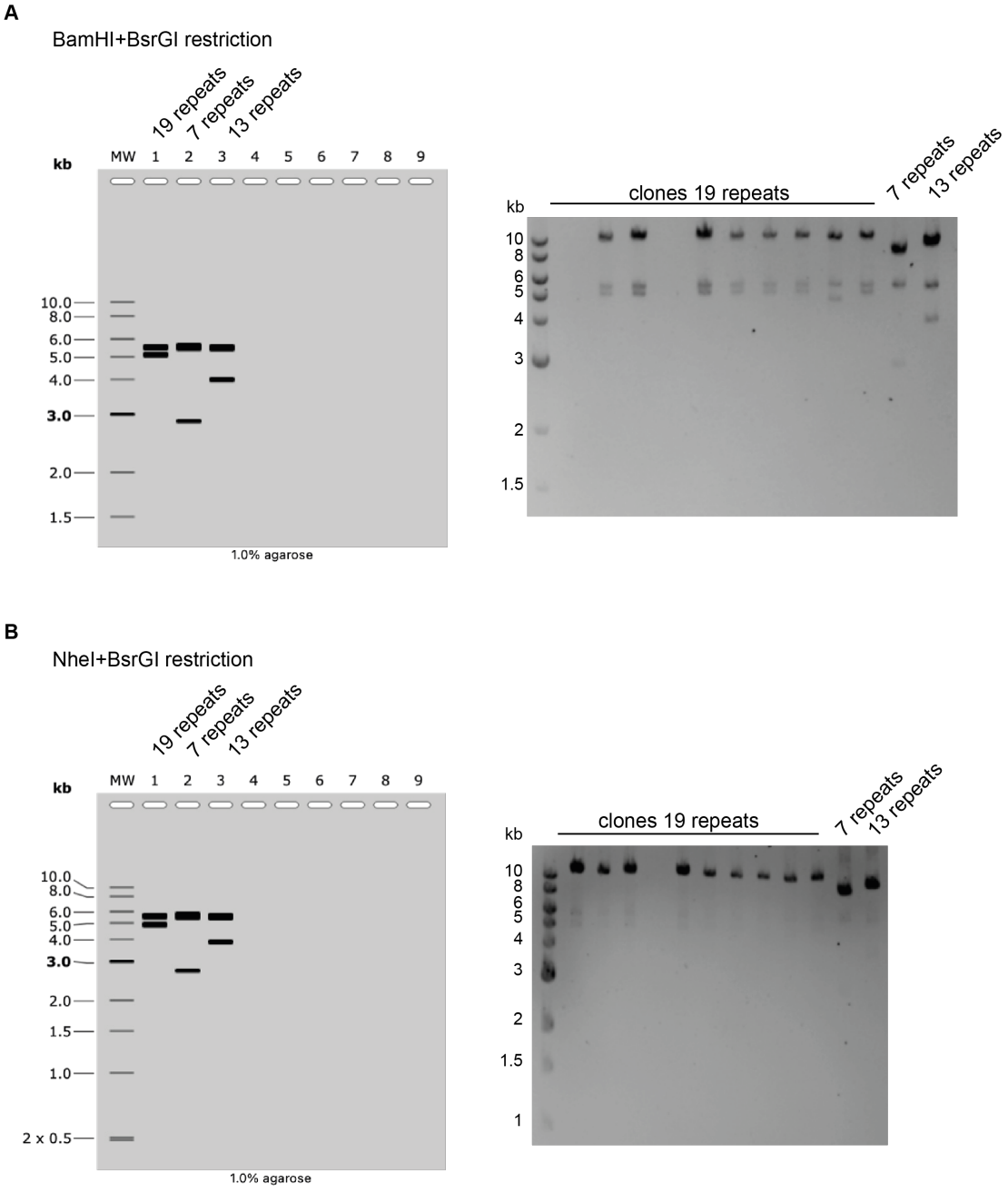

Figure 2.24: **Cloning of artificial crosslinkers with 19 D18 domains.** Simulations of bands on agarose gel (left) and agarose gel (right) of plasmids containing artificial crosslinkers with 7, 13 or 19 D18 domains cut with BamHI and BsrGI (A) or NheI and BsrGI (B) restriction enzymes. Agarose gels on the left were simulated using SnapGene. The images of agarose gels have inverted contrast.

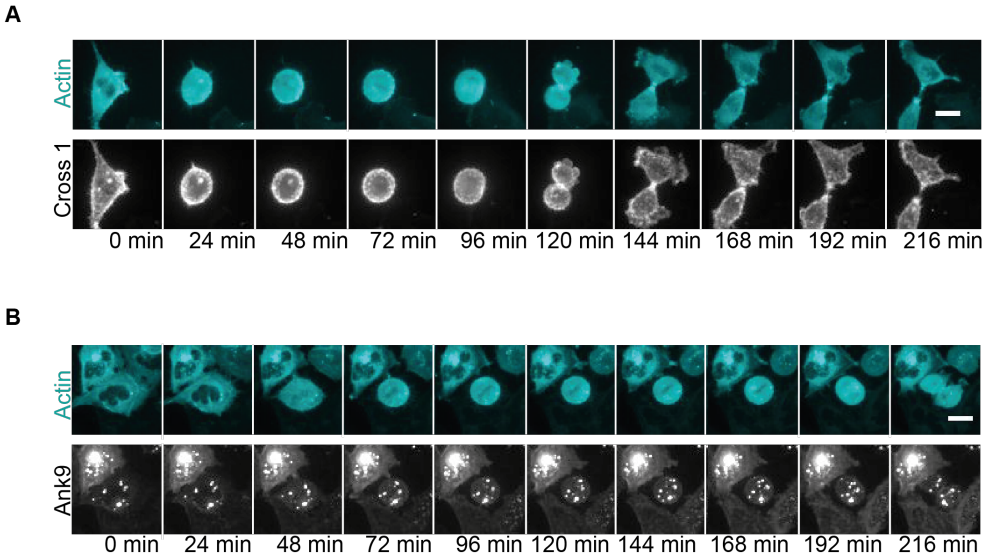

Figure 2.25: **Ank crosslinkers expression during cell division.** Timelapse acquired with live spinning disk microscopy of cells transiently expressing small (A) Cross1 or big (B) Ank9 artificial crosslinkers (white) designed and stably expressing actin (cyan) during cell division. Scale bar= 20 µm.

We firstly attempted to use ankyrin based, Ank repeat domains to create artificial crosslinkers, which was better characterised before the start of this project [Parmeggiani et al., 2015]. However, before this project, synthetic proteins with Ank repeat domains were not used in mammalian cells. Therefore, I firstly tested whether proteins expressing Ank domains actually get expressed in mammalian cells. We created two pcDNA 3.1 plasmids for two proteins with different number of repeat domains. Cross1 was a smaller protein containing 5 repeat domains. Ank9 was created by adding 9 more Ank repeats to the original Cross1 protein. I expressed plasmids domain either encoding Cross1 or Ank9 in HeLa cells stably expressing actin-RFP (Figure 2.25). Both artificial crosslinkers were successfully expressed in HeLa cells. Cells expressing these crosslinkers were able to successfully divide. Cross1 colocalised with actin in spread cells and during division. In contrast, whether Ank9 colocalised with actin in spread cells was less clear and it did not seem to localise to the cortex during division due to high levels of aggregation (Figure 2.25B). Aggregates were very bright making any other localisation impossible to distinguish. Since I wanted to use artificial crosslinkers with as many repeat domains as possible, I concluded that artificial crosslinkers designed with Ank repeats were not suitable.

Dr. Fabio Parmeggiani thus designed a new set of artificial crosslinkers (using the same principles as with Ank) replacing Ank with D18 repeat domains [Baker et al., Brunette et al., 2015]. When expressed in HeLa cells, D18 repeat based crosslinkers colocalised

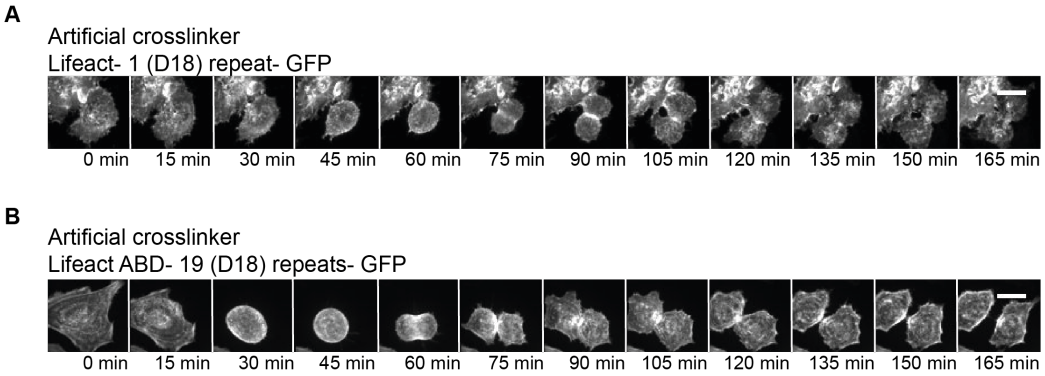

Figure 2.26: **D18 crosslinkers expression during cell division.** Timelapse acquired with live spinning disk microscopy of cells expressing artificial crosslinkers (white) designed with (A) 1 or (B) 19 D18 domains during cell division. Scale bar= 20 µm.

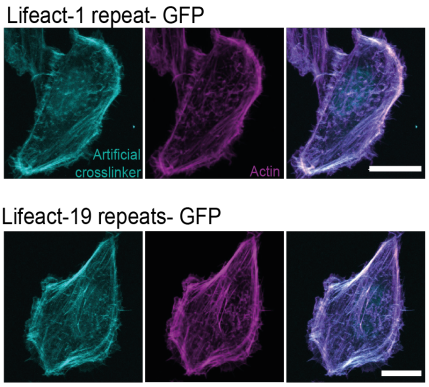

Figure 2.27: **Fluorescent labelling of artificial crosslinkers with D18 repeats stably expressed in cells.** Artificial crosslinkers (nanobody-Alexa-647 against GFP, cyan), actin (phalloidin-Alexa-568, magenta). Scale bar= 20 µm.

with actin in spread cells, and during cell division (Figure 2.26, 2.27). Importantly, cells divided successfully and during division artificial crosslinkers containing 1, 7, 13 or 19 D18 domains continued to colocalise with actin. 19 D18 domains was the highest number tested as at higher numbers the protein was predicted to start curling. Taken together, I concluded that D18 repeat domain-based artificial crosslinkers are a suitable tool to study the role of crosslinker size for its localisation within the actin cortex and its role in tension generation. For the rest of the study, I used 1 repeat and 19 repeats D18 artificial crosslinker as the two extremes of the small and large artificial crosslinker.

2.2.2 Artificial crosslinkers with different actin binding domains and different fluorescent tags

We included unique restriction sites in the sequences for artificial crosslinkers. We included unique restriction sites on each site of the repeat domain, actin binding domain (ABD)

Number of repeats	Actin binding domain (ABD)	Fluorescent protein
1	Lifeact (LA)	eGFP
7	Lifeact (LA)	eGFP
13	Lifeact (LA)	eGFP
19	Lifeact (LA)	eGFP
1	Utrophin 1-240 (U)	eGFP
7	Utrophin 1-240 (U)	eGFP
13	Utrophin 1-240 (U)	eGFP
19	Utrophin 1-240 (U)	eGFP
1	Lifeact (LA)	mCherry
19	Lifeact (LA)	mCherry
1	Utrophin 1-240 (U)	mCherry
19	Utrophin 1-240 (U)	mCherry

Table 2.3: **Combinations of the number of repeats, actin binding domains and fluorescent tags in cloned artificial crosslinkers.** Artificial crosslinkers with different number of repeats, actin binding domains and fluorescent proteins in artificial crosslinkers cloned created in this project are available in pcDNA 3.1 plasmid.

and fluorescent protein sequence (Figure 2.23A,C). These restriction sites allowed us to increase the number of repeat domains within the artificial crosslinker and thus its size (see above Design of artificial crosslinkers of different sizes) as well as modulate fluorescent proteins and actin binding domains.

The properties of the actin binding domain (ABD), its dynamics and strength of binding to actin would affect the crosslinking activity of the artificial crosslinkers. Technically, if the binding is too weak or too transient crosslinking could not be achieved. Similarly, ABDs with strong affinity for actin that bind over longer periods of time could lead to a crosslinking that is too strong for optimal cortical tension generation [Chugh et al., 2017, Ding et al., 2017]. Therefore, finding an actin binding domain that would lead to simultaneous binding of both sides of the artificial crosslinker but would not over-stabilise the actin network, was key to the design of the artificial crosslinkers.

Original constructs of the artificial crosslinkers contained sequence encoding Lifeact, a 17 amino acids long peptide frequently used to label F-actin, as an ABD [Riedl et al., 2008]. Lifeact effectively labels F-actin in live cells but it turnovers quickly on F-actin ($\sim$ 0.4 s). Therefore, two Lifeact domains might not lead to very strong crosslinking. I thus decided to also test an alternative ABD alongside Lifeact. The utrophin CH domain (260 amino acids on the N-terminal of utrophin) is another popular probe for labelling actin in live

cells [Winder et al., 1995]. Utrophin has a much longer (1 s) dwell time on actin filaments compared to lifeact (0.1 s) [Harris et al., 2020], leading to stronger binding. I cloned new artificial crosslinkers in which I replaced the Lifeact ABD with utrophin CH domain to be able to compare crosslinkers with different ABDs.

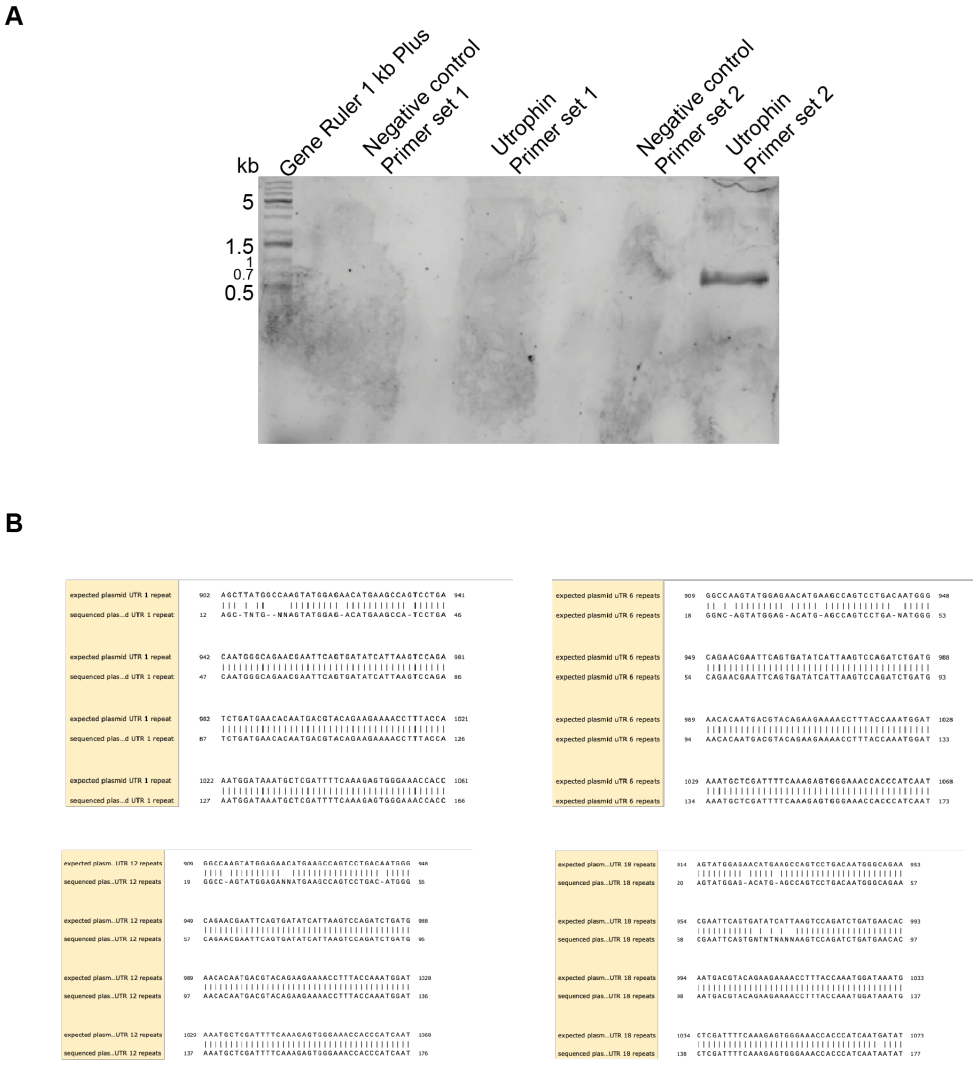

Figure 2.28: **Replacing Lifeact with utrophin actin binding domain.** (A) Agarose gel of PCR product with HindIII and BamHI restriction sites of utrophin actin binding domain (786 bp). Utrophin was successfully cloned with primer set 2 but not with primer set 1. The image of agarose gels has an inverted contrast. (B) Example of alignment after sequencing using T7 forward primer after cloning utrophin in artificial crosslinkers. Alignment was performed with SnapGene.

I confirmed that utrophin was successfully cloned in the sequence of the artificial crosslinkers by restriction reaction and Sanger sequencing (Figure 2.28B). With these cloning steps I expanded my collection of artificial crosslinkers of four different sizes with Lifeact ABD with another four artificial crosslinkers of similar sizes but a different actin binding properties due to utrophin (Table 2.3).

The sequence of the original set of artificial crosslinkers and later created utrophin artificial crosslinkers also encoded a fluorescent protein sequence to allow for visualisation of the crosslinkers via fluorescence microscopy. Initially, this sequence was eGFP (green fluorescent protein). eGFP has an excitation wavelength of 488 nm and was used in artificial crosslinkers with 1, 7, 13, and 19 repeats. Therefore, we would not be able to directly compare and colocalise this initial set of artificial crosslinkers with different sizes or with any other structure labelled with probes of similar excitation wavelength.

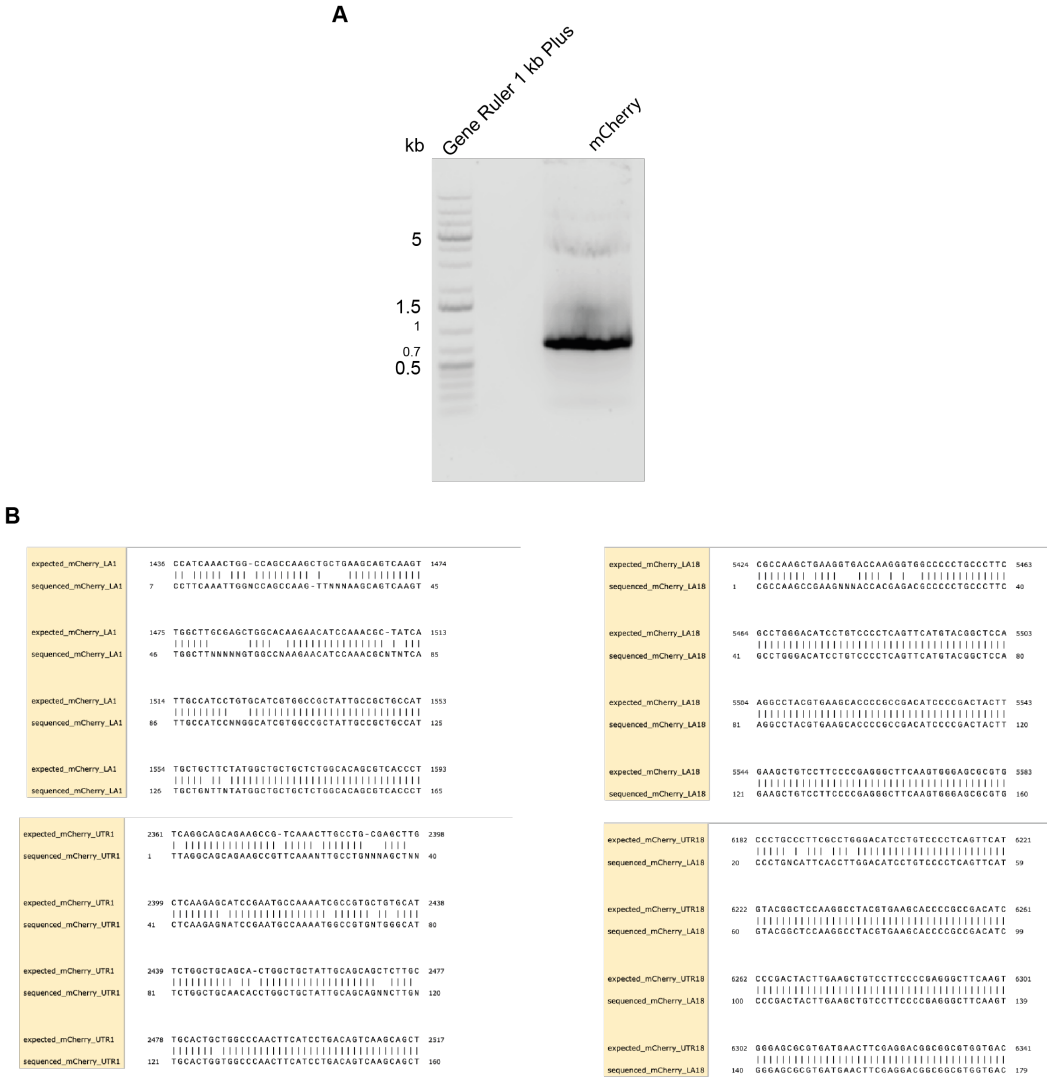

Figure 2.29: **Replacing GFP with mCherry tag.** (A) Agarose gel of PCR product with KpnI and XhoI restriction sites of mCherry (709 bp). The image of agarose gels has an inverted contrast. (B) Example of the alignment after sequencing using BGH reverse primer after cloning mCherry in the artificial crosslinkers. Alignment was performed with SnapGene.

To expand our toolbox of artificial crosslinkers and to allow for co-expression of artificial crosslinkers of different sizes and comparison of their sizes, I cloned mCherry (excitation

wavelength 587 nm) in the artificial crosslinkers. After cloning mCherry sequence with suitable restriction sites for restriction-ligation (Figure 2.29A), I replaced eGFP sequences with mCherry in artificial crosslinkers with 1 and 19 repeats with both Lifeact and utrophin ABDs. I confirmed that mCherry was successfully cloned in the sequence of the artificial crosslinkers with restriction reaction and Sanger sequencing (Figure 2.29B).

By cloning mCherry in place of eGFP in artificial crosslinkers I created four additional plasmids (Table 2.3) and thus enabled the expression and visualisation of crosslinkers of different sizes simultaneously or with other proteins in the 488 nm excitation range.

Taken together, besides original commercially synthesised plasmid for expression of artificial crosslinkers, I cloned 10 more plasmids expanding my collection to artificial crosslinkers of four different sizes, with two different ABDs, and two different fluorescent tags.

2.2.3 Expression of artificial crosslinkers with different sizes and different actin-binding domains in mammalian cells

After, designing the sequences encoding artificial crosslinkers with 1 and 19 repeats, with either Lifeact or utrophin ABD, I confirmed that all these led to an expression of differently sized proteins that localise to actin in live cells, which can successfully divide.

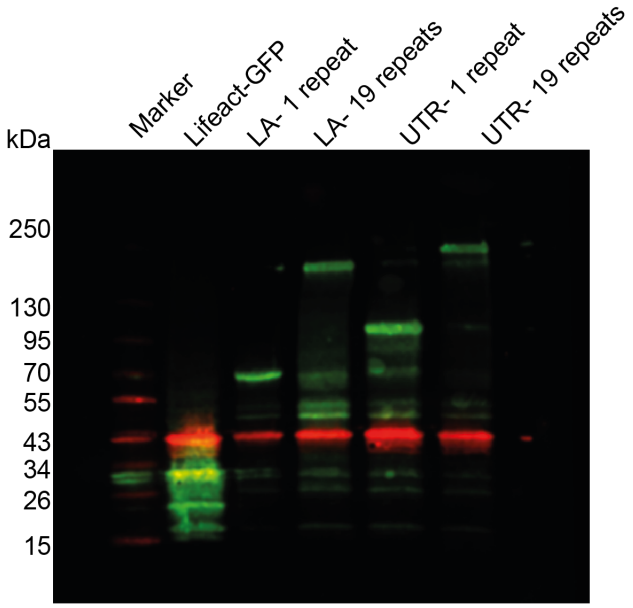

Figure 2.30: **Western blot of whole cell lysates expressing 1 and 19 D18 repeats artificial crosslinkers.** Western blot against GFP (green) and GAPDH (red, loading control) of cell lysates transiently expressing artificial crosslinkers with 1 or 19 domains with Lifeact (LA) or utrophin (UTR) actin binding domains.

To confirm that upon expression the sequences for artificial crosslinkers led to crosslinkers of different sizes, I performed a western blot of cell lysates expressing artificial crosslinkers (Figure 2.30). I lysed the cells transiently expressing artificial crosslinkers and probed the membrane with an antibody against GFP, which is part of the sequence of artificial crosslinkers. Although SDS in this experiment led to denaturation of proteins meaning that only monomers were present on the membrane, it clearly showed that proteins with 1 or 19 repeats had different molecular weights. Molecular weights of artificial crosslinkers detected by western blots matched molecular weights predicted with Snapgene. Predicted molecular weights were 67 kDa, 178 kDa, 95 kDa, 205 kDa for Lifeact 1 repeat, Lifeact 19 repeats, utrophin 1 repeat, and utrophin 19 repeats respectively.

The molecular weight of a protein is not directly proportional to the size of a protein, but I also compared molecular weights of the artificial crosslinkers to the molecular weights of other actin crosslinkers which are similar in size to the expected sizes of the artificial crosslinkers. Artificial crosslinkers containing 19 repeats are predicted to be $\sim$ 30 nm long which is comparable to the size of alpha-actinin. Alpha actinin has a molecular weight of $\sim$ 105 kDa and artificial crosslinkers with 19 repeats had molecular weight of $\sim$ 180 kDa. Artificial crosslinkers with 1 repeat is expected to be quite similar in size to plastin. Plastin has a molecular weight of $\sim$ 70 kDa, which is also similar to the molecular weight of artificial crosslinker with 1 repeat. These similarities suggest that the size of artificial crosslinkers is close to the expected sizes. Taken together, these observations suggest that plasmids encoding artificial crosslinkers indeed led to expression of proteins with different sizes within cells.

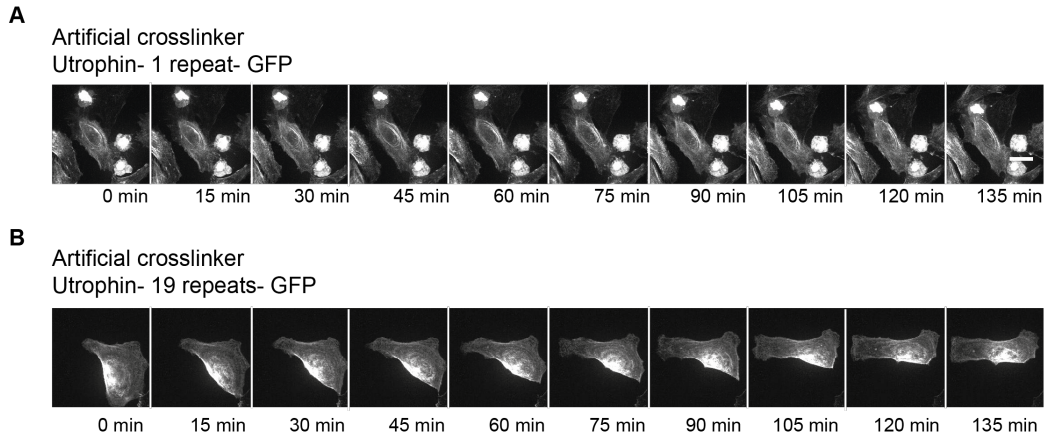

Figure 2.31: **1 and 19 repeats crosslinkers with utrophin actin binding domain expression during cell division.** Timelapse of live spinning disk confocal imaging of cells expressing artificial crosslinkers with utrophin actin binding domain designed with 1 (A) or 19 (B) D18 domains during cell division. Scale bar= 20 µm.

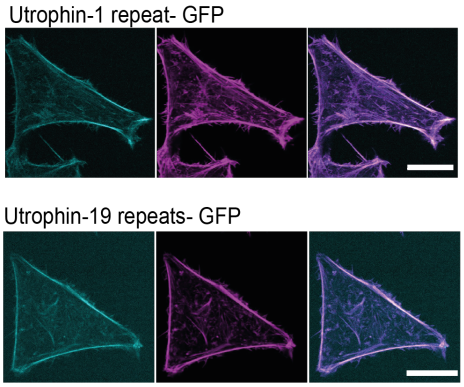

Figure 2.32: **Fluorescent labelling of artificial crosslinkers with utrophin ABD stably expressed in cells.** Artificial crosslinkers (nanobody-Alexa-647 against GFP, cyan), actin (phalloidin-Alexa-568, magenta). Scale bar= 20 µm.

To be able to explore localisation and effects on cell mechanics of artificial crosslinkers in mammalian cells, I tested artificial crosslinkers with Lifeact and utrophin ABD for their expression in mammalian cells (Figure 2.26, 2.31). Transient transfection of artificial crosslinkers led to protein levels high enough for their visualisation during live imaging. However, there were high levels of cell death in cells expressing utrophin crosslinkers. Cell death is relatively common following transfection most likely due to high overexpression of proteins and toxicity of transfection reagents. An additional disadvantage of transient transfection for protein expression, is the extra step it requires before each experiment. I thus decided to create cell lines stably expressing artificial crosslinkers. In stable cell lines, all cells express protein of interest but with lower variability in its expression. Stably expressed in cells, artificial crosslinkers successfully localised to actin structures (Figure 2.27, 2.32). However, the levels of expression were low and required high laser power for their visualisation.

Taken together, sequences encoding artificial crosslinkers resulted in proteins with different molecular weights that can be transiently or stably expressed in mammalian cells.

2.2.4 Effects of artificial crosslinkers on the duration of cell division and mitotic cell shape

To investigate the role of artificial crosslinkers on cortex mechanics, I firstly asked if the artificial crosslinkers of different sizes impact various aspects of cell division and if there are any differences in the effects of crosslinkers with different sizes (Figure 2.33, 2.34).

I used polyclonal cell lines stably expressing artificial crosslinkers and measured the time it

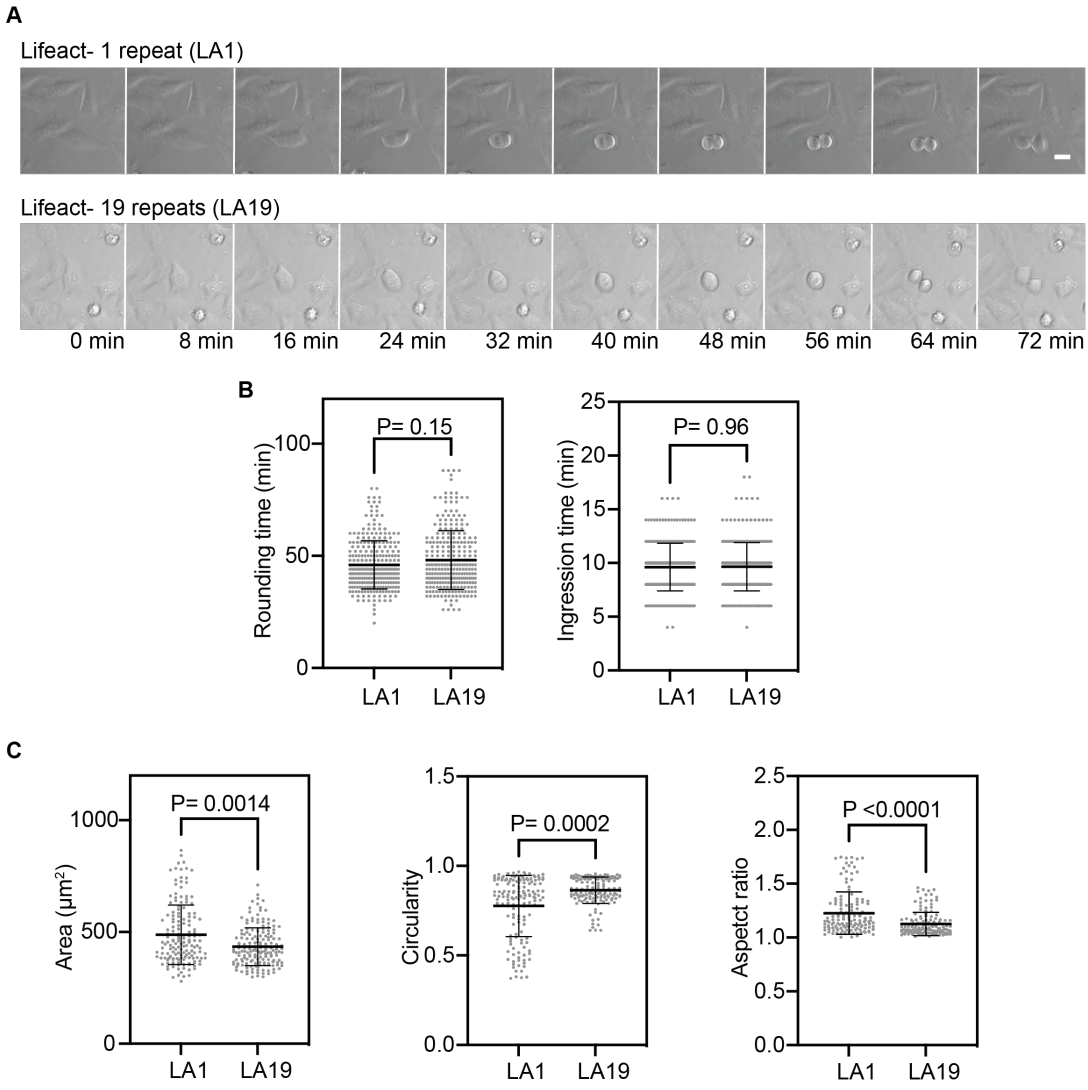

Figure 2.33: **The effects of Lifeact artificial crosslinkers during cell division.** (A) Timelapse of brightfield images of cells stably expressing artificial crosslinkers with 1 repeat (top) or 19 repeats (bottom) and Lifeact actin binding domain. (B) Timing of cell rounding and cleavage furrow ingression and (C) area, circularity and aspect ratio of cells stably expressing artificial crosslinkers. Scale bar= 20 µm. Graph, mean ±1 standard deviation. Data points were pooled from 3 independent experiments (performed on different days). The data were not normally distributed and were compared with Mann-Whitney test.

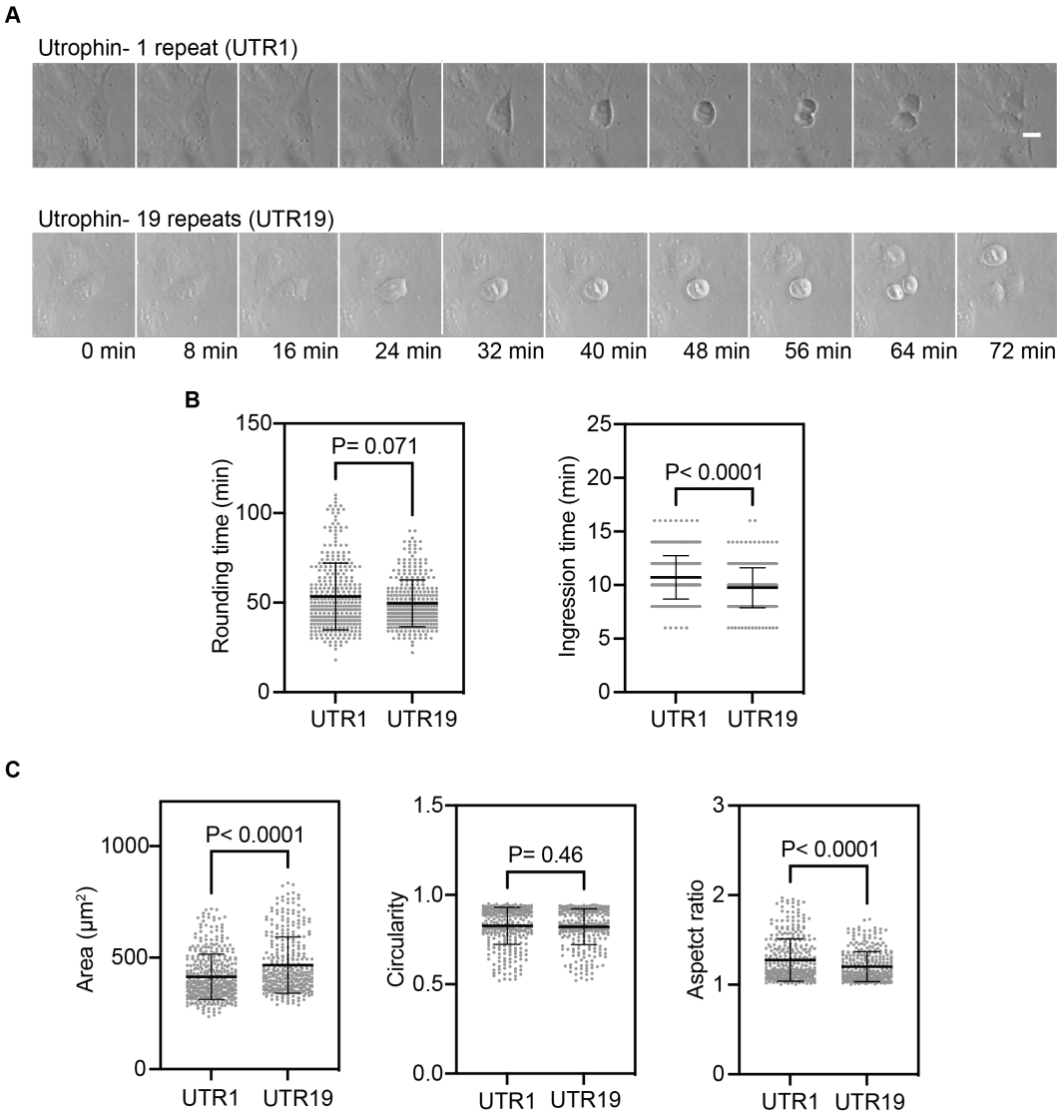

Figure 2.34: **The effects of utrophin artificial crosslinkers during cell division.** (A) Timelapse brightfield images of cells stably expressing artificial crosslinkers with 1 repeat (top) or 19 repeats (bottom) and utrophin actin binding domain. (B) Timing of cell rounding and cleavage furrow ingression and (C) area, circularity and aspect ratio of cells stably expressing artificial crosslinkers. Scale bar= 20 µm. Graph, mean ±1 standard deviation. Data points were pooled from 3 independent experiments (performed on different days). The data were not normally distributed data sets were compared with Mann-Whitney test.

took for cells to round up at the onset of mitosis and the time from anaphase to cytokinesis (cleavage furrow ingression time). Since in stable cell lines all cells are expressing artificial crosslinkers, I was able to image cell division via brightfield microscopy. I compared the effects on cell division of expression of artificial crosslinkers with 1 and 19 repeats to represent the smallest and biggest possible size with either Lifeact or utrophin ABD. I measured the time of cell rounding from the last time frame before I was able to see the start of cellular contraction until the last frame in which chromosomes were aligned. For the time of cleavage furrow ingression, I measured the time from the time point when the chromosomes first start segregating until the cleavage furrow completely ingresses. There were no significant differences in cell rounding time between cells expressing crosslinkers with different sizes with either Lifeact or utrophin ABD (Figure 2.33B, 2.34B). Interestingly, cleavage furrow ingression in cells expressing 19 repeats crosslinkers with utrophin ABD took significantly less time (P-value$<$ 0.0001) than in cells expressing shorter crosslinkers with only 1 repeat (Figure 2.34B). On average cells expressing 1 and 19 repeats artificial crosslinkers with utrophin ABD took 11 $\pm$ 2 min and 10 $\pm$ 2 min to complete furrow ingression, respectively. Notably, given the 2 min time resolution despite statistical significance this difference might not be very meaningful. There was no difference between 1 and 19 repeat crosslinkers with Lifeact ABD (P-value= 0.96) (Figure 2.33). To confirm that cells expressing longer artificial crosslinker and utrophin actin binding domain are indeed faster in furrow ingression, the process will need to be examined at higher time resolution in the future. However, if indeed there are differences in dynamics of division between artificial crosslinkers with Lifeact or utrophin ABD, even at higher temporal resolution, these could be due to differences in binding properties between these two ABDs. These potential differences in cleavage furrow ingression between cells expressing crosslinkers with 1 and 19 repeats observed for utrophin, might suggest that crosslinkers of different sizes have different effects on cellular mechanics.

Round mitotic shape is another key feature of cell division determined by cellular mechanics. I thus compared the cell shape in mitosis of cells expressing artificial crosslinkers with 1 or 19 repeats (Figure 2.33C, 2.34C). I measured cell shape parameters on the images of live cells expressing artificial crosslinkers, in the last frame where chromosomes are aligned, before they start segregating. Using ImageJ, I manually segmented cells in 2D to measure cell area, circularity and aspect ratio. Interestingly, cells expressing crosslinkers with either utrophin or Lifeact ABD differed in shape when comparing 1 or 19 repeats (Figure 2.33C, 2.34C).

Cells expressing 19 repeats with Lifeact ABD crosslinkers were smaller, more circular and had a smaller aspect ratio compared to cells expressing 1 repeat crosslinkers with Lifeact ABD with respective P-values of 0.0014, 0.002 and < 0.0001. However, artificial crosslinkers with utrophin ABD only significantly differed in cellular area (P-value< 0.0001) and aspect ratio (P-value< 0.001). Interestingly, cells expressing longer (19 repeats) artificial crosslinker with utrophin ABD had smaller aspect ratio but they were bigger compared to cells expressing 1 repeat artificial crosslinker with utrophin ABD. At this stage, shapes of cells expressing artificial crosslinkers of different sizes were only compared in 2D in the midplane of mitotic cells. For a more detailed understanding of how different artificial crosslinkers affect cell shape and in particular cell volume, cells will need to be compared in 3D. The 3D comparison of cell shape will require a more complex experimental set-up and a more advanced analysis. Still, these data suggest, that the variation in size of crosslinkers affects mitotic cell shape.

Taken together, artificial crosslinkers of different sizes affect mitotic cell shape and potentially cleavage furrow ingression (when used with a utrophin ABD). This suggests that the size of a crosslinker could play a role in controlling cortical mechanics. However, to understand the actual effect of artificial crosslinkers a more direct measurement of cortical mechanics was needed.

2.2.5 Effects of artificial crosslinkers on cortex tension in mitosis

To further investigated the role of artificial crosslinkers on cortical tension, I collaborated with Dr. Alex Winkel (Franze lab, University of Cambridge) to measure cortical tension using Atomic Force Microscopy (AFM).

A protocol for measuring cortical tension of round cells using AFM was previously established in the lab [Chugh et al., 2017, Truong Quang et al., 2021], based on a published protocol [Fischer-Friedrich et al., 2014]. In this protocol cells are compressed by flat cantilever and tension is calculated from the force exerted by the cell [Stewart et al., 2011]. Cells were transfected with artificial crosslinkers $\sim$ 24h before the measurement and blocked in mitosis with STLC. We measured tension of round mitotic cells which have the most prominent cortex. To measure tension, we tried to select cells with the highest GFP signal to measure the samples with the highest expression of the artificial crosslinkers and thus potentially the most prominent phenotype to establish whether artificial crosslinkers can affect cortical tension in mitosis (Figure 2.35).

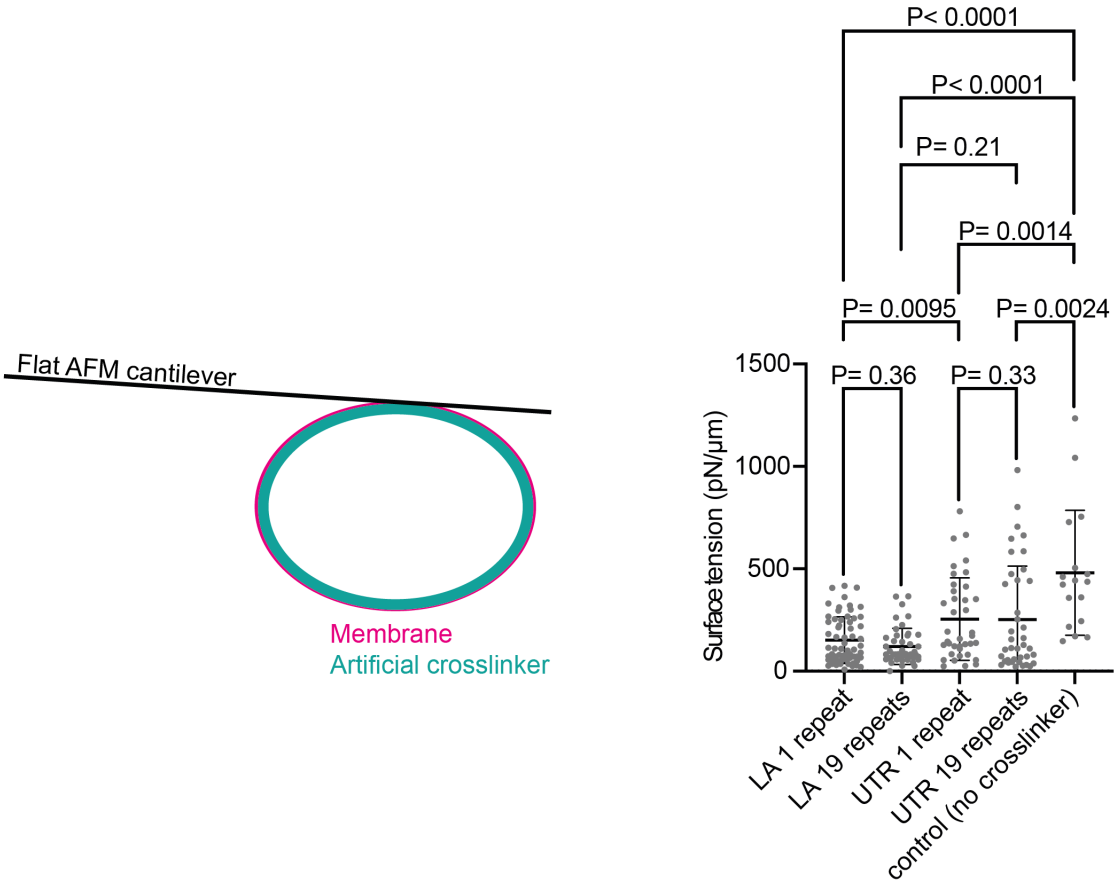

Figure 2.35: **Cortical tension of mitotic cells expressing artificial crosslinkers.** Cortical tension of cells transiently expressing artificial crosslinkers with 1 or 19 repeats and Lifeact or utrophin actin binding domain was measured with Atomic Force Microscopy (AFM) (schematic, left). Cells were compressed by a flat cantilever and cortical tension was calculated from a force exerted by a cell onto the cantilever during the compression. Cells were synchronised in mitosis and control cells were untransfected cells synchronised in mitosis. Graph: mean ±1 standard deviation. Data points were pooled from 3 independent experiments (performed on different days), except the control experiment which was only performed once. Datasets did not pass normality tests and were compared with Mann-Whitney test. AFM measurements were performed by Dr Alex Winkel, University of Cambridge.

Mitotic cells overexpressing artificial crosslinkers with Lifeact ABD 1 and 19 repeats and utrophin ABD with 1 and 19 repeats had mean cortical tensions 152 of ± 114 pN/ µm, 121 ± 88 pN/ µm, 254 ± 201 pN/ µm, 252 ± 261 pN/ µm, respectively. The average cortical tension of control untransfected cells was 480 ± 305 pN/ µm. Overall, cells overexpressing artificial crosslinkers had significantly lower tension compared to untransfected cells and cells expressing 1 repeat Lifeact artificial crosslinker had a significantly lower tension compared to cells with 1 repeat utrophin artificial crosslinker. Of note, all datasets of the tension have a large standard deviation and a higher number of measurements might allow a more reliable comparison. In these experiments only non-transfected cells were used as a control. In the future, the effect of only actin binding domain or non-dimerised artificial crosslinkers on cortical tension should also be compared with the effect of artificial crosslinkers.

We detected no difference in cortical tension between mitotic cells overexpressing crosslinkers of different sizes (Figure 2.35, right). However, the tension was measured for round mitotic cells and data from live cell imaging of stable cell lines expressing utrophin artificial crosslinkers suggest that artificial crosslinkers of different sizes might affect tension-driven cell shape changes after metaphase, during cleavage furrow ingression. In round mitotic cells, actin cortex organisation is rather homogeneous around the cell without any tension gradients [Chugh et al., 2017]. In contrast during cleavage furrow, there is gradient in cortical tension and differences in cortical organisation between the furrow and the poles [Matzke et al., 2001]. Therefore, I speculated that artificial crosslinkers of different sizes potentially localise differently during cytokinesis (at the poles vs furrow) and thus differently affect gradients in cortical tension.

2.2.6 Localisation of artificial crosslinkers of different sizes during cytokinesis

To ask whether there are any differences in the enrichment of artificial crosslinkers with different sizes at the cleavage furrow and the cell poles, I imaged cells transiently overexpressing artificial crosslinkers with 1 or 19 repeats undergoing cell division using spinning disk confocal microscopy (Figures 2.26, 2.31, 2.36). Transient overexpression led to a higher fluorescent signal compared to stable cell line and thus required much lower laser power, resulting in lower phototoxicity and cell death. Cells overexpressing artificial crosslinkers with a Lifeact ABD at levels high enough for their visualisation were more likely to successfully divide than those overexpressing artificial crosslinkers with a utrophin ABD.

This is likely due to differences in binding properties of different ABDs [Belin et al., 2014, Harris et al., 2020]. Therefore, I firstly focused on the localisation of artificial crosslinkers with a Lifeact ABD (Figure 2.36).

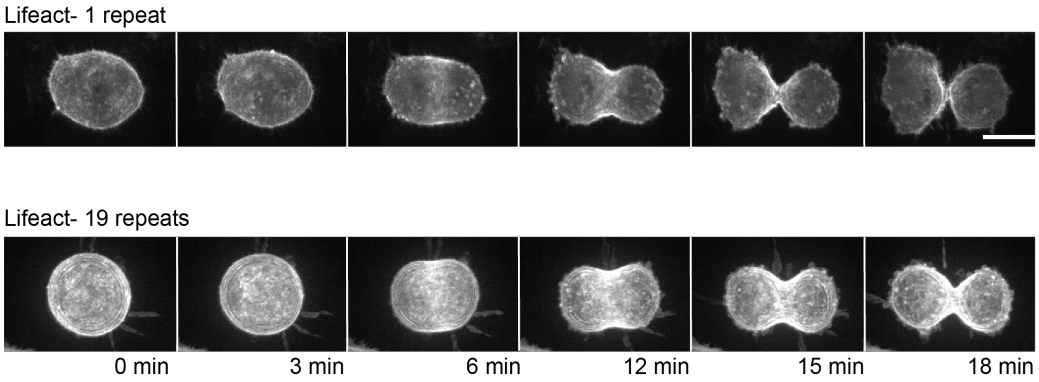

Figure 2.36: **Live imaging of cell division of cells expressing artificial crosslinkers.** Timelapse of cell division of cells transiently expressing artificial crosslinkers with Lifeact ABD and 1 (top) or 19 (bottom) repeats imaged by spinning disk confocal microscopy. Given the changes in cell height throughout the cell division, images were taken in Z-stacks which are projected as maximum projections. Images are representative of time frames of single cells used for quantification of fluorescent intensity of artificial crosslinkers along the cell contour. Scale bar= 20 µm.

To quantify the signal of artificial crosslinkers in the cortex during division, I firstly segmented the cortex and extracted the intensity values along the cell contour using a similar workflow as that described in Kelkar et al. [2022], developed by Dr Diana Khoromskaia (Francis Crick Institute) (Figure 2.37). Firstly, I segmented the cell cortex using the FIJI plug-in JFilament [Smith et al., 2010] (see Methods for details on parameters). Then, using a ROI of the segmented cortex, I manually identified the furrow using Speckle TrackerJ [Smith et al., 2011] by selecting the crossing of the short axis of the cell and the cell contour. Finally, I extracted cortical intensities along the contour with respect to the cleavage position using a custom written FIJI plug-in (by Dr. Diana Khoromskaia) (Figure 2.38A).

To compare levels of enrichment at the furrow of artificial crosslinkers with different sizes during cell division, Dr. Ruby Peters developed an analysis workflow to normalise and scale the intensities of different cells (Figure 2.38) to allow for averaging of cortical intensities of multiple cells (Figure 2.39) and for comparing these based on crosslinker size (Figure 2.37). Firstly, I (visually) identified a consistent starting frame (Frame 1), defined as 2 frames prior to anaphase onset (clear elongation of rounded cells). We then analysed 6 frames in total for each of the cells. Firstly, fluorescent intensity profiles (along the cell cortex) for each frame were normalised to the cortical intensity of the cell in mitosis (Frame 1)

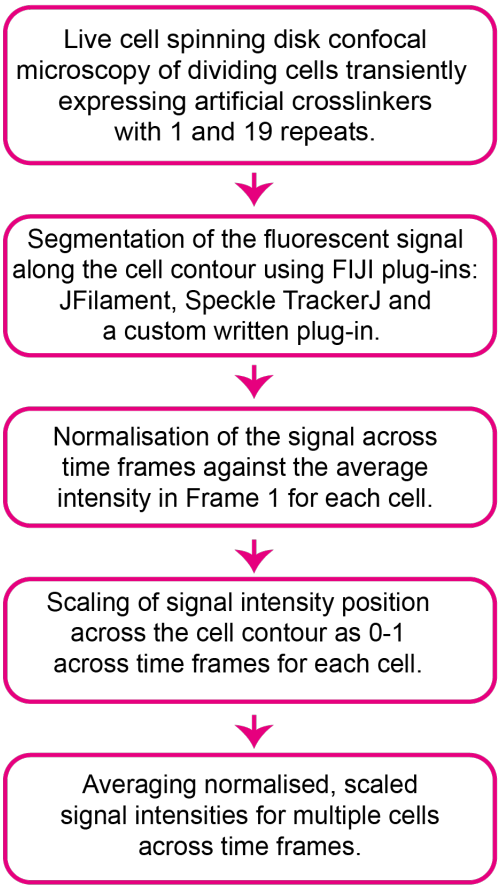

Figure 2.37: **Analysis workflow of fluorescent intensity of artificial crosslinkers along the contour of dividing cells.** In order to compare fluorescent intensity of the artificial crosslinkers with different sizes during cell division, a multi-step analysis was performed. After acquisition of images of live cells dividing, the cortical signal was segmented for each cell across time frames, then to be able to compare sample sizes of comprising of multiple cells for each conditions, the intensities for individual cells were normalised and scaled.

(Figure 2.38B), to account for changes in expression levels of transiently transfected cells. Then, the distance along the cell contour was scaled between 0 and 1 for each cell such that changes in cell sizes did not impact the averaging of intensities at arbitrary positions along the cell contour (Figure 2.38C). Together, these steps allowed for averaging of intensities along the cortex for multiple cells, for different time frames, and a comparison of the localisation of different crosslinkers (Figure 2.39).

Only cells without signal from neighbouring cells, that would otherwise artificially increase the cortical intensity, were included in this analysis to prevent any confounding signal affecting the average intensity. This strongly limits the experimental output of the imaging which led to the data presented here being only preliminary and will need to be supplemented with higher numbers in the future. At this stage of the investigation

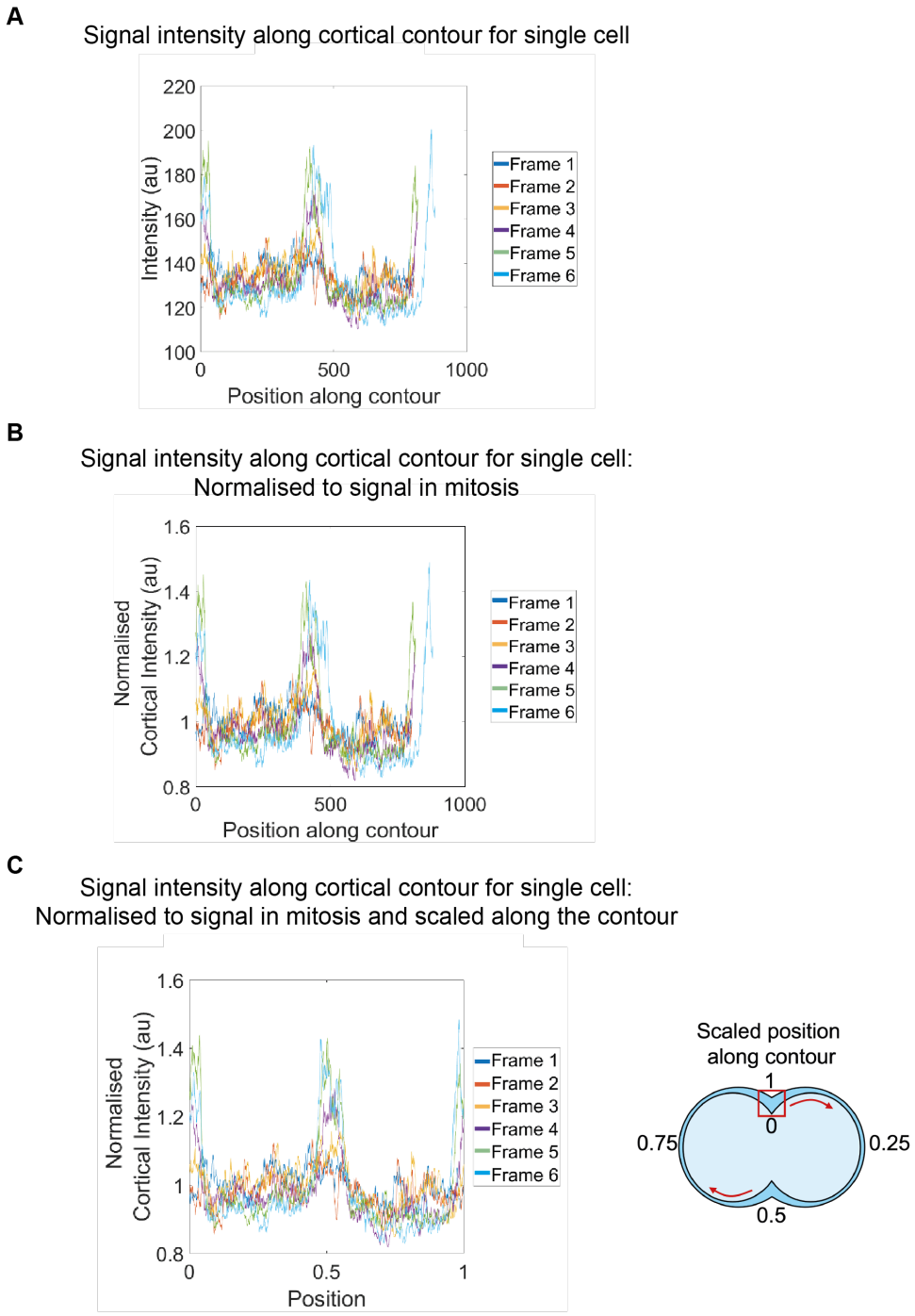

Figure 2.38: **Fluorescent artificial crosslinker signal intensity along the cell cortex during cytokinesis.** Cortical GFP (artificial crosslinker) signal intensity during cytokinesis along the cell contour (cortex) for an example cell. (A) Intensity values of the segmented cell cortex as extracted by a custom built plug-in for a single cell [Kelkar et al., 2022]. Position along the contour is relative to user input of cleavage furrow formation. (B) Intensity values for each frame from (A) normalised to the intensity values in mitosis (defined as the start frame, Frame 1). (C) Normalised signal intensity values for a single cell scaled across the cell contour between 0-1 (as illustrated in the schematic on the right). Intensities of each individual cell were normalised to mitotic intensity and scaled to allow for averaging among multiple cells. Frame 1= mitosis, Frame 7= cleveage ingression, time step between frames= 3 min. Analysis depicted in B and C was carried out by Dr Ruby Peters (Paluch lab, University of Cambridge).

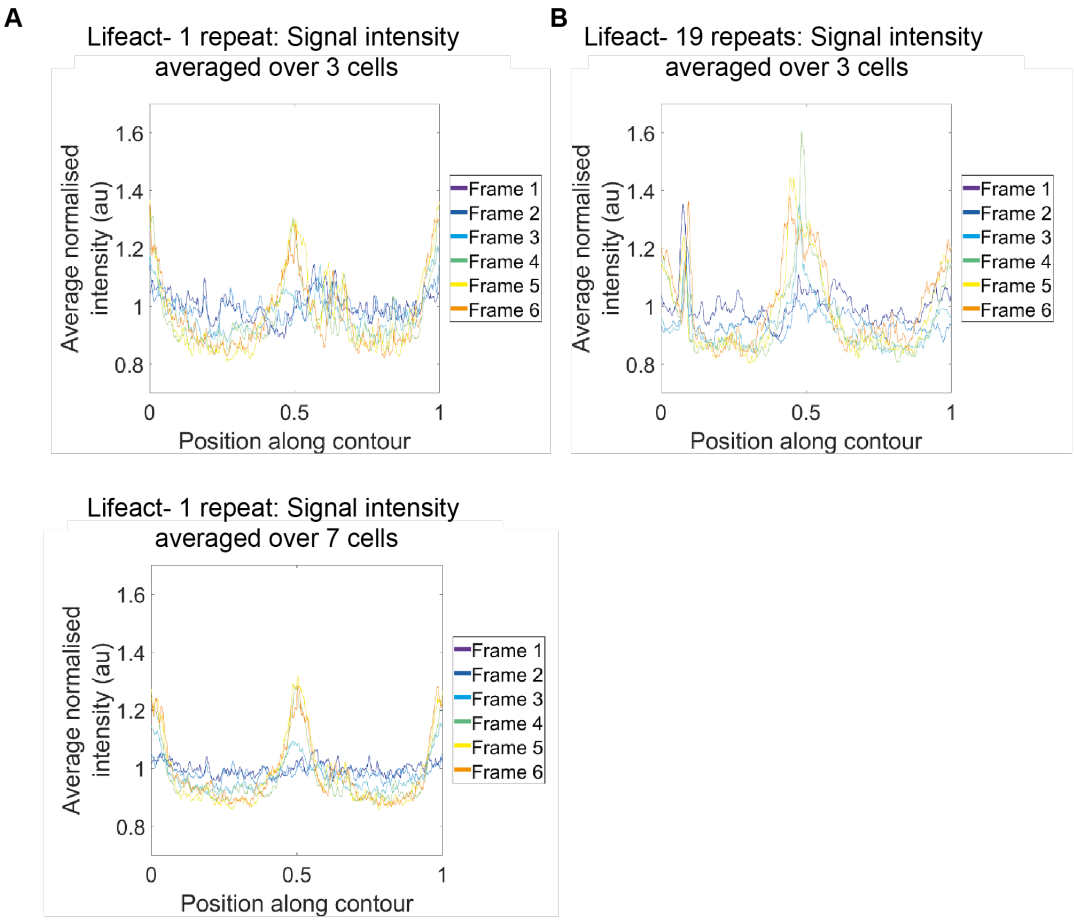

Figure 2.39: **Average fluorescent artificial crosslinker signal intensity along the cell cortex during cytokinesis.** Average, normalised and scaled cortical intensities (GFP, artificial crosslinker) across the cell contour from n= 3 (top) and n= 7 (bottom) cells transiently overexpressing artificial crosslinker with 1 repeat (A) or 19 repeats (B) and Lifeact ABD. Frame 1= mitosis, Frame 7= cleveage ingression, time step between frames= 3 min. Analysis was carried out by Dr. Ruby Peters (Paluch lab, University of Cambridge).

maximum projections from Z-steps of a dividing cells were used for the analysis. Cell height drastically changes between mitosis and cytokinesis, including the distance of the cleavage furrow from the coverslips. Cells were thus acquired in multiple Z-planes. For the ease of processing the live movies and locating dividing cells, these were then projected as maximum projection. In the control steps, after higher cell numbers will be acquired, signal intensity along the contour will need to be measured also in the images without maximum projection.

Taken together, we have developed an analysis workflow to allow for a comparison of cortical enrichment of artificial crosslinkers at the cleavage furrow relative to cell poles during cell division. However, due to experimental challenges, the numbers are too low

for any conclusions to be drawn about differences in localisation between crosslinkers with different sizes.

2.2.7 Nanoscale organisation of the actin cortex and artificial crosslinkers in mitosis

Effect of artificial crosslinkers on cortical thickness in mitosis

Finally, I focused on the nansocale organisation of the actin cortex in cells expressing artificial crosslinkers. Firstly, I investigated whether artificial crosslinkers of different sizes affect cortical thickness.

To understand how artificial crosslinkers affect cortical organisation (and thus cortical tension), I used a method previously established in the lab to measure cortical thickness of HeLa cells via STORM [Truong Quang et al., 2021]. I measured cortical actin thickness of mitotic cells stably expressing artificial crosslinkers with Lifeact or utrophin ABD and 1 or 19 repeats. Cells, synchronised in mitosis, were fixed and labelled for F-actin using phalloidin conjugated to an Alexa-647 fluorophore and imaged in the cellular midplane via STORM. Cortical thickness was measured as the full width at half maximum (FWHM) of the transversal intensity profiles across the boundary of cells (Figure 2.40A, B).

The mean cortical actin thickness of cells expressing Lifeact ABD with 1 repeat, 19 repeats, and utrophin ABD with 1 and 19 domains as well as control cells was 169 $\pm$ 23 nm, 165 $\pm$ 14 nm, 172 $\pm$ 23 nm, 180 $\pm$ 31 nm, 142 $\pm$ 17 nm, respectively (Figure 2.40B). There was no significant difference in actin thickness between cells expressing crosslinkers of different sizes or different ABDs. However, compared to control cells, cells with artificial crosslinkers (regardless of size or ABD) had a significantly higher actin thickness with P-values of 0.001, 0.0046, < 0.0001, < 0.0001 for cells expressing artificial crosslinkers with Lifeact ABD with 1 repeat, 19 repeats, and utrophin ABD with 1 and 19 domains, respectively. This is somewhat consistent with the previous observation on cortical tension, which was significantly lower for cells expressing artificial crosslinkers with utrophin ABD compared to control cells but with no differences in tension between crosslinkers of different sizes (Figure 2.35). Interestingly, crosslinkers with Lifeact ABDs seem to lead to a thicker cortex but do not seem to affect mitotic tension. Taken together, these data suggest that artificial crossslinkers do affect actin organisation in the cortex which could account for differences in tension measured by AFM.

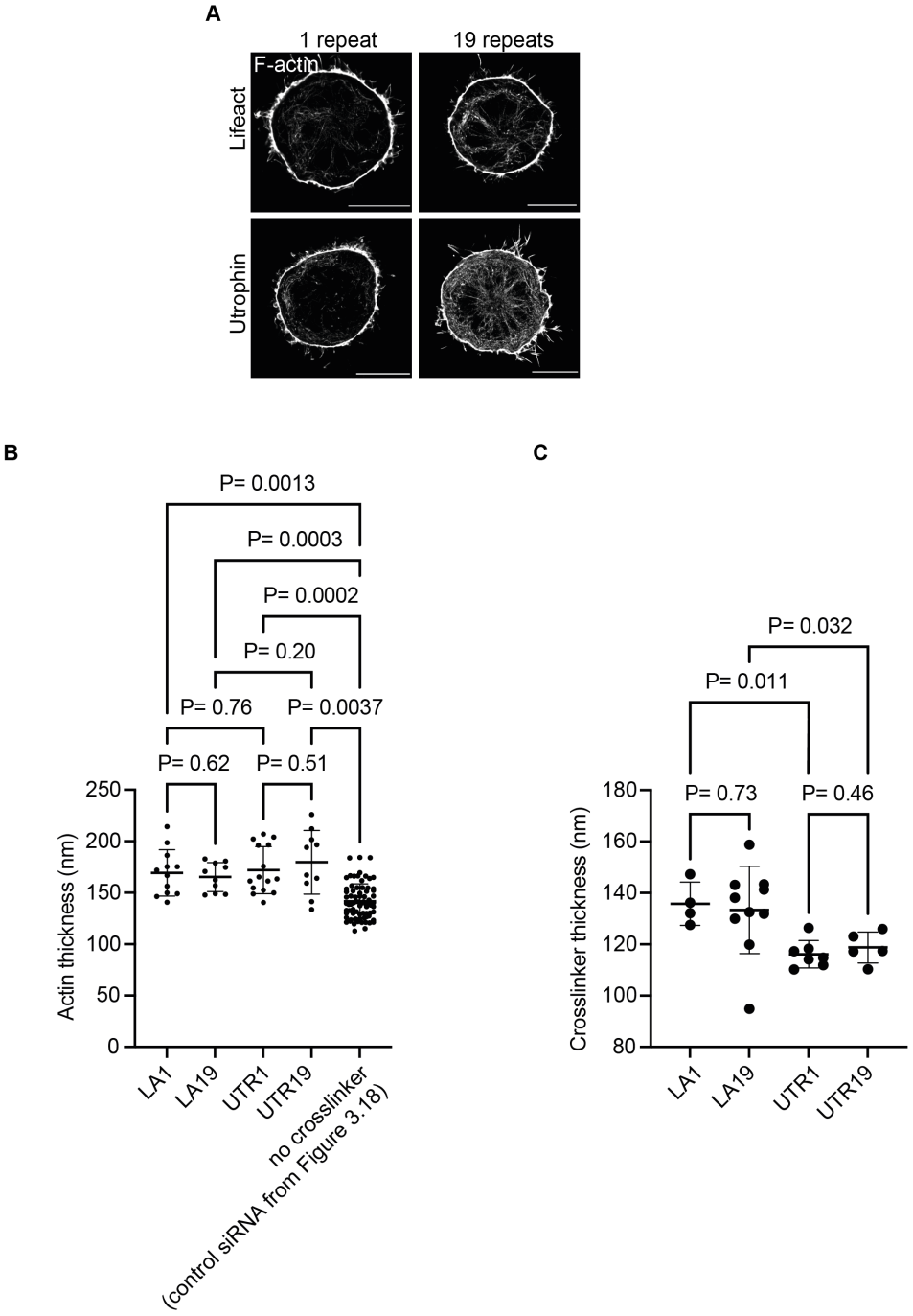

Figure 2.40: **Thickness of cortical actin and the cortical layer of artificial crosslinkers in mitotic cells.** (A) Stochastic optical reconstruction microscopy (STORM) reconstructed image of the actin cortex at the cellular midplane of cells stably expressing artificial crosslinkers with Lifeact (LA) and utrophin (UTR) ABDs. White= F-actin (phalloidin). Scale bar= 10 µm. (B) Cortical actin thickness measured as the full width at half maximum (FWHM) of their transversal intensity profiles across the cell boundary of cells expressing artificial crosslinkers and control cells from Figure 2.17B. Data points were pulled across 3 independent experiments. Normally distributed samples were compared with Welch's t-test. (C) Cortical thickness of artificial crosslinkers. Graph, ±1 mean standard deviation, 1 experiment. Normally distributed samples were compared Welch's t-test.

Nansocale localisation of the artificial crosslinkers within the actin cortex

When I imaged cells expressing artificial crosslinkers with confocal microscopy (Figure 2.26, 2.31, 2.27), there were no obvious differences in the localisation of the the actin crosslinkers within actin networks. However, the differences might be below the resolution limit (200 nm) of light microscopy. I thus decided to examine the localisation of crosslinkers during cell division using advanced imaging and analysis methods.

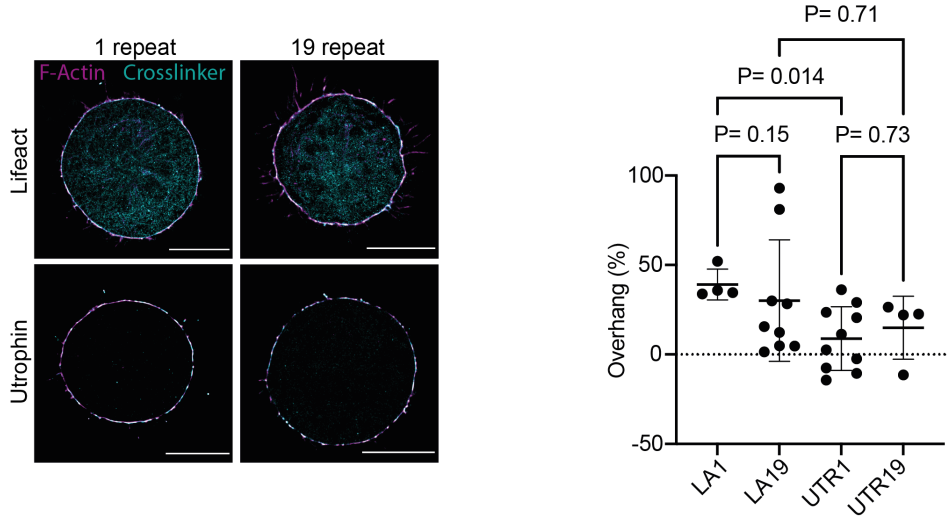

Figure 2.41: **Two colour STORM localisation of artificial crosslinkers within the actin cortex.** Two-color STORM reconstructed image of artificial crosslinkers (cyan) and F-actin (magenta) in mitotic cells (left). Distance between the peaks of the actin and artificial crosslinker fluorescence profiles across the cortex (right), defined as the overhang percentage between the two intensity profiles. Scale bar= 10 µm. Graph: mean Graph, ±1 mean standard deviation, 1 experiment. Statistics: Dataset did not pass the test for normal distribution and was thus compared with Mann-Whitney test.

To localise artificial crosslinkers within the actin cortex at a higher resolution, I used a protocol recently established in the lab [Truong Quang et al., 2021]. With this method proteins of interest can be localised with respect to the cortical actin using 2-colour STORM. In cells stably expressing artificial crosslinkers with GFP fluorescent proteins, I used a GFP booster nanobody conjugated to Alexa-647 and phalloidin conjugated to Alexa-568, and imaged midplane of cells synchronised in mitosis (see Methods). I then compared the overlap between actin and artificial crosslinker by comparing the distance between the peaks of transverse intensity profiles of these two proteins. Using a custom made MATLAB GUI [Truong Quang et al., 2021], I was able to measure the proportion of artificial crosslinker that did not completely overlap with actin and was instead shifted towards the cytoplasm (Figure 2.41). While the number of analysed cells was low in certain conditions due to technical challenges, there seemed to be no significant difference in the overlap of

the crosslinkers with the actin cortex between cells expressing artificial crosslinkers with different sizes. However, to confirm this a higher sample number is needed.

Technical difficulties that led to a low sample number were mainly due to the low labelling density of crosslinker which led to a low quality of reconstructed images. The image quality was often too low for analysis of the overhang of the artificial crosslinkers with actin. This low labelling density was most likely due to a low expression of crosslinkers which could be improved by transient transfection, yet this would also lead to fewer cells expressing artificial crosslinkers in the sample. While transient transfection might improve the signal in the future, the experimental complexity would increase due to a number of conditions that would need to be satisfied.

While it is difficult to conclude that there is indeed no difference in the overlap of the artificial crosslinkers with the actin cortex, these results would be somewhat consistent with the findings related to cortical tension and thickness in mitotic cells expressing artificial crosslinkers, where no difference in cortical tension or thickness was observed based on the size of the crosslinkers.

Alternative multi-colour super-resolution approaches for mapping actin binding proteins within the cortex

Although artificial crosslinkers with different sizes did not seem to localise differently with respect to the cortical actin, ideally I also wanted to map them with respect to each other and potentially other cortical components.

However, blinking, which is key to reconstruction of STORM images can only be achieved with certain fluorophores, which often limits STORM imaging to two colours. Blinking dynamics suitable for image reconstruction, required by STORM, can most easily be achieved with Alexa-647 and potentially Alexa-568. In our set up, achieving high quality two-colour STORM is challenging, particularly when other proteins than F-actin (labelled with phalloidin) are labelled with Alexa-568. Therefore, the localisation of crosslinkers with respect to other proteins than F-actin could only be inferred from their localisation with respect to F-actin. To be potentially able to directly localise artificial crosslinkers with respect to each other and with other actin-binding proteins, I thus explored other techniques for super-resolution imaging. Specifically, I tested DNA-PAINT and Expansion Microscopy (ExM).

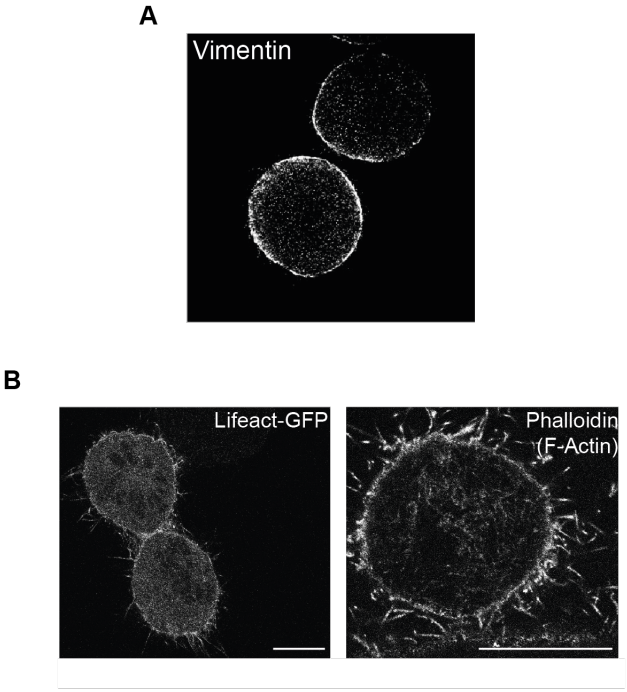

Figure 2.42: **DNA-Paint and Expansion Microscopy (ExM) of the cellular cortex.** (A) DNA-PAINT of cortical vimentin at a midplane of mitotic cell. (B) Expansion microscopy of cortical actin in mitosis imaged with scanning confocal microscope. Scale bar= 20 µm (approximate size of unexpanded cell).

DNA-PAINT uses DNA strands to link flourophores to the structures of interest [Jungmann et al., 2014]. Free floating imager strands conjugated to fluorophores transiently bind to complementary docking strands bound to molecules of interest via secondary antibodies. A blinking effect is achieved from the constant binding and unbinding of the imager and docking strands. This blinking is similar to that of photoswitchable dyes used for STORM and uses same reconstruction approaches. DNA-PAINT removes some of the limitations of STORM related to photoswitchable fluorophores. Constant influx of imager strands limits photo-bleaching. Therefore, the resolution can be increased by increasing the acquisition time. Additionally, while STORM mostly only works in two colours (568 and 647) there is no such limitation with DNA-PAINT. The number of proteins localised in a sample can be increased by washing and replacing the imager strands linked to the same fluorophore but complementary to docking strands labelling different proteins [Almada et al., 2019, Jungmann et al., 2014]. I thus tested DNA-Paint with a sub-cortical protein vimentin (Figure 2.42A), which was recently shown to localise just underneath the actin cortex in mitotc cells [Serres et al., 2020]. I decided to test vimentin because antibodies that lead to good labelling of vimentin are available commercially and the cortical

vimentin imaging with DNA-Paint could be compared to published STORM images of vimentin at the cortex of mitotic HeLa cells [Serres et al., 2020]. So far, DNA-PAINT was mostly used in TIRF mode, which only illuminates a layer closest to the coverslip while imaging of the cortex requires imaging of a midplane of a cell. Imaging of a midplane of a cell can be done in a HiLO mode, which increases signal to noise ratio of an image without limiting the distance from a coverslip at which sample can be imaged. In the DNA-PAINT set up, unbound imager strands freely float in the sample and can still be detected during image acquisition and thus increase background noise. The exposure of these free floating imager strands is higher in HiLO than TIRF mode, thus increasing the background noise. The increase in background noise requires an increase in imaging time for a similar resolution. It took more than 2h to acquire a single image of vimentin at the cortex as shown in Figure 2.42A. Therefore, using DNA-PAINT would require significant optimisation to decrease the imaging time. Additionally, the current lack of working antibodies against actin crosslinkers (Figure 2.1) is also a consideration in choosing DNA-PAINT. Labelling proteins of interest with different tags and applying imager strands to those would limit the number of proteins that can be imaged in the same sample. I thus decided against using DNA-PAINT for mapping of artificial crosslinkers within the cortex.

I also tested Expansion Microscopy (ExM) for localising actin binding proteins within the cortex at a higher resolution. For ExM, proteins in a sample are embedded in a hydrogel. This hydrogel gets physically expanded which increases the actual distances between embedded proteins. This allows for imaging of samples at a higher resolution with any microscope [Tillberg et al., 2016]. With ExM, samples can be labelled with antibodies either before or after expansion. The option of labelling after expansion would offer an interesting revenues for imaging of the actin cortex given how dense it is. Within dense structure the expansion prior to labelling can actually allow for labelling of features which are otherwise inaccessible by the antibodies.

To be able to use ExM for visualisation of actin cortex, I firstly focused on labelling F-actin. Classical phalloidin, which is most frequently used as F-actin label due to its good signal to noise ratio, does not work well in combination with ExM as it cannot get crosslinked in the hydrogel. So, to be able to visualise actin in expanded cells I tested alternative methods of labelling (Figure 2.42). I tested various actin antibodies however none yielded a strong specific binding with good signal to noise ratio. I obtained much better results with Lifeact-GFP. Lastly, Robert Neely (University of Birmingham) gifted

us a sample of a recently developed and at the time unpublished phalloidin specifically adjusted for the use in expansion microscopy [Wen et al., 2020] (Figure 2.42B, right). This label led to a good signal with scanning confocal microscopy (Olympus IX83) but could most likely be even better with Airyscan. I concluded that in the future ExM could be a good option for localising multiple actin binding proteins within the cortex.

Taken together, DNA-PAINT and particularly ExM offer alternative approaches to STORM, which would allow imaging of multiple proteins simultaneously at the super-resolution level and thus offer a further insight into nanoscale organisation of the actin-cortex and the role of the size of proteins for their localisation.

Overall, there are more than 922 proteins present in the actin cortex. During cell division, changes in levels of some of these proteins (eg. septins) affect mitotic cell shape. However, levels of known regulators of cortical tensions, actin crosslinkers, do not change in interphase and mitotic cortices. To ask which other protein properties, specifically its size, affect the role of crosslinkers could be regulated, we developed artificial crosslinkers. Given the dense, thin structure of the actin cortex, super-resolution techniques including STORM, DNA-PAINT or ExM will be key for investigating its organisation of dense and mapping the localisation of different cortical proteins and exploring the role of properties size or other properties.

Chapter 3

Discussion and Future directions

3.1 Experimental set-up for proteomic analysis of interphase and mitotic cortices

To identify proteins regulating cortical tension, we compared the proteomic composition of interphase and mitotic cortices. To this aim, we performed mass spectrometry on blebs isolated from interphase and mitotic cells. Isolated blebs were previously shown to re-assemble dynamic actin cortex similar to the cortex of the cells [Biro et al., 2013, Cassani, 2019]. For each of the bleb isolations used for mass spectrometry, I confirmed re-assembly of the actin cortex within the blebs by fluorescent staining (Figure 2.5). By using isolated blebs, we were able to enrich for the cortical components and detect differences in cortical levels of proteins not only due to overall differences in cellular levels [Heusel et al., 2020] but also due to changes in protein localisation (Figure 2.13). Isolated blebs also led to a more exhaustive list of cortical proteins compared to a previous proteomic characterisation of interphase and mitotic F-actin-binding proteins, where these were enriched for by a pull down of polymerised actin filaments [Serres et al., 2020]. Overall, by isolating blebs we successfully highly enriched for the cortex.

Interphase and mitotic cells were used because of established differences in cortical tension between these stages of the cell cycle [Chugh et al., 2017, Fischer-Friedrich et al., 2014, Serres et al., 2020, Stewart et al., 2011, Toyoda et al., 2017]. Due to their small size, measuring cortical tension of isolated blebs is challenging. However, blebs isolated from interphase cells exhibit less round shapes compared to blebs from mitosis. We hypothesised that these differences in shape indicate differences in cortical tension. These technical

challenges measuring cortical tension of isolated blebs by AFM might be overcome by replacing flat cantilevers (Figure 2.35) [Chugh et al., 2017] with wedged AFM cantilevers [Fischer-Friedrich et al., 2014]. Indeed, I worked with a Master student Garance Dombret on establishing a protocol for wedged cantilevers in the lab, however the project was interrupted by the COVID pandemic. Measuring the cortical tension of blebs will be an interesting future project.

The quantification of protein levels, obtained by mass spectrometry, applied in this project, is based on peptide-counting. While this approach was successfully used in the past for protein quantification, it is considered only semi-quantitative. Since samples are analysed separately in different mass spectrometry runs, detected differences between samples might be due to the mass spectrometry analysis and not biological differences [Lundgren et al., 2010]. To avoid this limitation, we initially planned to use Tandem Mass Tag (TMT) mass spectrometry, a quantitative mass spectrometry method in which peptides from different samples are tagged with a set of isotopic tags with the same mass and identical chemical structure [Dayon and Sanchez, 2009]. These tags allow for identification of the sample of origin for the peptides, even though peptides from different samples are analysed in the same mass spectrometry run. However, TMT requires a much higher (at least 5 times higher) starting protein amount (approximately 250 µg) compared to peptide-counting. Even for the semi-quantitative approach, we required 60 T175 culture flasks of cells as a starting material for a single replicate of blebs isolated from mitotic cells. Therefore, we concluded that using TMT without pooling across multiple biological replicates was impossible. The approach used still showed reproducible differences between biological replicates (Figure 2.12), suggesting that this is a good approach for identifying changes in protein levels between interphase and mitotic cortices.

3.2 Proteins detected by mass spectrometry

With the mass spectrometry, we identified 1793 proteins in interphase blebs and 2164 proteins in mitotic blebs. By narrowing down our list to proteins detected in both stages of the cell cycle and to actin related proteins, we eventually focused on septins and their role in regulating mitotic rounding. However, there are other proteins detected in this study that might be important in tension generation.

Overall, we identified 2268 different proteins in blebs. Firstly, we narrowed down this list to 922 proteins detected in both interphase and mitotic blebs (Figure 2.9A). With this step,

we excluded multiple nuclear proteins that were detected only in mitotic blebs. We did not focus on these proteins as we assumed their presence in the blebs was mainly an artifact of increased levels in the cytoplasm due to the nuclear envelope breakdown. Nonetheless, some of these proteins such as anillin [Field and Alberts, 1995] might translocate to the cortex during mitosis and have a role in organising the cortical actin network during cell division. Thus, an interesting avenue for the future is focusing on proteins detected only in either interphase or mitotic blebs and investigate their role in cortex tension generation.

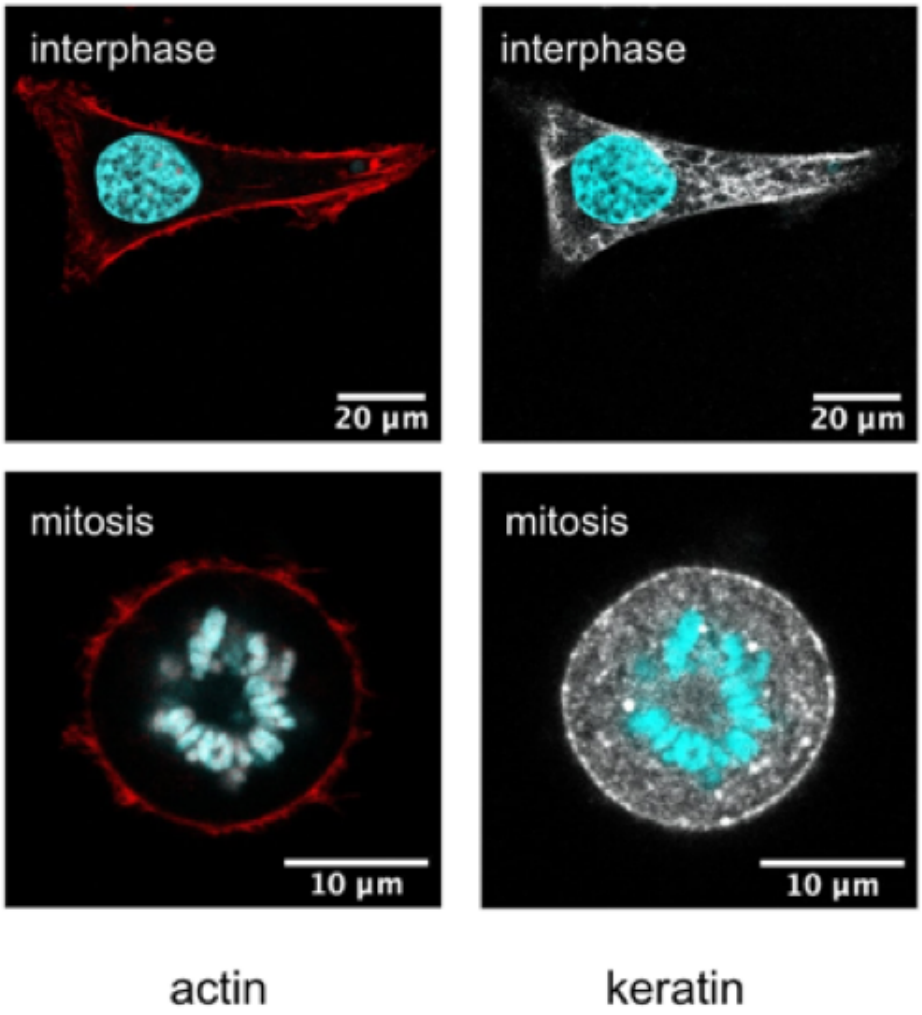

Figure 3.1: **Keratin localisation in interphase and mitotic cells.** Fluorescent staining of keratin in mitotic cells suggests cortical localisation. White= keratin, red= phalloidin. Acquired by Mark Carrington.

Among the proteins, detected in blebs that change in levels, were also other cytoskeletal proteins such as microtubules along with microtubule-binding proteins and intermediate filaments as well as trafficking proteins. While in this study, we focused on known actin-related proteins to identify new regulators of cortex mechanics, these other groups of

proteins represent other avenues for the future research. In particular, other cytoskeletal proteins are being increasingly shown to affect cortical mechanics [Dogterom and Koenderink, 2018, Duarte et al., 2019, Serres et al., 2020]. Even septins bind both microtubules and actin [Spiliotis, 2018]. The intermediate filament vimentin was recently shown to control actin cortex mechanics during cell division potentially by providing an additional structural support to the cortex [Duarte et al., 2019, Serres et al., 2020]. Interestingly, another intermediate filament, keratin, was detected in the blebs and various isoforms of keratin consistently increased in mitotic blebs compared to interphase blebs. When vimentin was identified as a cortical regulator through a previous proteomic screen, keratin was excluded as a potential contaminant [Serres et al., 2020]. Consistent increase of keratin in mitotic blebs within the triplicates, suggests that this increase might be an actual phenotype. Mark Carrington, whom I supervised during a rotation project, performed preliminary experiments to localise keratin within round mitotic cells and observed cortical localisation of keratin by immunostaining (Figure 3.1). Therefore, keratin might be another type of intermediate filaments besides vimentin, interacting with the actin cortex.

Finally, an interesting avenue for the future will be an investigation of how are the proteins detected in blebs regulated. The increase in protein levels in blebs can be due to increased expression of the proteins or due to protein translocation. A systematic comparison of changes in protein levels in cells vs blebs such as Figure 2.13 for all proteins detected in blebs will offer an insight into a reason for changes in protein levels between interphase and mitosis cortices. Additionally, understanding changes in the protein activity and not just their levels would offer a more comprehensive insight into a control of cortical tension. To this aim, phospho-proteomics of cortex enriched blebs will be an interesting avenue for the future which might firstly require additional optimisation of sample preparation.

Taken together, the mass spectrometry of isolated blebs from interphase and mitosis highlighted a number of proteins that changed in levels and might be important in tension regulation. In particular, the results suggest that multiple other cytoskeletal components interact with the actin cortex during cell division.

3.3 Septins as regulators of cortex mechanics

Through proteomic analysis of interphase and mitotic blebs, we identified septins, and particularly septin 9, as regulators of tension-driven mitotic rounding.

Septins are key regulators of cell division in yeast cells, where they form an hourglass structure separating the bud from the mother [Bridges and Gladfelter, 2015]. Over 60 proteins were shown to localise in a septin-dependant manner in yeast cell division, suggesting an important scaffolding property of septins. Septins were also shown to affect cell division of mammalian cells. Depletion in septins 2, 7, and 11 led to defects in cytokinesis and depletion in septin 9 delayed abscission [Estey et al., 2010]. But, although septins 2 and 9 seem to localise to the mitotic cortex [Estey et al., 2010], whether septins also affect the cortex and cellular shape during earlier stages of mammalian cell division has previously received little attention. In this project, I identified septin 9 as a regulator mitotic cell shape and the timing of mitotic rounding (Figure 2.16). I also investigated the role of septins 2, 7 and 8 during cell division and observed a difference in mitotic cell shape upon their depletion (Figure 2.19).

Septin 9 was the only member of SEPT3 family of septins detected in blebs. SEPT3 family is unique compared to other septin families because it only appears in septin octamers and not hexamers [Mostowy and Cossart, 2012, Spiliotis and Nakos, 2021]. Septin 9 and 6 are the only septins that were detected as monomers in mammalian cells. Additionally, septin 9 is the only septin paralogue with microtubule-binding motif and was shown to have an unique role during midbody abscission [Estey et al., 2010, Kim et al., 2011]. Septin 9 was also the only septin shown to consistently decrease mitotic rounding force [Toyoda et al., 2017]. Finally, only mouse null mutants of septin 9 and septin 7 were identified as embryonically lethal [Kinoshita, 2008]. Taken together, septin 9 might have a unique function also during mitotic rounding and metaphase.

Alternatively, septins normally assemble into heterohexamers and octamers and further into higher order structures such as filaments and rings. Therefore, different septins might affect cortex mechanics individually or as a complex. We briefly addressed this question by measuring the expression of septins by qPCR upon depletion of septin 2, 7, 8, and 9 but only detected slight changes in other septins (Figure 2.18). These results do not suggest any consistent compensation mechanisms between septins. However, qPCR only measures expression levels and other experiments will be required to investigate whether depletion of one septin affect cortical levels of other septins. This can be addressed through immunofluorescent staining of the septins upon depletion of other septins. However, I was not able to find good commercially available antibodies for multiple different septins and previous studies mostly used custom made antibodies against septins [Estey et al., 2010,

Spiliotis et al., 2005].

Given the different structures that septins can form and their interactions with multiple components of the cytoskeleton, unveiling the precise molecular mechanisms of how they affect mitotic cell shape will be challenging. Septin oligomers have multiple actin-binding domains and the complex can then act as an actin crosslinker [Spiliotis and Nakos, 2021]. Septin filaments and rings might provide structural support similar to vimentin [Serres et al., 2020]. Of note, septins also bind microtubule filaments [Spiliotis, 2018] and although whether interactions with microtubules affect cortical tension is not yet understood, septins might play a role in this interaction. Finally, septin 2 was shown to colocalise with NMII in dividing cells and potentially acts as a scaffold to promote myosin phosphorylation during division [Joo et al., 2007] and septins can also interact with other actin regulators such as anillin or cofilin [Kinoshita et al., 2002, Smith et al., 2015]. Better characterisation of septin interaction with anillin in mammalian cells will be important for understanding how septins affect cortical actin and the regulation of cortical levels of septins during the cell cycle.

I briefly investigated whether septins affect cortical mechanics through actin organisation by measuring cortical thickness in cells depleted in septin 9 and septin 7 (Figure 2.17, 2.20). Only a potentially mild increase in cortical thickness upon septin 9 depletion suggests that changing actin organisation is not the main mechanism through which septins control cortex mechanics. In the future, the affect of septins on other properties of actin architecture as well as other actin binding proteins, in particular myosin will need to be examined to understand how septins affect cortex mechanics.

Taken together, in this project I showed a role for septins in controlling cortex mechanics. Investigating the mechanisms by which septin control cortex mechanics will be an interesting avenue for future studies.

3.4 The potential of artificial crosslinkers to study the role of the size in actin networks and beyond

In the second part of this thesis, I described the development of artificial crosslinkers and the (preliminary) findings on their role in cortex tension generation and their cortical localisation. We developed artificial crosslinkers by utilising D18 repeat domains, which allowed me to change the size of the protein independently of other properties. These ar-

tificial crosslinkers are between ~ 5 and ~ 35 nm long (Figure 2.22). Artificial crosslinkers also have an actin-binding domain and a fluorescent protein sequence. Due to unique restriction sites, artificial crosslinkers can be easily modified (Figure 2.23, 2.29, 2.28). We created artificial crosslinkers to investigate the role of the size of actin crosslinkers in their localisation within the cortex and the role in tension generation independently of other features. The range of sizes of artificial crosslinkers allows us to examine the artificial crosslinkers comparable in size to small actin crosslinkers (eg. fascin and plastin), and medium-sized crosslinkers (eg. alpha-actinin).

Through tension measurements by AFM, I only observed differences in cortical tension between cells expressing artificial crosslinkers and control untransfected cells, but no differences related to the size of the crosslinkers. To confirm that the observed differences to control cells are due to the crosslinking of artificial crosslinkers, their effects will need to be compared to the effects of just the ABD in the future.

I also compared the effects of artificial crosslinkers with different sizes on the division dynamics of cells expressing artificial crosslinkers. Similarly to tension, I did not observe any differences in the time cells expressing different crosslinkers took to round up. I also tested whether artificial crosslinkers affect cleavage furrow ingression during cytokinesis which is a process driven by gradients in cortical tension [Maddox and Burridge, 2003, Matzke et al., 2001]. During furrow ingression, the cortex also has different organisation at the cell poles vs the furrow. I quantified the furrow ingression time and only observed minor differences between crosslinkers with different sizes (Figure 2.34). I also observed some differences in a mitotic cell shape in 2D of cells expressing artificial crosslinkers with different sizes. In these experiments, I only compared the effects different crosslinkers had on cell division dynamics since the main focus of this study was to compare the roles of different crosslinker sizes in the cortex. However, for a better characterisation of the crosslinking activity of the artificial crosslinkers, it will be interesting to compare division dynamics of cells expressing artificial crosslinkers to the cells expressing only ABDs used in the artificial crosslinkers. While I only examined the localisation of artificial crosslinkers in a low number of cells due to experimental complexity, the preliminary findings do not show any differences between differently sized crosslinkers. Overall, artificial crosslinkers of different sizes do not majorly differ in their effects on mechanical properties of the dividing cells.

While artificial crosslinkers of different sizes seem to only minimally affect division dy-

namics of unconfined cells in culture, any differences might be more prominent under confinement. The actin cortex is particularly important in ensuring successful and normal cell division on cells in confined environments [Lancaster et al., 2013]. Compression of the cells increased the severity of division-related defects such as multipolar spindles, chromosomal bridges, chromosomal lagging and unsuccessful segregation upon depletion of vimentin [Serres et al., 2020]. So far, I only examined the effects of different sizes of crosslinkers on mitotic rounding and cleavage ingression, while cortex-related defects also include other phenotypes such as unsuccessful spindle formation or chromosomal missegregation [Cadart et al., 2014]. Therefore for broader understanding of the role of crosslinker size on mechanics of cell division, their effects on cells under the confinement, and a wider range of division related phenotypes will be important to consider.

The data with artificial crosslinkers similar in size to small (fascin, plastin) and intermediate (alpha-actinin) crosslinkers suggest that the size of the crosslinkers does not majorly affect their localisation within the cortex and role in cortical tension generation. However, before concluding that crosslinkers do not segregated within the cortex due to their size, it will be important to include bigger artificial crosslinkers (eg. $\sim$ 100 nm long, similar to filamin) to the comparison of crosslinkers with different sizes. Larger differences in the length of crosslinker were predicted to lead to a higher capacity of crosslinker sorting [Freedman et al., 2019]. However, artificial crosslinkers, we generated, will not enable us to test the size of bigger actin crosslinkers because they are predicted to start bending at $\sim$ 18 repeats (35 nm), which effectively decreases the distance between ABDs.

So far, I have only focused on the role of the size of the artificial crosslinkers within the actin cortex. No obvious differences in the localisation of artificial crosslinkers with different sizes were observed in spread cells imaged through a scanning confocal microscope (Figure 2.27). However, spread HeLa TDS cell used in these experiments have relatively irregular shapes which makes actin distribution hard to compare. Therefore, to be able to compare and quantify potential differences in localisation of the artificial crosslinkers within different actin structures of spread cells, cell shape will need to be standardised. This can be achieved by plating cells expressing differently sized artificial crosslinkers on micropatterns [Théry, 2010]. While some differences in the localisation of artificial crosslinkers within different actin structures of spread cells may be observed by confocal microscopy when using the micropatterns, some differences may only be detectable at the nanoscale. Super-resolution microscopy will allow us to also investigate nanoscale differ-

ences within individual fibres and potential size exclusion of differently sized crosslinkers to the edges of individual actin bundles. Other factors such as bundling affinity or binding dynamics and actin polymerisation rate in non-equilibrium systems alongside the protein size might drive segregation of crosslinkers observed *in vitro* [Freedman et al., 2019, Winkelman et al., 2016]. However, protein size is also predicted to be important during other biological processes such as during macrophage phagocytosis or for T cell receptor triggering of intercellular signalling [Bakalar et al., 2018, Davis and van der Merwe, 2006]. Therefore, employing artificial crosslinkers to understand the role of the size in different actin structures will be an interesting avenue for the future.

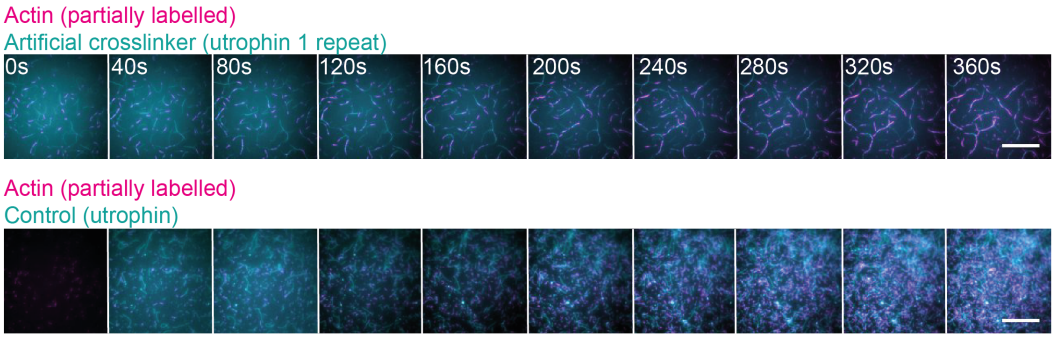

Figure 3.2: ***In vitro* actin bundling by artificial crosslinkers.** Purified artificial crosslinker (1 repeat utrophin ABD) bundles actin (top) in reconstituted system. Just utrophin ABD (bottom) did not bundle actin. Actin filaments are only partially labelled. Scale bar= 50 µm. Experiments were performed in collaboration with Antoine Jégou at Institut Jacques Monod, Paris.

Artificial crosslinkers offer a novel approach to investigate the role of protein size within different actin networks in cells. However, artificial crosslinkers are synthetic proteins and their size was only computationally predicted. We cannot visualise individual artificial crosslinkers within mammalian cells and measure their actual size. To measure the actual size of the artificial crosslinkers, they will need to be purified. Indeed, we included a His-tag into the original sequence for artificial crosslinkers to allow for their purification. We also established a collaboration with Guillaume Romet-Lemonne and Antoine Jégou from Institut Jacques Monod and are currently working on purifying the artificial crosslinkers. Besides the size measurements, we will also be able to use purified artificial crosslinkers to investigate the role of their size within *in vitro* actin networks (Figure 3.2) and thus investigate their role and ability to segregate independently of other cytoskeletal proteins or other properties than the size.

Finally, the nucleotide sequence for artificial crosslinkers includes multiple restriction sites, which allow us to modulate crosslinker size (Figure 2.24), ABD (Figure 2.28) or fluorescent

protein sequence (Figure 2.29). While I have already utilised these to make bigger artificial crosslinkers, to replace Lifeact ABD with utrophin ABD, and to replace GFP with RFP, these unique restriction sites can be used even more broadly. Firstly, we can modulate promoter sequence to allow for chemical or optogenetic induction of transcription and thus more precise control of expression. ABD can also be swapped for a different sequence not just for binding actin but also other cellular components. In this way, artificial crosslinkers can be repurposed to explore the organisation of other cellular components. Taken together, artificial crosslinkers can be a versatile tool broadly used to investigate the organisation of the actin cortex, other actin structures or even other features of the cells.

3.5 Towards a map of nanoscale organisation of the cortex

In this project, I identified a number of proteins present in the cortex and I explored how the size of actin-binding proteins affects their cortical localisation. However, protein size is not the only feature driving protein localisation and actin-network organisation [Christensen et al., 2017, Freedman et al., 2019]. Therefore, to understand how actin cortex is organised at the molecular level, a map of the nanoscale organisation of the actin cortex and localisation of different groups of cortical proteins similar to a map of cell adhesions [Kanchanawong et al., 2010], will most likely offer an additional insight into the control of cortex dynamics.

A few proteins have already been localised within the actin cortex and were shown to localise differently within the actin cortex at the nanoscale level by STORM [Truong Quang et al., 2021]. However, due to chemical limitations which make STORM buffers most compatible with only a few dyes, cortical proteins can only be localised with respect to actin using this approach. To be able to image multiple proteins simultaneously, I tested two other super-resolution approaches, DNA-PAINT and Expansion Microscopy (ExM) (Figure 2.42), which can be used to label multiple structures on the same sample.

DNA-PAINT uses a similar imaging set-up to PALM/STORM however the labelling approach is different. Proteins are labelled by unique DNA strands while the same fluorphore can be used for as many proteins as needed [Tillberg et al., 2016]. When I tested DNA-PAINT for imaging the actin cortex the major issue was backround fluorescence signal from free floating imager DNA strands. The actin cortex of mitotic cells is imaged at the cellular midplane, which is ~ 10 µm above the coverslip. Imaging at this height cannot be

done in TIRF modality, which reduces the amount of background from free-floating DNA strands. Therefore, I concluded that for imaging of the actin cortex by DNA-PAINT, substantial optimisation will be required. New approaches to DNA-PAINT, such as that using FRET-based probes [Auer et al., 2017], where a DNA-PAINT imager strand acts as a donor to DNA-PAINT docking strand, might be successful in reducing the background during mid-plane imaging of the cell cortex.

Additionally, I tested ExM as a potential approach for visualising multiple actin binding proteins simultaneously. ExM improves the resolution of the sample by increasing a physical distance between structures of interest and as such can be used with conventional light microscopes [Asano et al., 2018]. In ExM, proteins are labelled following standard immunofluorescent labelling protocols. ExM samples can either be labelled pre- or post-expansion. In particular, post-expansion labelling creates extra space for the antibodies to bind and was recently used to visualise protein organisations within dense cellular structures where in non-expanded samples antibodies for different proteins compete for the space [Gambarotto et al., 2018]. Given the density of the actin cortex, such approach might offer additional insight into the localisation of cortical proteins.

3.6 Conclusions

While cortical tension is mainly controlled by NMII, more recently actin organisation was also shown to be important in controlling cortical tension [Chugh et al., 2017]. Cortical organisation can be controlled by a range of factors.

In this thesis, I systematically identified proteins present in the cortices from interphase and mitosis, which differ in tension. By showing that one of the proteins, septin 9, changes in levels between these two states actually affects cell shape, I demonstrated the potential of this dataset to identify regulators of cortical tension. Overall, I created a resource to facilitate the understanding of which proteins affect cortical tension through changes in their cortical levels.

Additionally, I have created artificial crosslinkers to examine how differences in the size of the actin crosslinkers affects their localisation and role in tension generation independently of other properties. So far, I have not detected major differences in the cortical localisation and tension based on the size of the artificial crosslinkers. However, artificial crosslinkers can be used to explore the organisation of the other actin structures as well as expanded

to other cellular components.

Taken together, here I show the role of molecular (protein levels) and physical (protein size) mechanisms at the nanoscale in controlling the organisation and the tension of the actin cortex.

Chapter 4

Materials and Methods

4.1 Cell culture and cell lines

4.1.1 Cell culture conditions

HeLa cells from MPI-CBG Technology Development Studio (TDS) were cultured in DMEM Glutamax (Thermo Fischer Scientific) supplemented with 10 % fetal bovine serum (FBS) (Thermo Fischer Scientific), 1 % Penicillin-Streptomycin (Thermo Fischer Scientific), and 1 % L-Glutamine (Thermo Fischer Scientific). For passaging, cells were detached from culturing flasks with Trypsin-EDTA (Thermo Fischer Scientific). Cells were regularly tested for mycoplasma. Cells were cultured at 37 °C with 5 % CO_2.

4.1.2 Plasmid and siRNA transfection

For siRNA depletion, cells were transfected with Lipofectamine RNAiMAX Transfection Reagent (Thermo Fischer Scientific) and siRNA molecules in OPTIMEM medium. Per 1 well of a 6 well plate, 4 µL of 20 µM stock siRNA was incubated with 4.5 µL Lipofectamine RNAiMAX in 530 µL OPTIMEM for 15 min before transfection. SiRNA molecules used: ON-TARGET plus Human SEPT9 pool siRNA (Horizon Discoveries, 006373-00), ON-TARGET plus Human SEPT2 pool siRNA (Horizon Discoveries, 010614-00), ON-TARGET plus Human SEPT7 pool siRNA (Horizon Discoveries, 011607-00), ON-TARGET plus Human SEPT8 pool siRNA (Horizon Discoveries, 010647-00), and Non-targeting Control pool (Horizon Discoveries, 001810-10).

Plasmids were transfected with Fugene HD Transfection Reagent (Promega) in OPTIMEM medium. For plasmids with artificial crosslinkers 2 µg plasmid DNA, 6 µL Fugene, 500

µL OPTIMEM per each well of a 6-well plate were incubated for 15 min before transfection. Plasmids used are listed in Table 2.3. Artificial crosslinker sequences commercially synthesised are stated in Appendix A.

4.1.3 Stable cell lines

Polyclonal HeLa TDS stable lines with artificial crosslinkers were created through transient transfection of 10 µg of plasmid DNA and 30 µL of Fugene HD Transfection Reagent and selection with geneticin (0.5 mg/mL in culturing medium).

4.1.4 Cell synchronisation

Cells were synchronised in interphase with 2 mM thymidine for approximately 22 h, and in prometaphase with 2 µM S-Trityl-L-cystine (STLC) for 16 h. Mitotic cells were further enriched for with a mitotic shake-off.

4.2 Bleb isolation

Thymidine and STLC were removed from the cells at the beginning of the bleb isolation. Blebs were isolated from either mitotic cells synchronised with STLC and detached with a mitotic shake-off or cells synchronised in interphase with thymidine and detached with trypsin (at 37°C). Trypsin was deactivated with cell culturing medium, followed by centrifugation at 164 g for 3 min, and exchanging medium for fresh culturing medium. Blebbing was induced by addition of either 1.7 µM (interphase) or 2.4 µM (prometaphase) Latrunculin B (Sigma Aldrich), immediately followed by shaking on a horizontal benchtop shaker for 15 min at room temperature to detach the blebs from the cells. Latrunculin B was then washed out through centrifugation of isolated blebs (and cells) at 4410 g for 6 minutes and re-suspended in intracellular buffer (0.01 M sodium chloride, 0.28 M pH 7.2 L-glutamic acid, 0.014 M magnesium sulphate, 0.013 M calcium chloride, 0.020 M pH 6.8 EGTA, 0.04 % M pH 7.2 HEPES, in dH2O, potassium hydroxide was used to adjust the pH). To separate entire cells and isolated blebs, cells were firstly pelleted with a 4 min centrifugation at 100 g. The supernatant was then filtered with 5 µm Satorious Minisart filters (FIL6602, Minisart) to remove the remaining cells and any larger debris. Collected blebs were then pelleted with a centrifugation at 16100 g for 5 min and incubated in a solution containing an exogeneous ATP regeneration system (energy mix) and alpha-toxin to permeabilise the bleb membrane (5 % A-Hemolysin alpha-toxin (1 mg/mL; H9395, Sigma Aldrich), 2 % energy mix (50 mg/mL UTP, 50 mg/mL ATP, 255 mg/mL creatine

phosphate), 2 % creatine kinase (10 mg/mL), in intracellular buffer) for 10 min, followed by centrifugation at 16100 g for 5 min and resuspended in 500 µL re-suspension buffer (50 % intracellular buffer, 44 % dH20, 1 % energy mix, 5 % creatine kinase) for 20 min.

4.3 Mass spectrometry and analysis

4.3.1 Mass spectrometry

To obtain sufficient material for mass spectrometry analysis, isolated blebs were prepared using 15 T175 flasks of cells synchronised in interphase and 60 T175 flasks of cells synchronised in mitosis, in three experimental replicates for each phase of the cell cycle. Purified blebs were lysed directly in the Laemelli sample buffer. For mass spectrometry analysis, Coomassie-stained gel bands were excised and subjected to in-gel trypsin digestion, as described previously [Carrière et al., 2008]. The resulting peptides were extracted and subjected to capillary liquid chromatography (LC)-tandem mass spectrometry (LC-MS/MS) using a high-resolution hybrid mass spectrometer LTQ-orbitrap XL (Thermo Fisher Scientific). Experiments were performed in triplicates. Database searches were performed against The Uniprot SwissProt Human database (containing 20 347 protein entries) using PEAK Studio (version 8.5) as a search engine, with trypsin specificity and three missed cleavage sites allowed. Methionine oxidation, Lysine acetylation, Cysteine carbamidomethylation, Serine/Threonine/Tyrosine phosphorylation and asparagine/glutamine deamidation were set as variable modifications. The fragment mass tolerance was 0.01 Da and the mass window for the precursor was ± 10 ppm. The data were visualised with Scaffold (version 4.8.6) and the minimum number of peptides per protein was set to 2 for data analysis. Spectral counts for each protein was divided by the total number of peptides detected in the specific replicate considered and multiplied by the total number of peptides detected in the first interphase replicate to normalise for experimental variation between replicates. Mass spectrometry was performed by Dr.Geneviève Lavoie and proteomic analyses were performed at the Center for Advanced Proteomics Analyses (CAPCA).

4.3.2 Gene Ontology and candidate list curation

For Gene Ontology (GO) analysis, the statistical overrepresentation test function from PantherDB (http://www.pantherdb.org/) was used. Actin-related proteins from the bleb extracts were identified by comparing the list with previous mass spectrometry analysis

of the F-actin interactome in interphase and mitotic cells [Serres et al., 2020], and by manually adding known actin related proteins.

4.4 Western blots

4.4.1 Sample preparation for western blots

Cells were lysed directly in Laemelli sample buffer. To remove DNA, samples were boiled at 95°C for 10 min and sonicated for 15 min in 30 s ON, 45 s OFF cycles. Protein concentrations were measured with Pierce 660 nm Protein Assay (Thermo Fischer Scientific, catalogue number: 22660). Unless specified, the same amount of samples (30 µg) was loaded.

4.4.2 Western blots and transfer to the membrane

Samples were loaded NuPage 4-12 % Bis-Tris Protein gels (Thermo Fischer Scientific) or 4–15 % Mini-PROTEAN TGX Stain-Free Protein gels (Biorad) and run respectively at 80 V for 30 min followed by 130 V for 90 min or 200 V as per the manufacturer's instructions. Proteins were transferred to a nitrocellulose membrane (Thermo Fischer Scientific) using the BioRad transfer system at 100 V for 60 min at 4 °C or with Trans-Blot Turbo Mini PVDF Transfer Packs using Trans-Blot Turbo Transfer System (Biorad). The membrane was blocked for 30 min with the Odyssey Blocking Buffer (TBS) (Licor). For fluorescent western blots, PageRuler Prestained NIR Protein Ladder were used and for ECL, PageRuler Plus Prestained Protein Ladder were used.

4.4.3 ECL and fluorescent western blots imaging

Most of the membranes were imaged using Odyssey fluorescent imaging system but some were visualised on film using an ECL system (Figure 2.6). In both cases, membranes were stained overnight with primary antibodies at 4 °C, followed by 3 washes with PBS and 0.1 % tween (PBST). Incubation with secondary antibodies was done at room temperature for 1-2 h.

4.4.4 Fluorescent western blots analysis

Fluorescent signal on western blots was quantified using Image Studio Lite (Licor). For median background estimation only the top and bottom option was selected for signal calculation. Unless specified differently, GAPDH was used as a loading control.

4.4.5 Antibodies for western blots

For western blots, primary antibodies were diluted in in 5 % milk in PBS with 0.1 % tween and diluted 1:1000 from manufacturer's concentration unless specified differently. The following primary antibodies were used for probing of western blot membranes: phospho-histone H3 (Cell Signalling, 9713S, 1:500 dilution), beta-actin (Santa Cruz Biotechnology, 47778), cyclin B (Santa Cruz Biotechnology, 245) septin 9 (Sigma-Aldrich, HPA042564), GAPDH (Abcam, ab8245, 1:5000 dilution) , filamin A (Santa Cruz Biotechnology, 28284), ezrin-radixin-moesin (Cell Signalling, 3142), myosin RLC (Cell Signalling, 3672), phospho-myosin RLC (Cell Signalling, 3675), Histone H3 (Abcam, 1791), alpha-actinin 1 (Abcam, ab18061), GFP (Chromotek, 3h9).

For fluorescent western blots secondary staining goat anti rabbit and goat anti mouse IRDye 800 CW or 680RD (Licor) secondary antibodies were diluted 1:5000 from stock.

4.5 Quantitative polymerase chain reaction (qPCR)

Cells were collected 24 and 48 hours after siRNA treatment and the total RNA was extracted using RNeasy mini Kit (Qiagen). Reverse-transcription was done with the cDNA Reverse Transcription Kit (Applied Biosystems), as per manufacturer's instructions. For each qPCR assay, a standard curve was performed to ensure that the efficacy of the assay. The Viia7 qPCR instrument (Life Technologies) was programmed with an initial step of 20 s at 95 °C, followed by 40 cycles of 1 s at 95 °C and finally 20 s at 60 °C was used to detect amplification level. Relative expression was calculated using the Expression Suite software (Life Technologies), and normalised using ACTB and GAPDH. The following primers were used for expression measurements: SEPT2 forward- AAGGCAATACACAACAAGGTGA, reverse- TTCTTCAATTTCATCCAGAATCC; SEPT6 forward- TCGTCCAGCGAGTCAAAGAG, reverse- TCTCGTCCTGGTGCAGTTTC; SEPT7 forward- GAAGTTAATGGCAAAAGGGTCA, reverse- TCAAGTCCTGCATGTGTGTTC; SEPT8 forward- TTC AGGACAGCGATGGTGAC, reverse- CTCCTTCCTCTGCAGCTCAC; SEPT9 forward-CGGGACCTTCTCATCAGG, reverse- GGTACGCCTCGAAGTGGAT; SEPT10 forward-GTTGCTTCTGCCCTCCGG, reverse- CGGTGAAGCGGCTGTATCAG; SEPT11 forward-TTACTACAGTCCCAGGCCCA, reverse- TGGCTTGCCAGGCTTTATGT. ACTB and GAPDH were used as endogenous controls using the following primers ACTB forward-CCATCTACGAGGGGTATGCC, reverse- GCGCTCGGTGAGGATCTTC; GAPDH forward-AGCCACATCGCTCAGACAC, reverse- GCCCAATACGACCAAATCC.

4.6 Design of artificial crosslinkers

Artificial crosslinkers were designed using Elfin database [Yeh et al., 2018, 2020] by Fabio Parmeggiani. Proteins were designed based on previously published sequences [Baker et al., Brunette et al., 2015, Fallas et al., 2016, Parmeggiani et al., 2015].

4.7 DNA cloning

Plasmids with artificial crosslinkers with 1 repeat and 7 repeats and lifeact ABD as well as the insert plasmid with 6 repeats (Figure 2.23) were commercially synthesised (Thermo Fischer). Sequences are stated in Appendix A.

4.7.1 Polymerase chain reaction (PCR)

To replace Lifeact ABD with utrophin ABD and GFP with mCherry DNA sequences via cloning, appropriate restriction sites were introduced to the utrophin and mCherry sequences via polymerase chain reaction (PCR).

To modify the utrophin sequence a pCS2-Gfp-UTR (Utr-CH) plasmid (a gift from Marie Terret) was used. To introduce HindIII and BamHI restriction sites, the combination of forward (AGCTTCAAGCTTATGGCCAAGTATGGAGAACATGA) and reverse (GCTACAGGATCCGTCTATGGTGACTTGCTGAGGTAG) primers was used with Taq polymerase (NEB, M0273). The temperature of the cycles was optimised with touchdown PCR starting for 30 s at 95°C, followed by 12 cycles of 25 s 95 °C, 45 s at 68 °C (with 1°C decrease in each cycle), followed by 10 cycles of 30 s at 95 °C, 45 s at 56 °C, 45 s at 68 °C, completed by 5 min elongation at 68 °C.

To introduce KpnI and XhoI sites into the mCherry sequence, the plasmid pH2B-mCherry-IRES-puro2, (a gift from Daniel Gerlich, Addgene plasmid number 21045), was used with a combination of forward (AACGGGGTACCAGCGGAATGGTGAGCAAGG) and reverse (ATCCGGCCTCGAGCTTGTACAGCTCG) or forward (AACGGGGTACCAGCGGAATGGTGAGCAAGGGCGAG) and reverse (ATCCGGCCTCGAGCTTGTA CAGCTCGTCCATGCC). The sequence was amplified with Taq polymerase following the manufacturer's procedure starting at 95 °C for 30s, followed by 35 cycles of 30 s at 95 °C, 1 min at 62 °C and 30 s at 68 °C, completed by 5 min elongation at 68 °C.

4.7.2 Restriction and ligation reactions

To create plasmids with 12 or 18 additional D18 domains, an insert plasmid with 6 repeats (Figure 2.23B) was cut with BamHI-HF and BsaI restriction enzymes and pcDNA 3.1+ plasmid with 7 or 13 repeats was cut with BamHI-HF and NheI-HF using Cutsmart (NEB) buffer via 1 h incubation at 37 °C. Products were run on the agarose gel, the insert and the main plasmid were excised and ligated with T4 ligase for 15 min. The correct size of the cloned plasmids was confirmed by restriction reaction with PstI (13 repeats), and NheI-HF with BsrGI, and BamHI-HF with BsrGI for 19 repeats. When cloning additional repeat domains bacterial transformations were performed with Stbl2 bacteria at 30 °C.

To replace Lifeact with utrophin, plasmids containing Lifeact and PCR products of utrophin were cut with HindIII-HF and BamHI-HF, followed by size separation of restricted products on an agarose gel and excision. Similarly, to replace GFP with mCherry, plasmids and mCherry PCR product were cut with KpnI-HF and XhoI. In both cases, Cutsmart buffer was used and restriction reaction was carried out for 1 h at 37 °C. Restricted inserts and plasmids were ligated with T4 ligase.

To facilitate the cloning, Snapgene software was used to simulate the separation of DNA fragments on agarose gels and predict products of restriction-ligation reactions.

4.7.3 Sanger sequencing

Cloning of utrophin and mCherry in the plasmids with artificial crosslinkers was confirmed with Sanger sequencing. Due to a high number of repeat domains cloning of additional repeats could not be confirmed with Sanger sequencing. Sanger sequencing was commercially performed using standard primers T7 forward and CMV forward for utrophin and BGH reverse sequencing primers for mCherry. Sequence allignments were done with Snapgene software (www.snapgene.com).

4.8 Microscopy

4.8.1 Fixed sample preparation

Isolated blebs and round cells (in suspension) (from experiments in Figure 2.2) were spun on poly-L-lysine coated 25 mm coverslips by centrifugation at 460 g for 10 min. Cells were fixed with 4 % paraformaldehyde (PFA) in PBS for 10 min, followed by 10 min permeabilisation with 0.2 % Triton X-100 at room temperature. Blebs were fixed with

combined permeabilisation-fixation for 6 min with 4 % PFA in intracellular buffer with 0.2 % Triton X-100 followed by 14 min fixation with 4 % PFA in intracellular buffer at room temperature, followed by three washes with PBS. Samples were stained with DAPI and Phalloidin-AlexaFluor-568 (1:500 dilution) for 1 h, followed by three washes with PBS.

Fo experiments in Table 2.1 and Figure 2.1 where different antibodies against actin crosslinkers were tested, the first fixation approach tested was with paraformaldehyde (PFA) in cytoskeleton buffer with sucrose (CBS), following a protocol previously used in the lab for the staining of the actin cortex. Specifically, samples were firstly incubated with 4 % PFA in CBS (10 mM MES, 138 mM KCl, 3 mM MgCl2, 2 mM EGTA, in H20, pH 7.4, and 4.51 % sucrose) with 0.2 % Triton X-100 for 6 min followed by 14 min fixation in 4 % PFA in CBS. The same fixation was also tested with PHEM buffer (60 mM PIPES, 25 mM HEPES, 10 mM EGTA, 2 mM MgCl2) in place of CBS.

For glutaraledhyde fixation the following methods were tested with CBS and PHEM buffers: 0.2 % glutaraldehyde 0.1 % Triton X-100 fixation for 10 min, followed by 15 min quench (1 mg/ml 0.1 % NaBH4) and 15 min block (3 % bovine serum albumin-BSA in PBS); 2 % glutaraldehyde 1 % Triton X-100 fixation for 15 min, followed by 15 min quench (1 mg/ml 0.1 % NaBH4); 1 % glutaraldehyde 0.2 % Triton X- 100 fixation for 15 min, followed by 15 min quench (1 mg/ml 0.1 % NaBH4); 0.1 % glutaraldehyde with 1 % paraformaldehyde, and 0.3 % Triton X-100 for 1 min followed by 10 min 0.5 % glutaraldehyde.

In these experiments testing different antibodies against actin crosslinkers after fixation, cells were blocked with 3 % bovine serum albumin (BSA) and 0.01 % Triton X-100 diluted in PBS for 30 min at room temperature. This was followed by 1 h incubation with primary antibody (diluted 1:100 in PBS 0.01 % Triton X-100) at room temperature. Incubation with secondary antibody (1:250 dilution), DAPI (1:10000 dilution), and phalloidin conjugated to Alexa fluorphores (1:500 dilution) was also carried out at room temperature for 1 h. Coverslips with samples were sealed on the glass slides with Vectashield.

For super-resolution (STORM) experiments, samples were fixed for 6 min with 4 % PFA in CBS (10 mM MES, 138 mM KCl, 3 mM MgCl2, 2 mM EGTA, in H20, pH 7.4, and 4.51 % sucrose) with 0.2 % Triton X-100 followed by 14 min with 4 % PFA in CBS and further permeabilised for 10 min with 0.5 % Triton X-100 in PBS. Samples were blocked for 30 min in 5 % BSA in PBS before staining.

4.8.2 Laser scanning confocal microscopy of fixed samples

Samples from Figure 2.2, 2.5 were imaged with an Olympus FluoView FV1200 Confocal Laser Scanning Microscope using a 60x oil objective (NA 1.4). Samples in Figure 2.1 were imaged using an Olympus FluoView FV1200 Confocal Laser Scanning Microscope using a 60x oil objective (NA 1.4) and a Leica TCS SP5 Confocal Microscope with Leica DMI6000 microscope using 63x oil objective (NA 1.4). Samples in Figure 2.27 were imaged with a Leica TCS SP8 Confocal Microscope 60x oil objective (NA 1.4).

4.8.3 Live imaging and analysis of cell shape and timing of division

30 min prior to live imaging, the culture medium was changed to Leibovitz's L-15 (Thermo Fischer Scientific) medium supplemented with 10 % FBS and 1 % Penicillin-Streptomycin. If samples were transfected with plasmids or siRNA, this treatment was performed 24 h prior to imaging.

In Figures 2.16, 2.33, 2.34, cells were imaged for 15h at 37°C every 2 min on an inverted Olympus IX81 microscope, controlled via Velocity interface, and a Hamamatsu Flash 4.0v2 sCMOS camera. Imaging was performed with the brightfield setting under a 20x air objective. Cell shape was analysed with manual segmentation using the measure feature of the FIJI image analysis software [Schindelin et al., 2012]. Mitotic cell shape was measured in the cellular mid-plane, at the last frame of metaphase, i.e. the last frame where aligned chromosomes were observed, prior to anaphase onset and chromosome segregation.

In Figure 2.25, cells were imaged with an Ultraview Vox Microscope consisting of Nikon TiE inverted stand attached to a Yokogawa CSU-X1 spinning disc scan head with a Hamamatsu C9100-13 EMCCD detector controlled by Velocity software. Cells were imaged fo 15 h at 37 °C every 2 min with 488 nm and 569 nm laser.

In Figures 2.26 and 2.31, cells were imaged with an inverted Olympus IX81 microscope, controlled via Velocity interface, and a Hamamatsu Flash 4.0v2 sCMOS camera with CSU-X1 Spinning Disk head and Perkin Elmer MLS1 base laser engine. Samples were imaged with 488 nm laser every 3 min overnight.

4.8.4 Quantification of cortical levels of artificial crosslinkers during cell division

To measure fluorescent intensity along the cortex contour maximum projections of Z-stacks acquired in 2 µm Z-steps with a spinning disk confocal microscope were used. The fluorescent intensity of artificial crosslinkers along the cortex of live cells undergoing division was measured by firstly segmenting the cortex using the FIJI plug in JFilament [Smith et al., 2010]. The 2D modality of JFilament 2D was selected and curve type was set to contour. The following parameters were used for segmentation in each time frame: alpha- 15, beta- 10, gamma- 400, weight 0.5, stretch force- 10, deform iterations-100, point spacing- 3, image smoothing- 1.01. After the snakes were tracked through all frames, snakes were saved and ROIs were created from these snakes using 2D plug-in modality of JFilament. Finally, using the ROI information ellipses were fitted along the cells using a custom macro, written by Dr Diana Khoromskaia. These were then used with a FIJI plug-in Speckle TrackerJ [Smith et al., 2011] to identify the cleavage furrow as the intersection of the short axis of the ellipse and the snake of the cortex contour. Finally a custom written FIJI plug-in by Dr Diana Khoromskaia was used to extract intensity values along the segmented cell contour with respect to cortex. Dr. Ruby Peters developed a custom MATLAB workflow to average intensities of individual cells throughout cell division. Firstly, the intensity values obtained for each individual cell from timeframes during cell division were normalised to the average intensity in mitosis of the cell (2 frames before cell elongation, Frame 1). Then, the intensity values across the contour were scaled on 0-1 axis with 0 and 1 representing the same point in the cleavage furrow (Figure 2.39) and scaled for the distance from the furrow. Finally, these values were averaged for multiple cells across timeframes with all starting in mitosis (Frame 1), 2 frames before elongation.

4.8.5 Stochastic Reconstruction Optical Microscopy (STORM)

Samples were plated on 35 mm Dish High Precision 1.5 Coverslips (MatTek, P35G-0.170-14-C). For single colour imaging samples were stained by 1 h incubation with 1:200 Phalloidin-AlexaFluor-647 diluted in PBS. For two-colour imaging samples were stained by 1 h incubation with 1:200 Phalloidin-AlexaFluor-568 diluted 1:200 and 1:100 GFP nanobody Booster-AlexaFluor647 (Chromotek, gb2AF647) in PBS. Samples were imaged with a STORM buffer of 45 mM TRIS, 10 mM NaCl, 10 % glucose, 5U/mL Pyranose Oxidase, 35 mM MEA, 40 ug/mL catalase and 2 mM cyclooctatetraene (COT) as previously

described [Olivier et al., 2013].

Samples were imaged using a Zeiss Elyra 7 microscope set-up for single molecule localisation using a 64x objective with NA 1.46. Cells were imaged in their midplane (approximately 10 nm above the coverslip) in TIRF mode. Laser power was at 100 % with 20 ms exposure for 10000 frames (for single colour imaging) and 20000 frames (for 2 colour imaging) with 561 nm and 642 nm laser lines. During acquisition low laser power (up to 10 %) of back pumping with 405 nm laser was added. Samples were imaged by two sCMOS cameras.

After acquisition single molecule localisations were rendered and corrected for drift using model-based correction, grouped, and filtered for localisation precision 5-50 nm and number of photons 500-5000 using Gaussian distribution for 10 nm pixel with the in built ZEN Black processing software. To correct for chromatic aberration and drift during the acquisition, multi-colour fluorescent beads (TetraSpeck 0.1 mm diameter, Thermo Fischer Scientific) were added to the samples. The misalignment between two channels acquired by different cameras was further corrected by a custom written MATLAB script (courtesy of Dr Leila Muresan, University of Cambridge). Cortical thickness and overlap between actin and crosslinkers were analysed with a custom written MATLAB GUI, detecting fluorescence peak of the cortical profile and measuring the full width at half maximum (FWHM) of the cortical profile [Truong Quang et al., 2021].

4.8.6 DNA-Paint

For DNA-PAINT experiments, secondary antibodies were conjugated to a DNA docking strand (gift from Dr Pedro Pereira, Dr Ricardo Henriques lab). Samples were washed with 500 mM NaCl in PBS after fixation and imaged after addition of imager strands linked to ATTO655 (1:1,000 dillution) [Schnitzbauer et al., 2017]. DNA-PAINT samples were imaged on Zeiss Elyra PS 1 microscope with PALM settings using a 100x NA 1.46 oil objective in HiLO mode. 642 nm laser line was used with 200 ms exposure using PALM settings. Images were reconstructed by Dr Pedro Pereira.

4.8.7 Expansion microscopy

For expansion microscopy a protocol from Asano et al. [2018] was followed. Briefly, proteins were anchored with Acryloyl X-SE (Life technologies, A20770) resuspended in 500 µm anhydrous DMSO (0.1 mg/mL) overnight. Gelation solution was prepeared from 94 %

monomer solution (86 mg/mL sodium acrylate, 25 mg/mL acrylamide, 1.5 mg/mL N,N-Methylenebisacrylamide, 117 mg/mL NaCl, 1x PBS), 2 % accelerator solution (TEMED from 10 % stock) solution, 2 % APS (from 10 % stock solution). Samples were incubated in the gelation solution for 2 h, followed by overnight digestion at room temperature with digestion buffer (50 mM Tris pH 8.0, 1 mM EDTA, 0.5 % Triton X-100, 0.8 M guanidine HCl, proteinase K final concentration 8 units/mL) . Samples were then expanded with water and imaged with an Olympus FluoView FV1200 Confocal Laser Scanning Microscope using a 60x oil objective (NA 1.4).

4.8.8 Atomic force microscopy

To measure cortical tension, cells were transfected with artificial crosslinkers 24 h before the experiment and synchronised in mitosis using STLC 12 h before the experiment. For AFM experiments, mitotic cells were enriched for with a mitotic shake off and spun (460 g, 3 min) on the polylysine (PLL) coated FluoroDish (World Precision Instruments, FD35). 10 min before data acquisition cells were incubated with 0.01 % CellMaskTM Deep Red Plasma membrane Stain (Thermo Fisher Scientific). To prevent cells from progressing through cell division, STLC was kept in the imaging medium (Leibovitz's L-15 with 5 % FBS and 1 % Penicillin-Streptomycin) medium throughout the imaging. Cells with the brightest GFP (readout of expression of artificial crosslinkers) were selected for measurement.

Tension measurements were performed by Dr Alex Winkel as previously described in Cassani [2019], Chugh et al. [2017], Yanagida et al. [2022] using a set-up combining JPK CellHesion 200 (Bruker Corporation) and a DSD2 Differential Spinning Disk (Andor) both mounted on a DMi8 inverted microscope (Leica). Cells were compressed by tipless silicon cantilevers (ARROW-TL1-50) with a spring constant of 0.03 N/m. Cortical tension calculation was based on model from Fischer-Friedrich et al. [2014] and was previously described [Cassani, 2019, Chugh et al., 2017, Serres et al., 2020, Yanagida et al., 2022].

4.9 Statistical analysis

Mass spectrometry results were analysed using Excel (Microsoft). Prism (GraphPad Software) was used for other experiments. In Figures 2.33, 2.34, 2.35 outliers were removed using ROUT (Q=1 %) method. Multiple cells were examined in each of at least three independent experiments unless indicated differently in the figure legends. Independent

experiments were performed on different days including cell plating, treatment, sample preparation, and imaging. Datasets for the same conditions from the independent experiments were compared and if there were no statistical differences, the datasets were pooled for a statistical comparison of different conditions using higher total number of data points. Each dataset was tested for normality of data distribution using Prism. The normality distribution test informed the follow-up comparison of samples from different conditions. Samples that passed normality test were compared using Welch's t-test and non-normally distributed datasets using Mann-Whitney test to account for unpaired data points.

4.10 Figures

Schematics were created using Illustrator (Adobe) and BioRender.com.

Bibliography

B. Alberts, A. Johnson, J. Lewis, D. Morgan, M. Raff, K. Roberts, and P. Walter. *Molecular biology of the cell*. Garland Science, Taylor and Francis Group, New York, 6 edition, 2014.

P. Almada, P. M. Pereira, S. Culley, G. Caillol, F. Boroni-Rueda, C. L. Dix, G. Charras, B. Baum, R. F. Laine, C. Leterrier, and R. Henriques. Automating multimodal microscopy with NanoJ-Fluidics. *Nature Communications*, 10(1):1–9, 2019.

J. Alvarado, M. Sheinman, A. Sharma, F. C. MacKintosh, and G. H. Koenderink. Molecular motors robustly drive active gels to a critically connected state. *Nature Physics*, 9:591–597, 2013.

N. E. Amine, A. Kechad, S. Jananji, and G. R. Hickson. Opposing actions of septins and Sticky on Anillin promote the transition from contractile to midbody ring. *Journal of Cell Biology*, 203(3):487–504, 2013.

S. M. Asano, R. Gao, A. T. Wassie, P. W. Tillberg, F. Chen, and E. S. Boyden. Expansion microscopy: Protocols for imaging proteins and RNA in cells and tissues. *Current Protocols in Cell Biology*, 56:1–41, 2018.

A. Auer, M. T. Strauss, T. Schlichthaerle, and R. Jungmann. Fast, background-free DNA-PAINT imaging using FRET-based probes. *Nano Letters*, 17:6428–6434, 2017.

M. H. Bakalar, A. M. Joffe, E. M. Schmid, S. Son, M. Podolski, and D. A. Fletcher. Size-Dependent Segregation Controls Macrophage Phagocytosis of Antibody-Opsonized Targets. *Cell*, 174(1):131–142.e13, 2018.

D. Baker, J. Fallas, G. Ueda, W. Sheffler, and V. Nguyen. Computational design of self-assembling cyclic protein homo-oligomers, US10818377B2. The U.S. Patent and Trademark Office. 27.10.2020.

J. R. Bamburg and B. W. Bernstein. ADF/Cofilin. *Current Biology*, 18(7):273–275, 2008.

J. R. Bartles. Parallel actin bundles and their multiple actin-bundling proteins. *Current Opinion in Cell Biology*, 12(1):72–78, 2000.

J. R. Beach, L. Shao, K. Remmert, D. Li, E. Betzig, and J. A. Hammer. Nonmuscle myosin II isoforms coassemble in living cells. *Current Biology*, 24(10):1160–1166, 2014.

B. J. Belin, L. M. Goins, and R. D. Mullins. Comparative analysis of tools for live cell imaging of actin network architecture. *BioArchitecture*, 4(6):189–202, 2014.

J. M. Belmonte, M. Leptin, and F. Nédélec. A theory that predicts behaviors of disordered cytoskeletal networks. *Molecular systems biology*, 13(9):941, 2017.

M. Bergert, S. D. Chandradoss, R. A. Desai, and E. Paluch. Cell mechanics control rapid transitions between blebs and lamellipodia during migration. *Proceedings of the National Academy of Sciences of the United States of America*, 109(36):14434–14439, 2012.

M. Bergert, A. Erzberger, R. A. Desai, I. M. Aspalter, A. C. Oates, G. Charras, G. Salbreux, and E. K. Paluch. Force transmission during adhesion-independent migration. *Nature Cell Biology*, 17(4):524–529, 2015.

M. Biro, Y. Romeo, S. Kroschwald, M. Bovellan, A. Boden, J. Tcherkezian, P. P. Roux, G. Charras, and E. K. Paluch. Cell cortex composition and homeostasis resolved by integrating proteomics and quantitative imaging. *Cytoskeleton*, 70(11):741–754, 2013.

M. Bovellan, Y. Romeo, M. Biro, A. Boden, P. Chugh, A. Yonis, M. Vaghela, M. Fritzsche, D. Moulding, R. Thorogate, A. Jégou, A. J. Thrasher, G. Romet-Lemonne, P. P. Roux, E. K. Paluch, and G. Charras. Cellular control of cortical actin nucleation. *Current Biology*, 24(14):1628–1635, 2014.

D. Bray and J. White. Cortical flow in animal cells. *Science*, 239(4842):883–888, 1988.

A. Bretscher. Fimbrin is a cytoskeletal protein that crosslinks F-actin in vitro. *Proceedings of the National Academy of Sciences of the United States of America*, 78(11):6849, 1981.

A. A. Bridges and A. S. Gladfelter. Septin form and function at the cell cortex. *Journal of Biological Chemistry*, 290(28):17173–17180, 2015.

T. Brunette, F. Parmeggiani, P.-S. Huang, G. Bhabha, D. C. Ekiert, S. E. Tsutakawa, G. L. Hura, J. A. Tainer, and D. Baker. Exploring the repeat protein universe through computational protein design. *Nature*, 528(7583):580–584, 2015.

C. Cadart, E. Zlotek-Zlotkiewicz, M. Le Berre, M. Piel, and H. K. Matthews. Exploring the function of cell shape and size during mitosis. *Developmental Cell*, 29(2):159–169, 2014.

K. G. Campellone and M. D. Welch. A Nucleator arms race: cellular control of actin assembly. *Molecular Cell Biology*, 3(March):237–251, 2010.

L. Cao, A. Yonis, M. Vaghela, E. H. Barriga, P. Chugh, M. B. Smith, J. Maufront, G. Lavoie, A. Méant, E. Ferber, M. Bovellan, A. Alberts, A. Bertin, R. Mayor, E. K. Paluch, P. P. Roux, A. Jégou, G. Romet-Lemonne, and G. Charras. SPIN90 associates with mDia1 and the Arp2/3 complex to regulate cortical actin organization. *Nature Cell Biology*, 22(7):803–814, 2020.

A. Carrière, M. Cargnello, L. A. Julien, H. Gao, É. Bonneil, P. Thibault, and P. P. Roux. Oncogenic MAPK signaling stimulates mTORC1 activity by promoting RSK-mediated raptor phosphorylation. *Current biology*, 18(17):1269–1277, 2008.

D. A. D. Cassani. *Mechanics and architecture of the cellular actomyosin cortex*. PhD thesis, University College London, 2019.

A. Chaigne, C. Campillo, N. S. Gov, R. Voituriez, J. Azoury, C. Umaña-Diaz, M. Almonacid, I. Queguiner, P. Nassoy, C. Sykes, M. H. Verlhac, and M. E. Terret. A soft cortex is essential for asymmetric spindle positioning in mouse oocytes. *Nature Cell Biology*, 15(8):958–966, 2013.

F. Y. Chan, A. M. Silva, J. Saramago, J. Pereira-Sousa, H. E. Brighton, M. Pereira, K. Oegema, R. Gassmann, and A. X. Carvalho. The ARP2/3 complex prevents excessive formin activity during cytokinesis. *Molecular Biology of the Cell*, 30(1):96–107, 2019.

G. Charras and E. Paluch. Blebs lead the way: How to migrate without lamellipodia. *Nature Reviews Molecular Cell Biology*, 9(9):730–736, 2008.

G. T. Charras. A short history of blebbing. *Journal of Microscopy*, 231(3):466–478, 2008.

G. T. Charras, C. K. Hu, M. Coughlin, and T. J. Mitchison. Reassembly of contractile actin cortex in cell blebs. *Journal of Cell Biology*, 175(3):477–490, 2006.

G. T. Charras, M. Coughlin, T. J. Mitchison, and L. Mahadevan. Life and times of a cellular bleb. *Biophysical Journal*, 94(March):1836–1853, 2008.

A. S. Chikina, T. M. Svitkina, and A. Y. Alexandrova. Time-resolved ultrastructure of the cortical actin cytoskeleton in dynamic membrane blebs. *Journal of Cell Biology*, 218(2):445–454, 2019.

J. R. Christensen, G. M. Hocky, K. E. Homa, A. N. Morganthaler, S. E. Hitchcock-Degregori, G. A. Voth, and D. R. Kovar. Competition between tropomyosin, fimbrin, and ADF/cofilin drives their sorting to distinct actin filament networks. *eLife*, 6 (e23152), mar 2017.

P. Chugh and E. K. Paluch. The actin cortex at a glance. *Journal of Cell Science*, 131 (14):1–9, 2018.

P. Chugh, A. G. Clark, M. B. Smith, D. A. D. Cassani, K. Dierkes, A. Ragab, P. P. Roux, G. Charras, G. Salbreux, and E. K. Paluch. Actin cortex architecture regulates cell surface tension. *Nature Cell Biology*, 19(6):689–697, 2017.

A. G. Clark and E. Paluch. *Mechanics and Regulation of Cell Shape During the Cell Cycle*, volume 53. 2011.

A. G. Clark, K. Dierkes, and E. K. Paluch. Monitoring actin cortex thickness in live cells. *Biophysical Journal*, 105(3):570–580, 2013.

A. G. Clark, O. Wartlick, G. Salbreux, and E. K. Paluch. Stresses at the cell surface during animal cell morphogenesis. *Current Biology*, 24(10):484–494, 2014.

S. J. Davis and P. A. van der Merwe. The kinetic-segregation model: TCR triggering and beyond. *Nature Immunology 2006 7:8*, 7(8):803–809, 2006.

L. Dayon and J.-C. Sanchez. *Quantitative methods in proteomics*, volume 531. Springer Protocols, 2009.

S. K. Dey, R. K. Singh, S. Chattoraj, S. Saha, A. Das, K. Bhattacharyya, K. Sengupta, S. Sen, and S. S. Jana. Differential role of nonmuscle myosin II isoforms during blebbing of MCF-7 cells. *Molecular Biology of the Cell*, 28(8):1034–1042, 2017.

W. Y. Ding, H. T. Ong, Y. Hara, J. Wongsantichon, Y. Toyama, R. C. Robinson, F. Nédélec, and R. Zaidel-Bar. Plastin increases cortical connectivity to facilitate robust polarization and timely cytokinesis. *Journal of Cell Biology*, 216(5), 2017.

M. Dogterom and G. H. Koenderink. Actin–microtubule crosstalk in cell biology. *Nature Reviews Molecular Cell Biology*, 20(1):38–54, 2018.

S. Duarte, Á. Viedma-Poyatos, E. Navarro-Carrasco, A. E. Martínez, M. A. Pajares, and D. Pérez-Sala. Vimentin filaments interact with the actin cortex in mitosis allowing normal cell division. *Nature Communications*, 10(1):1–19, 2019.

M. Edwards, A. Zwolak, D. A. Schafer, D. Sept, R. Dominguez, and J. A. Cooper. Capping protein regulators fine-tune actin assembly dynamics. *Nature Reviews Molecular Cell Biology*, 15(10):677–689, 2014.

E. H. Egelman. The structure of F-actin. *Journal of muscle research and cell motility*, 6 (2):129–151, 1985.

H. Ennomani, G. Letort, C. Guerin, J. L. Martiel, W. Cao, F. Nedelec, E. M. De La Cruz, M. Thery, and L. Blanchoin. Architecture and connectivity govern actin network contractility. *Current Biology*, 26(5):616–626, 2016.

M. P. Estey, C. Di Ciano-Oliveira, C. D. Froese, M. T. Bejide, and W. S. Trimble. Distinct roles of septins in cytokinesis: SEPT9 mediates midbody abscission. *Journal of Cell Biology*, 191(4):741–749, 2010.

J. A. Fallas, G. Ueda, W. Sheffler, V. Nguyen, D. E. McNamara, B. Sankaran, J. H. Pereira, F. Parmeggiani, T. J. Brunette, D. Cascio, T. R. Yeates, P. Zwart, and D. Baker. Computational design of self-assembling cyclic protein homo-oligomers. *Nature Chemistry*, 9(4):353–360, 2016.

A. M. Fenix, N. Taneja, C. A. Buttler, J. Lewis, S. B. Van Engelenburg, R. Ohi, and D. T. Burnette. Expansion and concatenation of nonmuscle myosin IIA filaments drive cellular contractile system formation during interphase and mitosis. *Molecular Biology of the Cell*, 27(9):1465–1478, 2016.

C. M. Field and B. M. Alberts. Anillin, a contractile ring protein that cycles from the nucleus to the cell cortex. *Journal of Cell Biology*, 131(1):165–178, 1995.

E. Fischer-Friedrich, A. A. Hyman, F. Julicher, D. J. Muller, and J. Helenius. Quantification of surface tension and internal pressure generated by single mitotic cells. *Scientific Reports*, 4(6213):4–11, 2014.

S. L. Freedman, C. Suarez, J. D. Winkelman, D. R. Kovar, G. A. Voth, A. R. Dinner, and G. M. Hocky. Mechanical and kinetic factors drive sorting of F-actin cross-linkers

on bundles. *Proceedings of the National Academy of Sciences of the United States of America*, 116(33):16192–16197, 2019.

M. Fritzsche, C. Erlenkämper, E. Moeendarbary, G. Charras, and K. Kruse. Actin kinetics shapes cortical network structure and mechanics. *Science Advances*, 2(4):1–13, 2016.

K. Fujiwara and T. D. Pollard. Fluorescent antibody localization of myosin in the cytoplasm, cleavage furrow, and mitotic spindle of human cells. *Journal of Cell Biology*, 71 (3):848–875, 1976.

D. Gambarotto, F. U. Zwettler, M. Le Guennec, M. Schmidt-Cernohorska, D. Fortun, S. Borgers, J. Heine, J. G. Schloetel, M. Reuss, M. Unser, E. S. Boyden, M. Sauer, V. Hamel, and P. Guichard. Imaging cellular ultrastructures using expansion microscopy (U-ExM). *Nature Methods*, 16(1):71–74, 2018.

M. L. Gardel, F. Nakamura, J. H. Hartwig, J. C. Crocker, T. P. Stossel, and D. A. Weitz. Prestressed F-actin networks cross-linked by hinged filamins replicate mechanical properties of cells. *Proceedings of the National Academy of Sciences of the United States of America*, 103(6):1762–1767, 2006.

J. Gilden and M. F. Krummel. Control of cortical rigidity by the cytoskeleton: Emerging roles for septins. *Cytoskeleton*, 67(8), 2010.

J. K. Gilden, S. Peck, Y. C. M. Chen, and M. F. Krummel. The septin cytoskeleton facilitates membrane retraction during motility and blebbing. *Journal of Cell Biology*, 196(1):103–114, 2012.

F. Gittes, B. Mickey, J. Nettleton, and J. Howard. Flexural rigidity of microtubules and actin filaments measured from thermal fluctuations in shape. *The Journal of cell biology*, 120(4):923–934, 1993.

A. S. Gladfelter, J. R. Pringle, and D. J. Lew. The septin cortex at the yeast mother–bud neck. *Current Opinion in Microbiology*, 4(6):681–689, 2001.

P. J. Goldschmidt-Clermont, M. I. Furman, D. Wachsstock, D. Safer, V. T. Nachmias, and T. D. Pollard. The control of actin nucleotide exchange by thymosinβ4 and profilin. A potential regulatory mechanism for actin polymerization in cells. *Molecular Biology of the Cell*, 3(9):1015–1024, 1992.

E. D. Goley and M. D. Welch. The ARP2/3 complex: an actin nucleator comes of age. *Nature Reviews Molecular Cell Biology*, 7(10):713–726, 2006.

A. R. Harris, P. Jreij, B. Belardi, A. M. Joffe, A. R. Bausch, and D. A. Fletcher. Biased localization of actin binding proteins by actin filament conformation. *Nature Communications 2020 11:1*, 11(1):1–13, 2020.

M. Heusel, M. Frank, M. Köhler, S. Amon, F. Frommelt, G. Rosenberger, I. Bludau, S. Aulakh, M. I. Linder, Y. Liu, B. C. Collins, M. Gstaiger, U. Kutay, and R. Aebersold. A global screen for assembly state changes of the mitotic proteome by SEC-SWATH-MS. *Cell Systems*, 10(2):133–155.e6, 2020.

T. Hodge and J. T. V. Cope. A myosin family tree. *Journal of Cell Science*, 113:3353–3354, 2000.

K. C. Holmes, D. Popp, W. Gebhard, and W. Kabsch. Atomic model of the actin filament. *Nature*, 347(6288):44–49, 1990.

S. Jansen, A. Collins, C. Yang, G. Rebowski, T. Svitkina, and R. Dominguez. Mechanism of actin filament bundling by fascin. *The Journal of Biological Chemistry*, 286(34): 30087–30096, 2011.

L. W. Janson, J. Kolega, and D. L. Taylor. Modulation of contraction by gelation/solation in a reconstituted motile model. *Journal of Cell Biology*, 114(5):1005–1015, 1991.

E. Joo, M. C. Surka, and W. S. Trimble. Mammalian SEPT2 Is required for scaffolding nonmuscle myosin II and its kinases. *Developmental Cell*, 13(5):677–690, 2007.

R. Jungmann, M. S. Avendaño, J. B. Woehrstein, M. Dai, W. M. Shih, and P. Yin. Multiplexed 3D cellular Ssuper-resolution imaging with DNA-PAINT and Exchange-PAINT. *Nature Methods*, 11(3):313–8, 2014.

P. Kanchanawong, G. Shtengel, A. M. Pasapera, E. B. Ramko, M. W. Davidson, H. F. Hess, and C. M. Waterman. Nanoscale architecture of integrin-based cell adhesions. *Nature*, 468(7323):580–584, 2010.

M. Kelkar, P. Bohec, M. B. Smith, V. Sreenivasan, A. Lisica, L. Valon, E. Ferber, B. Baum, G. Salbreux, and G. Charras. Spindle reorientation in response to mechanical stress is an emergent property of the spindle positioning mechanisms. *Proceedings of the National Academy of Sciences*, 119(26), 2022.

M. S. Kim, C. D. Froese, M. P. Estey, and W. S. Trimble. SEPT9 occupies the terminal positions in septin octamers and mediates polymerization-dependent functions in abscission. *Journal of Cell Biology*, 195(5):815–826, 2011.

M. Kinoshita. Insight into septin functions from mouse models. In *The Septins*, pages 319–336. John Wiley & Sons, Ltd, 2008.

M. Kinoshita, C. M. Field, M. L. Coughlin, A. F. Straight, and T. J. Mitchison. Self- and actin-templated assembly of mammalian septins. *Developmental Cell*, 3(6):791–802, 2002.

M. G. Klein, W. Shi, U. Ramagopal, Y. Tseng, D. Wirtz, D. R. Kovar, C. J. Staiger, and S. C. Almo. Structure of the actin crosslinking core of fimbrin. *Structure*, 12:999–1013, 2004.

G. H. Koenderink and E. K. Paluch. Architecture shapes contractility in actomyosin networks. *Current Opinion in Cell Biology*, 50:79–85, 2018.

D. Krueger, T. Quinkler, S. A. Mortensen, C. Sachse, and S. de Renzis. Cross-linker–mediated regulation of actin network organization controls tissue morphogenesis. *Journal of Cell Biology*, 218(8):2743–2761, 2019.

K. Kruse and F. Jülicher. Actively contracting bundles of polar filaments. *Physical Review Letters*, 85(8):1778–1781, 2000.

O. M. Lancaster and B. Baum. Shaping up to divide: Coordinating actin and microtubule cytoskeletal remodelling during mitosis. *Seminars in Cell & Developmental Biology*, 34: 109–115, 2014.

O. M. Lancaster, L. Berre, A. Dimitracopoulos, D. Bonazzi, E. Zlotek-zlotkiewicz, R. Picone, T. Duke, M. Piel, and B. Baum. Mitotic rounding alters cell geometry to ensure efficient bipolar spindle formation. *Developmental Cell*, 25:270–283, 2013.

T. Lecuit and P. F. Lenne. Cell surface mechanics and the control of cell shape, tissue patterns and morphogenesis. *Nature Reviews Molecular Cell Biology*, 8(8):633–644, 2007.

M. G. Lee and P. Nurse. Complementation used to clone a human homologue of the fission yeast cell cycle control gene cdc2. *Nature*, 327(6117):31–35, 1987.

M. Lenz, T. Thoresen, M. L. Gardel, and A. R. Dinner. Contractile units in disordered actomyosin bundles arise from F-actin buckling. *Physical Review Letters*, 108(23): 238107, 2012.

R. Levayer and T. Lecuit. Biomechanical regulation of contractility : Spatial control and dynamics. *Trends in Cell Biology*, 22(2):61–81, 2012.

Y. Li. *The dynamic F-actin cross-linker alpha-actinin is tailored for contractile ring assembly during cytokinesis in Schizosaccharomyces pombe*. PhD thesis, University of Chicago, 2014.

C. Litschko, S. Brühmann, A. Csiszár, T. Stephan, V. Dimchev, J. Damiano-Guercio, A. Junemann, S. Körber, M. Winterhoff, B. Nordholz, N. Ramalingam, M. Peckham, K. Rottner, R. Merkel, and J. Faix. Functional integrity of the contractile actin cortex is safeguarded by multiple Diaphanous-related formins. *Proceedings of the National Academy of Sciences of the United States of America*, 116(9):3594–3603, 2019.

J. S. Logue, A. X. Cartagena-Rivera, M. A. Baird, M. W. Davidson, R. S. Chadwick, and C. M. Waterman. Erk regulation of actin capping and bundling by Eps8 promotes cortex tension and leader bleb-based migration. *eLife*, 4:1–31, 2015.

D. H. Lundgren, S. I. Hwang, L. Wu, and D. K. Han. Role of spectral counting in quantitative proteomics. *Expert Review of Proteomics*, 7(1):39–53, 2010.

A. S. Maddox and K. Burridge. RhoA is required for cortical retraction and rigidity during mitotic cell rounding. *Journal of Cell Biology*, 160(2):255–265, 2003.

J. L. Maître, H. Berthoumieux, S. F. G. Krens, G. Salbreux, F. Jülicher, E. Paluch, and C. P. Heisenberg. Adhesion functions in cell sorting by mechanically coupling the cortices of adhering cells. *Science*, 338(6104):253–256, 2012.

J.-L. Maître, H. Turlier, R. Illukkumbura, B. Eismann, R. Niwayama, F. Nédélec, and T. Hiiragi. Asymmetric division of contractile domains couples cell positioning and fate specification. *Nature*, 536(7616):344–348, 2016.

J. Marquardt, X. Chen, and E. Bi. Septin assembly and remodeling at the cell division site during the cell cycle. *Frontiers in Cell and Developmental Biology*, 9:3358, 2021.

R. Matzke, K. Jacobson, and M. Radmacher. Direct, high-resolution measurement of furrow stiffening during division of adherent cells. *Nature Cell Biology*, 3(6):607–610, 2001.

P. Maupin and T. D. Pollard. Arrangement of actin filaments and myosin-like filaments in the contractile ring and of actin-like filaments in the mitotic spindle of dividing HeLa

cells. *Journal of Ultrastructure and Molecular Structure Research*, 94(1):92–103, jan 1986.

M. Mavrakis, Y. Azou-Gros, F. C. Tsai, J. Alvarado, A. Bertin, F. Iv, A. Kress, S. Brasselet, G. H. Koenderink, and T. Lecuit. Septins promote F-actin ring formation by crosslinking actin filaments into curved bundles. *Nature Cell Biology 2014 16:4*, 16 (4):322–334, 2014.

M. Mayer, M. Depken, J. S. Bois, F. Jülicher, and S. W. Grill. Anisotropies in cortical tension reveal the physical basis of polarizing cortical flows. *Nature*, 467(7315):617–621, 2010.

R. K. Meyer and U. Aebi. Bundling of actin filaments by alpha-actinin depends on its molecular length. *Journal of Cell Biology*, 110(6):2013–2024, 1990.

S. C. Mockrin and E. D. Korn. Acanthamoeba profilin interacts with G-actin to increase the rate of exchange of actin-bound adenosine 5'-triphosphate. *Biochemistry*, 19(23): 5359–5362, 1980.

S. Mostowy and P. Cossart. Septins: The fourth component of the cytoskeleton. *Nature Reviews Molecular Cell Biology*, 13(3):183–194, 2012.

S. Mostowy, S. Janel, C. Forestier, C. Roduit, S. Kasas, J. Pizarro-Cerdá, P. Cossart, and F. Lafont. A role for septins in the interaction between the Listeria monocytogenes invasion protein InlB and the Met receptor. *Biophysical Journal*, 100(8):1949–1959, apr 2011.

M. Murrell, P. W. Oakes, M. Lenz, and M. L. Gardel. Forcing cells into shape: the mechanics of actomyosin contractility. *Nature Reviews Molecular Cell Biology*, 16(8): 486–498, 2015.

M. P. Murrell and M. L. Gardel. F-actin buckling coordinates contractility and severing in a biomimetic actomyosin cortex. *Proceedings of the National Academy of Sciences*, 109(51):20820–20825, 2012.

F. Nakamura, E. Osborn, P. A. Janmey, and T. P. Stossel. Comparison of filamin A-induced cross-linking and Arp2/3 complex-mediated branching on the mechanics of actin filaments. *Journal of Biological Chemistry*, 277(11):9148–9154, 2002.

F. Nakamura, T. P. Stossel, and J. H. Hartwig. The filamins: Organizers of cell structure and function. *Cell Adhesion & Migration*, 5(2):160–169, 2011.

R. Nambiar, R. E. McConnell, and M. J. Tyska. Control of cell membrane tension by myosin-I. *Proceedings of the National Academy of Sciences of the United States of America*, 106(29):11972–11977, 2009.

A. Narita, T. Oda, and Y. Maéda. Structural basis for the slow dynamics of the actin filament pointed end. *The EMBO Journal*, 30(7):1230–1237, 2011.

K. Oegema, M. S. Savoian, T. J. Mitchison, and C. M. Field. Functional analysis of a human homologue of the drosophila actin binding protein anillin auggests a role in cytokinesis. *Journal of Cell Biology*, 150(3):539–552, 2000.

D. B. Oelz, B. Y. Rubinstein, and A. Mogilner. A Combination of actin treadmilling and cross-linking drives contraction of random actomyosin arrays. *Biophysical Journal*, 109 (9):1818–1829, 2015.

N. Olivier, D. Keller, P. Gönczy, and S. Manley. Resolution doubling in 3D-STORM imaging through improved buffers. *PLoS ONE*, 8(7):e69004, 2013.

K. Ong, C. Wloka, S. Okada, T. Svitkina, and E. Bi. Architecture and dynamic remodelling of the septin cytoskeleton during the cell cycle. *Nature Communications*, 5(1):1–10, 2014.

E. Paluch and C.-P. Heisenberg. Biology and physics of cell shape changes in development. *Current Biology*, 19(17):790–799, 2009.

E. K. Paluch and E. Raz. The role and regulation of blebs in cell migration. *Current Opinion in Cell Biology*, 25(5):582–590, 2013.

F. Parmeggiani and P.-S. Huang. Designing repeat proteins: a modular approach to protein design. *Current Opinion in Structural Biology*, 45:116–123, 2017.

F. Parmeggiani, P.-S. Huang, S. Vorobiev, R. Xiao, K. Park, S. Caprari, M. Su, J. Seetharaman, L. Mao, H. Janjua, G. T. Montelione, J. Hunt, and D. Baker. A General computational approach for repeat protein design. *Journal of Molecular Biology*, 427 (2):563–575, 2015.

T. D. Pollard. Mechanism of actin filament self-assembly and regulation of the process by actin-binding proteins. *Biophysical Journal*, 49(January):149–151, 1986.

T. D. Pollard. Actin and actin-binding proteins. *Cold Spring Harbor Perspectives in Biology*, 8(8), 2016.

T. D. Pollard and M. S. Mooseker. Direct measurement of actin polymerization rate constants by electron microscopy of actin filaments nucleated by isolated microvillus cores. *Journal of Cell Biology*, 88(3):654–659, 1981.

T. D. Pollard, L. Blanchoin, and R. D. Mullins. Molecular mechanisms controlling actin filament dynamics in nonmuscle cells. *Annual Review of Biophysics and Biomolecular Structure*, 11(3):313–8, 2000.

S. P. Ramanathan, J. Helenius, M. P. Stewart, C. J. Cattin, A. A. Hyman, and D. J. Muller. Cdk1-dependent mitotic enrichment of cortical myosin II promotes cell rounding against confinement. *Nature Cell Biology*, 17(2):148–159, 2015.

E. M. Reichl, Y. Ren, M. K. Morphew, M. Delannoy, J. C. Effler, K. D. Girard, S. Divi, P. A. Iglesias, S. C. Kuo, and D. N. Robinson. Interactions between myosin and actin crosslinkers control cytokinesis contractility dynamics and mechanics. *Current Biology*, 18(7):471–480, 2008.

J. Riedl, A. H. Crevenna, K. Kessenbrock, J. H. Yu, D. Neukirchen, M. Bista, F. Bradke, D. Jenne, T. A. Holak, Z. Werb, M. Sixt, and R. Wedlich-Soldner. Lifeact: a versatile marker to visualize F-actin. *Nature Methods*, 5(7):605–607, 2008.

G. Salbreux, G. Charras, and E. Paluch. Actin cortex mechanics and cellular morphogenesis. *Trends in Cell Biology*, 22(10):536–545, 2012.

M. Sato, W. H. Schwarz, and T. D. Pollard. Dependence of the mechanical properties of actin/α-actinin gels on deformation rate. *Nature 1987 325:6107*, 325(6107):828–830, 1987.

N. Sato, N. Funayama, A. Nagafuchi, S. Yonemura, S. Tsukita, and S. Tsukita. A gene family consisting of ezrin, radixin and moesin. Its specific localization at actin filament/-plasma membrane association sites. *Journal of Cell Science*, 103(1):131–143, 1992.

J. Schindelin, I. Arganda-Carreras, E. Frise, V. Kaynig, M. Longair, T. Pietzsch, S. Preibisch, C. Rueden, S. Saalfeld, B. Schmid, J. Y. Tinevez, D. J. White, V. Hartenstein, K. Eliceiri, P. Tomancak, and A. Cardona. Fiji: An open-source platform for biological-image analysis. *Nature Methods*, 9(7):676–682, 2012.

J. Schnitzbauer, M. T. Strauss, T. Schlichthaerle, F. Schueder, and R. Jungmann. Super-resolution microscopy with DNA-PAINT. *Nature Protocols*, 12(6):1198–1228, 2017.

T. E. Schroeder. Actin in Dividing Cells: Contractile Ring Filaments Bind Heavy Meromyosin. *Proceedings of the National Academy of Sciences*, 70(6):1688–1692, 1973.

J. Sedzinski, M. Biro, A. Oswald, J.-Y. Tinevez, G. Salbreux, and E. Paluch. Polar actomyosin contractility destabilizes the position of the cytokinetic furrow. *Nature*, 476 (7361):462–6, 2011.

M. P. Serres, M. Samwer, B. An Truong Quang, G. Lavoie, U. Perera, D. Görlich, G. Charras, M. Petronczki, P. P. Roux, and E. K. Paluch. F-Actin interactome reveals vimentin as a key regulator of actin organization and cell mechanics in mitosis. *Developmental Cell*, 52(2):210–222, 2020.

M. S. Shutova and T. M. Svitkina. Mammalian nonmuscle myosin II comes in three flavors. *Biochemical and Biophysical Research Communications*, 506(2):394–402, 2018.

M. S. Shutova, W. A. Spessott, C. G. Giraudo, and T. Svitkina. Endogenous Species of Mammalian Nonmuscle Myosin IIA and IIB Include Activated Monomers and Heteropolymers. *Current Biology*, 24(17):1958–1968, 2014.

C. Smith, L. Dolat, D. Angelis, E. Forgacs, E. T. Spiliotis, and V. E. Galkin. Septin 9 exhibits polymorphic binding to F-actin and inhibits myosin and cofilin activity. *Journal of Molecular Biology*, 427(20):3273–3284, 2015.

M. B. Smith, H. Li, T. Shen, X. Huang, E. Yusuf, and D. Vavylonis. Segmentation and tracking of cytoskeletal filaments using open active contours. *Cytoskeleton*, 67(11): 693–705, 2010.

M. B. Smith, E. Karatekin, A. Gohlke, H. Mizuno, N. Watanabe, and D. Vavylonis. Interactive, computer-assisted tracking of speckle trajectories in fluorescence microscopy: Application to actin polymerization and membrane fusion. *Biophysical Journal*, 101(7): 1794–1804, 2011.

I. Spector, N. R. Shochet, Y. Kashman, and A. Groweiss. Latrunculins: Novel marine toxins that disrupt microfilament organization in cultured cells. *Science*, 219(4584): 493–495, 1983.

E. T. Spiliotis. Spatial effects - site-specific regulation of actin and microtubule organization by septin GTPases. *Journal of Cell Science*, 131(1), 2018.

E. T. Spiliotis and K. Nakos. Cellular functions of actin- and microtubule-associated septins. *Current Biology*, 31(10):651–666, 2021.

E. T. Spiliotis, M. Kinoshita, and W. J. Nelson. A mitotic septin scaffold required for mammalian chromosome congression and segregation. *Science*, 307(5716):1781–1785, 2005.

M. P. Stewart, J. Helenius, Y. Toyoda, S. P. Ramanathan, D. J. Muller, and A. a. Hyman. Hydrostatic pressure and the actomyosin cortex drive mitotic cell rounding. *Nature*, 469 (7329):226–230, 2011.

M. P. Stewart, Y. Toyoda, A. A. Hyman, and D. J. Müller. Tracking mechanics and volume of globular cells with atomic force microscopy using a constant-height clamp. *Nature Protocols*, 7(1):143–154, 2012.

T. M. Svitkina. Actin Cell Cortex: Structure and Molecular Organization. *Trends in Cell Biology*, 30(7):556–565, 2020.

N. Taneja and D. T. Burnette. Myosin IIA drives membrane bleb retraction. *Molecular Biology of the Cell*, 30(9):1051–1059, 2019.

N. Taneja, M. R. Bersi, S. M. Baillargeon, V. Gama, W. D. Merryman, and D. T. Burnette Correspondence. Precise tuning of cortical contractility regulates cell shape during cytokinesis. *Cell Reports*, 31:107477, 2020.

M. Théry. Micropatterning as a tool to decipher cell morphogenesis and functions. *Journal of Cell Science*, 123(24):4201–4213, 2010.

D. W. Thompson. *On growth and form.* Cambridge University Press, Cambridge, canto clas edition, 2014.

P. W. Tillberg, F. Chen, K. D. Piatkevich, Y. Zhao, C.-C. J. Yu, B. P. English, L. Gao, A. Martorell, H.-J. Suk, F. Yoshida, E. M. DeGennaro, D. H. Roossien, G. Gong, U. Seneviratne, S. R. Tannenbaum, R. Desimone, D. Cai, and E. S. Boyden. Protein-retention Expansion Microscopy of cells and tissues labeled using standard fluorescent proteins and antibodies. *Nature Biotechnology*, 34:1–9, 2016.

J.-Y. Tinevez, U. Schulze, G. Salbreux, J. Roensch, J.-F. Joanny, and E. Paluch. Role of cortical tension in bleb growth. *Proceedings of the National Academy of Sciences of the United States of America*, 106(44):18581–6, 2009.

A. J. Tooley, J. Gilden, J. Jacobelli, P. Beemiller, W. S. Trimble, M. Kinoshita, and M. F. Krummel. Amoeboid T lymphocytes require the septin cytoskeleton for cortical integrity and persistent motility. *Nature Cell Biology*, 11(1):17–26, 2009.

Y. Toyoda, C. J. Cattin, M. P. Stewart, I. Poser, M. Theis, T. V. Kurzchalia, F. Buchholz, A. A. Hyman, and D. J. Müller. Genome-scale single-cell mechanical phenotyping reveals disease-related genes involved in mitotic rounding. *Nature Communications*, 8(1):1266, 2017.

B. A. Truong Quang, R. Peters, D. A. D. Cassani, P. Chugh, A. G. Clark, M. Agnew, G. Charras, and E. K. Paluch. Extent of myosin penetration within the actin cortex regulates cell surface mechanics. *Nature Communications 2021 12:1*, 12(1):1–12, 2021.

J. M. Tyler, J. M. Anderson, and D. Branton. Structural comparison of several actin-binding macromolecules. *The Journal of Cell Biology*, 85(2):489–495, 1980.

N. Vadnjal, S. Nourreddine, G. Lavoie, M. Serres, P. P. Roux, and E. K. Paluch. Proteomic analysis of the actin cortex in interphase and mitosis. *Journal of Cell Science*, 135(16), 2022.

M. Vicente-Manzanares, X. Ma, R. S. Adelstein, and A. R. Horwitz. Non-muscle myosin II takes centre stage in cell adhesion and migration. *Nature Reviews Molecular Cell Biology*, 10(11):778–790, 2009.

G. Wen, M. Vanheusden, A. Acke, D. Valli, R. K. Neely, V. Leen, and J. Hofkens. Evaluation of direct grafting strategies via trivalent anchoring for Enabling Lipid Membrane and Cytoskeleton Staining in Expansion Microscopy. *ACS Nano*, 14(7):7860–7867, 2020.

J. G. White and G. G. Borisy. On the mechanisms of cytokinesis in animal cells. *Journal of Theoretical Biology*, 101(2):289–316, 1983.

S. J. Winder, L. Hemmings, S. K. Maciver, S. J. Bolton, J. M. Tinsley, K. E. Davies, D. R. Critchley, and J. Kendrick-Jones. Utrophin actin binding domain: analysis of actin binding and cellular targeting. *Journal of Cell Science*, 108(1):63–71, 1995.

J. D. Winkelman, C. Suarez, G. M. Hocky, A. J. Harker, A. N. Morganthaler, J. R. Christensen, G. A. Voth, J. R. Bartles, and D. R. Kovar. Fascin- and a -actinin-bundled networks contain intrinsic structural features that drive protein sorting. *Current Biology*, 26(20):2697–2706, 2016.

J. Xu, D. Wirtz, and T. D. Pollard. Dynamic cross-linking by α-actinin determines the mechanical properties of actin filament networks. *Journal of Biological Chemistry*, 273 (16):9570–9576, 1998.

K. Yamamoto, K. Otomo, T. Nemoto, S. Ishihara, H. Haga, A. Nagasaki, Y. Murakami, and M. Takahashi. Differential contributions of nonmuscle myosin IIA and IIB to cytokinesis in human immortalized fibroblasts. *Experimental Cell Research*, 376(1):67–76, 2019.

S. Yamashiro, Y. Yamakita, R. Ishikawa, and F. Matsumura. Mitosis-specific phosphorylation causes 83K non-muscle caldesmon to dissociate from microfilaments. *Nature*, 344 (6267):675–678, 1990.

A. Yanagida, E. Corujo-Simon, C. K. Revell, P. Sahu, G. G. Stirparo, I. M. Aspalter, A. K. Winkel, R. Peters, H. De Belly, D. A. Cassani, S. Achouri, R. Blumenfeld, K. Franze, E. Hannezo, E. K. Paluch, J. Nichols, and K. J. Chalut. Cell surface fluctuations regulate early embryonic lineage sorting. *Cell*, 185(5):777–793, 2022.

C. T. Yeh, T. J. Brunette, D. Baker, S. McIntosh-Smith, and F. Parmeggiani. Elfin: An algorithm for the computational design of custom three-dimensional structures from modular repeat protein building blocks. *Journal of Structural Biology*, 201(2):100–107, 2018.

C. T. Yeh, L. Obendorf, and F. Parmeggiani. Elfin UI: A graphical interface for protein design with modular building blocks. *Frontiers in Bioengineering and Biotechnology*, 8 (568318):1242, 2020.

R. Zaidel-Bar, G. Zhenhuan, and C. Luxenburg. The contractome – a systems view of actomyosin contractility in non-muscle cells. *Journal of Cell Science*, 128(12):2209–2217, 2015.

Appendix A

Appendix A: DNA sequence of D18 artificial crosslinkers

A.1 Artificial crosslinker sequence with 1 D18 repeat

The following sequence was commercially synthesised and inserted in pcDNA 3.1+ backbone plasmid. The sequence includes Lifeact actin binding domain, dimerisation domain, 1 D18 based repeat and GFP [Baker et al., Brunette et al., 2015, Fallas et al., 2016, Parmeggiani et al., 2015]. The sequence corresponds to plasmid map in Figure 2.23A:

AAGCTTGTCATGGGCGTGGCCGACTTGATCAAGAAGTTCGAGTCC
ATCTCCAAGGAGGAGGGATCCGGCGATATCGAGAAGCTGTGCAAG
AAGGCCGAGAGCGAGGCCAGAGAAGCCAGATCTAAGGCCGAGGAA
CTGAGACAGAGACACCCTGATTCTCAGGCCGCCAGAGATGCCCAG
AAACTGGCCTCTCAGGCTGAGGAAGCTGTGAAGCTAGCCTGCGAA
CTGGCCCAAGAGCACCCCAATGCCGATATTGCCAAGCTGTGTATC
AAGGCCGCCTCTGAAGCCGCCGAAGCCGCTTCTAAAGCTGCCGAA
CTGGCTCAGAGACATCCCGATAGCCAGGCCGCTAGGGATGCTATT
AAGCTGGCTAGTCAGGCCGCTGAGGCCGTGAAACTGGCTTGTGAA
CTCGCTCAAGAACACCCTAACGCCAAGATCGCCAAACTGTGCATC
ATTGCCGCCGCTCTGGCTGCCGAGGCTGCATCTAAAGCAGCTGAG
CTGGCCCAGCGGCATCCAGATTCTCAAGCTGCAAGGGACGCCATC
AAACTGGCCAGCCAAGCTGCTGAAGCAGTCAAGTTGGCTTGCGAG
CTGGCACAAGAACATCCAAACGCTATCATTGCCATCCTGTGCATC

GTGGCCGCTATTGCCGCTGCCATTGCTGCTTCTATGGCTGCTGCT
CTGGCACAGCGTCACCCTGATAGCCAAGCAGCCCGGGATGCAATC
AAGCTCGCTTCTCAGGCAGCAGAAGCCGTCAAACTTGCCTGCGAG
CTTGCTCAAGAGCATCCGAATGCCAAAATCGCCGTGCTGTGCATT
CTGGCTGCAGCACTGGCTGCTATTGCAGCAGCTCTTGCTGCACTG
CTGGCCCAACTTCATCCTGACAGTCAAGCAGCTCGCGACGCCATT
AAGTTGGCATCACAAGCCGCAGAGGCTGTCAAGTTGGCCTGTGAA
TTGGCTCAAGAGCATCCAAACGCCGACATTGCCGAGAAGTGCATC
CTGCTGGCTATCCTGGCAGCTCTGCTGGCAATTTTGGCTGCCCTG
CTTGCCATGCTGCACCCCGATTCTGATCTGGCTAGAGCCCTGATC
GATCTGGCCTCAGAGCTGGCCGAAGAGGTCAAAGAGAGATGCGAA
CGGGGTACCAGCGGAATGGTGAGCAAGGGCGAGGAGCTGTTCACC
GGGGTGGTGCCCATCCTGGTCGAGCTGGACGGCGACGTAAACGGC
CACAAGTTCAGCGTGTCCGGCGAGGGCGAGGGCGATGCCACCTAC
GGCAAGCTGACCCTGAAGTTCATCTGCACCACCGGCAAGCTGCCC
GTGCCCTGGCCCACCCTCGTGACCACCCTGACCTACGGCGTGCAG
TGCTTCAGCCGCTACCCCGACCACATGAAGCAGCACGACTTCTTC
AAGTCCGCCATGCCCGAAGGCTACGTCCAGGAGCGCACCATCTTC
TTCAAGGACGACGGCAACTACAAGACCCGCGCCGAGGTGAAGTTC
GAGGGCGACACCCTGGTGAACCGCATCGAGCTGAAGGGCATCGAC
TTCAAGGAGGACGGCAACATCCTGGGGCACAAGCTGGAGTACAAC
TACAACAGCCACAACGTCTATATCATGGCCGACAAGCAGAAGAAC
GGCATCAAGGTGAACTTCAAGATCCGCCACAACATCGAGGACGGC
AGCGTGCAGCTCGCCGACCACTACCAGCAGAACACCCCCATCGGC
GACGGCCCCGTGCTGCTGCCCGACAACCACTACCTGAGCACCCAG
TCCGCCCTGAGCAAAGACCCCAACGAGAAGCGCGATCACATGGTC
CTGCTGGAGTTCGTGACCGCCGCCGGGATCACTCTCGGCATGGAC
GAGCTGTACAAGGGCCTCGAGCACCACCATCACCATCACTAA

A.2 Insert plasmid with 6 D18 repeats

Plasmid containing 6 D18 repeats was commerically synthesised to allow cloning of additional repeats in the original pcDNA 3.1+ plasmid with one repeat (see Results and Materials and Methods). Plasmid map corresponding to the entire sequence is shown in Figure 2.23B:

CTAAATTGTAAGCGTTAATATTTTGTTAAAATTCGCGTTAAATTTTT
GTTAAATCAGCTCATTTTTTAACCAATAGGCCGAAATCGGCAAAATC
CCTTATAAATCAAAAGAATAGACCGAGATAGGGTTGAGTGGCCGCTA
CAGGGCGCTCCCATTCGCCATTCAGGCTGCGCAACTGTTGGGAAGGG
CGTTTCGGTGCGGGCCTCTTCGCTATTACGCCAGCTGGCGAAAGGGG
GATGTGCTGCAAGGCGATTAAGTTGGGTAACGCCAGGGTTTTCCCAG
TCACGACGTTGTAAAACGACGGCCAGTGAGCGCGACGTAATACGACT
CACTATAGGGCGAATTGAAGGAAGGCCGTCAAGGCCGCATGGATCCG
GCGATATCGAGAAGCTGTGCAAGAAGGCCGAGAGCGAGGCCAGAGAA
GCCAGATCTAAGGCCGAGGAACTGAGACAGAGACACCCTGATTCTCA
GGCCGCCAGAGATGCCCAGAAACTGGCCTCTCAGGCTGAGGAAGCTG
TGAAGCTAGCCTGCGAACTGGCCCAAGAGCACCCCAATGCCGATATT
GCCAAGCTGTGTATCAAGGCCGCCTCTGAAGCCGCCGAAGCCGCTTC
TAAAGCTGCCGAACTGGCTCAGAGACATCCCGATAGCCAGGCCGCTA
GGGATGCTATTAAGCTGGCTAGTCAGGCCGCTGAGGCCGTGAAACTG
GCTTGTGAACTCGCTCAAGAACACCCTAACGCTGATATCGCCAAACT
CTGCATTAAGGCTGCCAGCGAGGCTGCCGAAGCTGCCAGTAAAGCAG
CTGAGCTGGCCCAGCGTCATCCAGATTCACAAGCTGCTAGGGACGCC
ATCAAACTGGCCAGCCAAGCTGCTGAAGCAGTCAAGTTGGCTTGCGA
GCTGGCACAAGAACATCCAAACGCAGACATAGCTAAGCTCTGCATCA
AAGCCGCAAGCGAAGCCGCAGAGGCTGCCTCAAAAGCAGCAGAACTG
GCACAAAGGCACCCAGACAGCCAGGCTGCACGGGATGCAATCAAACT
TGCTTCTCAGGCAGCCGAGGCTGTCAAATTGGCCTGTGAATTGGCTC
AAGAGCATCCGAACGCCGACATTGCAAAATTGTGCATCAAGGCAGCT
TCCGAGGCAGCAGAGGCCGCATCAAAGGCTGCTGAGCTTGCACAGAG
GCATCCTGACTCACAAGCAGCACGCGACGCCATTAAGTTGGCATCAC
AGGCCGCAGAAGCCGTCAAGCTCGCCTGTGAACTTGCACAAGAACAT
CCCAATGCAGATATCGCAAAACTGTGCATCAAAGCTGCATCTGAGGC
TGCTGAAGCCGCCTCTAAGGCAGCAGAGCTTGCCCAAAGACATCCCG
ACTCTCAGGCTGCCCGTGATGCCATTAAGCTCGCTTCTCAAGCAGCT
GAAGCCGTGAAACTTGCCTGCGAGCTTGCTCAAGAGCATCCTAATGC
TGACATAGCTAAACTGTGTATTAAGGCAGCAAGTGAAGCTGCCGAGG
CCGCAAGCAAAGCAGCCGAACTTGCCCAACGTCACCCTGATAGCCAA
GCAGCAAGAGATGCTATCAAACTCGCATCCCAAGCTGCAGAGGCAGT

GAAACTAGCGAGACCCTGGGCCTCATGGGCCTTCCTTTCACTGCCCG
CTTTCCAGTCGGGAAACCTGTCGTGCCAGCTGCATTAACATGGTCAT
AGCTGTTTCCTTGCGTATTGGGCGCTCTCCGCTTCCTCGCTCACTGA
CTCGCTGCGCTCGGTCGTTCGGGTAAAGCCTGGGGTGCCTAATGAGC
AAAAGGCCAGCAAAAGGCCAGGAACCGTAAAAAGGCCGCGTTGCTGG
CGTTTTTCCATAGGCTCCGCCCCCCTGACGAGCATCACAAAAATCGA
CGCTCAAGTCAGAGGTGGCGAAACCCGACAGGACTATAAAGATACCA
GGCGTTTCCCCCTGGAAGCTCCCTCGTGCGCTCTCCTGTTCCGACCC
TGCCGCTTACCGGATACCTGTCCGCCTTTCTCCCTTCGGGAAGCGTG
GCGCTTTCTCATAGCTCACGCTGTAGGTATCTCAGTTCGGTGTAGGT
CGTTCGCTCCAAGCTGGGCTGTGTGCACGAACCCCCCGTTCAGCCCG
ACCGCTGCGCCTTATCCGGTAACTATCGTCTTGAGTCCAACCCGGTA
AGACACGACTTATCGCCACTGGCAGCAGCCACTGGTAACAGGATTAG
CAGAGCGAGGTATGTAGGCGGTGCTACAGAGTTCTTGAAGTGGTGGC
CTAACTACGGCTACACTAGAAGAACAGTATTTGGTATCTGCGCTCTG
CTGAAGCCAGTTACCTTCGGAAAAAGAGTTGGTAGCTCTTGATCCGG
CAAACAAACCACCGCTGGTAGCGGTGGTTTTTTTGTTTGCAAGCAGC
AGATTACGCGCAGAAAAAAAGGATCTCAAGAAGATCCTTTGATCTTT
TCTACGGGGTCTGACGCTCAGTGGAACGAAAACTCACGTTAAGGGAT
TTTGGTCATGAGATTATCAAAAAGGATCTTCACCTAGATCCTTTTAA
ATTAAAAATGAAGTTTTAAATCAATCTAAAGTATATATGAGTAAACT
TGGTCTGACAGTTATTAGAAAAATTCATCCAGCAGACGATAAAACGC
AATACGCTGGCTATCCGGTGCCGCAATGCCATACAGCACCAGAAAAC
GATCCGCCCATTCGCCGCCCAGTTCTTCCGCAATATCACGGGTGGCC
AGCGCAATATCCTGATAACGATCCGCCACGCCCAGACGGCCGCAATC
AATAAAGCCGCTAAAACGGCCATTTTCCACCATAATGTTCGGCAGGC
ACGCATCACCATGGGTCACCACCAGATCTTCGCCATCCGGCATGCTC
GCTTTCAGACGCGCAAACAGCTCTGCCGGTGCCAGGCCCTGATGTTC
TTCATCCAGATCATCCTGATCCACCAGGCCCGCTTCCATACGGGTAC
GCGCACGTTCAATACGATGTTTCGCCTGATGATCAAACGGACAGGTC
GCCGGGTCCAGGGTATGCAGACGACGCATGGCATCCGCCATAATGCT
CACTTTTTCTGCCGGCGCCAGATGGCTAGACAGCAGATCCTGACCCG
GCACTTCGCCCAGCAGCAGCCAATCACGGCCCGCTTCGGTCACCACA
TCCAGCACCGCCGCACACGGAACACCGGTGGTGGCCAGCCAGCTCAG

ACGCGCCGCTTCATCCTGCAGCTCGTTCAGCGCACCGCTCAGATCGG
TTTTCACAAACAGCACCGGACGACCCTGCGCGCTCAGACGAAACACC
GCCGCATCAGAGCAGCCAATGGTCTGCTGCGCCCAATCATAGCCAAA
CAGACGTTCCACCCACGCTGCCGGGCTACCCGCATGCAGGCCATCCT
GTTCAATCATACTCTTCCTTTTTCAATATTATTGAAGCATTTATCAG
GGTTATTGTCTCATGAGCGGATACATATTTGAATGTATTTAGAAAAA
TAAACAAATAGGGGTTCCGCGCACATTTCCCCGAAAAGTGCCAC

A.3 Artificial crosslinker sequence with 7 D18 repeats

By inserting 6 D18 repeat domians from insert plasmid into pcDNA 3.1+ plasmid with artificial crosslinker with 1 repeat (see above), a new plasmid with a bigger crosslinker was commercially synthesised. I used the same approach to synthesise 12 and 18 repeat artificial crosslinker. This is DNA sequence of the artificial crosslinker with 6 added repeats. The sequence corresponds to plasmid map in Figure 2.23C:

AAGCTTGTCATGGGCGTGGCCGACTTGATCAAGAAGTTCGAGTCCAT
CTCCAAGGAGGAGGGATCCGGCGATATCGAGAAGCTGTGCAAGAA
GGCCGAGAGCGAGGCCAGAGAAGCCAGATCTAAGGCCGAGGAACT
GAGACAGAGACACCCTGATTCTCAGGCCGCCAGAGATGCCCAGAA
ACTGGCCTCTCAGGCTGAGGAAGCTGTGAAGCTAGCCTGCGAACT
GGCCCAAGAGCACCCCAATGCCGATATTGCCAAGCTGTGTATCAA
GGCCGCCTCTGAAGCCGCCGAAGCCGCTTCTAAAGCTGCCGAACT
GGCTCAGAGACATCCCGATAGCCAGGCCGCTAGGGATGCTATTAA
GCTGGCTAGTCAGGCCGCTGAGGCCGTGAAACTGGCTTGTGAACT
CGCTCAAGAACACCCTAACGCTGATATCGCCAAACTCTGCATTAA
GGCTGCCAGCGAGGCTGCCGAAGCTGCCAGTAAAGCAGCTGAGCT
GGCCCAGCGTCATCCAGATTCACAAGCTGCTAGGGACGCCATCAA
ACTGGCCAGCCAAGCTGCTGAAGCAGTCAAGTTGGCTTGCGAGCT
GGCACAAGAACATCCAAACGCAGACATAGCTAAGCTCTGCATCAA
AGCCGCAAGCGAAGCCGCAGAGGCTGCCTCAAAAGCAGCAGAACT
GGCACAAAGGCACCCAGACAGCCAGGCTGCACGGGATGCAATCAA
ACTTGCTTCTCAGGCAGCCGAGGCTGTCAAATTGGCCTGTGAATT
GGCTCAAGAGCATCCGAACGCCGACATTGCAAAATTGTGCATCAA
GGCAGCTTCCGAGGCAGCAGAGGCCGCATCAAAGGCTGCTGAGCT

TGCACAGAGGCATCCTGACTCACAAGCAGCACGCGACGCCATTAA
GTTGGCATCACAGGCCGCAGAAGCCGTCAAGCTCGCCTGTGAACT
TGCACAAGAACATCCCAATGCAGATATCGCAAAACTGTGCATCAA
AGCTGCATCTGAGGCTGCTGAAGCCGCCTCTAAGGCAGCAGAGCT
TGCCCAAAGACATCCCGACTCTCAGGCTGCCCGTGATGCCATTAA
GCTCGCTTCTCAAGCAGCTGAAGCCGTGAAACTTGCCTGCGAGCT
TGCTCAAGAGCATCCTAATGCTGACATAGCTAAACTGTGTATTAA
GGCAGCAAGTGAAGCTGCCGAGGCCGCAAGCAAAGCAGCCGAACT
TGCCCAACGTCACCCTGATAGCCAAGCAGCAAGAGATGCTATCAA
ACTCGCATCCCAAGCTGCAGAGGCAGTGAAACTAGCCTGCGAACT
GGCCCAAGAGCACCCCAATGCCGATATTGCCAAGCTGTGTATCAA
GGCCGCCTCTGAAGCCGCCGAAGCCGCTTCTAAAGCTGCCGAACT
GGCTCAGAGACATCCCGATAGCCAGGCCGCTAGGGATGCTATTAA
GCTGGCTAGTCAGGCCGCTGAGGCCGTGAAACTGGCTTGTGAACT
CGCTCAAGAACACCCTAACGCCAAGATCGCCAAACTGTGCATCAT
TGCCGCCGCTCTGGCTGCCGAGGCTGCATCTAAAGCAGCTGAGCT
GGCCCAGCGGCATCCAGATTCTCAAGCTGCAAGGGACGCCATCAA
ACTGGCCAGCCAAGCTGCTGAAGCAGTCAAGTTGGCTTGCGAGCT
GGCACAAGAACATCCAAACGCTATCATTGCCATCCTGTGCATCGT
GGCCGCTATTGCCGCTGCCATTGCTGCTTCTATGGCTGCTGCTCT
GGCACAGCGTCACCCTGATAGCCAAGCAGCCCGGGATGCAATCAA
GCTCGCTTCTCAGGCAGCAGAAGCCGTCAAACTTGCCTGCGAGCT
TGCTCAAGAGCATCCGAATGCCAAAATCGCCGTGCTGTGCATTCT
GGCTGCAGCACTGGCTGCTATTGCAGCAGCTCTTGCTGCACTGCT
GGCCCAACTTCATCCTGACAGTCAAGCAGCTCGCGACGCCATTAA
GTTGGCATCACAAGCCGCAGAGGCTGTCAAGTTGGCCTGTGAATT
GGCTCAAGAGCATCCAAACGCCGACATTGCCGAGAAGTGCATCCT
GCTGGCTATCCTGGCAGCTCTGCTGGCAATTTTGGCTGCCCTGCT
TGCCATGCTGCACCCCGATTCTGATCTGGCTAGAGCCCTGATCGA
TCTGGCCTCAGAGCTGGCCGAAGAGGTCAAAGAGAGATGCGAACG
GGGTACCAGCGGAATGGTGAGCAAGGGCGAGGAGCTGTTCACCGG
GGTGGTGCCCATCCTGGTCGAGCTGGACGGCGACGTAAACGGCCA
CAAGTTCAGCGTGTCCGGCGAGGGCGAGGGCGATGCCACCTACGG
CAAGCTGACCCTGAAGTTCATCTGCACCACCGGCAAGCTGCCCGT

GCCCTGGCCCACCCTCGTGACCACCCTGACCTACGGCGTGCAGTG
CTTCAGCCGCTACCCCGACCACATGAAGCAGCACGACTTCTTCAA
GTCCGCCATGCCCGAAGGCTACGTCCAGGAGCGCACCATCTTCTT
CAAGGACGACGGCAACTACAAGACCCGCGCCGAGGTGAAGTTCGA
GGGCGACACCCTGGTGAACCGCATCGAGCTGAAGGGCATCGACTT
CAAGGAGGACGGCAACATCCTGGGGCACAAGCTGGAGTACAACTA
CAACAGCCACAACGTCTATATCATGGCCGACAAGCAGAAGAACGG
CATCAAGGTGAACTTCAAGATCCGCCACAACATCGAGGACGGCAG
CGTGCAGCTCGCCGACCACTACCAGCAGAACACCCCCATCGGCGA
CGGCCCCGTGCTGCTGCCCGACAACCACTACCTGAGCACCCAGTC
CGCCCTGAGCAAAGACCCCAACGAGAAGCGCGATCACATGGTCCT
GCTGGAGTTCGTGACCGCCGCCGGGATCACTCTCGGCATGGACGA
GCTGTACAAGGGCCTCGAGCACCACCATCACCATCACTAA

Appendix B

Appendix B: Paper: Proteomic analysis of the actin cortex in interphase and mitosis

Results described in the section Interphase and mitotic cells differ in the protein composition of the actin cortex were used for a manuscript titled Proteomic composition of the actin cortex in interphase and mitosis [Vadnjal et al., 2022]. The manuscript can be found bellow.

© 2022. Published by The Company of Biologists Ltd | Journal of Cell Science (2022) 135, jcs259993. doi:10.1242/jcs.259993

TOOLS AND RESOURCES

Proteomic analysis of the actin cortex in interphase and mitosis

Neza Vadnjal[1,2], Sami Nourreddine[3,‡], Geneviève Lavoie[3], Murielle Serres[1,*], Philippe P. Roux[3,4] and Ewa K. Paluch[1,2,§]

ABSTRACT

Many animal cell shape changes are driven by gradients in the contractile tension of the actomyosin cortex, a thin cytoskeletal network supporting the plasma membrane. Elucidating cortical tension control is thus essential for understanding cell morphogenesis. Increasing evidence shows that alongside myosin activity, actin network organisation and composition are key to cortex tension regulation. However, owing to a poor understanding of how cortex composition changes when tension changes, which cortical components are important remains unclear. In this article, we compared cortices from cells with low and high cortex tensions. We purified cortex-enriched fractions from cells in interphase and mitosis, as mitosis is characterised by high cortical tension. Mass spectrometry analysis identified 922 proteins consistently represented in both interphase and mitotic cortices. Focusing on actin-related proteins narrowed down the list to 238 candidate regulators of the mitotic cortical tension increase. Among these candidates, we found that there is a role for septins in mitotic cell rounding control. Overall, our study provides a comprehensive dataset of candidate cortex regulators, paving the way for systematic investigations of the regulation of cell surface mechanics.

This article has an associated First Person interview with the first author of the paper.

KEY WORDS: Actin, Cell cortex, Cell division, Cortical tension, Mass spectrometry, Septin

INTRODUCTION

Changes in animal cell shape are largely controlled by the actin cytoskeleton. In particular, the actomyosin cortex, a thin (∼150 nm thick) network of actin, myosin and associated proteins underneath the plasma membrane, drives contraction-based cellular deformations (reviewed in Salbreux et al., 2012; Chugh and Paluch, 2018). Contractile tension is generated in the cortex by myosin motors pulling on actin filaments, and increasing cortical tension promotes cell rounding. For instance, a strong increase in cortical tension at the onset of mitosis typically leads cells to round up in prometaphase (Stewart et al., 2011; Cadart et al., 2014). The resulting mitotic rounded shape provides the space required for spindle assembly, positioning, and accurate chromosome separation (reviewed in Lancaster and Baum, 2014). Furthermore, gradients in cortical tension lead to local contractions and induce cell shape changes driving processes such as cell division, cell migration and epithelial morphogenesis (reviewed in Levayer and Lecuit, 2012; Chugh and Paluch, 2018). Given its importance in the regulation of cell shape, it is thus essential to systematically identify the key factors controlling cortical tension.

The role of myosin motors in cortical tension generation has been extensively characterised (Tinevez et al., 2009; Murrell et al., 2015; Ramanathan et al., 2015; Truong Quang et al., 2021). However, a number of recent studies have highlighted the importance of other actin-binding proteins. In particular, regulators of actin filament nucleation and length, as well as crosslinkers, have been shown to play a role in the control of cortical tension (Bergert et al., 2012; Chugh et al., 2017; Ding et al., 2017; reviewed in Koenderink and Paluch, 2018). Furthermore, intermediate filaments have been shown to contribute to the cortical tension increase observed in mitotic cells (Duarte et al., 2019; Serres et al., 2020). Taken together, the emerging view is that cortical tension is controlled by a variety of mechanisms that modulate myosin activity and actin network organisation, as well as cortex interactions with other cytoskeletal networks. However, systematic investigations of cortex tension regulation have been significantly hindered by our limited understanding of how cortical composition changes when tension changes.

In this Tools and Resources article, we set out to systematically investigate which actin-related proteins display different levels at the cortex in cells with high and low cortical tension. To this aim, we analysed the protein composition of actin cortices in cells synchronised in interphase and mitosis, because mitotic cells display considerably higher cortical tension compared to interphase cells (Chugh et al., 2017). We used purified cellular blebs, as we have previously shown that blebs assemble a cortex similar to the cellular cortex, and can be isolated from cells, yielding cortex-enriched cellular fractions (Biro et al., 2013; Bovellan et al., 2014). We compared, using mass spectrometry, the composition of blebs separated from interphase and mitotic cells. We identified 922 different proteins consistently present in blebs from both mitotic and interphase cells, among which 238 were actin-related proteins. Finally, we investigated one of the candidates identified, the septin family of proteins, and showed that septins regulate mitotic cell rounding, highlighting the potential of our dataset to identify new cortex and cell shape regulators. Taken together, our systematic analysis generates a list of candidate regulators of the cortical remodelling taking place at mitosis entry. It also identifies septins, and in particular septin 9, as important regulators of cortex-driven cell rounding at the transition between interphase and mitosis.

[1]Laboratory for Molecular Cell Biology, University College London, London WC1E 6BT, UK. [2]Department of Physiology, Development and Neuroscience, University of Cambridge, Cambridge CB2 3DY, UK. [3]Institute for Research in Immunology and Cancer, Université de Montréal, Montreal QC, H3T 1J4, Canada. [4]Department of Pathology and Cell Biology, Faculty of Medicine, Université de Montréal, Montreal, QC, H3T 1J4, Canada.
*Present address: Institut Pasteur, 75015 Paris, France. ‡Present address: Department of Bioengineering, University of California San Diego, La Jolla, CA 92093-0412, CA, USA.

§Author for correspondence (ekp25@cam.ac.uk)

N.V., 0000-0003-4790-0068; P.P.R., 0000-0002-5962-0250; E.K.P., 0000-0003-4691-2323

Handling Editor: Michael Way
Received 4 March 2022; Accepted 7 July 2022

Journal of Cell Science (2022) 135, jcs259993. doi:10.1242/jcs.259993

RESULTS

Isolation of actin cortex-enriched blebs from cells synchronised in interphase and mitosis

We obtained synchronised rounded interphase (low cortex tension) and mitotic (high tension) cells using a protocol previously used in our laboratory (Chugh et al., 2017). Specifically, to enrich for cells in interphase, HeLa cells were synchronised in G1/S phase using thymidine (Fig. 1A, see Materials and Methods for details). Synchronised interphase cells were then detached and maintained in suspension (Fig. 1B, upper panel). To obtain mitotic cells, HeLa cells were synchronised in prometaphase using S-trityl-L-cystine (STLC). Mitotic cells were further enriched by mechanically separating them from adherent cells through a mitotic shake-off (Fig. 1B, bottom panel). We have previously shown that following this protocol, rounded interphase cells display a continuous cortex that can be compared to the cortex of mitotic cells, but display a cortical tension four-fold lower than mitotic cells, as measured by atomic force microscopy flat cantilever compression (Chugh et al., 2017). Finally, we checked synchronisation efficiency by DNA staining of the synchronised cell populations (Fig. 1B), and by immunoblotting for levels of the mitotic markers phosphorylated histone H3 and cyclin B (Fig. 1C). This confirmed that our synchronisation procedure yielded cell populations of predominantly rounded interphase and mitotic cells.

We then purified blebs to enrich for actin cortex components from synchronised rounded cells (Fig. 1D) by adapting a protocol we previously established (Biro et al., 2013; see Materials and Methods for details). In brief, blebbing was induced using the actin depolymerizing drug latrunculin B (Spector et al., 1983) and blebs were detached from cells by shear stress. We observed that mitotic HeLa cells yielded much fewer isolated blebs than the constitutively blebbing M2 cells used in previous studies (Biro et al., 2013; Bovellan et al., 2014). To account for this limited output, we considerably increased the amounts of cells used. Furthermore, in our protocol, blebs were isolated from non-adherent cells; we thus added a stringent filtration step to ensure the removal of entire cells from the cortex preparation (Fig. 1D). As previously described (Biro et al., 2013), latrunculin B was washed out (at Step 4, Fig. 1D), the bleb membrane was permeabilised with haemolysin A, and an exogeneous creatine phosphate-based ATP regeneration system was added to the buffer to facilitate cortex re-assembly (Step 6 in Fig. 1D, see Materials and Methods for details). We then imaged actin in samples of isolated blebs from each replicate prior to mass spectrometry. The blebs displayed a clearly defined actin cortex, confirming that the isolated blebs contain all the components required for successful cortex assembly (Fig. 1E; Fig. S1A). Furthermore, we confirmed that bleb lysates were enriched in actin and actin-binding proteins and displayed lower levels of nuclear proteins compared to what was found in whole-cell lysates (Fig. S1B). Taken together, our data show that this purification protocol successfully isolated cortical fractions from cells synchronised in interphase and mitosis.

Proteomic analysis of actin cortex-enriched blebs from interphase and mitotic cells

To identify proteins potentially involved in the regulation of cortical tension, we analysed blebs isolated from interphase and mitotic cells using liquid chromatography (LC)-tandem mass spectrometry (LC-MS/MS). For this, purified blebs from three biological replicates for each condition were lysed in denaturing Laemmli buffer and proteins were resolved by SDS-PAGE (Fig. 2A). Proteins were then subjected to in-gel trypsin digestion, and purified peptides were analysed by LC-MS/MS. Overall, we identified 117,088 unique peptides from 2268 unique proteins in interphase and mitosis (Fig. 2B,C; Table S1). To account for variations between experiments, the total number of spectra identified for each protein was normalised to the total spectral count detected within each replicate, using the first interphase replicate as a reference (see Materials and Methods for details). For further analysis, we only considered proteins that were detected from at least two unique peptides and with an average spectral count of two or higher in triplicates from both phases of the cell cycle, narrowing down the list to 922 proteins (Fig. 2D; Table S2). These criteria allowed us to focus on proteins that were consistently and reliably detected in our samples. Furthermore, focusing on proteins present in both interphase and mitosis eliminated multiple nuclear proteins that were detected at high levels in mitotic blebs but absent in interphase blebs (Table S1), likely due to increased cytoplasmic levels of nuclear components following nuclear envelope breakdown. Out of the 922 proteins selected, myosin heavy chain IIA (MYH9), actin (ACTG1) and filamin A (FLNA) were the most abundant based on spectral counts, which reflect both protein abundance and size (Fig. 2E). Of note, differentiating actin isoforms in mass spectrometry is challenging because of the high degree of conservation between isoforms (98.9% amino acid identity between ACTG1 and ACTB for instance), and resulting high degree of overlap between identified peptides. Thus, ACTG1 corresponds to various actin isoforms present in our samples. Overall, many of the most abundant proteins identified were actin-related proteins (Fig. 2E, bright pink dots).

To globally characterise the composition of the identified protein dataset, we next performed a Gene Ontology (GO) analysis for cellular components, molecular functions and biological processes (Fig. 2F; Fig. S1C,D). Cellular component GO terms describing actin filament (P=4.7×10^{-11}), actomyosin (P=3.8×10^{-14}), cell cortex (P=1.6×10^{-25}) and actin cytoskeleton (P=3.7×10^{-38}) were enriched for in our dataset (Fig. 2F). Analysis of molecular functions and biological processes GO terms further supports a high representation of actin-related proteins in isolated blebs (Fig. S1C, D). Taken together, our observations suggest that isolated blebs are indeed enriched in actin cortex components, and are thus a good model system to compare cortex composition between interphase and mitosis.

Analysis of actin-related proteins in cortex-enriched blebs from interphase and mitotic cells

To identify potential regulators of cortical tension, we next compared the levels of individual proteins detected in blebs isolated from cells in interphase and mitosis (Fig. 3A; Table S2). Only 180 out of the 922 proteins detected displayed a significant difference in protein levels between interphase and mitosis (corresponding to a P<0.05 data points above the dashed line in Fig. 3A), suggesting that cortex composition is largely similar between these two phases of the cell cycle. To narrow down our candidate list, we focused on actin-related proteins. These were selected based on a previously published list of F-actin-binding proteins identified by pull-down of F-actin-binding cellular fractions (Serres et al., 2020), complemented by manual curation to select further actin-related factors. Based on these criteria, we found 238 actin-related proteins in the cortex-enriched blebs (bright pink dots on Fig. 3A,B; Table S3). This narrowed down list included many proteins known to directly bind and regulate actin filaments, as well as membrane and adhesion proteins, the intermediate filament proteins vimentin and keratin, and various Rho-GTPases

Journal of Cell Science (2022) 135, jcs259993. doi:10.1242/jcs.259993

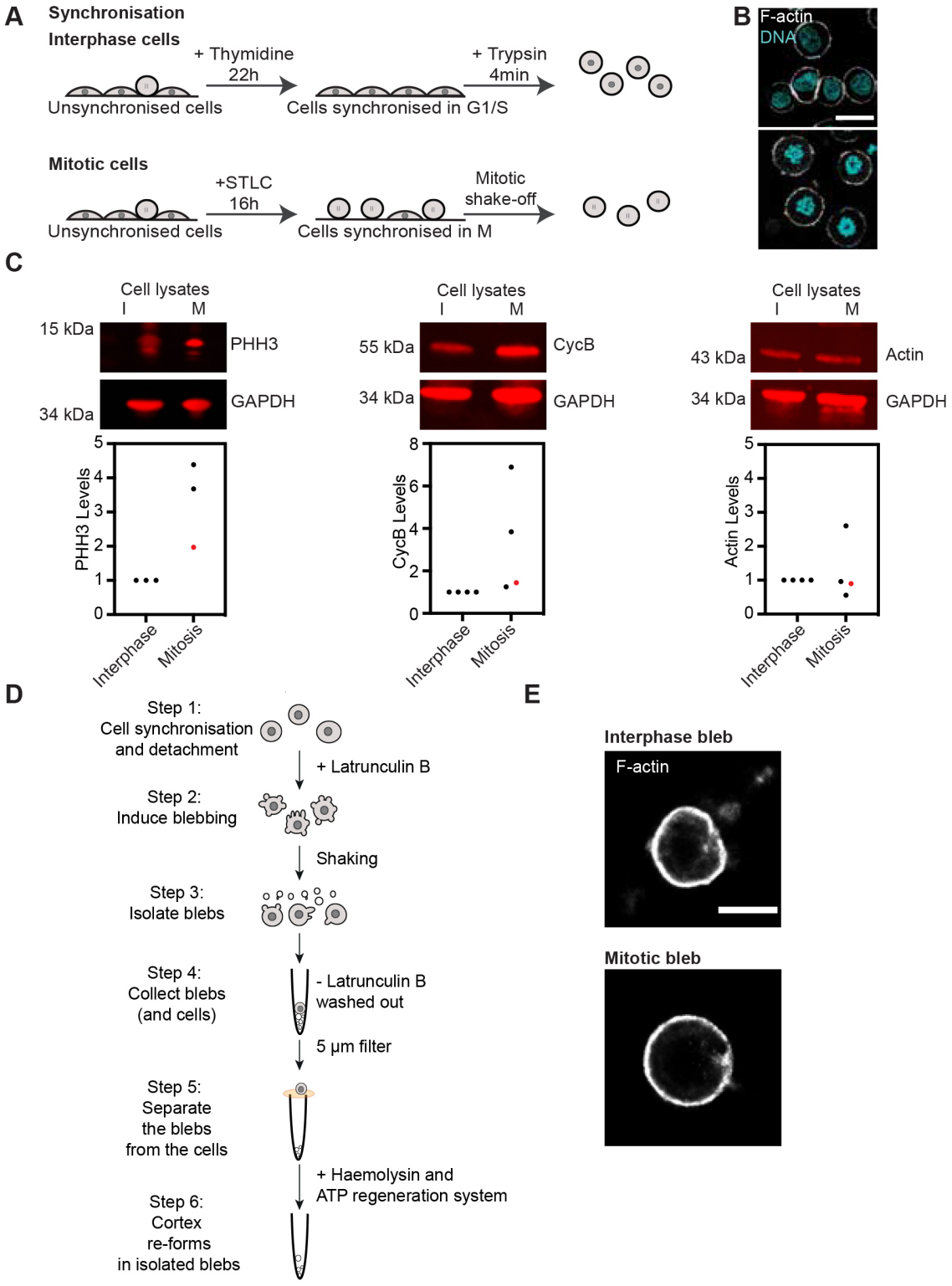

Fig. 1. See next page for legend.

and their regulators. Notably, the other proteins found in blebs included tubulins and microtubule-binding proteins, as well as multiple factors involved in intracellular trafficking, which might also indirectly interact with the actin cortex (Tables S1, S2). Out of the 238 identified actin-related proteins, 54 significantly changed in levels between interphase and mitotic blebs to a $P<0.05$. Although this cut-off is somewhat arbitrary given the small number of experimental replicates inherent to a mass spectrometry study, this reduced list (Table 1) represents actin-related proteins that most consistently changed levels in cortex-enriched blebs between interphase and mitotic cells. Finally, we verified that there was a high degree of reproducibility between experimental replicates in

Journal of Cell Science

Fig. 1. Isolation of cortex-enriched blebs from interphase and mitotic cells. (A) Schematic describing cell synchronisation in interphase (top) and mitosis (bottom). Prior to bleb isolation, cells were synchronised in interphase (G1/S phase) with a 22 h thymidine treatment, detached from the dish and rounded up using trypsin. For synchronisation in mitosis, the cell population was first enriched for mitotic cells with a 16 h treatment with the Eg5 inhibitor STLC, which prevents bipolar spindle formation, followed by a mitotic shake-off. (B) Representative confocal images of synchronised interphase (upper panel) and mitotic (lower panel) cells. Cyan, DAPI (DNA); white, phalloidin (F-actin). DAPI staining shows nuclear organisation of DNA in cells synchronised in interphase and condensed chromosomes in cells synchronised in mitosis. Scale bar: 20 µm. (C) Representative fluorescent western blots (upper panels), and related quantifications (lower panels) of mitotic markers [phosphorylated histone H3 (PHH3) and cyclin B] and actin levels (control) in interphase and mitotic cell lysates, confirming cell cycle phase synchronisation at the cell population level. Membranes are representative of n=4 samples used for quantification. GAPDH, loading control. For quantification, protein levels were normalised to the loading control (GAPDH) and interphase conditions. Red datapoints on graphs correspond to the samples represented in the images of western blot membranes (upper panels). (D) Schematic depicting the bleb isolation protocol. Blebs were isolated from round cells synchronised in interphase or mitosis (as described in A) (step 1). Blebbing was induced with treatment with the actin depolymerising drug latrunculin B (step 2). Blebs were detached from the cells with shear stress (step 3) and separated blebs were isolated from the cells using a 5 µm filter (steps 4, 5). Re-assembly of a dynamic actin cortex was induced in blebs through addition of a creatine phosphate-based ATP regeneration system and the alpha-toxin haemolysin, to permeabilise the bleb membranes to allow for ATP regeneration system uptake (step 6, see Materials and Methods for details). Step 1 was performed at 37°C and steps 2–6 were performed at room temperature. (E) Stochastic optical reconstruction microscopy (STORM) of the actin cortex in blebs isolated from interphase (upper panel) and mitotic (lower panel) cells. Isolated blebs were pre-treated with the ATP regeneration system (steps 5, 6 in D) prior to imaging. White, phalloidin (F-actin). Scale bar: 2 µm. Images in B and E are representative of three independent experiments.

our mass spectrometry analysis of the identified 54 proteins (Fig. S2A,B).

Several of the identified proteins had previously been shown to change levels between interphase and mitosis (Fig. 3C). In particular, we found that the levels of cyclin-dependent kinase 1 (CDK1), a known cell cycle regulator that increases in mitosis (Lee and Nurse, 1987), and anillin, a cortical protein that translocates from the nucleus to the actin cortex in mitosis (Field and Alberts, 1995) were higher in mitotic compared to interphase blebs. Furthermore, the intermediate filament protein vimentin displayed strongly increased levels in mitotic blebs, consistent with recent findings demonstrating a role for vimentin in the mitotic cortex (Duarte et al., 2019; Serres et al., 2020). Finally, caldesmon displayed lower levels in mitotic compared to interphase blebs, consistent with previous observations showing that caldesmon dissociates from actin filaments during mitosis (Yamashiro et al., 1990). Together, these observations suggest that our mass spectrometry analysis successfully identifies proteins for which cortical levels change between interphase and mitosis.

We then compared the changes in bleb protein levels between interphase and mitosis to a published dataset reporting changes in protein levels in whole-cell lysates of interphase and mitotic HeLa cells (Heusel et al., 2020) (Fig. S2C). We focused on the 54 proteins reported in Table 1. Interestingly, although most of the proteins that increased in mitotic blebs also increased in cells, for most proteins, the extent of the increase was higher in blebs than in cells. Furthermore, most proteins that showed decreased levels in mitotic blebs, displayed increased levels in mitotic cells. Together, these observations suggest that differences in cortical composition between interphase and mitosis are not only the result of differences in expression levels, but are tightly regulated through differential cortical recruitment.

Finally, we further scrutinised our dataset by comparing our list of 238 actin-related cortical proteins to a published targeted screen of proteins involved in the generation of the mitotic rounding force (Toyoda et al., 2017). We found that 103 out of the 238 actin-related proteins detected in blebs had been tested in this mechanical screen. Out of these, 10 were shown to reproducibly and significantly reduce mitotic rounding force upon depletion (Table S3). These 10 regulators of cortex mechanics included the heavy chain of non-muscle myosin IIA (MYH9), which served as a positive control in the mechanical screen (Toyoda et al., 2017), upstream regulators of actomyosin dynamics (RAC1 and ROCK2), the septin SEPT9, and proteins involved in the control of actin organisation. This last category included proteins affecting actin polymerisation and nucleation (DIAPH1, PFN1, DBN1 and CYFIP1), and actin bundling and crosslinking (ACTN4 and FSCN1). Mechanisms of how actin length regulators (e.g. DIAPH1 and PFN1) and crosslinkers (e.g. ACTN4) affect force generation in actomyosin networks have been explored previously (Logue et al., 2015; Ennomani et al., 2016; Chugh et al., 2017). Furthermore, MYH9 and SEPT9 were the only two proteins out of the 10 cortex mechanics regulators to also show a significant change in cortical levels in our mass spectrometry analysis (Table 1). We thus decided to focus on the role of septins, and septin 9 in particular, in cortex regulation for the rest of the study.

A role for the septin protein family in the regulation of the mitotic cortex

We next asked whether septins could play a role in the regulation of the cortex reorganisation between interphase and mitosis. Septins 2 and 9 have been previously shown to localise to the prometaphase cell cortex (Estey et al., 2010), but their role at the mitotic cortex remains unclear. Interestingly, our data indicate that the levels of several members of the septin family increase at the cortex between interphase and mitosis, with septin 8 and 9 displaying the most significant increase (Figs 3A and 4A). Proteins of the septin family assemble into higher-order structures, including filaments, and are increasingly considered a component of the cytoskeleton (reviewed in Mostowy and Cossart, 2012; Spiliotis, 2018). Septins are generally classified into four different homology subgroups (SEPT2, SEPT3, SEPT6 and SEPT7), with members of the same subgroup displaying some redundancy for the formation of oligomers and filaments. Septin 9 is the only member of the SEPT3 subgroup detected in blebs, and it also displayed a statistically significant change in cortical levels between interphase and mitosis in our analysis (Figs 3A and 4A, Table 1) and its depletion has been shown to significantly decrease mitotic rounding forces in a mechanical screen (Toyoda et al., 2017). We thus decided to first investigate the role of septin 9 in the regulation of the mitotic cortex.

We first assessed whole-cell levels of septin 9 and found that not only cortical (Fig. 4A) but overall septin 9 levels increase between interphase and mitosis (Fig. S3A), suggesting that septin 9 might play an important role in cell division. We thus depleted septin 9 (Fig. 4B,C) and examined the resulting effects on the cortex-driven mitotic rounding by analysing cell shape and cell division dynamics using live-cell imaging (Fig. 4C–E; Fig. S3B–D, Movies 1, 2). Septin 9-depleted cells showed strong mitotic rounding defects affecting metaphase cell shape and rounding time, whereas the cleavage ingression time was not significantly affected (Fig. 4D,E, Fig. S3C,D). In particular, septin 9-depleted cells took slightly

Journal of Cell Science (2022) 135, jcs259993. doi:10.1242/jcs.259993

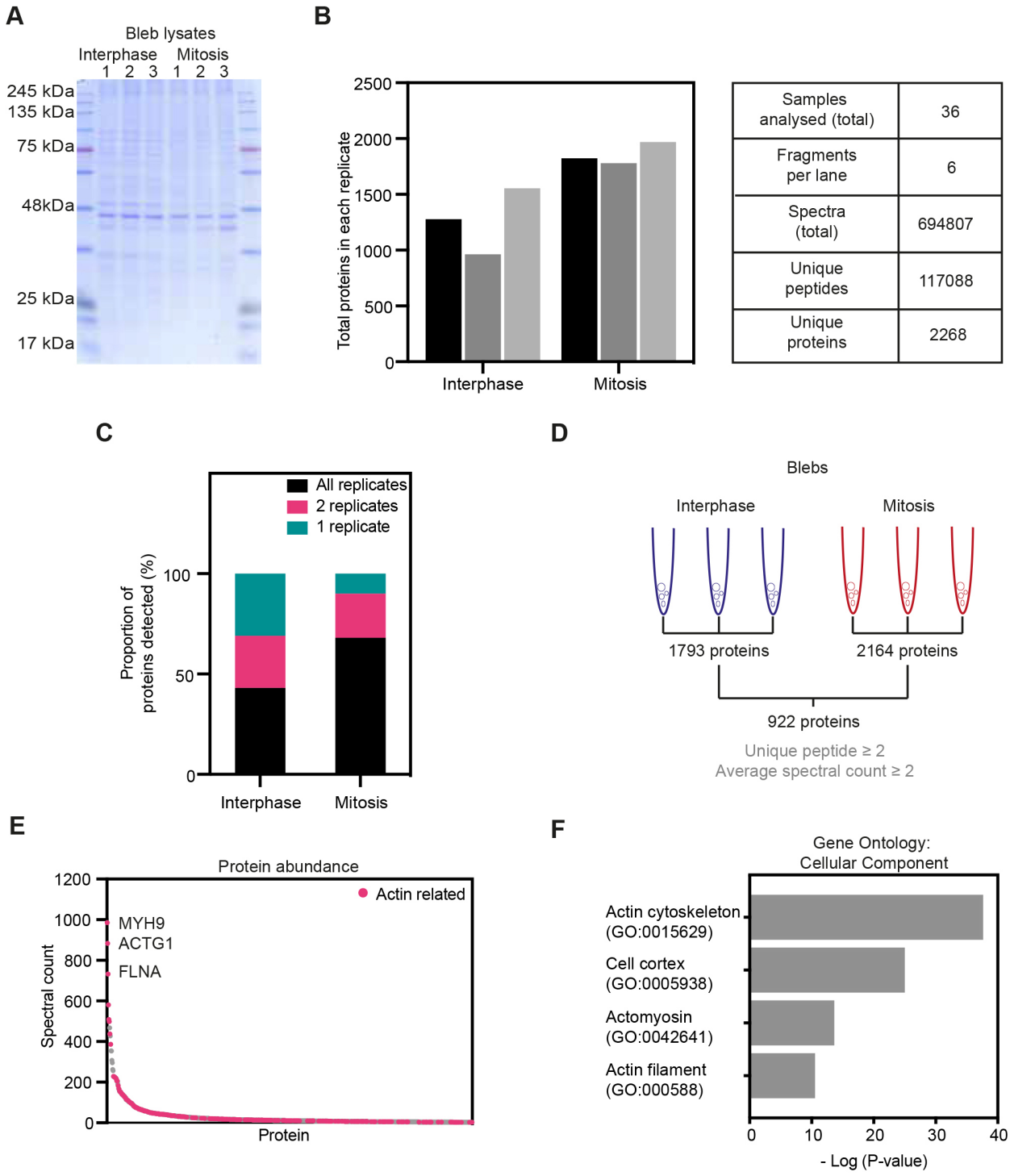

Fig. 2. Proteomic analysis of blebs isolated from interphase and mitotic cells. (A) Coomassie staining of isolated blebs from interphase and mitosis in the three experimental replicates used for mass spectrometry. (B) Quantification of the number of proteins (left) and other overall readouts of the mass spectrometry analysis of samples from A. (C) Percentage of proteins detected in all, two or one of the replicates. (D) Schematic summarising the process of protein selection for further analysis. Mass spectrometry detected 1793 and 2164 different proteins in blebs isolated from interphase and mitotic cells, respectively. Out of these, 922 proteins with a unique peptide number above 2 and normalised spectral count above 2 were present in both interphase and mitotic blebs; these proteins were selected for further analysis. (E) Average normalised spectral counts in all (three per condition) replicates from interphase and mitotic blebs of the 922 proteins selected as described in D. Bright pink dots, actin-related proteins. The proteins with the highest average spectral count were myosin heavy chain IIA (MYH9), actin (ACTG1) and filamin A (FLNA). (F) Gene Ontology (GO) analysis of the selected 922 proteins, focusing on GO terms for 'cellular components' related to cell surface enrichment.

Journal of Cell Science (2022) 135, jcs259993. doi:10.1242/jcs.259993

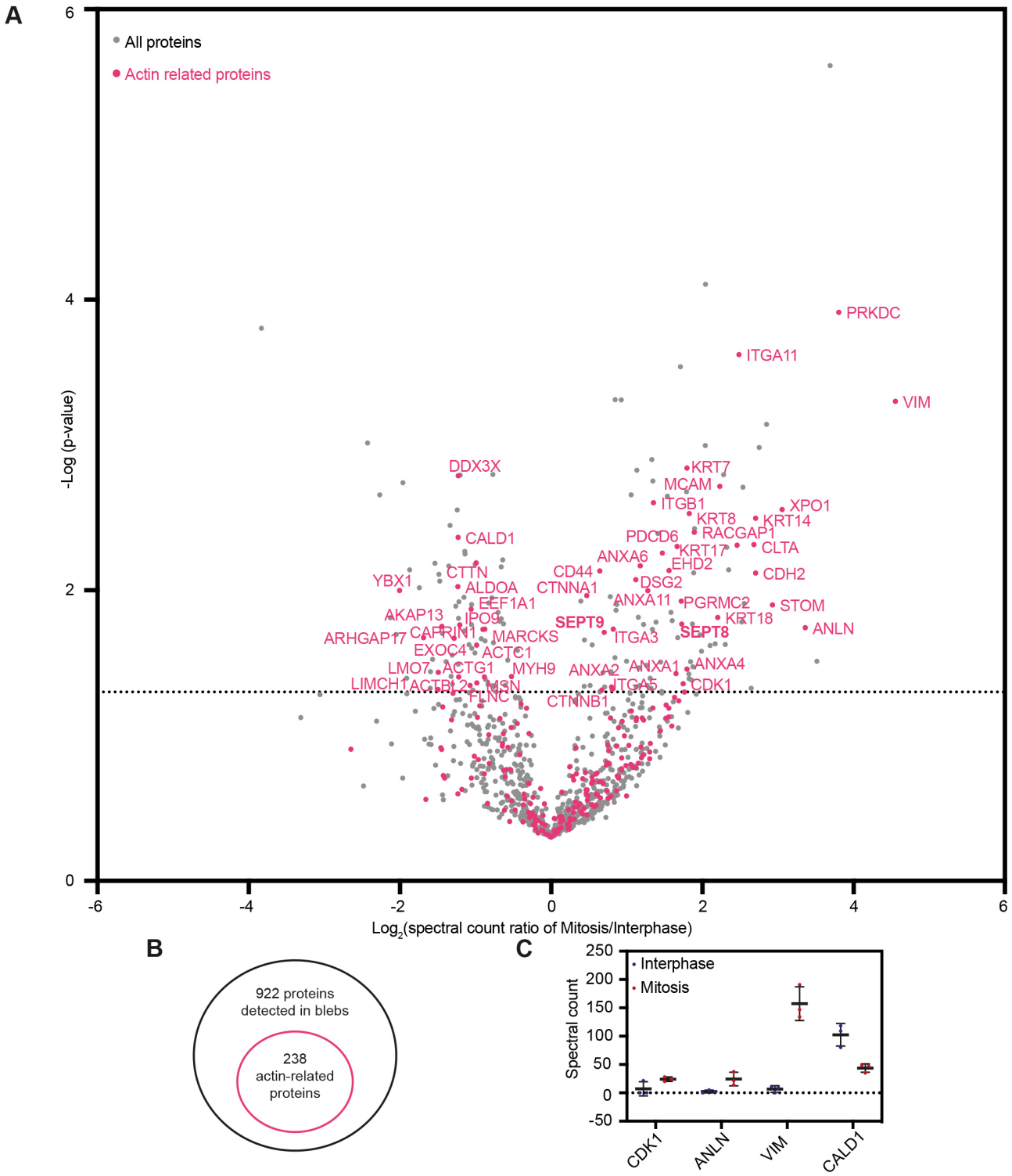

Fig. 3. Changes in cortical levels of actin-binding proteins between interphase and mitosis. (A) Volcano plot of the 922 selected proteins detected in blebs, showing the enrichment (*x*-axis) and the significance of this enrichment (*P*-values, *y*-axis) between interphase and mitosis. Dotted line highlights $-\log_{10}$ (*P*-value)=1.3, corresponding to *P*-value=0.05; three independent replicates; statistics unpaired one-tailed Student's *t*-test. Bright pink dots: actin-related proteins. (B) Schematic of actin-related proteins among all proteins detected in blebs. (C) Spectral counts in the mass spectrometry analysis of mitotic and interphase blebs for proteins known to change in levels at the cortex between interphase and mitosis. Each data point corresponds to an individual replicate, with mean±s.d. shown. Spectral counts were normalised to account for variation between experiments.

longer to round up at the onset of mitosis (Fig. S3D) and displayed larger and less circular equatorial shapes in metaphase (as imaged in the cellular midplane, Fig. 4C–E), as well as a significantly higher aspect ratio (Fig. S3C) compared to control cells. Taken together, our dataset identifies septin 9 as an important regulator of cell rounding at the onset of mitosis.

Journal of Cell Science (2022) 135, jcs259993. doi:10.1242/jcs.259993

Table 1. Actin-related proteins detected in isolated blebs showing a significant difference in levels between interphase and mitosis

Protein symbol	Ratio of spectral count (Mitosis/Interphase)	*P*-value	Mitotic rounding force changes
Enriched in mitotic cortex fraction			
VIM	23.49	0.00050	n.t.
PRKDC	13.96	0.00012	n.t.
ANLN	10.27	0.018	no change
XPO1	8.31	0.0028	n.t.
STOM	7.61	0.013	n.t.
KRT14	6.52	0.0032	n.t.
CDH2	6.51	0.0076	n.t.
CLTA	6.42	0.0048	n.t.
ITGA11	5.60	0.00024	no change
KRT17	5.50	0.0049	n.t.
MCAM	4.69	0.0019	n.t.
KRT18	4.61	0.015	n.t.
RACGAP1	3.72	0.0040	no change
KRT8	3.55	0.0030	n.t.
ANXA4	3.47	0.035	n.t.
KRT7	3.47	0.0014	n.t.
CDK1	3.35	0.044	no change
SEPT8	3.31	0.017	potentially lower force
PGRMC2	3.30	0.012	n.t.
PDCD6	3.17	0.0050	n.t.
ANXA1	3.14	0.037	n.t.
EHD2	2.95	0.0073	n.t.
ITGAV	2.77	0.0055	no change
ITGB1	2.55	0.0025	no change
ANXA11	2.43	0.010	n.t.
ANXA6	2.26	0.0068	n.t.
DSG2	2.17	0.0084	n.t.
ITGA3	1.77	0.018	no change
ITGA5	1.75	0.048	no change
ANXA2	1.74	0.046	n.t.
SEPT9	1.63	0.019	lower force
CTNNB1	1.59	0.049	no change
CD44	1.56	0.0074	n.t.
CTNNA1	1.39	0.011	no change
Enriched in interphase cortex fraction			
YBX1	0.25	0.01	n.t.
ARHGAP17	0.31	0.021	n.t.
LIMCH1	0.35	0.048	n.t.
LMO7	0.36	0.037	n.t.
AKAP13	0.37	0.018	n.t.
EXOC4	0.41	0.021	n.t.
ALDOA	0.43	0.0094	no change
CALD1	0.43	0.0043	no change
DDX3X	0.43	0.0016	n.t.
ACTG1	0.43	0.039	no change
IPO9	0.43	0.017	n.t.
ACTBL2	0.48	0.045	n.t.
EEF1A1	0.48	0.014	n.t.
CTTN	0.50	0.0065	n.t.
ACTC1	0.51	0.024	no change
FLNC	0.51	0.043	n.t.
CAPRIN1	0.53	0.019	n.t.
MSN	0.54	0.039	no change
MARCKS	0.54	0.019	no change
MYH9	0.70	0.039	lower force

Fold-change and exact *P*-values were calculated from normalised spectral counts detected in blebs in three experimental replicates. Statistics: unpaired one-tailed Student's *t*-test. Right column, rounding force changes upon protein depletion, as reported in Toyoda et al. (2017); n.t., not tested – protein not examined in the mechanical screen in Toyoda et al. (2017); no change, protein for which no change was detected with any of the esiRNA tested; potentially lower force, protein for which the change in rounding force was detected with some but not all of the esiRNA sequences tested; lower force, protein for which rounding force changed with all esiRNA sequences tested in Toyoda et al. (2017).

Finally, we asked whether members of other septin homology groups also affected mitotic shape (Fig. S4). We tested how depletion of other septins affected metaphase cell circularity, as well as rounding and ingression times. We focused on septin 2 and septin 7, the only representatives of the SEPT2 and SEPT7 septin homology groups detected in isolated blebs (Fig. 4A), and septin 8, the member of the SEPT6 homology group that displayed the most significant change in levels between interphase and mitotic blebs (Fig. 4A; the other members of the SEPT6 group detected in blebs were septin 6, septin 10 and septin 11). We found that depletion of septin 2, septin 7 and septin 8 resulted in decreased equatorial circularity in metaphase cells, but we observed no significant change in mitotic rounding or ingression times with the exception of a slight increase in ingression time upon septin 7 depletion (Fig. S4B–D). Finally, to exclude potential compensation effects between different septins, we tested, using quantitative (q)PCR, how depletion of specific septins affected expression levels of other septins (Fig. S4A). Even though, following depletion of specific septins, slight changes in levels of some of the other septins were detected, these changes were small and did not suggest any clear pattern of compensation. Taken together, our data suggest that multiple members of the septin protein family act together to affect cell shape mechanics in early mitosis, highlighting the effectiveness of our dataset for identification of cell surface mechanics regulators.

DISCUSSION

Here, we compared the composition of the actin cortex between interphase and mitosis, through mass spectrometry of cellular blebs isolated from synchronised rounded interphase and mitotic cells. Our previous work has shown that our purification protocol yields blebs displaying a cortex similar to the cellular cortex, as assessed by confocal and scanning electron microscopy, and that the isolated blebs display active contractions, confirming the presence of contractility regulators (Biro et al., 2013; Bovellan et al., 2014). We have verified that blebs isolated from cells synchronised in interphase and mitosis re-assemble an actin cortex (Fig. 1E; Fig. S1A), and are enriched in cortical components and depleted in nuclear components (Fig. S1B). Directly measuring cortical tension in isolated blebs is technically challenging due to their small size. Nonetheless, we observed that the blebs isolated from interphase cells tended to display less round shapes than those isolated from mitotic cells (see Fig. 1E for an example), suggesting that interphase blebs might display a lower cortical tension. Taken together, our observations indicate that bleb isolation constitutes a simple protocol for the purification of cellular fractions enriched for actin cortex components from interphase (low cortical tension) and mitotic (high cortical tension) cells. As a result, unlike previous studies where the protein composition of whole-cell lysates (Heusel et al., 2020) or re-polymerised F-actin-binding fractions (Serres et al., 2020) were compared between interphase and mitosis, our approach directly compares cortex-enriched cellular fractions. As such, our study can detect differences in protein levels at the cortex that are due to changes in either protein expression or protein localisation (Fig. S2C).

Our study identifies a dataset of 922 proteins detected in both interphase and mitotic blebs, out of which 238 are actin related. These 238 proteins represent a candidate list for the regulation of the cortex remodelling upon mitosis entry (Table S3). Analysis of our candidate list pointed to the septin family as a potential and underexplored regulator of the mitotic cortex. Septins were first identified as key regulators of yeast cytokinesis (reviewed in Gladfelter et al., 2001). In mammalian cells, several septins have also been shown to interact with actomyosin networks and with the plasma membrane (reviewed in Spiliotis and Nakos, 2021).

Journal of Cell Science (2022) 135, jcs259993. doi:10.1242/jcs.259993

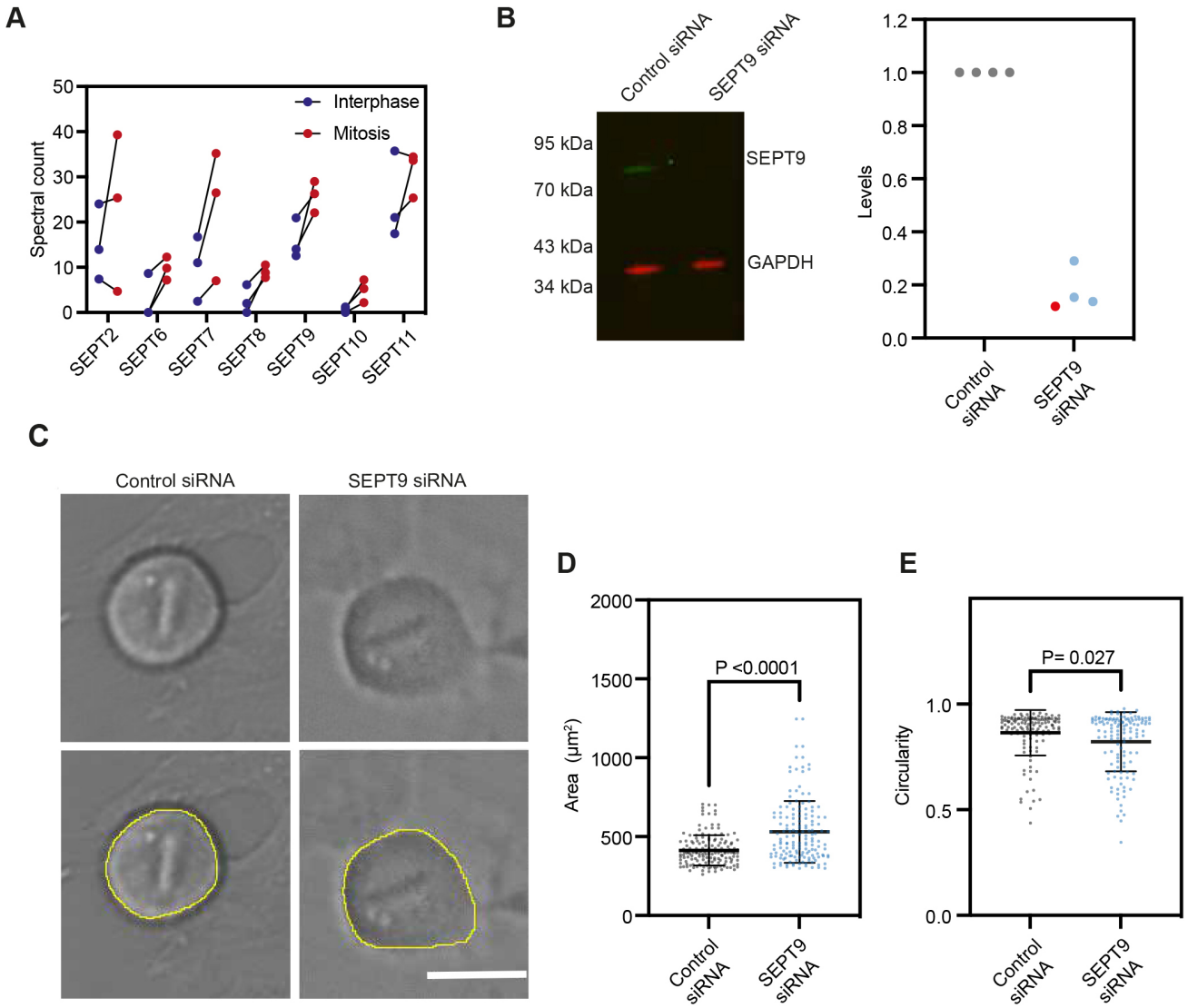

Fig. 4. Septin 9 regulates mitotic rounding. (A) Normalised spectral counts for septins detected in the mass spectrometry analysis of interphase and mitotic blebs; each data point corresponds to an individual replicate. Unpaired one-tailed Student's *t*-test: *P*-values= 0.26, 0.050, 0.12, 0.017, 0.019, 0.024, 0.18 for SEPT2, 6, 7, 8, 9, 10 and 11, respectively. (B) Representative fluorescence western blot (left) and quantification (right) showing the decrease in septin 9 levels upon siRNA treatment. Membrane is representative of n=4 samples used for quantification. For quantification, protein levels were normalised to the loading control (GAPDH) and control siRNA conditions. Red datapoint on graph corresponds to the sample on the western blot membrane image (left panel). (C) Brightfield images of the cellular midplane of live mitotic cells treated with control and SEPT9 siRNA and example of manual segmentation (lower panel), that were used to analyse cell shape parameters. (D,E) Quantification of cell area (D) and circularity (defined as 4π*area/perimeter^2, E) in mitosis of control and SEPT9 siRNA-treated cells. Scale bar: 20 µm. Graph, mean±s.d., three independent experiments, n=156 (area), n=126 (circularity) cells for each control and SEPT9 siRNA-treated cells. Statistics, Mann–Whitney test.

Depletion of septins 2, 7 and 11 has been shown to affect cleavage furrow ingression, leading to multinucleated cells (Estey et al., 2010). In particular, septin 2 colocalises with non-muscle myosin II in dividing cells, potentially acting as a scaffold to promote myosin phosphorylation during cytokinesis (Joo et al., 2007). Furthermore, septin 9 depletion has been shown to interfere with midbody abscission following cytokinesis but did not affect cytokinesis (Estey et al., 2010; Kim et al., 2011). Interestingly, although septin 9 and septin 2 localise to the mitotic cortex during prometaphase (Estey et al., 2010), whether septins also affect the cortex and cellular shape during earlier stages of mammalian cell division, prior to cytokinesis, had previously received little attention. Our study suggests that septins already regulate the cortex in the very early stages of mitosis, and contribute to the changes in cell surface mechanics that drive cell rounding. We showed that members of all four septin homology groups affect metaphase cell shape. Septins from different groups are required for the formation of septin oligomers and filaments (reviewed in Mostowy and Cossart, 2012). How exactly specific septins are recruited to the mitotic cortex, and whether they regulate mitotic cortex mechanics and resulting cell rounding independently or act together through the formation of multimeric complexes and higher order structures, will constitute interesting avenues for future studies.

The identification of septins as regulators of the cortex-driven cell shape changes at mitosis entry highlights the potential of the dataset we generated in detecting important cortex regulators

among the multiple cortical components. More broadly, by systematically comparing the composition of the mitotic and interphase actin cortex, our study will be an important resource for investigations of mitotic shape changes, and of actin cortex mechanics in general.

MATERIALS AND METHODS

Cell culture, cell synchronization and siRNA treatment

HeLa cells from MPI-CBG Technology Development Studio (TDS) were cultured in DMEM Glutamax (Thermo Fisher Scientific) supplemented with 10% fetal bovine serum (FBS; Thermo Fisher Scientific), 1% penicillin-streptomycin (Thermo Fisher Scientific) and 1% L-glutamine (Thermo Fisher Scientific). For passaging, cells were detached from culturing flasks with Trypsin-EDTA (Thermo Fisher Scientific). Cells were regularly tested for mycoplasma.

Cells were synchronised in interphase with 2 mM thymidine for ∼22 h, and in prometaphase with 2 µM S-trityl-L-cystine (STLC) for ∼16 h. Mitotic cells were further enriched by undertaking a mitotic shake-off. Thymidine and STLC were removed from the cells before bleb isolation.

For siRNA-mediated depletion, cells were transfected with ON-TARGET plus Human SEPT9 pool siRNA (Horizon Discoveries, 006373-00), ON-TARGET plus Human SEPT2 pool siRNA (Horizon Discoveries, 010614-00), ON-TARGET plus Human SEPT7 pool siRNA (Horizon Discoveries, 011607-00), ON-TARGET plus Human SEPT8 pool siRNA (Horizon Discoveries, 010647-00) or non-targeting control pool siRNA (Horizon Discoveries, 001810-10) using Lipofectamine™ RNAiMAX Transfection Reagent (Thermo Fisher Scientific) in antibiotic-free medium. Overnight imaging was performed 24–48 h after siRNA treatment and SEPT9 levels were checked by western blotting 48 h after the treatment.

Bleb isolation

Blebs were isolated from either mitotic cells synchronised with STLC and detached by undertaking a mitotic shake-off, or from cells synchronised in interphase with thymidine and detached with trypsin (at 37°C). Trypsin was deactivated through a dilution with cell culturing medium, followed by centrifugation at 164 ***g*** for 3 min and exchanging medium for fresh culturing medium. Blebbing was induced by addition of either 1.7 µM (interphase) or 2.4 µM (prometaphase) of latrunculin B (Sigma Aldrich), immediately followed by shaking on a horizontal benchtop shaker for 15 min at room temperature to detach the blebs from the cells. Latrunculin was then washed out through centrifugation of isolated blebs (and cells) at 4410 ***g*** for 6 min and re-suspension in intracellular buffer (0.01 M sodium chloride, 0.28 M pH 7.2 L-glutamic acid, 0.014 M magnesium sulphate, 0.013 M calcium chloride, 0.020 M pH 6.8 EGTA, 0.04 M pH 7.2 HEPES, in distilled H_2O; potassium hydroxide to adjust the pH of L-glutamic acid, EGTA and HEPES). To separate entire cells and isolated blebs, cells were firstly pelleted with a 4 min centrifugation at 100 ***g***. The supernatant was then filtered with 5 µm Satorious Minisart filters (FIL6602, Minisart) to remove remaining cells and any larger debris. Collected blebs were then pelleted with a centrifugation at 16,100 ***g*** for 5 min and incubated in a solution containing an exogeneous ATP regeneration system (energy mix) and α-toxin to permeabilise the bleb membrane [5% A-haemolysin α-toxin (1 mg ml^{-1}; H9395, Sigma-Aldrich), 2% energy mix (50 mg ml^{-1} UTP, 50 mg ml^{-1} ATP, 255 mg ml^{-1} creatine phosphate), 2% creatine kinase (10 mg ml^{-1}), in intracellular buffer] for 10 min, followed by centrifugation at 16,100 ***g*** for 5 min to remove α-toxin and resuspension of blebs in 500 µl re-suspension buffer (50% intracellular buffer, 44% distilled H_2O, 1% energy mix, 5% creatine kinase) for 20 min. Bleb isolation was performed at room temperature. Purified blebs were then lysed directly in the Laemmli sample buffer and the lysates were prepared for mass spectrometry.

Mass spectrometry

To obtain sufficient material for MS analysis, isolated blebs were prepared from 15 T175 flasks containing cells synchronised in interphase and 60 T175 flasks of cells synchronized in mitosis, in three experimental replicates for each phase of the cell cycle. After bleb isolation, samples were subjected to SDS-PAGE and Coomassie-stained gel bands were excised and subjected to in-gel trypsin digestion, as described previously (Carrière et al., 2008). The resulting peptides were extracted and subjected to capillary LC-MS/MS using a high-resolution hybrid mass spectrometer LTQ-orbitrap XL (Thermo Fisher Scientific). Experiments were performed in triplicates. Database searches were performed against Uniprot SwissProt Human database (containing 20,347 protein entries) using PEAK Studio (version 8.5) as search engine, with trypsin specificity and three missed cleavage sites allowed. Methionine oxidation, lysine acetylation, cysteine carbamidomethylation, serine/threonine/tyrosine phosphorylation and asparagine/glutamine deamidation were set as variable modifications. The fragment mass tolerance was 0.01 Da and the mass window for the precursor was ±10 ppm. The data were visualised with Scaffold (version 4.8.6) and minimum number of peptides per protein was set to two for data analysis. For normalisation, the total number of spectra identified for each protein was divided by the total spectral count detected in the specific replicate considered, and multiplied by the total spectral count detected in the first interphase replicate, thus normalising for experimental variation between replicates.

Gene Ontology and candidate list curation

For GO analysis, the statistical overrepresentation test function from PantherDB (http://www.pantherdb.org/) was used. Actin-related proteins from the bleb extracts were identified by comparing the list with previous mass spectrometry analysis of the F-actin interactome in interphase and mitotic cells (Serres et al., 2020), and by manually adding known actin related proteins.

Western blotting

Cells were lysed directly in Laemmli sample buffer, boiled and sonicated. 30 µg of total protein per sample was loaded on NuPage 4-12% Bis-Tris Protein gels (Thermo Fisher Scientific) or 4–15% Mini-PROTEAN TGX Stain-Free Protein gels (Bio-Rad) and run at 200 V as per the manufacturer's instructions. Proteins were transferred onto a nitrocellulose membrane (Thermo Fisher Scientific) using the Bio-Rad transfer system at 100 V for 60 min at 4°C or with Trans-Blot Turbo Mini PVDF Transfer Packs using Trans-Blot Turbo Transfer System (Bio-Rad). The membrane was blocked for 30 min with the Odyssey Blocking Buffer (TBS) (Licor) and stained overnight with primary antibodies at 4°C. Primary antibodies used were against: phospho-histone H3 (Cell Signalling, 9713S, 1:500 dilution), β-actin (Santa Cruz Biotechnology, 47778), cyclin B (Santa Cruz Biotechnology, 245) septin 9 (Sigma-Aldrich, HPA042564), GAPDH (Abcam, 8245, 1:5000 dilution), filamin A (Santa Cruz Biotechnology, 28284), ezrin-radixin-moesin (Cell Signalling, 3142), myosin RLC (Cell Signalling, 3672), phospho-myosin RLC (Cell Signalling, 3675), Histone H3 (Abcam, 1791) in 5% milk in PBS with 0.1% Tween 20. Antibodies were diluted 1:1000 unless stated otherwise. Following primary antibody incubation, membranes were washed three times with PBS with 0.1% Tween 20. Licor secondary antibodies conjugated to IRDyes were diluted 1:5000 in 5% milk in PBS with 0.1% Tween 20 and incubated with the membranes at room temperature for 60 min. Membranes were imaged with Odyssey FC system and the results were analysed with the Studio Lite software. Uncropped images of western blots from this paper are shown in Fig. S5.

qPCR

Cells were collected 24 and 48 h after siRNA treatment, and total RNA was extracted by using an RNeasy mini Kit (Qiagen) and reverse-transcribed using a cDNA Reverse Transcription Kit (Applied Biosystems), as described by the manufacturer. For each qPCR assay, a standard curve was performed to ensure the efficacy of the assay (between 90 and 110%). The Viia7 qPCR instrument (Life Technologies) was used to detect amplification level and was programmed with an initial step of 20 s at 95°C, followed by 40 cycles of 1 s at 95°C and 20 s at 60°C. Relative expression ($RQ=2^{-\Delta\Delta CT}$) was calculated using the Expression Suite software (Life Technologies), and normalization was done using both ACTB and GAPDH.

Levels of septins were measured using the following primers: SEPT2 forward, 5′-AAGGCAATACACAACAAGGTGA-3′, reverse- 5′-TTCTTCAATTTCATCCAGAATCC-3′; SEPT6 forward, 5′-TCGTCCAGCGAGTCAAAGAG-3′, reverse, 5′-TCTCGTCCTGGTGCAGTTTC-3′; SEPT7 forward, 5′-GAAGTTAATGGCAAAAGGGTCA, reverse, 5′-TCAAGTCCTGCATGTGTGTTC-3′; SEPT8 forward, 5′-TTCAGGACAGCGATGGTGAC, reverse, 5′-CTCCTTCCTCTGCAGCTCAC-3′; SEPT9 forward, 5′-CGGGACCTTCTCATCAGG, reverse, 5′-GGTACGCCTCGAAGTGGAT; SEPT10 forward, 5′-GTTGCTTCTGCCCTCCGG, reverse, 5′-CGGTGAAGCGGCTGTATCAG-3′; SEPT11 forward, 5′-TTACTACAGTCCCAGGCCCA, reverse, 5′-TGGCTTGCCAGGCTTTATGT-3′. ACTB and GAPDH were used as endogenous controls using the following primers ACTB forward, 5′-CCATCTACGAGGGGTATGCC-3′, reverse, 5′-GCGCTCGGTGAGGATCTTC-3′; GAPDH forward, 5′-AGCCACATCGCTCAGACAC-3′, reverse, 5′-GCCCAATACGACCAAATCC-3′.

Preparation of fixed samples for imaging

Samples, isolated blebs and cells were spun on poly-L-lysine coated 25 mm coverslips by centrifugation at 460 ***g*** for 10 min. Cells were fixed with 4% paraformaldehyde (PFA) in PBS for 10 min followed by 10 min permeabilisation with 0.2% Triton X-100 at room temperature. Blebs were fixed with combined permeabilisation-fixation for 6 min with 4% PFA in intracellular buffer with 0.2% Triton X-100 followed by 14 min fixation with 4% PFA in intracellular buffer at room temperature, followed by three washes with PBS. Samples were stained with DAPI and phalloidin–Alexa568 (1:500 dilution, Thermo Fisher Scientific, A12380) for 1 h, followed by three washes with PBS.

Samples were imaged using Olympus FluoView FV1200 Confocal Laser Scanning Microscope using a 60× oil objective (NA 1.4).

Live imaging and analysis

Cells we treated with siRNA for 24 h before the start of the overnight imaging. 30 min prior to imaging, the culture media was changed to Leibovitz's L-15 (Thermo Fisher Scientific) media supplemented with 10% FBS and 1% Penicillin-Streptomycin. Cells were imaged for 15 h at 37°C every 2 min on an inverted Olympus IX81 microscope, controlled via Velocity interface, and a Hamamatsu Flash 4.0v2 ScMOS camera. Imaging was performed with the brightfield setting under a 20× air objective.

Cell shape was analysed with manual segmentation using the measure feature of the FIJI image analysis software (Schindelin et al., 2012). Mitotic cell shape was measured in the cellular midplane (Fig. 4C; Fig. S3B), at the last frame of metaphase, i.e. the last frame where aligned chromosomes were observed, prior to anaphase onset and chromosome segregation. For a small subset of cells, even after cell rounding, the cells maintained protrusions that extended from the cell surface (see example in Fig. S3B). These protrusions were included in the cell contour; they occurred with comparable frequency in control and SEPT9 siRNA-treated cells. Rounding time was measured from the first frame where retraction of cell edges was observed (onset of rounding) to the first frame of completely round morphology; in cases where active rounding continued throughout metaphase, the end of rounding was set at the end of metaphase (last frame before chromosome separation onset). Ingression time was measured from the last frame where aligned chromosomes were observed (just before the onset of chromosome segregation) until the end of furrow ingression. Statistical analysis was performed for individual cells pooled over three independent experiments, sample numbers are reported in the figure legends.

STORM sample preparation, imaging and analysis

Samples were spun onto poly-L-lysine-coated 35 mm Dish High Precision 1.5 Coverslips (MatTek, P35G-0.170-14-C) by centrifugation at 460 ***g*** for 10 min. Samples were fixed for 6 min with 4% PFA in intracellular buffer with 0.2% Triton X-100 followed by 14 min with 4% PFA in intracellular buffer and further permeabilised for 10 min with 0.5% Triton X-100 in PBS. Samples were blocked for 30 min in 5% bovine serum albumin (BSA) in PBS before staining. Samples were stained by 1 h incubation with 1:200 phalloidin–Alexa-Fluor-647 (Thermo Fisher Scientific, A22287) diluted in PBS.

Samples were imaged with a buffer of 45 mM Tris-HCl, 10 mM NaCl, 10% glucose, 5 U/ml pyranose oxidase, 35 mM MEA, 40 µg/ml catalase and 2 mM cyclooctatetraene (COT) as previously described (Olivier et al., 2013).

Samples were imaged using the Zeiss Elyra 7 imaging set-up for single-molecule localisation using 64× objective with NA 1.46. Laser power was at 100% with 20 ms exposure for 10,000 frames. Acquisitions were corrected for drift using model-based correction, grouped and filtered for localisation precision 5–50 nm and number of photons 500–5000 using Gaussian distribution with the in-built Zeiss Black processing software.

Statistical analysis

Mass spectrometry results (Table 1; Tables S1–S3) were analysed using Excel Microsoft and Prism (GraphPad Software) was used for analysis of all other experiments. To compare means unpaired one-tailed Student's *t*-test was used or Mann–Whitney test for non-normally distributed samples as specified in the figure legends.

Acknowledgements

We thank all present and past Paluch lab members for critical discussions, Kevin Chalut, Ruby Peters and Iskra Yanakieva for comments on the manuscript, Guillaume Charras for feedback on the project and manuscript. Proteomic analyses were performed by the Center for Advanced Proteomics Analyses (CAPCA), a Node of the Canadian Genomic Innovation Network that is supported by the Canadian Government through Genome Canada.

Competing interests

The authors declare no competing or financial interests.

Author contributions

Conceptualization: N.V., E.K.P.; Methodology: N.V., S.N., M.S., P.P.R., E.K.P.; Formal analysis: N.V., S.N., P.P.R.; Investigation: N.V., G.L.; Data curation: N.V., S.N., M.S., P.P.R., E.K.P.; Writing - original draft: N.V., P.P.R., E.K.P.; Visualization: N.V., S.N.; Supervision: P.P.R., E.K.P.; Project administration: E.K.P.; Funding acquisition: P.P.R., E.K.P.

Funding

This work was supported by the Medical Research Council UK (MRC Programme Award MC_UU_12018/5 to E.K.P.), the European Research Council (Consolidator Grant 820188-NanoMechShape to E.K.P.), and grants from the Canadian Institutes of Health Research (MOP-142374 and PJT-152995 to P.P.R). P.P.R. is a Senior Scholar of the Fonds de la recherche du Québec-Santé (FRQS). N.V. was funded by a MRC LMCB PhD studentship. Open access funding provided by University of Cambridge. Deposited in PMC for immediate release.

Data availability

The raw mass spectrometry datasets have been deposited in ProteomeXchange through partner MassIVE under accession number PXD031308.

Peer review history

The peer review history is available online at https://journals.biologists.com/jcs/lookup/doi/10.1242/jcs.259993.reviewer-comments.pdf.

References

Bergert, M., Chandradoss, S. D., Desai, R. A. and Paluch, E. (2012). Cell mechanics control rapid transitions between blebs and lamellipodia during migration. *Proc. Natl Acad. Sci. USA* **109**, 14434-14439. doi:10.1073/pnas.1207968109

Biro, M., Romeo, Y., Kroschwald, S., Bovellan, M., Boden, A., Tcherkezian, J., Roux, P. P., Charras, G. and Paluch, E. K. (2013). Cell cortex composition and homeostasis resolved by integrating proteomics and quantitative imaging. *Cytoskeleton* **70**, 741-754. doi:10.1002/cm.21142

Bovellan, M., Romeo, Y., Biro, M., Boden, A., Chugh, P., Yonis, A., Vaghela, M., Fritzsche, M., Moulding, D., Thorogate, R. et al. (2014). Cellular control of cortical actin nucleation. *Curr. Biol.* **24**, 1628-1635. doi:10.1016/j.cub.2014.05.069

Cadart, C., Zlotek-Zlotkiewicz, E., Le Berre, M., Piel, M. and Matthews, H. K. (2014). Exploring the function of cell shape and size during mitosis. *Dev. Cell* **29**, 159-169. doi:10.1016/j.devcel.2014.04.009

Carrière, A., Cargnello, M., Julien, L.-A., Gao, H., Bonneil, É., Thibault, P. and Roux, P. P. (2008). Oncogenic MAPK signaling stimulates mTORC1 activity by promoting RSK-mediated raptor phosphorylation. *Curr. Biol.* **18**, 1269-1277. doi:10.1016/j.cub.2008.07.078

Chugh, P., Clark, A. G., Smith, M. B., Cassani, D. A. D., Dierkes, K., Ragab, A., Roux, P. P., Charras, G., Salbreux, G. and Paluch, E. K. (2017). Actin cortex

architecture regulates cell surface tension. *Nat. Cell Biol.* **19**, 689-697. doi:10.1038/ncb3525

Chugh, P. and Paluch, E. K. (2018). The actin cortex at a glance. *J. Cell Sci.* **131**, 1-9. doi:10.1242/jcs.186254

Ding, W. Y., Ong, H. T., Hara, Y., Wongsantichon, J., Toyama, Y., Robinson, R. C., Nédélec, F. and Zaidel-Bar, R. (2017). Plastin increases cortical connectivity to facilitate robust polarization and timely cytokinesis. *J. Cell Biol.* **216**, 1371-1386. doi:10.1083/jcb.201603070

Duarte, S., Viedma-Poyatos, Á., Navarro-Carrasco, E., Martínez, A. E., Pajares, M. A. and Pérez-Sala, D. (2019). Vimentin filaments interact with the actin cortex in mitosis allowing normal cell division. *Nature Commun.* **10**, 4200. doi:10.1038/s41467-019-12029-4

Ennomani, H., Letort, G., Guérin, C., Martiel, J.-L., Cao, W., Nédélec, F., De La Cruz, E. M., Thery, M. and Blanchoin, L. (2016). Architecture and connectivity govern actin network contractility. *Curr. Biol.* **26**, 616-626. doi:10.1016/j.cub.2015.12.069

Estey, M. P., Di Ciano-Oliveira, C., Froese, C. D., Bejide, M. T. and Trimble, W. S. (2010). Distinct roles of septins in cytokinesis: SEPT9 mediates midbody abscission. *J. Cell Biol.* **191**, 741-749. doi:10.1083/jcb.201006031

Field, C. M. and Alberts, B. M. (1995). Anillin, a contractile ring protein that cycles from the nucleus to the cell cortex. *J. Cell Biol.* **131**, 165-178. doi:10.1083/jcb.131.1.165

Gladfelter, A. S., Pringle, J. R. and Lew, D. J. (2001). The septin cortex at the yeast mother–bud neck. *Curr. Opin. Microbiol.* **4**, 681-689. doi:10.1016/S1369-5274(01)00269-7

Heusel, M., Frank, M., Köhler, M., Amon, S., Frommelt, F., Rosenberger, G., Bludau, I., Aulakh, S., Linder, M. I., Liu, Y. et al. (2020). A Global screen for assembly state changes of the mitotic proteome by SEC-SWATH-MS. *Cell Syst.* **10**, 133-155. doi:10.1016/j.cels.2020.01.001

Joo, E., Surka, M. C. and Trimble, W. S. (2007). Mammalian SEPT2 is required for scaffolding nonmuscle myosin II and its kinases. *Dev. Cell* **13**, 677-690. doi:10.1016/j.devcel.2007.09.001

Kim, M. S., Froese, C. D., Estey, M. P. and Trimble, W. S. (2011). SEPT9 occupies the terminal positions in septin octamers and mediates polymerization-dependent functions in abscission. *J. Cell Biol.* **195**, 815-826. doi:10.1083/jcb.201106131

Koenderink, G. H. and Paluch, E. K. (2018). Architecture shapes contractility in actomyosin networks. *Curr. Opin. Cell Biol.* **50**, 79-85. doi:10.1016/j.ceb.2018.01.015

Lancaster, O. M. and Baum, B. (2014). Shaping up to divide: coordinating actin and microtubule cytoskeletal remodelling during mitosis. *Semin. Cell Dev. Biol.* **34**, 109-115. doi:10.1016/j.semcdb.2014.02.015

Lee, M. G. and Nurse, P. (1987). Complementation used to clone a human homologue of the fission yeast cell cycle control gene cdc2. *Nature* **327**, 31-35. doi:10.1038/327031a0

Levayer, R. and Lecuit, T. (2012). Biomechanical regulation of contractility: spatial control and dynamics. *Trends Cell Biol.* **22**, 61-81. doi:10.1016/j.tcb.2011.10.001

Logue, J. S., Cartagena-Rivera, A. X., Baird, M. A., Davidson, M. W., Chadwick, R. S. and Waterman, C. M. (2015). Erk regulation of actin capping and bundling by Eps8 promotes cortex tension and leader bleb-based migration. *eLife* **4**, e08314. doi:10.7554/eLife.08314

Mostowy, S. and Cossart, P. (2012). Septins: the fourth component of the cytoskeleton. *Nat. Rev. Mol. Cell Biol.* **13**, 183-194. doi:10.1038/nrm3284

Murrell, M., Oakes, P. W., Lenz, M. and Gardel, M. L. (2015). Forcing cells into shape: the mechanics of actomyosin contractility. *Nat. Rev. Mol. Cell Biol.* **16**, 486-498. doi:10.1038/nrm4012

Olivier, N., Keller, D., Gönczy, P. and Manley, S. (2013). Resolution doubling in 3D-STORM imaging through improved buffers. *PLoS ONE* **8**, e69004. doi:10.1371/journal.pone.0069004

Ramanathan, S. P., Helenius, J., Stewart, M. P., Cattin, C. J., Hyman, A. A. and Muller, D. J. (2015). Cdk1-dependent mitotic enrichment of cortical myosin II promotes cell rounding against confinement. *Nat. Cell Biol.* **17**, 148-159. doi:10.1038/ncb3098

Salbreux, G., Charras, G. and Paluch, E. (2012). Actin cortex mechanics and cellular morphogenesis. *Trends Cell Biol.* **22**, 536-545. doi:10.1016/j.tcb.2012.07.001

Schindelin, J., Arganda-Carreras, I., Frise, E., Kaynig, V., Longair, M., Pietzsch, T., Preibisch, S., Rueden, C., Saalfeld, S., Schmid, B. et al. (2012). Fiji: An open-source platform for biological-image analysis. *Nat. Methods* **9**, 676-682. doi:10.1038/nmeth.2019

Serres, M. P., Samwer, M., Truong Quang, B. A., Lavoie, G., Perera, U., Görlich, D., Charras, G., Petronczki, M., Roux, P. P. and Paluch, E. K. (2020). F-Actin interactome reveals vimentin as a key regulator of actin organization and cell mechanics in mitosis. *Dev. Cell* **52**, 210-222. doi:10.1016/j.devcel.2019.12.011

Spector, I., Shochet, N. R., Kashman, Y. and Groweiss, A. (1983). Latrunculins: novel marine toxins that disrupt microfilament organization in cultured cells. *Science* **219**, 493-495. doi:10.1126/science.6681676

Spiliotis, E. T. (2018). Spatial effects - site-specific regulation of actin and microtubule organization by septin GTPases. *J. Cell Sci.* **131**, jcs207555. doi:10.1242/jcs.207555

Spiliotis, E. T. and Nakos, K. (2021). Cellular functions of actin- and microtubule-associated septins. *Curr. Biol.* **31**, 651-666. doi:10.1016/j.cub.2021.03.064

Stewart, M. P., Helenius, J., Toyoda, Y., Ramanathan, S. P., Muller, D. J. and Hyman, A. (2011). Hydrostatic pressure and the actomyosin cortex drive mitotic cell rounding. *Nature* **469**, 226-230. doi:10.1038/nature09642

Tinevez, J.-Y., Schulze, U., Salbreux, G., Roensch, J., Joanny, J.-F. and Paluch, E. (2009). Role of cortical tension in bleb growth. *Proc. Natl Acad. Sci. USA* **106**, 18581-18586. doi:10.1073/pnas.0903353106

Truong Quang, B. A., Peters, R., Cassani, D. A. D., Chugh, P., Clark, A. G., Agnew, M., Charras, G. and Paluch, E. K. (2021). Extent of myosin penetration within the actin cortex regulates cell surface mechanics. *Nature Commun.* **12**, 6511. doi:10.1038/s41467-021-26611-2

Toyoda, Y., Cattin, C. J., Stewart, M. P., Poser, I., Theis, M., Kurzchalia, T. V., Buchholz, F., Hyman, A. A. and Müller, D. J. (2017). Genome-scale single-cell mechanical phenotyping reveals disease-related genes involved in mitotic rounding. *Nature Commun.* **8**, 1266. doi:10.1038/s41467-017-01147-6

Yamashiro, S., Yamakita, Y., Ishikawa, R. and Matsumura, F. (1990). Mitosis-specific phosphorylation causes 83K non-muscle caldesmon to dissociate from microfilaments. *Nature* **344**, 675-678. doi:10.1038/344675a0

Figure S1

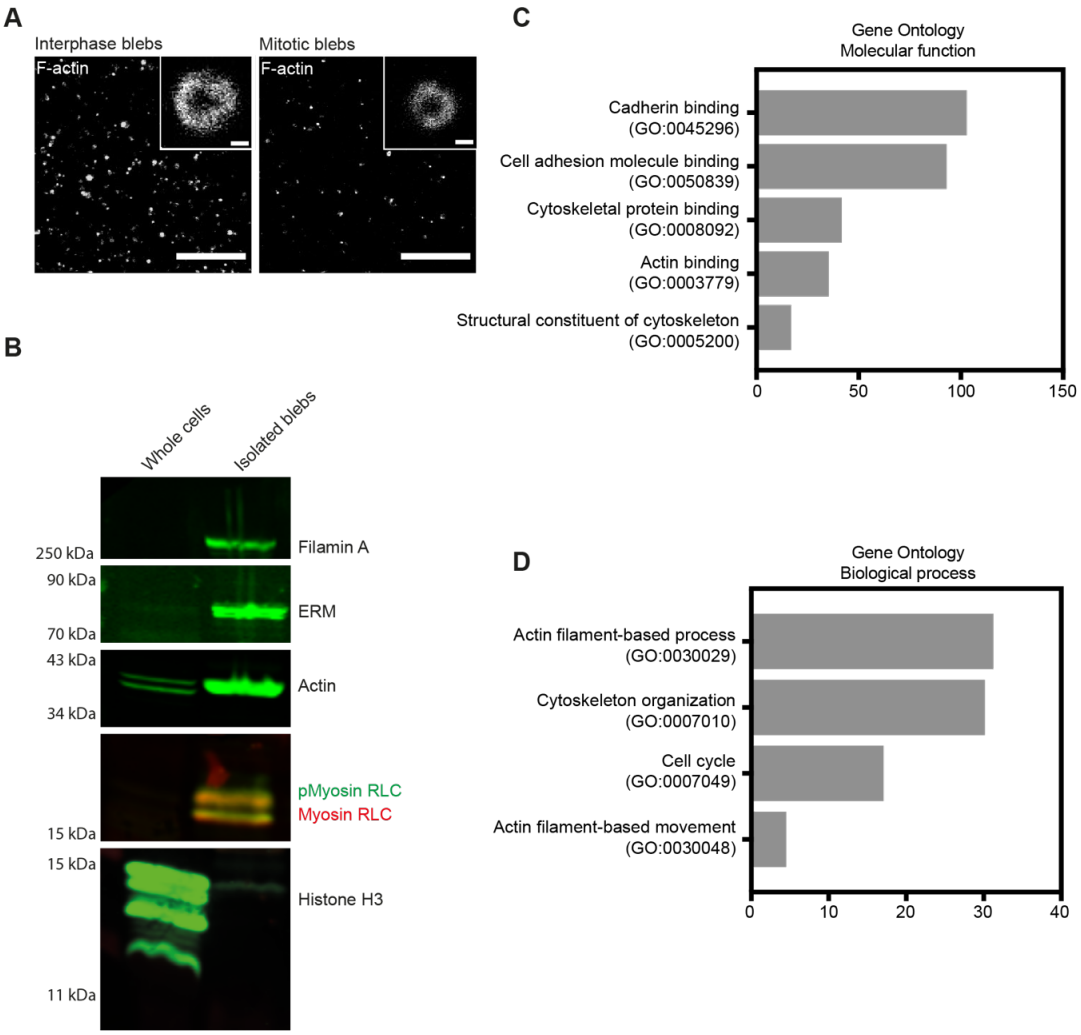

Fig. S1. Analysis of isolated blebs. (A) Representative confocal images of the actin cortex in blebs isolated from interphase (left) and mitotic (right) cells used for the proteomic analysis. The cortex was re-assembled after addition of an ATP regeneration system. White: phalloidin (F-actin). Insets: zoom-ed in individual blebs. Scale bars: 20 μm; 0.5 μm (inset). (B) Fluorescent western blot for filamin A, ERM (ezrin, radixin, moesin), actin, myosin regulatory light chain (RLC), phospho myosin RLC, actin and nuclear protein (histone H3) in whole cells and in isolated blebs (from unsynchronised cells). Equal amounts of total protein were loaded for western blot analysis as measured with Pierce Protein Assay. (C, D) Gene Ontology (GO) analysis of the selected 922 proteins, focusing on GO terms for molecular function (C) and biological function (D) related to the cell cortex.

Figure S2

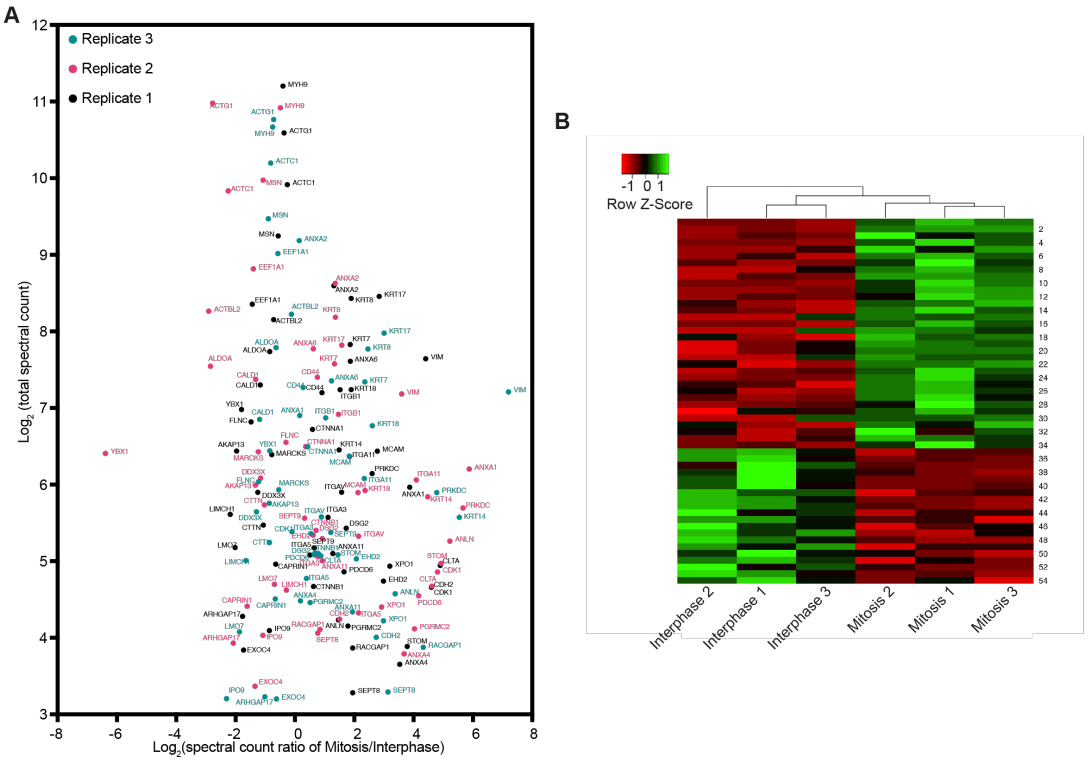

C

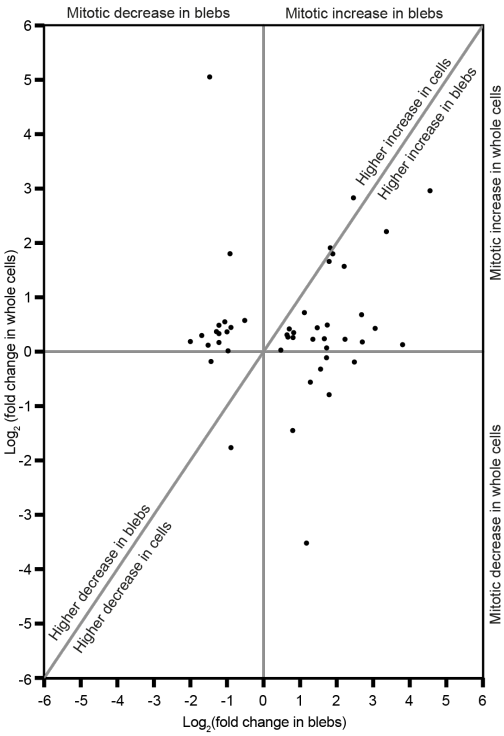

Mitotic decrease in blebs increase in cells			
Protein	Log_2FC bleb	Log_2FC cell	Ratio FC (bleb/cell)
FLNC	-0.971	0.0164	0.504
MYH9	-0.515	0.575	0.470
MSN	-0.889	0.447	0.396
CTTN	-1.00	0.365	0.388
ALDOA	-1.22	0.170	0.382
CALD1	-1.22	0.334	0.341
ACTBL2	-1.06	0.550	0.328
LIMCH1	-1.51	0.120	0.320
EXOC4	-1.29	0.370	0.317
IPO9	-1.22	0.487	0.307
ARHGAP17	-1.69	0.298	0.252
YBX1	-2.00	0.188	0.219
CAPRIN1	-0.916	1.80	0.152
LMO7	-1.47	5.05	0.0108

Mitotic decrease in blebs and cells			
Protein	Log_2FC bleb	Log_2FC cell	Ratio FC (bleb/cell)
MARCKS	-0.889	-1.76	1.83
AKAP13	-1.43	-0.179	0.419

Mitotic increase in blebs and cells			
Protein	Log_2FC bleb	Log_2FC cell	Ratio FC (bleb/cell)
PRKDC	3.80	0.132	12.7
XPO1	3.05	0.427	6.18
CDH2	2.70	0.177	5.76
CLTA	2.68	0.682	4.00
MCAM	2.23	0.230	4.00
SEPT8	1.73	0.068	3.16
VIM	4.55	2.96	3.01
PDCD6	1.66	0.236	2.69
CDK1	1.74	0.494	2.38
ANLN	3.36	2.21	2.23
ITGB1	1.35	0.231	2.17
ITGAV	1.47	0.438	2.05
KRT18	2.20	1.57	1.55
ITGA5	0.807	0.258	1.46
ITGA3	0.824	0.346	1.39
CTNNA1	0.475	0.0265	1.37
DSG2	1.12	0.719	1.32
CTNNB1	0.669	0.270	1.32
CD44	0.642	0.307	1.26
SEPT9	0.705	0.416	1.22
KRT7	1.80	1.66	1.10
RACGAP1	1.90	1.80	1.07
KRT8	1.83	1.91	0.945
KRT17	2.46	2.83	0.774

Mitotic increase in blebs decrease in cells			
Protein	Log_2FC bleb	Log_2FC cell	Ratio FC (bleb/cell)
ANXA6	1.18	-3.52	26.0
ITGA11	2.49	-0.186	6.37
ANXA4	1.80	-0.787	5.60
ANXA2	0.800	-1.45	4.74
EHD2	1.56	-0.321	3.68
ANXA11	1.28	-0.556	3.57
PGRMC2	1.72	-0.11	2.75

Fig. S2. Changes in levels of significantly changing actin binding proteins in blebs between interphase and mitosis. (A) Total interphase and mitosis spectral counts (log scale, y-axis) for the 54 actin-related proteins that significantly change in levels between interphase and mitotic blebs (listed in Table 1); x-axis shows enrichment between interphase and mitosis. Datapoints for all three experimental replicates are shown. (B) Heatmap of the levels (normalised spectral counts) of the 54 actin-related proteins listed in Table 1 in the different experimental replicates of interphase and mitotic blebs. (C) Mitotic enrichment of the 54 actin-related proteins reported in Table 1, in isolated blebs (x-axis) vs whole cells (y-axis). Protein levels for whole cells were taken from Heusel et al., 2020, where cells were synchronised in interphase using a double thymidine block and in mitosis with a thymidine block followed by synchronisation with nocodazole and mitotic shake-off. Mean spectral counts across 3 replicates of blebs were used to calculate enrichment. Spectral counts were normalised to account for variation between experiments.

Journal of Cell Science • Supplementary information

Figure S3

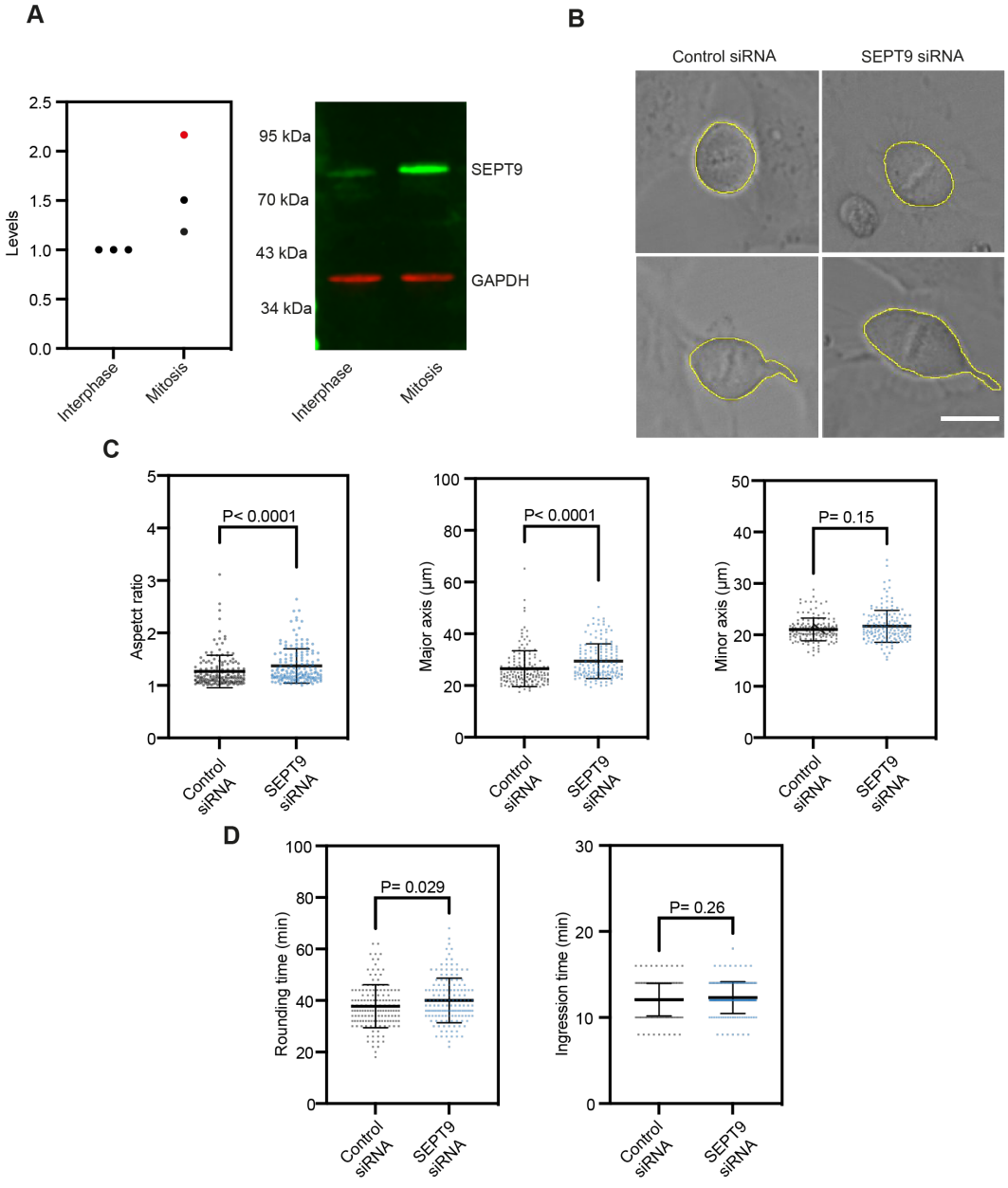

Fig. S3. Role of septin 9 in mitosis. (A) Representative fluorescent western blot (left panel), and related quantification (right panel), of septin 9 levels in mitotic and interphase whole cell lysates, normalised to the loading control (GAPDH) and relative to interphase levels. Membrane is representative of n=3 samples used for quantification. Red datapoint on the graph corresponds to the sample on the western blot membrane image (left panel). (B) Example of brightfield images of the cellular midplane of live mitotic cells treated with control and SEPT9 siRNA, that were used to analyse cell shape parameters (panel C and also Fig. 4D,E). A small subset of the cells, both in controls and in SEPT9 siRNA treated cells, displayed large protrusions

that did not retract during cell rounding (example pictures in lower row); these protrusions were included in cell shape quantification. Scale bar: 20 μm. (C) Quantification of cellular aspect ratio, major axis, and minor axis in mitosis in control and SEPT9 siRNA treated cells, n=156 for each control and SEPT9 siRNA treated sample. (D) Rounding and furrow ingression times in control and septin 9-depleted cells, n=149 (SEPT9 siRNA) and 151 (control). Graph, mean ± 1 standard deviation, 3 independent experiments; Statistics: Mann-Whitney test.

Figure S4

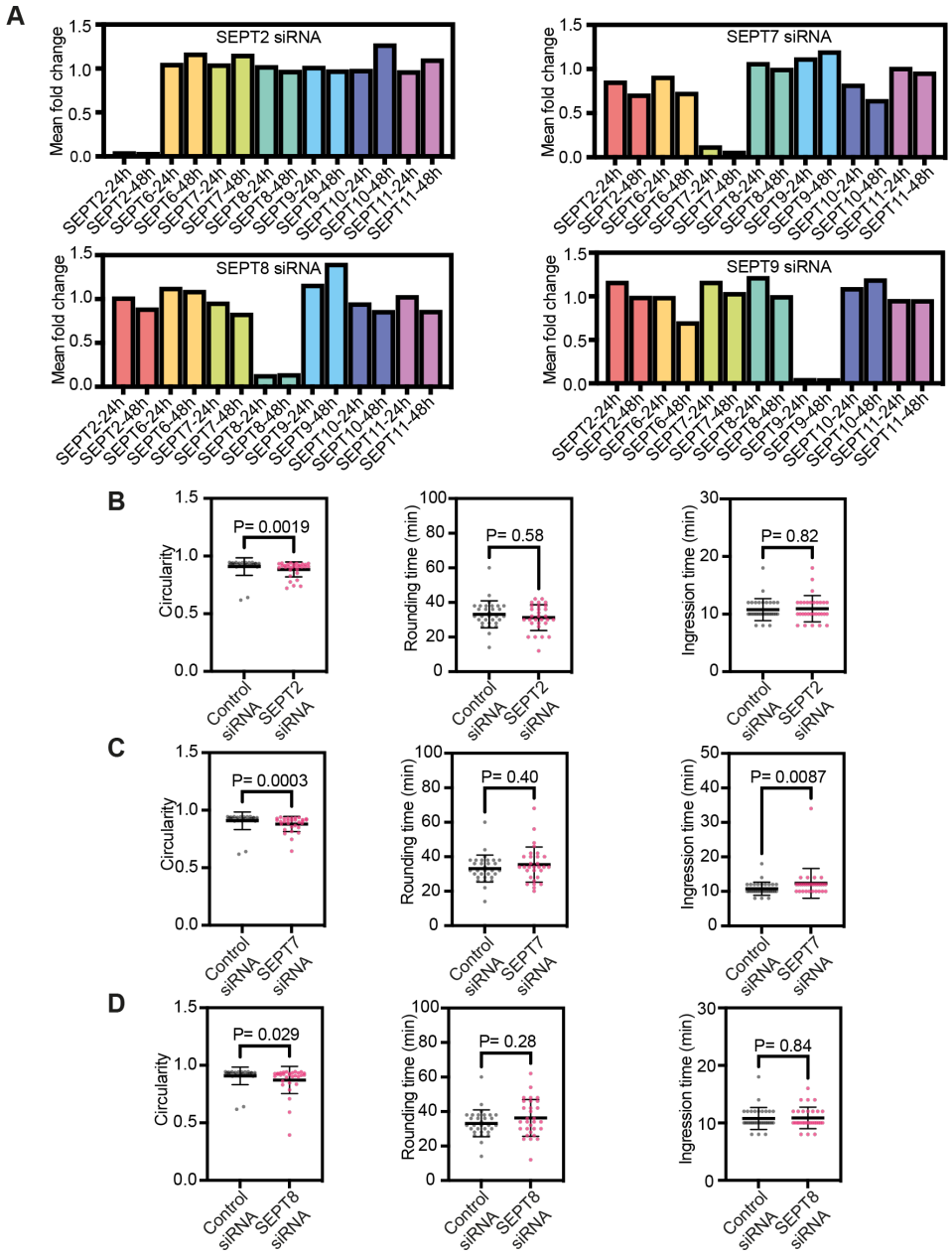

Fig. S4. Role of other septins in mitosis. (A) Cellular expression levels of SEPT2, SEPT6, SEPT7, SEPT8, SEPT9, SEPT10, SEPT11 24h and 48h after treatment with SEPT2, SEPT7, SEPT8, or SEPT9 siRNA. Levels are displayed as fold change compared to the levels observed in samples treated with control siRNA. Mean change of three experiments is displayed. (B-D) Quantification of circularity of metaphase cells, rounding and furrow ingression time for cells treated with control and (B) SEPT2, (C) SEPT7, (D) SEPT8 siRNA. Graph, mean ± 1 standard deviation, 3 independent experiments, n=30 for each sample, Statistics: Mann-Whitney test.

Blot Transparency.

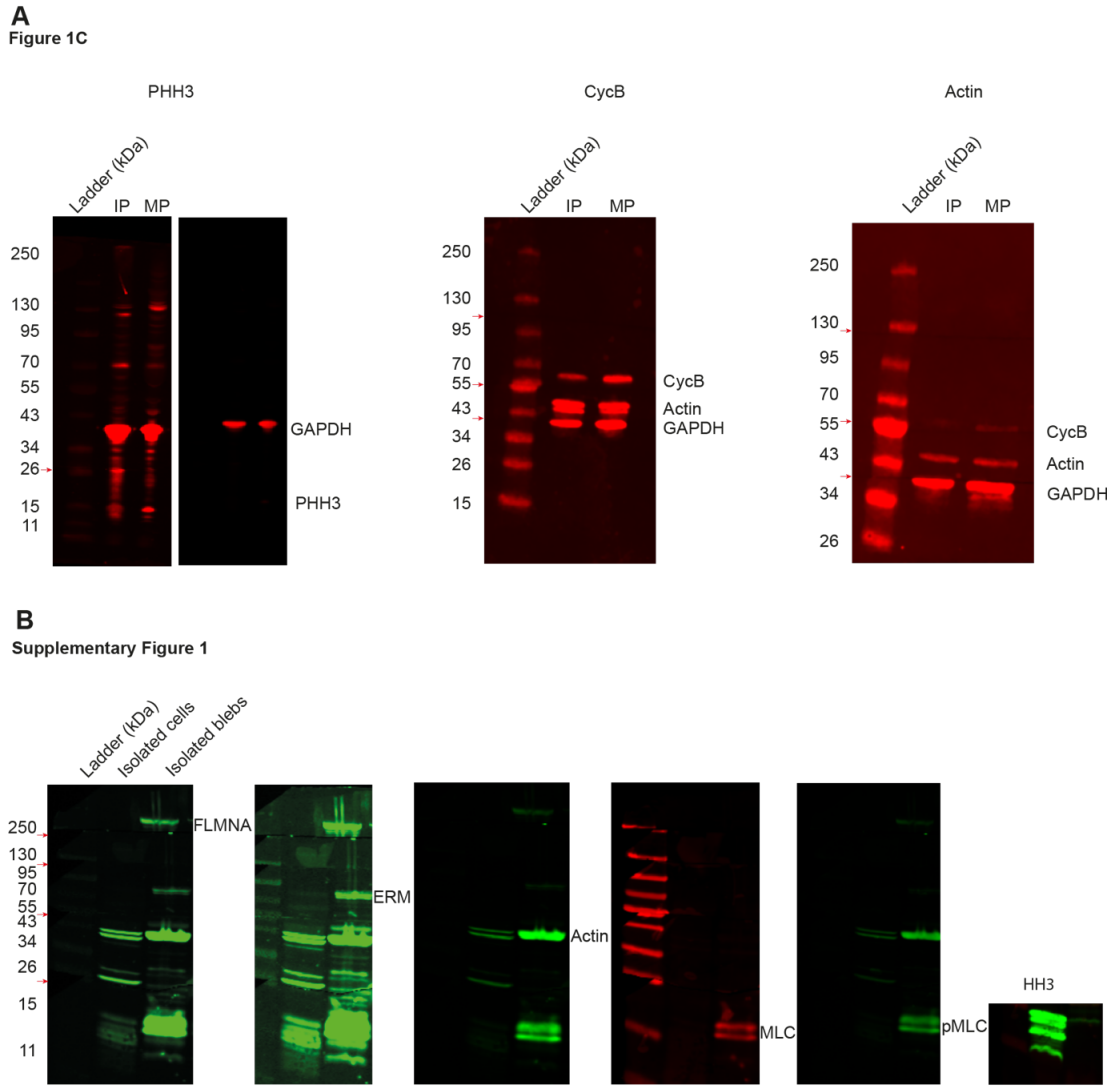

Fig. S5. Blot Transparency. Uncropped western blots corresponding to the blots displayed in various figures.
(A) Uncropped western blots for Figure 1C. PHH3: Uncropped blot stained for PHH3 and GAPDH. Left: Exposure used for imaging and quantification of PHH3, in which GAPDH signal was overexposed. Right: Exposure used for imaging of GAPDH signal. The membrane was cut at ~26 kDa, which can be noticed through misaligned protein markers at the corresponding molecular weight. CycB: Uncropped blot stained for CycB, actin and GAPDH. This image was used in Figure 1C as an example of cyclin staining. The membrane was cut at at ~40 kDa, ~55 kDa, and ~100 kDa, which can be noticed through misaligned protein markers at the corresponding molecular weights. Actin: Uncropped blot stained for CycB, actin and GAPDH. This image was used in Figure 1C as an example of actin staining. The membrane was cut at at ~40 kDa, ~55 kDa, and ~100 kDa, which can be noticed through misaligned protein marker

Journal of Cell Science • Supplementary information

at the corresponding molecular weights. Protein Ladder: PageRuler Prestained NIR Protein Ladder. (B) Uncropped western blots for Figure S1. Images of the same blot at different exposures, adjusted for quantification of levels of specific proteins highlighted on the right-hand side of each membrane image. The membrane was cut at the triangular marks noticeable on the left side of the blot. Before staining for HH3, the membrane (between 11 and 15 kDa) was stripped. Protein Ladder: PageRuler Prestained NIR Protein Ladder.

Red arrows indicate where the membranes were cut for antibody incubation and re-aligned for imaging.

Uncropped blots are not provided for Figure 4D and Supplementary Figure 4B as these figures already display large sections of uncropped blots.

Table S1. Proteins detected in blebs. Normalised spectral counts of all proteins detected by mass spectrometry of isolated blebs.

Click here to download Table S1

Table S2. Proteins detected in both interphase and mitotic blebs. Mean (normalised) spectral counts in interphase and mitosis, ratio of the means between mitosis and interphase (calculated from 3 replicates), and P-value calculated with Student's t-test, for the 922 proteins detected in both interphase and mitosis isolated bleb samples. Manually selected actin-related proteins (see Main text for list curation criteria) are highlighted in yellow.

Click here to download Table S2

Table S3. **Actin-related proteins detected in blebs.** Average PAI (spectra count normalised to molecular weight), ratio of the means, and P-value (calculated with Student's t-test) for the 238 actin-related proteins detected with blebs. Right column: rounding force changes upon esiRNA treatment against the proteins (as reported in Toyoda et al., 2017). Not tested: protein not examined; No change: protein for which no change was detected with any of the esiRNA tested; Potentially lower force: protein for which the change in rounding force was detected with some of the esiRNA sequences tested; Lower force: protein for which rounding force changed with all esiRNA sequences tested in (Toyoda et al., 2017).

Click here to download Table S3

Journal of Cell Science • Supplementary information

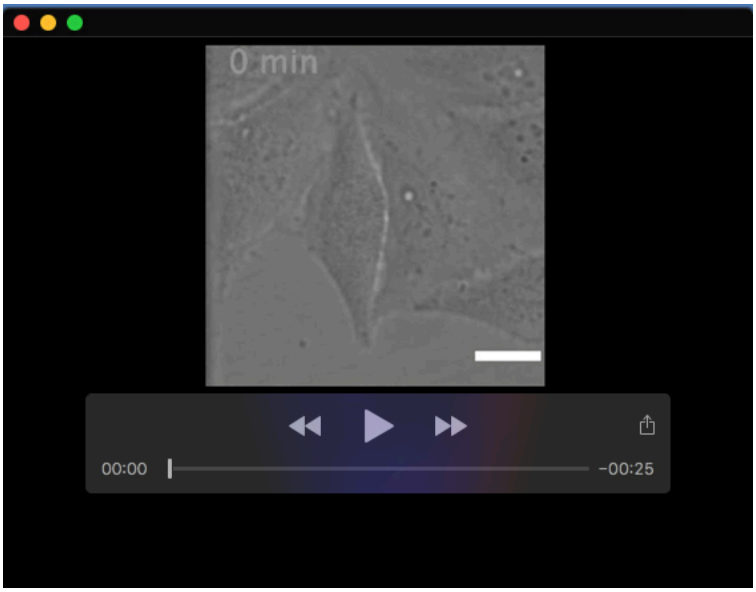

Movie 1. Dividing cell transfected with control siRNA. Movies from live-cell imaging were used for quantification of cell shape (Figure 4D-E, Supplementary Figure 4D). Time resolution= 2 min. Scale bar = 20 μm.

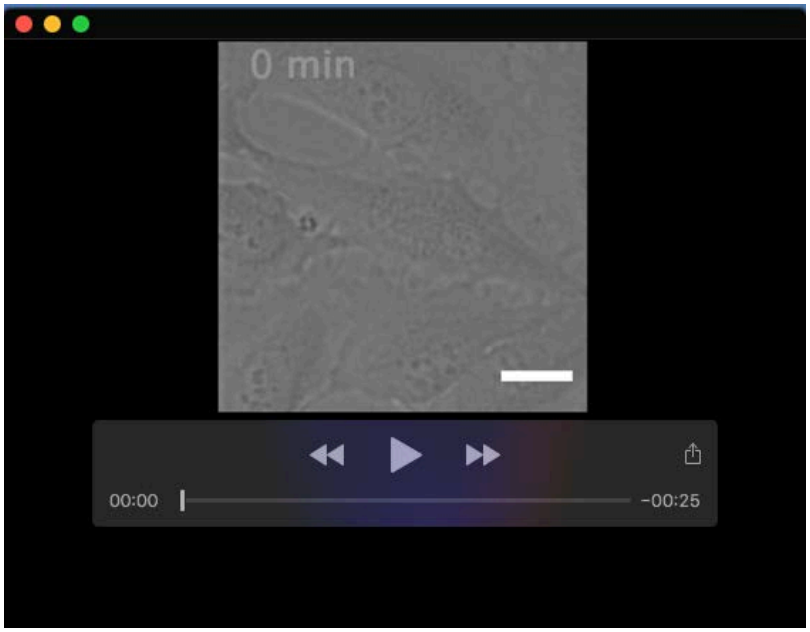

Movie 2. Dividing cell transfected with SEPT9 siRNA. Movies from live-cell imaging were used for quantification of cell shape (Figure 4D-E, Supplementary Figure 4D). Time resolution= 2 min. Scale bar = 20 μm.

Journal of Cell Science • Supplementary information